



The  
University  
Of  
Sheffield.

## **Practical Magnetic Tomography for Lead Batteries**

**By:**

Harry Thomas Harrison

A thesis submitted in partial fulfilment of the requirements for the degree of  
Doctor of Philosophy

The University of Sheffield  
Faculty of Engineering  
Department of Electronic and Electrical Engineering

October 2017



## **Abstract**

A variety of economic factors currently motivate the development of electrochemical energy storage. The effective use of renewable energy requires short term storage, for which electrochemical cells may be used. Electrified transport is also driving development; stored energy limits the range of electric vehicles. In hybrid vehicles, improved dynamic charge acceptance will help to optimise powertrain efficiency.

A non-invasive measurement of current distribution within a cell is a useful aid to understanding its operation and optimising its design. Here, the coupling between the cell current and the resulting magnetic field is exploited by taking measurements of magnetic flux density outside the cell and inferring the current distribution within. This technique may be termed magnetic tomography or magnetotomography.

In this thesis, a practical system is implemented in order to observe the current distribution within a single lead acid cell. An existing method of constraining and solving the inverse problem is adapted for use in conjunction with 3D finite element software, to make it suitable for modelling the complex geometry of a commercial electrode. Some tolerance of unknown material conductance is built into the solver method. An array of sensors is used to obtain a set of magnetic field measurements simultaneously, allowing temporally- and spatially-resolved current distribution images.

Solutions from the magnetic tomography system are verified against data from an array of ferrous cores, submerged in the electrolyte. Measurements are taken while the cell is operated at a current of approximately 0.625 C. The current distribution is found to be very uniform throughout most of the testing, although fatigue of the cell plates does lead to a non-uniform distribution. The magnetic tomography system is tested on both uniform and non-uniform distributions. Mean absolute errors of approximately 5 – 7 % are achieved. The effect of model errors on solution accuracy is investigated.

## **Acknowledgements**

I would like to thank my supervisors, Dr James Green and Professor David Stone, for their support and guidance, and for the opportunity to conduct this research in the first place.

Thanks to the students and staff who I've shared a space with, for sharing ideas and making the often solitary work enjoyable. Tea breaks are important. In particular, I'd like to thank Dave Hewitt, Glynn Cooke and everyone from ME01 as well as Tim Lewis-Roberts, Brett Harrison and Richard Hodgkinson.

The practical side of the project was often the most rewarding, and I'm indebted to all the extremely knowledgeable and patient EEE technical staff who helped turn rough ideas into tangible things. Wayne Frankish, David Miller, Dave Snowden, Richard Garraway, Dianne Webster, Kevin Jackson and Peter Trend have all had to put up with more than their share of my ill-informed questions.

My partner Rosa has put up with a lot of take-home stress, but her support has probably meant the difference between completing and not. Likewise, I am privileged to have always had the opportunity to pursue my interests with the full support of my family, to whom I am always grateful.

## Table of Contents

Abstract .....	i
Acknowledgements .....	ii
1 Introduction .....	1
1.1 Abbreviations and Symbols .....	1
1.1.1 Abbreviations .....	1
1.1.2 Mathematical symbols .....	1
1.2 Motivation .....	3
1.2.1 Stationary batteries and grid storage .....	4
1.2.2 Electric/hybrid car market .....	4
1.2.3 Lead batteries within the battery market .....	5
1.2.4 Causes of inhomogeneous current distribution and effects on performance .....	6
1.3 Thesis Outline and Contribution .....	8
1.4 Publications .....	10
2 Literature Review .....	11
2.1 Lead Acid Batteries Background .....	11
2.1.1 Overview .....	11
2.1.2 Chemical reactions .....	11
2.1.3 Open circuit voltage .....	12
2.1.4 Potentials during charge and discharge .....	12
2.1.5 Conduction in the electrolyte .....	13
2.1.6 History .....	14
2.2 Existing Current Distribution Measurement Methods .....	14
2.2.1 Modelling .....	14
2.2.2 Sense wires .....	15
2.2.3 Reference electrodes .....	16
2.2.4 Split electrodes .....	18
2.2.5 Magnetic resonance imaging .....	19

2.2.6	X-ray and neutron imaging methods .....	19
2.2.7	Flow-through magnetic sensor array .....	20
2.3	Magnetic Tomography .....	23
2.3.1	Solver methods.....	23
2.3.2	Practical considerations .....	33
2.4	Summary of Chapter 2 .....	34
3	Experimental Setup .....	35
3.1	System Definition .....	35
3.2	Magnetic Imaging System .....	36
3.2.1	Functional description.....	37
3.2.2	Hardware structure .....	38
3.2.3	Firmware .....	40
3.2.4	Solver.....	42
3.3	Internal Current Distribution Measurement.....	43
3.3.1	Reference electrode pair.....	43
3.3.2	Magnetic current sensor array.....	47
3.4	Cell.....	49
3.4.1	Initial design .....	49
3.4.2	Improved design.....	55
3.4.3	Bypass switch .....	59
3.5	Current Control .....	67
3.5.1	Requirements specification.....	67
3.5.2	Constructed design.....	67
3.6	Summary of Chapter 3 .....	69
4	Magnetic Tomography Solver Development .....	70
4.1	Problem Definition .....	70
4.2	2D Current Distributions .....	71
4.2.1	Gradient field.....	71

4.2.2	Matrix inversion .....	79
4.2.3	Extrapolating 3D from 2D.....	86
4.3	3D Current Distributions .....	88
4.3.1	Divergence-free models and special basis projection.....	88
4.3.2	Simulated 3D circuit .....	95
4.3.3	Using existing finite element software.....	99
4.3.4	Extending the basis to include plate resistance variation.....	104
4.3.5	Real 3D circuit.....	108
4.3.6	Using measured data as the basis.....	110
4.3.7	Alternative sensor placements and increased resolution.....	113
4.4	Summary of Chapter 4 .....	121
5	Development of Flow-Through Sensor .....	123
5.1	Simulation of Single Transducer.....	124
5.2	Design Development .....	125
5.2.1	Core layout .....	125
5.2.2	Leakage Compensation .....	136
5.2.3	Sensor choice .....	140
5.2.4	Fitting the Core to the Sensors.....	145
5.2.5	Chemical resistance testing.....	147
5.2.6	Plastics design and construction .....	148
5.3	System Integration and Testing.....	153
5.3.1	Multiplexing and firmware.....	153
5.3.2	Software .....	156
5.3.3	Verification and calibration .....	160
5.4	Summary of Chapter 5 .....	166
6	Experimental Verification of Magnetic Tomography System .....	167
6.1	Hypothesis and Motivation.....	168
6.2	Method.....	168

6.2.1	Experimental system .....	168
6.2.2	Procedure .....	172
6.3	Results and Discussion .....	176
6.3.1	Cell terminal voltage .....	176
6.3.2	Flow-through sensor measurements .....	179
6.3.3	Magnetic imaging results .....	181
6.4	Evaluation.....	196
6.4.1	Error sources .....	196
6.4.2	Validity of results.....	198
6.5	Summary of Chapter 6 .....	200
7	Conclusion and Future Work.....	202
7.1	Conclusion .....	202
7.2	Future Work .....	203
7.2.1	Short term improvements.....	204
7.2.2	Longer term improvements .....	205
8	References.....	207
	Appendix I – bh data for M330-35A Electrical Steel .....	215
	Appendix II – FTS Arduino Firmware .....	216
	Main.ino .....	216
	myHMC.cpp.....	218
	myHMC.h.....	222
	Appendix III – FTS Octave Code.....	223
	Main – rwcswitch.m .....	223
	Library.....	227
	Appendix IV – Solver Octave Code .....	230
	Main – regtools_ma.m .....	230
	Library.....	231
	Appendix V – Magnetic Imaging Code Acknowledgement .....	234



# 1 Introduction

## 1.1 Abbreviations and Symbols

### 1.1.1 Abbreviations

Standard chemical symbols (*e.g.* H<sub>2</sub>O, Pb) are used where appropriate. Some common abbreviations are adopted. A guide to these is given in

Table 1.1.

Abbreviation	Meaning
1D, 2D, 3D	1-Dimensional, 2-Dimensional, 3-Dimensional
AC	Alternating Current
DC	Direct Current
DPDT	Dual Pole Dual Throw, a class of switch
I <sup>2</sup> C	Inter-Integrated Circuit, a common communication protocol for interfacing integrated circuits
IC	Integrated Circuit
LSB	Least Significant Bit
MAE	Mean Absolute Error
MOSFET	Metal Oxide Semiconductor Field Effect Transistor
NPN	Bipolar junction transistor formed from alternately N-doped, P-doped, N-doped semiconductor. Switched 'on' with a positive base-emitter voltage.
PC	Personal Computer
PCB	Printed Circuit Board
PNP	Bipolar junction transistor formed from alternately P-doped, N-doped, P-doped semiconductor. Switched 'on' with a negative base-emitter voltage.
SoC	State of Charge
SPDT	Single Pole Dual Throw, a class of switch
USB	Universal Serial Bus, a common protocol for interfacing peripherals to a personal computer

Table 1.1 – Abbreviations used.

### 1.1.2 Mathematical symbols

All mathematical symbols used in the text are given in *italic lowercase* or *ITALIC UPPERCASE*. Vector quantities are given in **bold**. Matrices are given in **BOLD CAPITALS**. Components of a circuit are sometimes referred to by a letter and a number, *e.g.* R1, R2 to label two resistors in a circuit. These are given in the same font as the body text when referring to a component, but when used in an equation as a quantity they are given in italic, for example  $v = r_1/r_2$ . The transpose of a matrix **A** is denoted **A**\*

Tesla (T) is the SI unit of magnetic flux density, however it is common for commercial magnetic sensors to be specified in terms of Gauss ( $1 \text{ G} = 1 \times 10^{-4} \text{ T}$ ). Tesla is used preferentially but Gauss is used if it permits the reader to refer to a sensor's datasheet more easily.

<b>Symbol</b>	<b>Meaning</b>	<b>Unit, including value if a constant</b>
$\mathbf{i}$	Current vector	Ampere, A
$i$	Current magnitude	Ampere, A
$\mathbf{I}$	Set of currents	Ampere, A
$\mathbf{j}$	Current density vector	Ampere per metre, $\text{A m}^{-1}$
$\mathbf{J}$	Set of current densities	Ampere per metre, $\text{A m}^{-1}$
$v$	Voltage	Volt, V
$r$	Resistance	Ohm, $\Omega$
$\mathbf{R}$	Set of resistances	Ohm, $\Omega$
$\sigma$	Conductivity	Siemens per metre, $\text{S m}^{-1}$
$v_{gs}$	Gate-source voltage of a MOSFET	Volt, V
$v_s$	Source voltage of a MOSFET	Volt, V
$r_{dsON}$	Drain-source resistance of a MOSFET when switched on	Ohm, $\Omega$
$\mathbf{b}$	Magnetic flux density vector	Tesla, T or Gauss, G
$b$	Magnetic flux density magnitude (scalar)	Tesla, T or Gauss, G
$b_x, b_y, b_z$	$x$ , $y$ and $z$ components of $\mathbf{b}$ , respectively.	Tesla, T or Gauss, G
$\mathbf{B}$	One set of measurements of $\mathbf{b}$ (one measurement per sensor)	Tesla, T or Gauss, G
$\mathbf{B}_y$	A set of measurements of $b_y$ (or $b_x$ or $b_z$ depending on subscript)	Tesla, T or Gauss, G
$\mathbf{B}_s$	A multiple set of measurements of partial fields (one $\mathbf{B}$ per independent current segment in solver)	Tesla, T or Gauss, G
$\phi$	Magnetic flux	Weber, Wb
$S$	Reluctance	Inverse Henry, $\text{H}^{-1}$
$F_m$	Magnetomotive force	Ampere turn, A
$\mu$	Magnetic permeability	Henry per metre, $\text{H m}^{-1}$
$v_{cell}$	Terminal voltage of cell	Volt, V
$v_{oc}$	Open-circuit voltage of a cell	Volt, V
$R$	Gas constant	$8.314 \text{ J mol}^{-1} \text{ K}^{-1}$
$T$	Temperature	Kelvin, K

<b>Symbol</b>	<b>Meaning</b>	<b>Unit, including value if a constant</b>
$F$	Faraday constant	96485.33289(59) C mol <sup>-1</sup>
$\alpha$	Thermodynamic activity	Dimensionless
$(\eta_{ct})_{a,c}$	Charge transfer polarisation at the (a)node or (c)athode	Volt, V
$(\eta_c)_{a,c}$	Concentration polarisation at the (a)node or (c)athode	Volt, V
$D$	Diffusion coefficient	Metre squared per second, m <sup>2</sup> s <sup>-1</sup>
$C$	Concentration	Dimensionless
$q$	Ion flux	Mole per metre squared per second, mol m <sup>-2</sup> s <sup>-1</sup>
$\delta_L$	Boundary layer thickness	Metre, m
$T$	Circuit law matrix	Dimensionless
$K$	Electromagnetic coupling matrix	Henry per metre squared, H m <sup>-2</sup>
$\lambda$	Regularisation parameter	Dimensionless
$R_\lambda$	Approximation of inverse coupling matrix $K^{-1}$	Depends on units of $K$
$d$	Distance	Metre, m
$t$	Time	Second, s, minute
$l$	Length	Metre, m
$w$	Width	Metre, m
$c$	Thickness	Metre, m
$A$	Area	Metre squared, m <sup>2</sup>
$f$	Frequency	Hertz, Hz
$\hat{n}$	Unit normal vector	Dimensionless
$\nabla$	Del/Nabla, vector differential operator	Dimensionless

Table 1.2 – Mathematical symbols used.

## 1.2 Motivation

The work in this thesis is concerned with spatially-resolved measurements inside an electrochemical cell. The diversity of applications of electrochemical cells yields some very differently specified designs. The size of sensors and control circuits, as well as achievable mechanical tolerances, dictates that good spatial resolution is most easily achieved when studying a reasonably physically large cell. For this reason, the motivation for the study is

defined in relation to the relatively large batteries used in stationary or automotive energy storage applications rather than for those designed for consumer electronics, which are typically smaller.

### **1.2.1 Stationary batteries and grid storage**

Batteries may be used in stationary energy storage applications. A battery can store and recover a useful amount of energy reasonably quickly; they have lower specific energy and specific power than a combustible-fuel based system [1], but higher specific energy than a capacitor [2]–[4]. A battery converts the energy from electrical to chemical and back again very efficiently – typically more than 90 % of the charging energy is available on discharge [4]. They are employed to provide backup power for critical systems and for storing power from domestic photovoltaic systems [5]. Batteries are also increasingly used for load levelling at the grid scale [6], [7], motivated in part by the increasing use of renewable energies, some of which give an intermittent supply [8].

A battery used in this application must have a low cost per unit capacity, long life and be safe and reliable to operate [4], [6]. Battery technologies generally give a low total capital cost per Watt but have a high annualised life cycle cost per Watt when compared with other electrical energy storage technologies [9]. Currently the dominant grid-scale energy storage technology for rapid response is pumped hydro-electric storage [9], [10], which may typically have a capacity greater by a factor of < 100 (in terms of energy and power) than current battery energy storage systems. However, batteries have the advantage of modularity and portability as well as not being dependent on local geography [4].

### **1.2.2 Electric/hybrid car market**

Electrifying automobiles, either fully or through hybridisation with internal combustion engines, is presently an active area of research and development. The reason for this is to mitigate some of the serious negative environmental impacts of internal combustion engine vehicles, such as greenhouse gas emissions and toxic air pollution [2], [11]. A fully battery-powered vehicle is an idea which became popular in the very early days of automobile design, but was then superseded by internal combustion designs due to greater range offered by an internal combustion engine [2]. ‘Range anxiety’ is a term given to the influence on driver behaviour due to the typically shorter range and less convenient charging options offered by and for electric vehicles [12] compared with internal combustion-powered vehicles. Hybrid vehicles, using a powertrain composed of both internal combustion and electrical power, may

be refuelled just like a fully internal combustion-powered vehicle. This offers the same convenient experience to the user, while improving fuel economy. Exhaust gases are still produced, which impact negatively on local air quality. Fully electrified and hybrid vehicles offer the user reduced running costs (due to better fuel economy) in return for a usually higher initial cost [13]. The market share is predicted to increase by the majority of economic models, although the rate of increase depends heavily on the model used [13].

The hybridisation and electrification of vehicles requires high performance batteries in terms of energy density and specific energy [14], high current delivery (cold and warm cranking) [15], long service life [16], and dynamic charge acceptance [17]. In addition, cost of the batteries must be minimised [14] to bring the price of electric vehicles and hybrid electric vehicles to a level that is competitive with internal combustion engine vehicles. The wide variety of levels of hybridisation (plug-in hybrid, mild hybrid, micro-mild hybrid *etc.*) yields an equally wide variety of battery requirement specifications [17], [18]. Even in vehicles powered purely by internal combustion engines, stop-start functions as well as more sophisticated power management place more demand on the battery than in the traditional starting-lighting-ignition application [17].

### **1.2.3 Lead batteries within the battery market**

Lead batteries are easily and widely recycled – over 95 % of lead batteries sold in the US are recycled at the end of life [19]. Lead is hazardous to health and the environment, so while recycling is preferable to releasing into the environment, people involved in the supply chain can be harmed if procedures aren't made safe [20], [21]. Turner [20] provides an analysis of the lead commodity chain in the United States, showing how rates of recycling have been affected by economic and public health factors, and also the changing structure of the lead smelting and refining industry. The high specific energy ( $150 \text{ W h kg}^{-1}$ , [22], [23]) of lithium-ion batteries has led to their widespread use in consumer electronics. Lead batteries have a significantly lower specific energy ( $35 \text{ W h kg}^{-1}$  [22]). However, the low cost of lead batteries in  $\text{W h } \$^{-1}$  compared to lithium- or nickel-based batteries [24] means that it is the dominant chemistry (in the form of valve regulated lead acid or VRLA) used in electric bicycles in China. This market was the fastest growing vehicle market in the years 1999-2006 [25]. It is possible that the Chinese electric bicycle market will move towards lithium-ion in future as incomes increase (electric bicycles in Europe and Japan are more often lithium-ion based).

### 1.2.4 Causes of inhomogeneous current distribution and effects on performance

Consideration of the current path taken through a cell of large cross-section area provides some insight into why uniform current distribution does not always occur. Figure 1.1, part (a) shows a uniform electrolyte current, indicating that all areas of the cell plate are contributing to the cell terminal current equally. Part (b) shows the current within the plate which must be supported by the plate grid. The current in the plate ranges over approximately  $> 4$  orders of magnitude, between the terminal in the top left and the right edge of the plate. Therefore careful grid design is important to support the large currents near the terminal, while minimising weight.

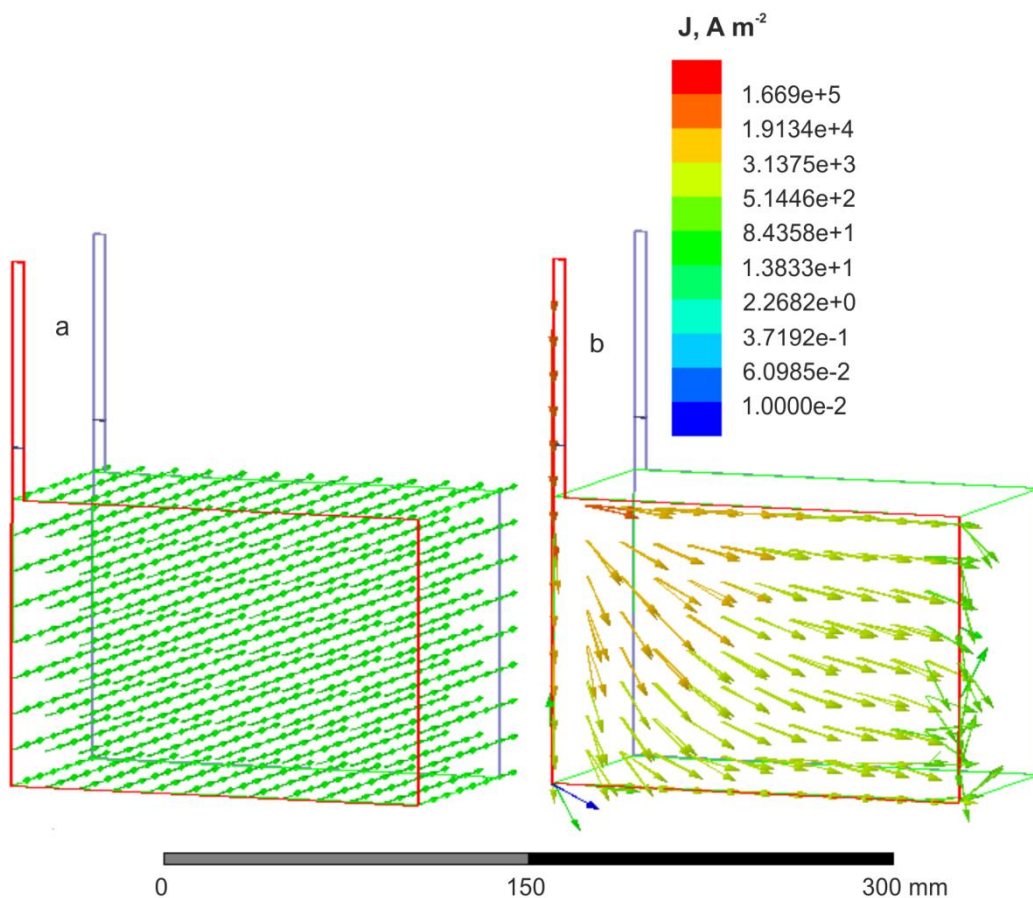


Figure 1.1 – Simulated current path through a cell. (a) shows the electrolyte current is uniform in this case. (b) shows that the resulting plate current is highly non-uniform.

In practice, the current density distribution in the electrolyte is not always uniform. Calábek *et al.* [26] demonstrate how commercial plate grids, when stripped of their active material and connected with parallel  $0.338 \Omega$  wires, do not support a current that is uniform across all the resistance wires. The largest  $i_{max}/i_{min}$  reported was 3.304, tabs positioned in corner of the plate, adjacent to one another. The smallest  $i_{max}/i_{min}$  was 1.730, achieved by positioning one

plate tab top centre and the opposing plate tab bottom centre. Grid design and resistance is also shown to strongly affect current distribution in models designed by Sunu and Burrows [27], [28], Král *et al.* [29] and Alagheband *et al.* [30]. Some discussion of their methodologies follows in Sections 2.2.1 and 2.2.2.

In addition to the effect of grid design, local current density also depends on local charge/discharge history. Guo *et al.* [31], [32] use reference electrode measurements to demonstrate a change in current distribution over the course of a discharge. Zhang *et al.* [33] use a segmented Li-Ion cell to allow measurements of individual segment currents. The current distribution is seen to move from being mostly concentrated near to the tab at the start of a discharge (due to voltage drops accumulating as distance from the tab increases), to being mostly concentrated in the region furthest from the tab at the end of the charge (due to these regions not having been discharged as deeply as those closer to the tab). These two methods are discussed in Sections 2.2.3 and 2.2.4

Inhomogeneous current density distribution has been linked with reduced dynamic charge acceptance [34]. It is offered as an explanation for the dependence of dynamic charge acceptance on the recent charging/discharging history of the battery, which has also been reported in [35]. Acid stratification is suggested as the cause of the inhomogeneous current distribution, since it is dependent on recent history of the battery. Acid stratification also causes premature sulphation in localised areas of the battery plate, even at modest overall depth of discharge for the whole cell [36]. This is acknowledged as a failure mechanism in lead acid cells [34], [37], [38]. Sunu and Burrows use potential non-uniformity around the plate as a figure of merit for cell performance [27]. An important factor determining the specific energy of a battery is the active mass utilisation – lead acid batteries perform poorly in practice compared to other battery chemistries (such as nickel metal-hydride and lithium-ion), and also compared to the theoretical maximum specific energy for a lead acid battery [23], [39]–[41]. Active mass utilisation is typically measured by taking the time integral of the current at the battery terminals, and measuring the mass of the active material, giving a capacity in units of  $\text{A h kg}_{\text{AM}}^{-1}$  [42]. The theoretical capacity of a given mass of active material is obtained by considering the atomic weights of Pb and/or  $\text{PbO}_2$  and the number of atoms needed to exchange an electron at each electrode [43]. By measuring localised current density, a localised measure of active mass utilisation is possible [28]. A non-uniform active mass utilisation means that some parts of the plate are underutilised (resulting in poor specific

energy) and some parts are over-utilised (resulting in damage due to deep discharge [44]). In addition, the mechanisms themselves which limit active mass utilisation are current-dependent; it has been found that the dominant process limiting active mass utilisation depends on the rate of charge/discharge (at high rates transport of acid through the active mass limits its utilisation [45] whereas at low rates it is the electronic conductivity of the active mass [40], [41]). Therefore knowledge of current distribution will give greater insight into the mechanisms governing the active mass utilisation at different locations around the cell plate. Gyenge *et al.* [42] develop a novel plate grid for lead acid batteries with improved active mass utilisation compared to a standard grid. They acknowledge that current distribution measurements could aid optimisation of active mass thickness.

As well as optimising performance, information on current distribution of a cell could be used to identify damage or wear to the cell. Active mass shedding, where the active mass falls from the plates and pools in the bottom of the battery case, is one failure mechanism for lead acid batteries. A summary of aging and failure of lead acid batteries by Ruetschi [36] gives examples of a plate which has shed its active mass over part of its area. Areas where active mass are not present would not be able to participate in the cell reaction and so there would be no current leaving the plate in these areas. Two other failure modes from the same paper are, firstly, capacity loss due to poor contact between the active mass and supporting grid and, secondly, short circuiting between plates due to movement of active mass. If the former occurs initially in one part of the plate area, then a reduced current density would be expected in that part of the cell, and so a current distribution measurement may be useful for showing the degradation of the plate by this method. In the latter case, short circuits occur towards the bottom of the cell due to shedding, or elsewhere around the plate if dendrites are formed [36]. Identifying the path of the short circuit current would differentiate between these two cases. Sulphation is another cause of capacity loss and failure, which may occur non-uniformly on battery plates, with a distribution that is dependent on charge/discharge rate [37], [46], [47].

### **1.3 Thesis Outline and Contribution**

Contributions are highlighted in bold.

*Chapter 2* - Background and literature review. The electrochemical behaviour of a lead acid cell is briefly described. A review of existing current distribution estimation and measurement methods is provided, followed by a more in-depth review of mathematical methods for solving magnetic tomography problems and practical examples of magnetic tomography.

*Chapter 3* - An experimental system for verifying a current distribution imaging system using magnetic sensors is proposed. The experiment involves operating a lead acid test cell in constant current mode, and taking magnetic measurements alongside some invasive current distribution measurements. An invasive current distribution measurement system, a test cell, and a current control system are developed. **A bypassing method for subtracting the ambient field is employed, which reduces the complexity of the electromagnetic inverse problem.** The operation and functions of an existing magnetic sensor array are described.

*Chapter 4* - The algorithm used to interpret current distribution from magnetic measurements. In general solving the current distribution-magnetic field inverse problem is considered non-trivial. A practical and problem-specific approach is utilised in order to identify suitable and valid constraints for the solution. An algorithm is developed based upon an existing one found in the literature. **Novel adaptations make it suitable for the study of lead acid cells. It is shown that the solver method is compatible with commercial 3D finite element software, which allows realistic representations of cell geometry and materials to be included in the forward model. A method of enhancing the tolerance of the solver to unknown material conductance is demonstrated.**

*Chapter 5* - The development of the invasive current distribution method to be used in the experimental system from Chapter 3. The sensor system is an array of ferrous core current sensors, which has previously been described for use with a fuel cell. In order to adapt the system to the lead acid test cell, a **novel ferrous core layout is employed. Some results on the interaction between adjacent cores are presented, and a method of compensating for this effect is employed.** Bespoke control circuitry and software is designed.

*Chapter 6* - The actual experiment conducted to verify the magnetic current distribution imaging system. A procedure is specified and the final hardware setup is given. Results are first presented from the invasive system described in Chapter 5. **This measurement method has never been conducted on a cell of this size.** It yields real measurements of current distribution which are resolved in time and in space. Then the interpreted magnetic measurements are presented and discussed in the context of some likely experimental uncertainties. **This is the first time that this type of non-invasive measurement using magnetic sensors has been conducted in the field of lead acid battery research.** Some investigation and discussion of the interaction between the two measurement methods is presented.

*Chapter 7* - Conclusions from the final results and the experimental design process. Results are compared with some that exist in the literature. The feasibility of the method is also compared against some existing methods. Some future work is suggested to improve accuracy and validity/applicability of current distribution measurements.

## **1.4 Publications**

The following article based on work contained in this thesis has been published –

H. T. Harrison, G. Cooke, D. A. Hewitt, D. A. Stone, and J. E. Green, “Magnetic tomography for lead acid batteries,” *J. Energy Storage*, vol. 12, pp. 1–10, 2017.

The following article is in progress –

H. T. Harrison, G. Cooke, D. A. Hewitt, D. A. Stone, and J. E. Green, “Practical Magnetic Tomography for Lead Acid Batteries: Verification and Validation of Results”

## 2 Literature Review

Existing research is presented here which is relevant to developing a non-invasive magnetic imaging system for measuring current distribution. The intended application is a lead acid battery, so some description of this battery chemistry is given in Section 2.1. Measuring or imaging current distribution in fuel cells and batteries is an ongoing research activity. The usefulness of a magnetic sensing approach must be compared against other available methods of measuring current distribution in cells. A variety of other methods reported in the literature are described in Section 2.2. Finally, magnetic tomography is discussed in Section 0. Work which exists in related fields is summarised, followed by a brief discussion of the practicality of constructing a magnetic sensing array system.

### 2.1 Lead Acid Batteries Background

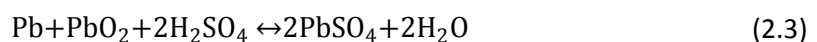
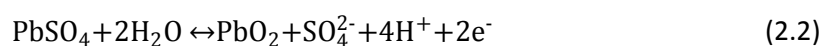
In the following section some background detail on lead acid batteries is presented. This includes some details of processes within the cell and some brief historical and economic context.

#### 2.1.1 Overview

A lead acid battery consists of a lead/lead sulphate cathode ('positive plate') and a lead dioxide/lead sulphate anode ('negative plate'), immersed in an aqueous sulphuric acid electrolyte (usually approximately 40 % concentration by weight).

#### 2.1.2 Chemical reactions

The equation for the reaction between the lead electrode and the electrolyte is given by (2.1) [48]. The reaction at the lead dioxide electrode is given by (2.2) [48]. (2.1) represents oxidation of lead, and (2.2) is the reduction of lead oxide. The overall cell reaction is given by (2.3) [19] - discharging is represented by moving from the left hand side to the right hand side and charging is from right to left.



If the battery is charged above the gassing voltage, then an overcharge reaction (2.4) [19] can begin. This is problematic as the hydrogen is flammable and also as it results in depletion of water in the electrolyte. Water lost through gassing can be replaced with deionised water.



### 2.1.3 Open circuit voltage

The combined potential of both electrodes is given by the Nernst Equation (2.5) [19].

$$v_{oc} = 2.047 + \frac{RT}{F} \ln\left(\frac{\alpha_{\text{H}_2\text{SO}_4}}{\alpha_{\text{H}_2\text{O}}}\right) \quad (2.5)$$

This voltage,  $v_{oc}$ , is known as the open-circuit voltage. It depends on temperature,  $T$ , as well as the electrolyte concentration. The two  $\alpha$  terms are the activities of hydrogen sulphate and water respectively. Activity is a measure of the quantity of material available for reaction or the effective concentration. The constant voltage value, 2.047 V, is calculated from the change in Gibbs free energy of the reaction [48].  $R$  is the gas constant  $8.314 \text{ J mol}^{-1} \text{ K}^{-1}$  and  $F$  is the Faraday constant 96487 Coulombs.

From (2.3) it is clear that discharging uses  $\text{H}_2\text{SO}_4$  and produces  $\text{H}_2\text{O}$ . Therefore the quantity  $\frac{\alpha_{\text{H}_2\text{SO}_4}}{\alpha_{\text{H}_2\text{O}}}$  will decrease as discharging progresses. The open circuit voltage decreases as a result.

### 2.1.4 Potentials during charge and discharge

In order to charge the battery the voltage applied must be higher than the open circuit voltage given above. When the battery discharges the voltage will be lower than the open circuit voltage. This is due to polarization and resistive losses in the cell [19]. When discharging with a current  $i$  through a resistive load,  $r$ , the terminal voltage is given by (2.6) [19].

$$v_{cell} = v_{oc} - [(\eta_{ct})_a + (\eta_c)_a] - [(\eta_{ct})_c + (\eta_c)_c] - ir_i = ir \quad (2.6)$$

Where  $(\eta_{ct})_a$  and  $(\eta_{ct})_c$  are the charge transfer or activation polarisations at the anode and cathode, respectively.  $(\eta_c)_a$  and  $(\eta_c)_c$  are the concentration polarizations at the anode and cathode.  $r_i$  is the internal resistance of the cell, due to the resistance of the electrolyte, the active mass and the plate grids.  $i$  is the current drawn from the battery. The concentration polarisation arises due to the concentration gradients near the electrodes (see Section 2.1.5). The polarization terms and  $ir_i$  all increase with  $i$ , so that increasing discharge current decreases the terminal voltage.  $r_i$  is the internal resistance of the cell. Sources of resistance in a lead acid battery are the active mass, plate grids onto which the porous lead and lead oxide is pasted and the electrolyte.

### 2.1.5 Conduction in the electrolyte

Charge moves through the electrolyte by ionic conduction. There are three mechanisms by which ions are transported in the electrolyte – convection/stirring, migration due to an electric field, and diffusion due to a concentration gradient [19]. Diffusion is typically the dominant process [19]. Fick's law (2.7) [19] gives the flux (amount passing through an area)  $q$  of an ion due to diffusion.

$$q = D \frac{\delta C}{\delta x} \quad (2.7)$$

Where  $\delta C/\delta x$  is concentration gradient and  $x$  is the distance from the electrode plate.  $D$  is the diffusion coefficient. By assuming the concentration gradient is approximately constant within a boundary layer of thickness  $\delta$ , and substituting  $i = nFqA$  (current per mole of active material utilised), (2.7) simplifies to (2.8) [19].

$$i = \frac{nFDA(C_B - C_E)}{\delta} \quad (2.8)$$

Where  $C_E$  is the concentration of the ion being used at the electrode surface and  $C_B$  is the bulk concentration of the ion in the electrolyte.  $n$  is the number of electrons involved in the electrode reaction (two in reactions (2.1) and (2.2)). By considering the situation when the electrode reaction uses enough of the ions to reduce  $C_E$  to 0, an expression is obtained for the maximum current possible due to the diffusion process (2.9) [19].

$$i_L = \frac{nFDAC_B}{\delta_L} \quad (2.9)$$

Where  $\delta_L$  is the boundary layer thickness at this limiting condition and  $i_L$  is the maximum diffusion current for an electrode of given area,  $A$ , and an electrolyte of given bulk concentration and diffusion coefficient,  $D$ . The concentration gradient (approximately equal to  $(C_B - C_E)/\delta$ ) causes a concentration potential,  $\eta_c$ , given by (2.10) [19].

$$\eta_c = \frac{RT}{nF} \ln \frac{C_B}{C_E} \quad (2.10)$$

Note that to reach the maximum possible diffusion current, when  $C_E = 0$ , would imply that the concentration polarisation approaches infinity. In practice, increasing the overvoltage would start another reaction [19], for example the gassing reaction (2.4).

### 2.1.6 History

The lead acid battery was invented by Planté in 1860 [49]. The theory of reaction shown in (2.3) was not proposed until 1882 (by Gladstone and Tribbs) and then was not proved experimentally until 1935 (by Haring and Thomas) [19]. The technology has been steadily developed over the past 150 years and active research into lead acid battery performance is ongoing ([29], [34], [44] plus others - see Section 2.2 for research into the current distribution in lead acid batteries).

## 2.2 Existing Current Distribution Measurement Methods

There is relatively little experimental (as opposed to simulation) work on the current distribution of lead acid batteries. However, similar research into fuel cells is much more active. Kalvyas *et al.* [50] provide a review of methods for measuring current distribution in polymer electrolyte fuel cells. Some techniques used in fuel cells are applicable to lead acid batteries, but not all. This is because the geometry of a fuel cell or flow battery can be more complex than a lead acid battery – it may include multiple layers, and a convoluted flow channel to transport the fuel around the electrode [1], [51]. By contrast, the cell of a parallel plate lead acid battery, such as those used for starting, lighting and ignition of an internal combustion engine vehicle, consists of two opposing faces of adjacent plates of approximately similar geometry with an absorbed aqueous or gelled electrolyte in between. The cell is then simply repeated and connected in series/parallel to increase the battery voltage/current. One plate may form part of either one or two cells, since the active mass may be pasted onto both faces of the plate, but the geometry of each cell is simple and repeating.

### 2.2.1 Modelling

Lead acid batteries have been modelled as electrochemical systems and as purely resistive systems. Newman and Tiedemann [52] develop a macrohomogeneous theory of the cell reactions, which is used by Kowal *et al.* in their study into current inhomogeneity and recent cycle history of a lead acid cell [34]. Sunu and Burrows incorporate a resistive model of the plate grids into an electrochemical model of the battery in order to predict potential and current density distributions [27], [28] and the effect of altering grid design. Due to the relative ease and speed of creating models compared to building a real grid, the authors were able to make comparisons between various proposed grid designs and dimensions in order to plot capacity against grid weight, aiding optimisation of specific energy. Král *et al.* [29] developed an equivalent circuit incorporating resistances of constituent parts of a lead acid cell as well as

the state of charge-dependent local polarisations to simulate non-uniformity of current distribution for different battery current take-off tab configurations. A degree of non-uniformity (defined as  $i_{max}/i_{min}$ ) of between nearly 1 (best case) to 11 (worst case) was reported. This was dependent on terminal lug design and positioning, as well as the state of charge. A similar approach was taken by Alagheband *et al.* using Comsol Multiphysics to investigate the effect of take-off tab position and also the effect of tapered grid members [30]. The degree of non-uniformity was found to be approximately between 2.8 and 4. All modelling approaches however sophisticated require verification against experimental results. This is not to say they aren't useful, rather that the field of study requires both simulation and experimental methods in order to advance.

### 2.2.2 Sense wires

One direct way to measure potential distribution around the plate (and thereby estimate current distribution by making assumptions about the resistivity of the electrolyte) is to attach sense wires to the grid. Calábek *et al.* [26] constructed a purely resistive model from a pair of unpasted lead acid cell plate grids, connected together by uniformly spaced resistance wires to simulate the electrolyte resistance. Using this apparatus they found that the uniformity of the current distribution can be improved by correct placement of the current take-off tabs. However, the authors acknowledge that removal of the highly conductive negative plate material is increasing the degree of non-uniformity and that their method is best used as a comparison between grid and terminal layouts [26].

Schulte *et al.* [37] connected four sense wires to the vertical edge of the negative plate grid, leaving most of the active mass in place. This allows indirect measurement of current distribution (assuming current distribution is uniform horizontally) in conjunction with pH measurements to identify acid stratification. Current distribution became less uniform after 1000 micro-cycles. The transient behaviour of the voltage dropped between the different measurement points allows comparison of the varying charge acceptance at different heights on the plate as well as the current distribution.

Sunu and Burrows [27], [28] took potential measurements taken around the plate area using wires attached to the plate grids. These were used in conjunction with a resistive model of the grid (obtained by dissecting an identical grid into typical vertical and horizontal beams) in order to calculate the current density distribution. Non-uniformity when discharging a fully charged cell at 5 A per plate was measured at 1.57. After 0.5 hours of discharging, the current

density becomes approximately uniform. Beyond this time, polarization of the plate counteracts the effect of the grid resistance such that the current density near the bottom of the plate is greater than that near the tabs, with a degree of non-uniformity of 1.22. A large variation is found amongst the different members which make up the grid. The grid members range in conductance from  $171 \Omega^{-1} - 3514 \Omega^{-1}$  ( $2.84 \times 10^{-4} - 5.84 \times 10^{-3} \Omega$ ). Furthermore the positive and negative grid members do not match in conductivity.

All three of the sense wire-based methods described are highly invasive as they require alteration to the battery plates. Schulte's method only provides 4 voltages which can be subtracted from each other, so only 3 regions between which current can be compared. Attaching more wires over the plate area would in principle be possible but re-pasting the plate, or some method of preserving the active mass, would be necessary in order to observe normal operation of the cell. Calábek's experimental setup is less comprehensive than similar simulated models. For example, it doesn't include the time-varying potentials that occur during a charge/discharge. However, it does provide some useful experimental verification for other investigations into tab placement such as [26], [29] and is qualitatively in agreement with both the results of both those studies.

### 2.2.3 Reference electrodes

A tool widely used to analyse electrolytic systems is the reference electrode. This is an electrode which has a known potential in the electrolyte of interest. They are often used to measure the potential of an unknown electrode. Newman and Tiedemann describe taking reference electrode measurements at various points around a cell to obtain potential and current distribution. They found current density to be very uniform ( $j_{max}/j_{min} \approx 1.02$ , estimated from their graph) for a cell of height 10 cm using a reference electrode to measure half-cell potential at a range of heights [53]. Reference electrodes have also been used by Guo *et al.* [32], [31] in pairs to measure the resistive voltage drop across the electrolyte when a current is passed through a lead acid cell. Figure 2.1 shows the arrangement of reference electrode pairs. The voltage drop is proportional to the electrolytic current which passes from point A to point B. The authors assumed that electrolyte conductance was uniform and constant. By scanning the pairs of electrodes in tandem around the cross sectional area of the cell, the local current across the cross sectional area can be found. The scan was achieved using three pairs of electrodes, which were first traced along contours 1-3 before being moved to trace contours 4-6.

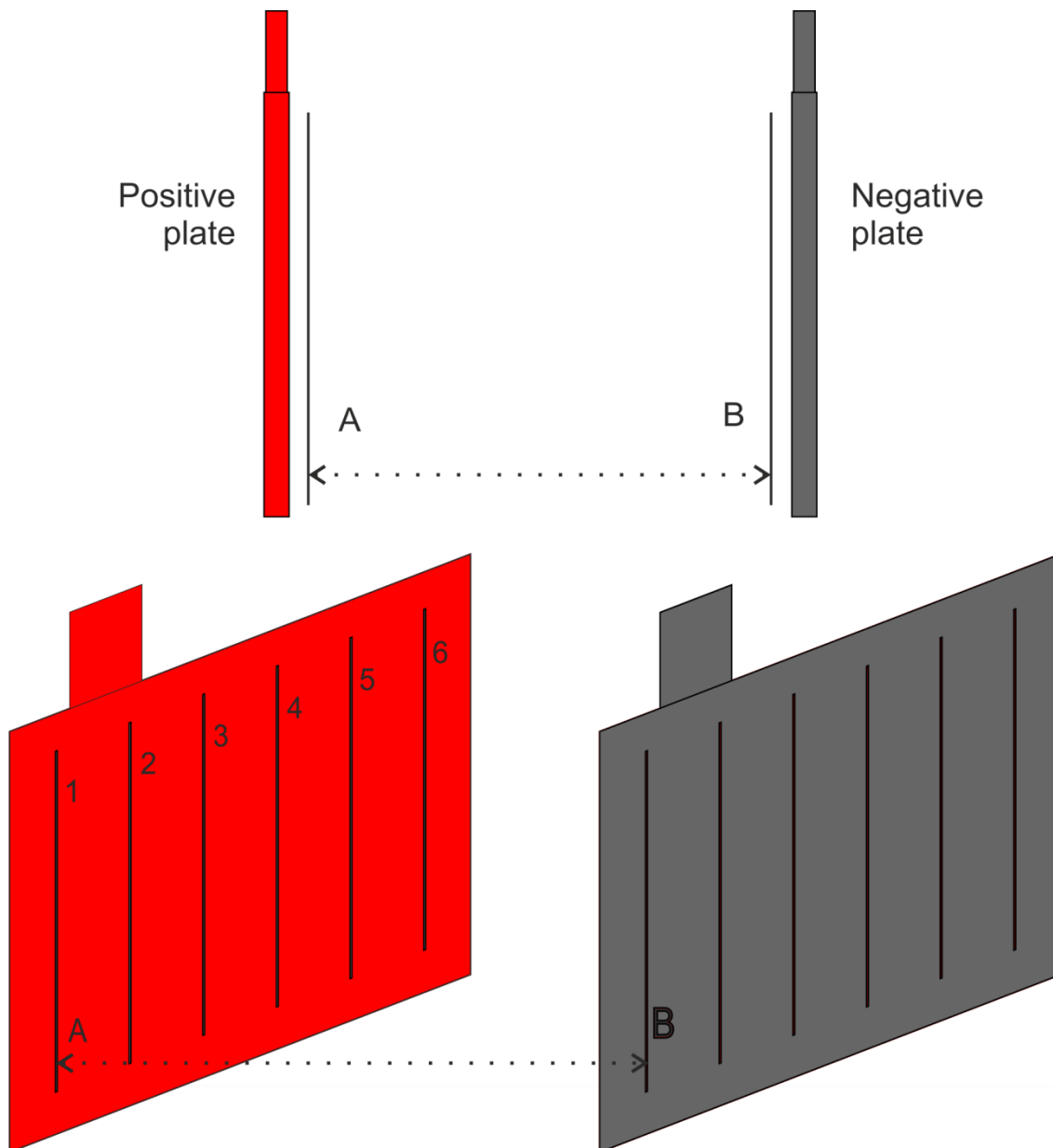


**Figure 2.1 – Arrangement of reference electrodes to provide differential voltage measurements across the electrolyte. Positions A and B form a pair. Three pairs are employed at a time, tracing contours 1-3 simultaneously, before moving the electrodes and tracing 4-6.**

For a cell discharging at 0.625 C (7.5 A), the degree of non-uniformity along a vertical slice of the cell was initially measured as approximately 1.125, becoming approximately 1.61 after 1 hour. The profile of this current density distribution is such that the current density is initially higher towards the bottom of the cell, with the current density peak moving to the middle of the cell as discharging progresses [32], [31]. This does not agree with the distributions found in [26], [28].

The reference electrode voltages will depend on electrolyte concentration, and the differential voltage between each electrode in a pair depends on electrolyte conductivity (which is dependent on concentration). It is unclear what steps were taken to eliminate acid stratification or to compensate readings for pH variation over the cell height. Like all scanning methods, there is a trade-off between spatial resolution of the current distribution image and the time taken to acquire the image. A scan time of 40s is reported [31], over which time it is likely that the cell state may have already changed, especially at higher rates. The repeated reading employed to cover contours 4-6 introduces a risk of different cell behaviour due to fatigue or a change in operating conditions between runs (such as temperature, acid stratification, state of charge). A high rate test is reported in [32] where three pairs of electrodes are fixed at different heights to give simultaneous readings at the expense of spatial resolution. A further disadvantage of scanning electrodes in the region between the plates is that it makes it difficult to compress the active mass in order to improve plate lifetime [36]. Reference electrode arrays have been reported for use with fuel cells [54].

The use of reference electrodes is less invasive than the sense wire method, as the cell plates themselves do not have to be modified. However, the plate separation must be much greater than that found in a commercial automotive lead acid battery in order to fit either one or two standard reference electrodes in between the plates, plus clearance for scanning the electrode position if a scanning method is being employed. An electrode which would fit into a 1-2 mm gap between plates has been created especially for research into lead acid batteries [55], but was used for electrochemical analysis rather than for spatially resolved current density measurements.

#### **2.2.4 Split electrodes**

Another invasive method is to divide the electrodes in the cell of interest into segments in order to allow connection of an ammeter to each segment directly. The currents can then all be connected to a bus wire to complete the circuit to the battery terminal. Zhang *et al.* divided the positive electrode of a lithium-ion cell into 10 segments along one dimension only, so that current could be plotted as a function of distance from the cell tab [33]. Current inhomogeneity *perpendicular* to the cell plate has been observed in a lithium-ion cell using a stack of working electrodes, giving some insight into the contribution to the reaction that is obtained by altering the thickness of the plate [56] (all the other examples in this paper are concerned with inhomogeneity in the plane *parallel* to the plates). Electrodes that are split ‘in

the plane' rather than stacked are commonly used in more diverse electrochemistry problems, two early examples being shown in [57], [58].

A drawback to using this method in the study of batteries is that one of the electrodes must be altered significantly. Therefore only the behaviour of one electrode can be studied at a time, as is the case in [33]. The contribution to the current distribution of the electrode which has been segmented is not measured by this method. This is not a problem in some electrochemistry problems such as [57], [58], where the pair of electrodes may be designed especially for the experimental setup. However, in the typical use of an automotive battery, the Ohmic potential losses in *both* plates can be significant contributors to current distribution [26]–[29] and so care must be taken when interpreting data taken from one plate only.

### 2.2.5 Magnetic resonance imaging

Some work has been undertaken on applying some established imaging techniques to batteries. Britton [59] provides a review of magnetic resonance imaging on electrically conductive and magnetically susceptible materials. This application of magnetic resonance imaging is not trivial as care must be taken to avoid eddy currents in conducting materials due to the strong applied magnetic field, and also distortions to the magnetic field due to any magnetically susceptible materials present. Britton *et al.* [60] perform magnetic resonance imaging on a zinc-air battery cell (comprising a zinc electrode, a titanium electrode and NaOH electrolyte). By this method it is possible to identify concentrations of different chemical species in the cell, so the transport of  $\text{Zn(OH)}_x^{2-}$  and  $\text{OH}^-$  ions through the electrolyte can be observed.

### 2.2.6 X-ray and neutron imaging methods

Pearse *et al.* [61] perform a 1-dimensional X-ray photoelectron spectroscopy scan of a specially-made  $\text{V}_2\text{O}_5$  electrode of very low width in a lithium-ion cell. Over the course of a discharge,  $\text{V}^{5+}$  ions are reduced to  $\text{V}^{4+}$ . Since these two ions exhibit different spectra, the relative concentration of the two species can be seen. The part of the electrode furthest from the tab is found to contain more  $\text{V}^{5+}$  and less  $\text{V}^{4+}$  than the part closest to the tab at the end of a discharge. Liu *et al.* [62] take a 45 mm x 40 mm  $\text{LiFePO}_4$  electrode which has been charged to 50 % SoC, and then perform an X-Ray diffraction scan over the electrode area. The scan is able to identify the concentration of  $\text{FePO}_4$  present, which is taken as a measure of local SoC. By this method, a 2-dimensional plot of SoC over the electrode area is constructed, which shows a strong inhomogeneity over the electrode area. Both the X-ray based methods

measure SoC distribution rather than current distribution. However these two quantities are related, since local charge is the integral of the local current. Measuring SoC can be convenient for scanning methods, as the current can be interrupted for the measurement so SoC is not changing during the scan time. The X-ray based methods are both quite low in validity – the 2D diffraction scan was conducted as a destructive test while the photoelectron spectroscopy method was only conducted along one dimension.

Using neutron diffraction imaging has been proposed to measure electrolyte concentration, during cell operation (giving insight into acid stratification), as well as showing the structure of the plate grid [63]. Neutron diffraction has previously been used to identify change in active mass composition after battery cycling using a ‘tear down’ approach. Material was removed from a battery which has been cycled 36 times and from one which had been cycled only 3 times, and a neutron diffraction image was taken of both samples to compare them [64].

### **2.2.7 Flow-through magnetic sensor array**

Since any electrical current will give rise to a magnetic field surrounding the current, measuring magnetic field would seem to be a convenient way of making non-contact current measurements. Indeed, standard ‘clamp’ current meters use a magnetic sensor as a transducer [65], [66]. A close relative of a clamp current meter is the current sensor array developed for measuring current distribution in a fuel cell [67]. A  $5 \times 8$  array of bespoke current sensors is placed between the current collector and the flow field of a large (approx. 190 mm x 300 mm) polymer electrolyte fuel cell. They are oriented to measure current transiting in or out of the current collector through the ferrous core aperture, with the plane of the sensor array and resulting image parallel to the current collector (Figure 2.2). A similar sensor array could in principle be applied to a parallel plate lead acid cell; an advantage of this method is that it can be used with any cell chemistry.

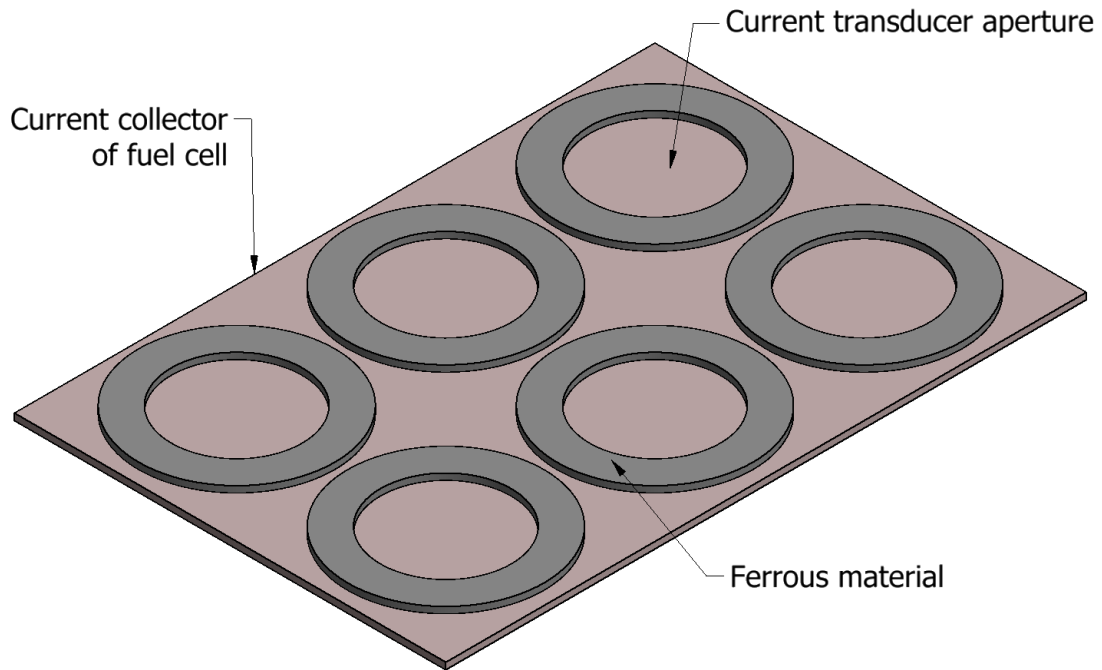


**Figure 2.2– Simplified array of current transducers arranged to measure current transiting the large face of the current collector.**

Each current sensor consists of a Hall effect magnetic field sensor, placed into an airgap cut into an annular ferrite core (Figure 2.3). The ferrite provides a low reluctance path for the magnetic flux which exists due to current which passes through its centre, so that the field measured by the Hall effect sensor is a function of the local current and the size of the airgap only. The ferrite core has a high value of relative magnetic permeability,  $\mu_r$ . The magnetic reluctance of the path around the current is composed of the reluctance of the path around the iron core,  $S_{core}$ , plus the reluctance of the airgap,  $S_{air}$ . The magnetic flux,  $\phi$ , around the core due to the current,  $i$ , is given by (2.11). If  $\mu_{r,core} \gg 1$  then  $S_{core} \ll S_{air}$  and the flux density,  $b$ , can be approximated by (2.12).

$$\phi = \frac{i}{S_{core} + S_{air}} \quad (2.11)$$

$$b = \frac{\phi}{A} = \frac{i}{S_{air} A} \quad (2.12)$$

Substituting  $S_{air} = \frac{l_{air}}{\mu_0 A}$  and  $b = \mu_0 h$  in to (2.12) gives an expression for magnetic field strength,  $h$ , in terms of current and airgap length,  $l_{air}$  (2.13). If the airgap length is known then a magnetic sensor can be used to measure the current,  $i$ . Magnetic field strength,  $h$ , is the

quantity used in much of the discussion of core geometry, due to the simplicity of dealing with (2.13). However, a magnetic sensor may be specified in terms of magnetic flux density,  $b$ . These two quantities are interchangeable if it is assumed that  $b = \mu_0 h$  at the location of the sensor.

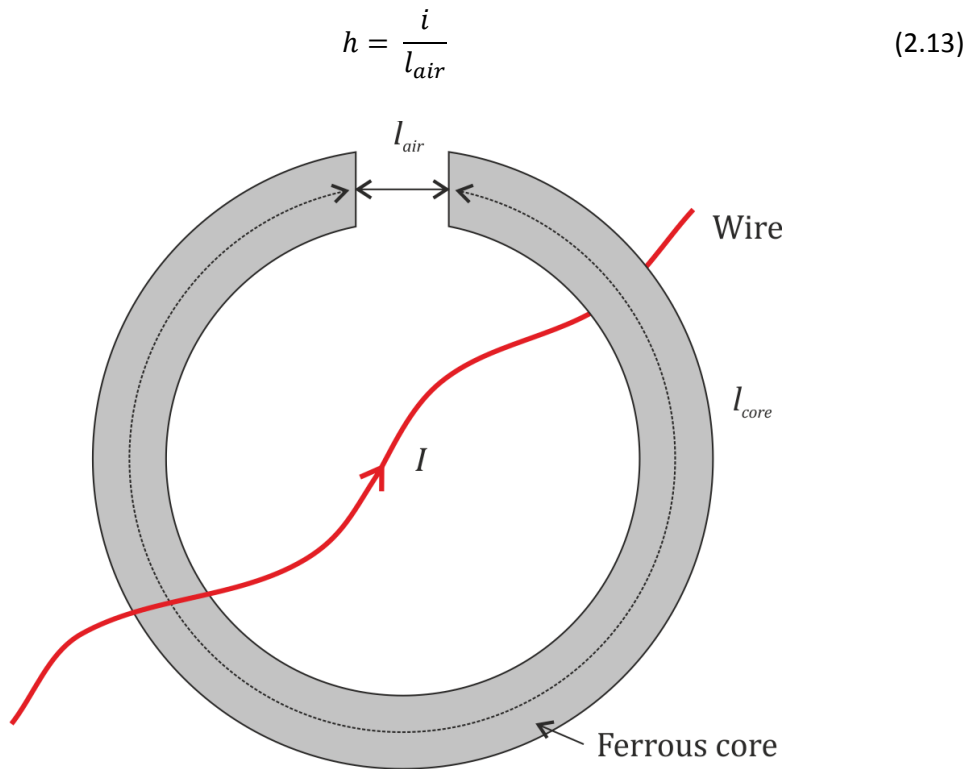


Figure 2.3 – Ferrous core with airgap as a current transducer. Magnetic field measured in the airgap is proportional to  $I$ .

## 2.3 Magnetic Tomography

Magnetic tomography (inferring an image, in this case of current distribution, from magnetic measurements) is frequently referred to as an ‘inverse problem’ (where calculating magnetic field from a known current distribution may be termed the ‘forward problem’). Solving the inverse problem is not a trivial task. Existing approaches to finding the solution are presented in Section 2.3.1. Some of these methods have been implemented in practice, whereas some may be simulation only. Some investigation is also conducted into the practicalities of constructing a suitable sensor system for magnetic tomography (Section 2.3.2).

### 2.3.1 Solver methods

The magnetic field due to the battery current also exists outside of the battery case, making a non-invasive measurement possible. Magnetic tomography is the technique of constructing an image of current distribution using external magnetic field measurements. If a current distribution is known, then the resulting magnetic field distribution may be calculated analytically (using the Biot-Savart law, Ampere’s law, or Maxwell’s magnetostatic equations) or by finite element methods. When calculating current distribution from the magnetic field using an inverse problem approach, the coupling between the current distribution to the magnetic field is known as the forward model. Information about both the magnetic field and the forward model is necessary to solve the inverse problem. The inverse problem may be ill-posed, which can cause large errors in solutions, and so Tikhonov regularisation is often used to find an approximate solution that is tolerant of errors [68]. Tikhonov regularisation aims to approximately solve the system  $\mathbf{K}\mathbf{x} = \mathbf{y}$  for  $\mathbf{x}$  yielding  $\mathbf{x} = \mathbf{K}^{-1}\mathbf{y}$ , by minimising (2.14).  $\mathbf{R}_\lambda$  is taken as an approximation of  $\mathbf{K}^{-1}$  and is calculated by (2.15), where  $\mathbf{I}$  is the identity matrix and  $\lambda$  is the ‘regularisation parameter’.

$$\min_x \{ \|\mathbf{K}\mathbf{x} - \mathbf{y}\|_2^2 + \lambda^2 \|\mathbf{x}\|_2^2 \} \quad (2.14)$$

$$\mathbf{R}_\lambda = (\lambda \mathbf{I} + \mathbf{K}^* \mathbf{K})^{-1} \mathbf{K}^* \quad (2.15)$$

A larger  $\lambda$  yields a more smoothed solution, a smaller  $\lambda$  can yield an overfitted solution. An optimum value of  $\lambda$  may be found using the L-curve method [68]. Plotting residual norm  $\|\mathbf{K}\mathbf{x} - \mathbf{y}\|_2$  against solution norm  $\|\mathbf{x}\|_2$  over a range of values of  $\lambda$ , results in an ‘L shaped’ curve (Figure 2.4). The corner of the L shape is considered an optimum value of  $\lambda$ . Notice that larger values of  $\lambda$  result in a larger residual norm while smaller values of  $\lambda$  result in a larger solution norm.

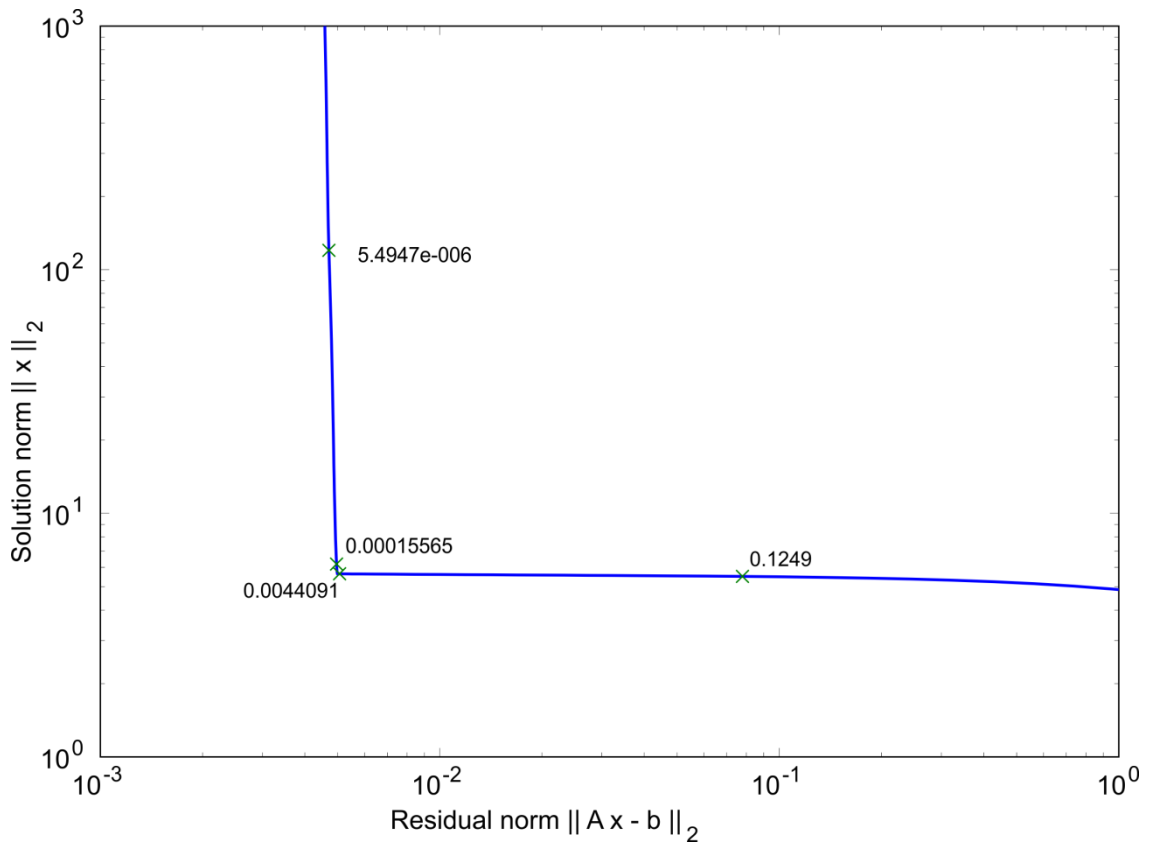


Figure 2.4 – An example L-curve. Data is from Hansen's 'Regtools' Matlab package [69].

Uniqueness must be considered when dealing with inverse problems – *i.e.*, if a given magnetic field could have been generated by more than one current distribution, then it may be impossible to know with certainty the current distribution from magnetic field measurements. It has been shown that the problem is more tractable under some conditions which are met in the case of a typical battery or fuel cell problem [70]. Firstly, the local current density  $\mathbf{j}$  arises from a gradient in electric potential  $v$  and conductance  $\sigma$ , according to (2.16).

$$\mathbf{j} = \sigma \nabla v \quad (2.16)$$

Secondly, the current within the cell exhibits zero divergence (there are no sources or sinks of current flux in the problem region) (2.17). This is equivalent to Kirchoff's current law in circuit analysis, where currents into a node must sum to zero.

$$\nabla \cdot \mathbf{j} = 0 \quad (2.17)$$

The third constraint is the boundary condition of the current flux (2.18) where  $g$  is some known constant and  $\hat{\mathbf{n}}$  is the unit vector normal to the problem boundary. This constraint is reasonable in practice, as the current entering or exiting the cell (the problem region) may be measured using an ammeter, even though the current distribution within the cell is unknown.

$$\hat{\mathbf{n}} \cdot \sigma \nabla \mathbf{j} = g \quad (2.18)$$

Finally, the assumption is made that cell currents are directed. That is that some direction  $\mathbf{d}$  exists for which (2.19) holds.

$$\mathbf{j} \cdot \mathbf{d} \geq 0 \quad (2.19)$$

It is shown that these constraints ensure that  $\mathbf{j} = 0$  results in measured magnetic field strength  $\mathbf{h} = 0$ , but they do not ensure uniqueness of solutions. However, by considering a projection of the solution onto a subspace using Tikhonov regularisation [68] to find an approximate solution, it is shown that solutions do converge on the correct answer. This is demonstrated on a numerical example.

One constraint which makes reconstruction easier is prior knowledge of the position of the possible current relative to the sensors, so a model which constrains the positions and directions of the current is commonly used. 2D problems (such as the current moving around a printed circuit board) have been solved where the distance from the sensor to the plane of the currents is known [71], [72]. Hofer *et al.* [72] apply magnetostatics in the spatial domain and the spatial frequency domain to a numerical simulated problem using current data generated in COMSOL Multiphysics. The spatial domain approach is adopted in this thesis. They adapt the integral form of the Biot-Savart law (2.20) (where  $\mathbf{r}$  denotes the 3 dimensional coordinates of the measurement point,  $\mathbf{r}'$  is the infinitesimal current element,  $V$  is the volume containing the current) for discrete current elements (2.21) (where the  $i^{\text{th}}$  element contains a current  $\mathbf{j}_i$  and has volume  $\Delta v_i$ ).

$$\mathbf{h}(\mathbf{r}) = \frac{1}{4\pi} \iiint_V \mathbf{j}(\mathbf{r}') \times \frac{\mathbf{r} - \mathbf{r}'}{|\mathbf{r} - \mathbf{r}'|^3} d^3\mathbf{r}', \quad \mathbf{r}' \in V \quad (2.20)$$

$$\mathbf{h}(\mathbf{r}) = \frac{1}{4\pi} \sum_i \iiint_{\Delta v_i} \mathbf{j}_i \times \frac{\mathbf{r} - \mathbf{r}'}{|\mathbf{r} - \mathbf{r}'|^3} dv(\mathbf{r}') \quad (2.21)$$

Restricting the current to 2 dimensions ( $x$  and  $y$ ) means that the cross product term is calculated by (2.22). The cross product defines the direction of the measured magnetic field from the direction and relative displacement of a current element, so this gives some insight into how a 2D current distribution may be interpreted from magnetic field measurements. The  $x$  and  $y$  components of  $\mathbf{h}$  are calculated from the local (no displacement in  $x$  or  $y$ ) current, such that  $h_x$  is proportional to  $j_y$  and  $h_y$  is proportional to  $-j_x$ . This behaviour is noted the

plots in [72] and also in this thesis (Figure 4.3). Equation (2.22) also shows that  $h_z$  is calculated from  $j_x$  and  $j_y$ . In fact Roth and Sepulveda [71] show that for a 2D-constrained problem such as this,  $\mathbf{j}_{xy}$  may be uniquely determined from  $\mathbf{h}_z$ .

$$\begin{pmatrix} j_x \\ j_y \\ 0 \end{pmatrix} \times \begin{pmatrix} x - x' \\ y - y' \\ z - z' \end{pmatrix} = \begin{pmatrix} j_y(z - z') \\ -j_x(z - z') \\ j_x(y - y') - j_y(x - x') \end{pmatrix} \quad (2.22)$$

Breaking up the cross product calculation into 3 dimensional components also leads to a method for capturing the coupling  $\mathbf{K}$  between the set of current density elements  $\mathbf{J}$  and set of magnetic field measurements  $\mathbf{H}$ . In matrix form this is expressed as (2.23) which expands to (2.24). When magnetic field  $\mathbf{H}$  is known, the desired calculation to obtain  $\mathbf{J}$  is (2.25).

$$\mathbf{H} = \mathbf{K} \cdot \mathbf{J} \quad (2.23)$$

$$\begin{bmatrix} h_{x,1} \\ h_{y,1} \\ h_{z,1} \\ h_{x,2} \\ \vdots \\ h_{x,m} \\ h_{y,m} \\ h_{z,m} \end{bmatrix} = \begin{bmatrix} 0 & k_{z,11} & \dots & 0 & k_{z,1n} \\ -k_{z,11} & 0 & \dots & -k_{z,1n} & 0 \\ k_{y,11} & -k_{x,11} & \dots & k_{y,1n} & k_{x,1n} \\ 0 & k_{z,21} & \dots & 0 & k_{z,2n} \\ \vdots & \vdots & \dots & \vdots & \vdots \\ 0 & k_{z,m1} & \dots & 0 & k_{z,mn} \\ -k_{z,m1} & 0 & \dots & -k_{z,mn} & 0 \\ k_{y,m1} & -k_{x,m1} & \dots & k_{y,mn} & -k_{x,mn} \end{bmatrix} \cdot \begin{bmatrix} j_{x,1} \\ j_{y,1} \\ j_{x,2} \\ j_{y,2} \\ \vdots \\ j_{x,n-1} \\ j_{x,n} \\ j_{y,n} \end{bmatrix} \quad (2.24)$$

$$\mathbf{J} = \mathbf{K}^{-1} \mathbf{H} \quad (2.25)$$

For a 2 dimensional current with magnetic field measured at a fixed distance away in the  $z$  direction,  $\mathbf{K}$  is populated according to (2.26), (2.27), (2.28).  $\mathbf{K}$  consists solely of dimensional information scaled by  $1/4\pi$ , so it remains constant if the relative orientation of current elements and magnetic sense points is kept constant. This has two useful implications. Firstly, computational cost may be reduced by saving  $\mathbf{K}$  for subsequent calculations. Secondly, it means that (2.23) is a linear relationship, provided geometry is kept constant.

$$k_{x,ij} = \frac{1}{4\pi} \frac{x_i - x_j}{\left[ (x_i - x_j)^2 + (y_i - y_j)^2 + z^2 \right]^{\frac{3}{2}}} \Delta v_j \quad (2.26)$$

$$k_{y,ij} = \frac{1}{4\pi} \frac{y_i - y_j}{\left[ (x_i - x_j)^2 + (y_i - y_j)^2 + z^2 \right]^{\frac{3}{2}}} \Delta v_j \quad (2.27)$$

$$k_{z,ij} = \frac{1}{4\pi} \frac{z}{\left[ (x_i - x_j)^2 + (y_i - y_j)^2 + z^2 \right]^{\frac{3}{2}}} \Delta v_j \quad (2.28)$$

Hofer *et al.* reconstruct  $\mathbf{J}$  using Tikhonov regularisation to solve (2.23) and present plots of reconstructed  $\mathbf{J}$  but do not quantify the solution performance in terms of a mean-squared or mean-absolute error. They also note that the defined problem space is excluding some currents which are contributing to the magnetic field measurement. As a remedial measure they propose simulating external currents using a finite element simulation but this is not implemented. Defining external currents sufficiently may be quite a complex task in practice, depending on how much sensitivity to ambient magnetic field the measurements are assumed to be. It also does not account for other sources of ambient magnetic field, such as the Earth's magnetic field or the presence of permanent magnets. In practice, ambient field is often removed by shielding or subtraction [73], [74].

In the study of fuel cells, quasi-2D models have been used to reconstruct current distribution by assuming negligible thickness [75], [76]. If thickness is non-negligible, then a 3D model must be used. Since the location of current is no longer restricted to a planar surface, some other constraints must be imposed. One approach is to construct an electric circuit model with similar geometry and conductance distribution to the cell of interest. The magnetic field measurements are then a function of the currents flowing in each element of the circuit model.

Hauer *et al.* [77] investigate methods of constraining the problem by imposing Kirchoff's current law (equivalent to a zero-divergence constraint on the current distribution). The first step is to define currents that sum to zero at each node by finding the 'adjacency matrix' which defines which wires are connected to which nodes in the circuit (Figure 2.5 shows a simple  $3 \times 3 \times 2$  network). The adjacency matrix  $\mathbf{T}$  has size  $(K \times N)$  where the nodes are numbered  $k = 1, \dots, K$  and wires are numbered  $w = 1, \dots, N$ . Each element  $T_{kw}$  is then assigned according to (2.29).

$$T_{kw} = \begin{cases} 1, & \text{wire } w \text{ starts at node } k \\ -1, & \text{wire } w \text{ ends at node } k \\ 0, & \text{otherwise} \end{cases} \quad (2.29)$$

For the example shown in Figure 2.5, the convention is adopted that a wire must point in the positive direction as indicated by the coordinate system. Then we have for example wire 7 starting at node 7 and ending at node 16. This is represented by setting  $T_{7,7} = 1$  and  $T_{7,16} = -1$ . Each wire is connected to precisely 2 nodes, but each node can connect an arbitrary number of wires (for example, node 5 is connected to 5 wires).

The boundary condition for the circuit is defined as a matrix  $\mathbf{c}$  of length  $K$ , defined according to (2.30). Compare this with the more general boundary condition (2.18). The principle is similar – since  $I_{term}$  is leaving the region of unknown current distribution it may be measured directly using an ammeter and so it is an appropriate constraint to use. For the example shown, the current take-off tabs could be situated at  $k_1$  and  $k_{10}$ , which would be represented by setting  $c_1 = I_{term}$  and  $c_{10} = -I_{term}$ , or vice versa (depending if the simulated cell is ‘charging’ or ‘discharging’).

$$c_k = \begin{cases} I_{term}, & \text{current enters circuit at node } k \\ -I_{term}, & \text{current exits circuit at node } k \\ 0, & \text{otherwise} \end{cases} \quad (2.30)$$

A current  $i_l$  flowing through wire  $l$  is then subject to (2.31), ensuring that currents at each node sum to zero *unless* it is the input or output node. The discretised current distribution is now subject to a zero divergence constraint analogous to (2.17).

$$\sum_{w=1}^N T_{kw} i_w = c_k \quad (2.31)$$

In order to fully calculate the circuit currents and voltages, information about the wire resistances is needed. This is implemented using mesh rules, where voltages around a closed loop of wires must equal to zero. This is formalised in (2.32), where wire meshes or loops are numbered  $m = 1, \dots, M$ , the resistance of wire  $w$  is denoted  $R_w$ . Elements of the mesh rule matrix are denoted  $S_{mw}$  and are set to 1 if mesh  $m$  passes through wire  $w$  in the positive direction, -1 if  $m$  passes through  $w$  in the negative direction, and 0 otherwise.

$$\sum_{w=1}^N S_{mw} (R_w i_w) = 0 \quad (2.32)$$

The Biot-Savart law is applied to get the coupling between the wire currents and the measured magnetic field. Since the current is now restricted to paths of negligible thickness but non-negligible length  $l_w$ , (2.21) becomes (2.33), where  $\mathbf{p}$  is a point along wire  $w$ . Aligning the wires orthogonally along the x, y, z axes makes the cross product calculation simpler, allowing a coupling matrix  $\mathbf{K}$  to be populated in a similar way to that shown in (2.26) - (2.28).

$$\mathbf{h}(\mathbf{r}) = -\frac{1}{4\pi} \sum_{w=1}^N \int_{l_w} \mathbf{j}_w \times \frac{\mathbf{r} - \mathbf{p}}{|\mathbf{r} - \mathbf{p}|^3} ds(\mathbf{p}) \quad (2.33)$$

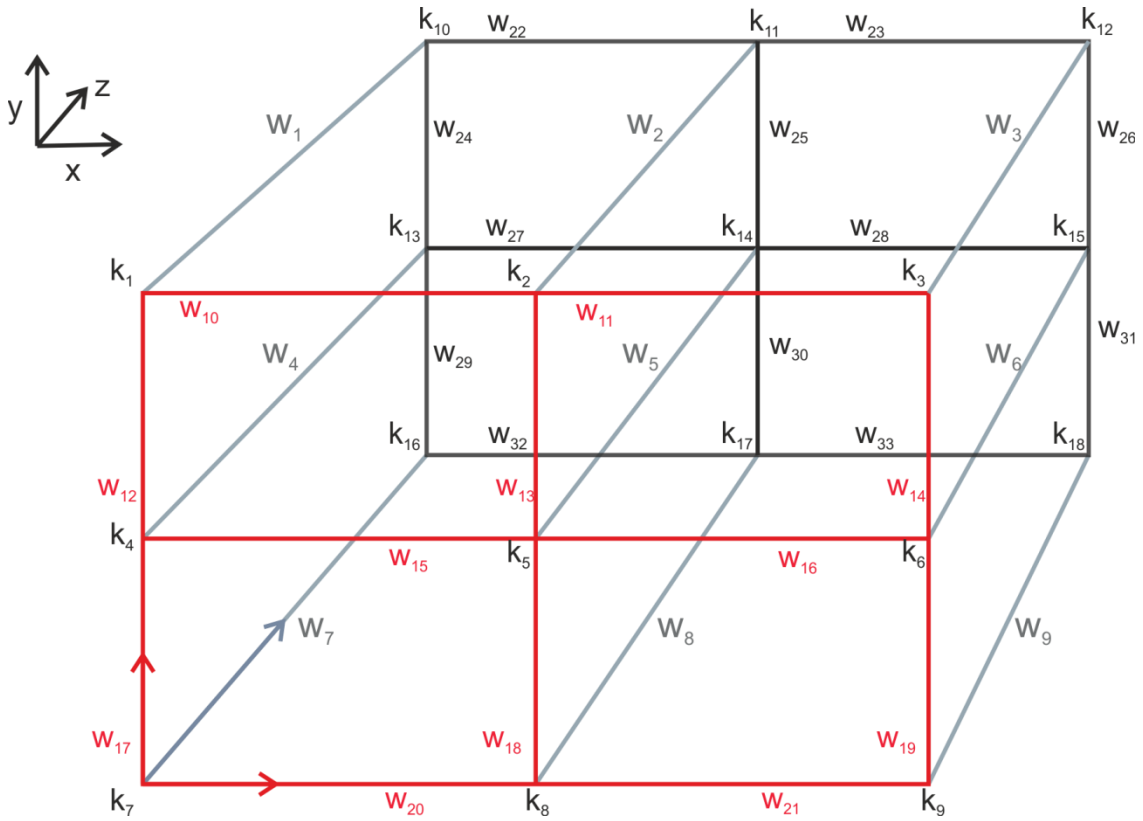


Figure 2.5 – A 3-D conductive volume modelled as discrete wires  $w_{1-33}$  and nodes  $k_{1-18}$ . To aid comparison with lead batteries, the red shaded wires represent the positive plate, the black shaded wires are the negative plate and the grey wires are the electrolyte.

Hauer *et al.* [77] apply this constraint in two different ways and compare the results. The first method is to calculate the nullspace  $N$  of the adjacency matrix  $T$  and applying Tikhonov regularisation to invert  $KN$ . The second method, termed ‘special basis projection’, is to treat the overall current distribution as a combination of the electrolyte currents, with the currents in the plates entirely determined by the electrolyte current distribution and the resistances in each branch of the circuit [77]. An assumption is made that the plate conductivity is uniform, and is much greater than that of the electrolyte. The unknown wire currents  $I$  are given as a weighted sum of partial currents  $I_s$  where the weighting coefficients are denoted  $\xi = (\xi_1, \dots, \xi_{N_E})$  (2.34) where  $N_E$  is the number of wires connected between the two plates representing the electrolyte.

$$I = \sum_{w_E=1}^{N_E} \xi_{w_E} I_{s,w_E} \quad (2.34)$$

$I_s$  has size  $(N \times N_E)$ .  $I_{s,1}$  is generated by setting the first electrolyte wire to a nonzero conductance, and the rest of the electrolyte wires to zero conductance and solving the circuit

subject to (2.31) and the defined conductances. Once  $\mathbf{I}_s$  has been computed, then any valid current distribution  $\mathbf{I}$  can be obtained by altering the unknown weighting coefficients  $\xi = (\xi_1, \dots, \xi_{N_E})$ .

The unknown weighting coefficients form a ‘basis’ or coordinate system defining the problem space, onto which the full current distribution vector  $\mathbf{I}$  is projected.  $\mathbf{I}$  is used rather than  $\mathbf{J}$  as it is more appropriate for dealing with circuit models. It is arguably quite conceptually simple from an electronic engineering perspective; analysing an electric circuit using superposition exploits linearity in a similar way [78]. A simplified case with 2 independent current sources ( $i_{s1}$  and  $i_{s2}$ ) and 2 magnetic measurement points ( $S_1$  and  $S_2$ ) is given in Figure 2.6.

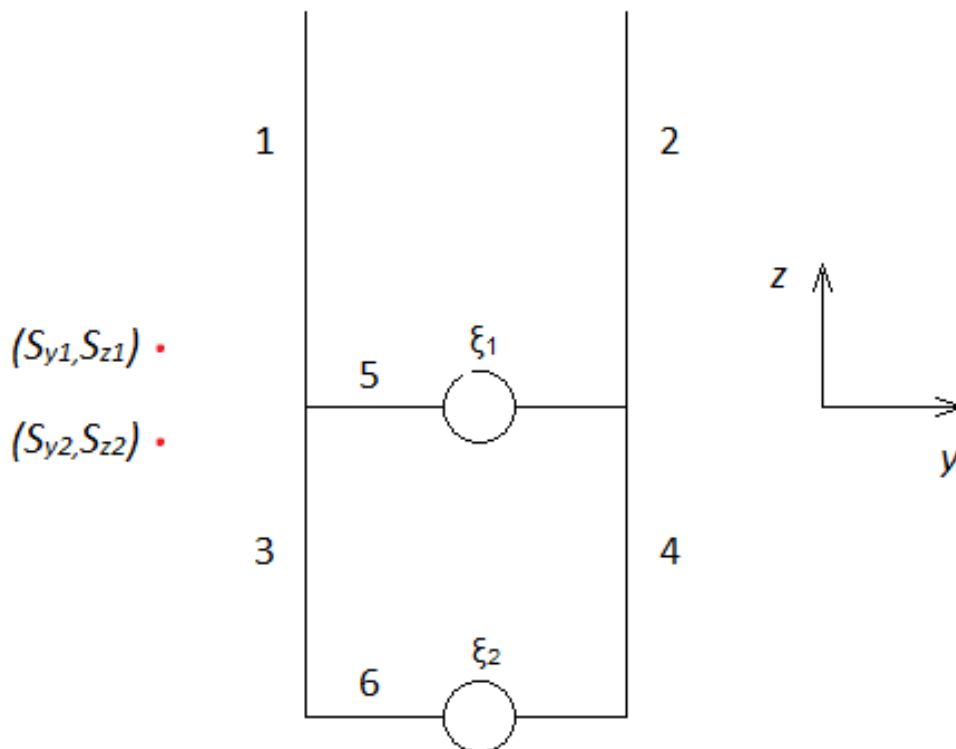


**Figure 2.6 - A 6-element circuit with 2 independent currents and 2 magnetic measurement points. The magnetic field can be calculated at each sensor location  $S$ , for each independent partial current path and a solution is formed by taking a linear combination of the 2 partial currents.**

Applying Kirchoff's current law (summing currents at each node to zero) to the circuit in Figure 2.6 gives each wire current  $i_{1-6}$  in terms of the two independent sources  $\xi_1$  and  $\xi_2$ . The equations for  $i_{1-6}$  may be expressed in matrix form (**Error! Reference source not**

**found.** and (2.36)).  $I_s$  is known in this case, from inspection of the current paths due to each current source.

$$\begin{bmatrix} i_1 \\ i_2 \\ i_3 \\ i_4 \\ i_5 \\ i_6 \end{bmatrix} = \begin{bmatrix} -1 & -1 \\ 1 & 1 \\ 0 & 1 \\ 0 & 1 \\ 1 & 0 \\ 0 & 1 \end{bmatrix} \begin{bmatrix} \xi_1 \\ \xi_2 \end{bmatrix} \quad (2.35)$$

$$\mathbf{I} = \mathbf{I}_s \boldsymbol{\xi} \quad (2.36)$$

Biot-Savart's law for a finite straight wire may be evaluated to calculate a linear relationship (2.37) between the current in the  $n^{th}$  of the six wires and the magnetic field at the  $m^{th}$  of the two measurement points, assuming that the relative orientation of the wire and the measurement point remains constant. This may be performed for each wire and each sensor location, yielding (2.38) and (2.39). Combining (2.36) with (2.39) gives a linear expression for  $\mathbf{B}$  in terms of  $\mathbf{I}_s$  (2.40).

$$\begin{bmatrix} b_{x,m} \\ b_{y,m} \\ b_{z,m} \end{bmatrix} = \begin{bmatrix} k_{3m-2,n} \\ k_{3m-1,n} \\ k_{3m,n} \end{bmatrix} i_n \quad (2.37)$$

$$\begin{bmatrix} b_{x1} \\ b_{y1} \\ b_{z1} \\ b_{x2} \\ b_{y2} \\ b_{z2} \end{bmatrix} = \begin{bmatrix} k_{11} & \cdots & k_{16} \\ \vdots & \ddots & \vdots \\ k_{61} & \cdots & k_{66} \end{bmatrix} \begin{bmatrix} i_1 \\ i_2 \\ i_3 \\ i_4 \\ i_5 \\ i_6 \end{bmatrix} \quad (2.38)$$

$$\mathbf{B} = \mathbf{K} \mathbf{I} \quad (2.39)$$

$$\mathbf{B} = \mathbf{K} \mathbf{I}_s \boldsymbol{\xi} \quad (2.40)$$

Applying the matrix  $\mathbf{T}$  ensures a divergence-free current distribution, since  $\mathbf{T}$  is derived by summing currents at each node to zero.  $\mathbf{K} \mathbf{I}_s$  is also smaller than  $\mathbf{K}$ , so the computational cost of inverting the forward model  $\mathbf{K} \mathbf{I}_s$  is less than that for inverting  $\mathbf{K}$ . It is also possible to solve the problem without explicitly calculating  $\mathbf{K} \mathbf{I}_s$ . By setting elements of  $\mathbf{I}_s$  to 1, one at a time, a set of partial magnetic fields  $\mathbf{B}_s$  is obtained (2.41). This is equivalent to treating the circuit and magnetic coupling  $\mathbf{K} \mathbf{I}_s$  as a 'black box' and solving by superposition of the independent current sources.

$$\mathbf{B}_{s,column\ 1} = \mathbf{K}I_s \begin{bmatrix} 1 \\ 0 \end{bmatrix}$$

$$\mathbf{B}_{s,column\ 2} = \mathbf{K}I_s \begin{bmatrix} 0 \\ 1 \end{bmatrix}$$

$$\mathbf{B}_s = \mathbf{K}I_s \tag{2.41}$$

Substituting (2.41) into (2.40) gives (2.42), which may be rearranged using a regularised inversion method (such as Tikhonov regularisation) to find  $\xi$  (2.43). The right hand side of (2.43) is obtained by measurement ( $\mathbf{B}$ ) and repeated simulations of partial fields ( $\mathbf{B}_s$ ).  $\xi$  defines the complete electrolyte current distribution (such as the currents in the  $y$ -direction wires  $w_{1-9}$  in Figure 2.5), which is useful if studying uniformity of the electrolyte current. It may also be used to calculate the complete circuit current information  $\mathbf{I}$  using (2.36) if required.

$$\mathbf{B} = \mathbf{B}_s \xi \tag{2.42}$$

$$\xi = \mathbf{B}_s^{-1} \mathbf{B} \tag{2.43}$$

Hauer *et al.* [77] provide a stability analysis of divergence free Tikhonov regularisation and special basis projection. Both methods are compared with a control model consisting of independent elements in the same positions (where currents could potentially exhibit divergence). Both constrained methods exhibit a greater stability and solution accuracy compared with the control, when applied to a simulated cell geometry typical of a fuel cell. The special basis projection provides the most accurate solutions of all the methods tested. An error of 5% was added to the simulated magnetic field data, resulting in between 5.53% - 9.75% reconstruction error in the current distribution, depending on separation of magnetic sensors from the simulated cell. The fuel cell under test has a cross section of 140 × 180 mm, which is of a similar magnitude to that of an automotive battery plate.

Both constrained methods require the branch resistances that accurately represent the conductance distribution in the cell. Since some studies [26]–[29] have shown that the conductance distribution of the cell has a significant effect on current distribution, then this would appear to be circular reasoning. However, it has also been widely shown that current distribution changes over the course of a cycle ([28], [29], [33], [34], [37], [31], [61]), with the hypothesis that this is due to some areas (those close to the tabs) being preferentially charged/discharged and becoming spent prematurely, *i.e.*, local current density is related to the charge state of the local active mass as well as the conductance distribution. One possible

difficulty which remains is the conductivity of the active mass itself, which depends on SoC [40]. This means that a forward model which is accurate at 100 % SoC may not be accurate at 50 % SoC. Hauer *et al.* [77] acknowledge that studying the effect of errors in the model constraints (presumably geometry and conductances) remains an open problem.

Another potential problem with constructing an accurate forward model arises when ferrous materials are consumed in the cell reaction. Any ferrous materials present in the cell under test must be also represented in the forward model as they will distort the magnetic field. In theory, if the quantity of ferrous material in the active mass is sufficient to cause significant distortion to the magnetic field, and a significant change in that quantity occurs over the course of the charge/discharge cycle then the forward model may not match the cell under test sufficiently accurately to allow solution of the problem. Apart from this potential complication, the inverse problem of solving current distribution from the magnetic field is applicable to any battery chemistry.

### 2.3.2 Practical considerations

The sensor type used for magnetic tomography must have an appropriate sensitivity. A quick estimate of the field resulting from a typical lead acid cell is given by the Biot-Savart law for a long straight wire (2.44) where  $b$  is the magnitude of magnetic field measured by the sensor,  $\mu_0$  is the permeability of free space,  $i$  is the current and  $d$  is the perpendicular distance from the sensor to the wire.

$$b = \frac{\mu_0 i}{2\pi d} \quad (2.44)$$

An estimate of  $i$  is given by dividing the cold cranking amps by the number of plate pairs connected in parallel in the battery. A typical value for cold cranking amps is approximately > 300 A, and a typical number of plate pairs is 10 (6 × two-sided positive plates interspersed by 5 × two sided negative plates, where all 10 sides of the negative plates, and all but the outer two positive plate sides take part in the cell reaction). Therefore  $i$  can be taken as 30 A. The distance from a sensor positioned next to a battery of width 200 mm must be at least 100 mm, so this can be taken as the value of  $d$ . This evaluates to give  $b = 6 \times 10^{-5}$  T. According to a review of magnetic sensor types [74], there are a variety of sensor types available which would meet the sensitivity requirement, of which magnetoresistive sensors are probably the most readily available presently.

Green *et al.* captured an image of the magnetic field caused by a lead acid battery in operation using an array of magnetoresistive sensors [79]. The low cost and size of magnetoresistive sensors means that they are well suited to magnetic sensing arrays (see also [80] for a similar array used for metal detection), allowing real-time measurements to be made. Hall effect sensors were used in the flow-through magnetic sensor array reported in [67]. These are inexpensive and compact [74], and so they could also be used in a sensor array application.

Magnetic tomography also has applications in biomedicine (known as magnetoencephalography, or the localisation of neural currents [81]), electronic engineering (non-destructive testing of circuit boards and integrated circuits [71]), and civil engineering (locating ferrous materials hidden in concrete [80], [82]). A superconducting quantum interference device is typically used in magnetoencephalography, where magnetic field may be as small as 1 pT [73], [81]. These are also the sensor of choice in some of the industrial applications, for example [70], [71], [76].

## **2.4 Summary of Chapter 2**

Literature has been studied in the fields of lead acid battery design and testing, non-invasive imaging, and magnetic sensing methods. This provides a basis for primary research into non-invasive imaging of a lead acid battery by magnetic tomography. The field of non-invasive imaging of current distribution of electrochemical cells is an area of active research, but there is a lack of *in operando* methods which can provide spatially- and temporally-resolved images. Magnetic tomography is a technique which has attracted research interest from the point of view of inverse problem theory, and examples exist of methods for tackling problems related to fuel cells, which have a geometry that is comparable to that of a lead acid cell. There also exist examples of the practical application of magnetic tomography for other problem geometries and applications, which provide some useful guidance for further practical work with magnetic sensors. However, a gap in the research field remains for an example of a practical application of magnetic tomography for measuring the current distribution in a lead acid cell.

### 3 Experimental Setup

The experimental work in this thesis centres on attempting to apply a magnetic tomography technique to the study of current distribution in a lead acid cell. This chapter provides an overview of the experimental system - first the overall experimental setup system is described, and then the subsystems are covered in more detail. Where appropriate, subsystem test results are presented.

Two aspects of the experimental system which require significant development work are the magnetic data solver and the internal current distribution measurement system. Descriptions of these two subsystems are included here so that all the subsystems are defined. However, the development of these two parts is covered separately in Chapters 4 and 5, respectively. Similarly, experimental procedure, results and discussion are presented in Chapter 6. Where the work in those chapters departs from what is covered in this one is indicated where appropriate.

#### 3.1 System Definition

**The aim of the experimental work in this thesis is to verify the performance of a magnetic tomography system. Experimentally verifying the magnetic imaging system requires gathering and interpreting data from the magnetic imaging system, and comparing it against current distribution measurements taken by some other, more direct, method. A system diagram of the experimental setup is given in**

Figure 3.1. Each subsystem in the diagram is described by a section in this chapter – the section numbers are given in the diagram.

The equipment for gathering the actual magnetic data is covered in Sections 3.2.1 to 3.2.3. It consists of an array of magnetoresistive sensors, connected via a microcontroller to a host PC which saves the magnetic data. Converting the measured magnetic data to an estimate of current distribution is performed by a solver algorithm, which is briefly described in Section 0. The detailed development of the solver algorithm is presented in Chapter 4.

In Section 3.3 the internal measurement system is described. A system of scanning reference electrode pairs is tried and found to be unsuitable (Section 3.3.1). A novel sensor array is proposed for this application. The design process of this device is presented in Chapter 5, and its relevant specifications as a subsystem are described in Section 3.3.2.

The test cell is constructed from a pair of electrodes taken from an automotive 12 V lead acid battery (Section 0). A single cell is used in order to simplify the geometry of the current paths. The cell current is controlled using a linear circuit (Section 3.5).

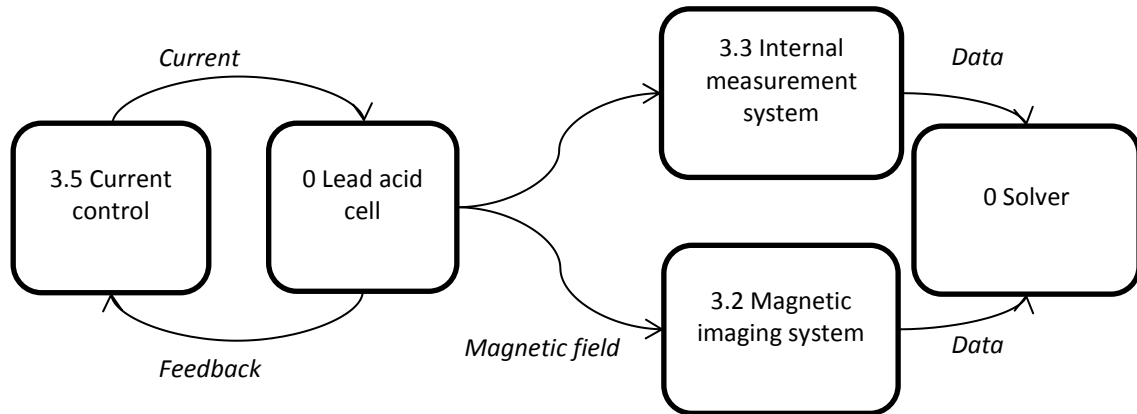


Figure 3.1 - Experiment hardware system diagram including section numbers.

## 3.2 Magnetic Imaging System

The sensor array provides a spatially resolved 2D array of magnetic field measurements. It has been used for previous studies on current distributions [79], [83]. Its operation is described in Sections 3.2.1 to 3.2.3. The magnetic data is then used as the input to a solver algorithm which estimates current distribution from the magnetic data (Section 0).

### 3.2.1 Functional description

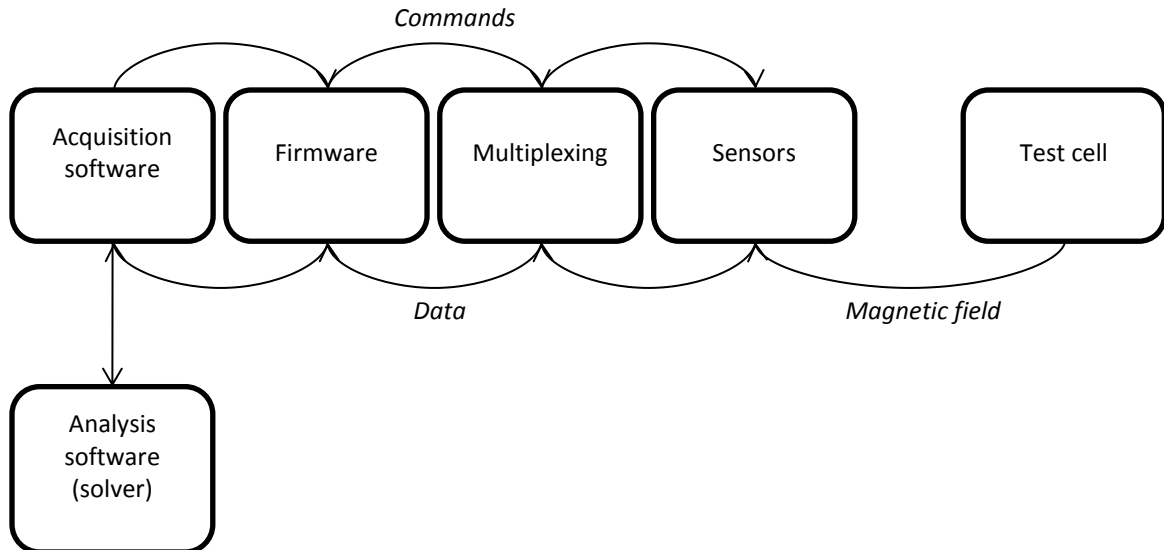


Figure 3.2 - System diagram showing hardware, firmware, software, analysis.

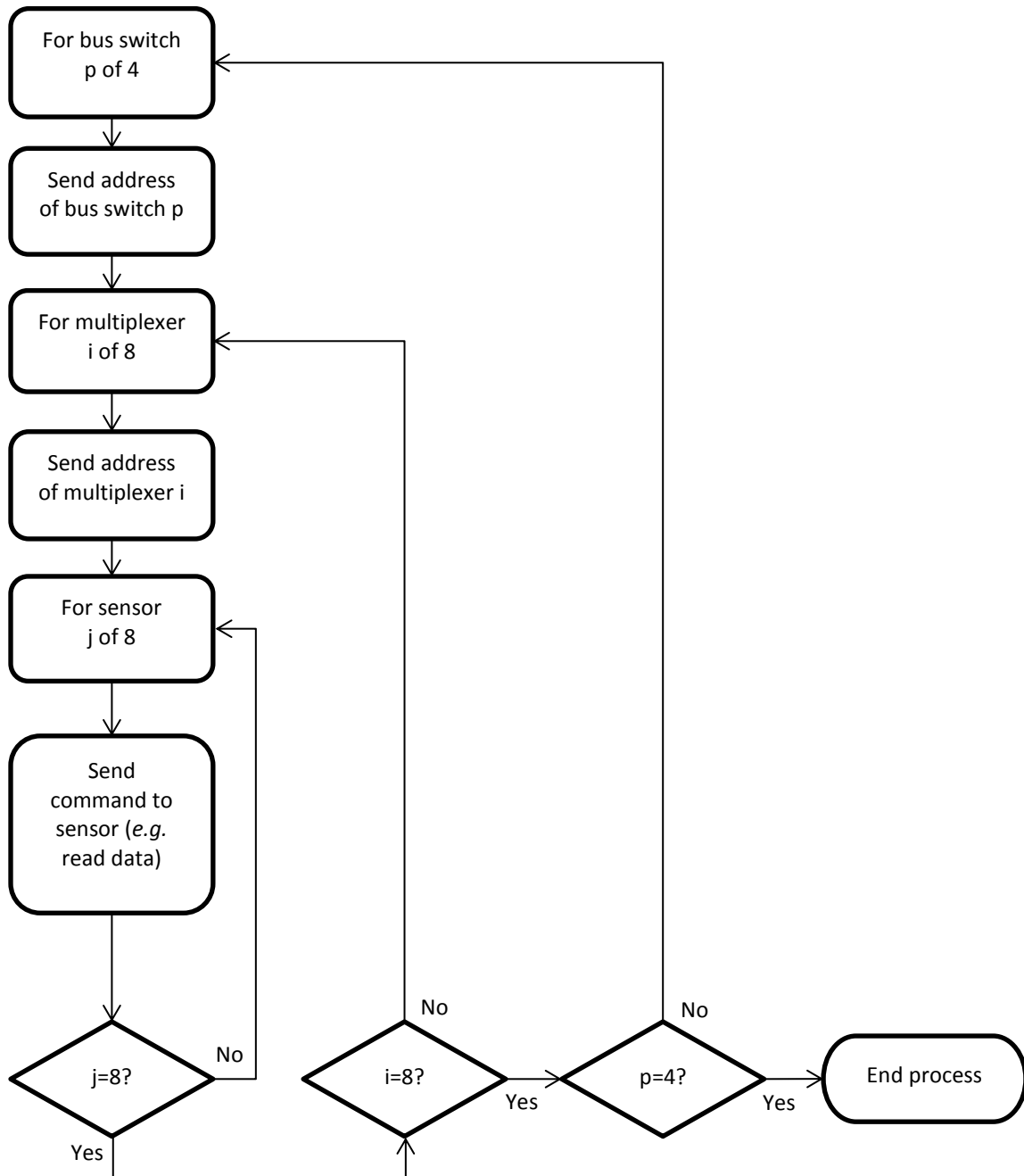
The firmware of the sensor array is run on a PIC18F4550 microcontroller. The firmware interprets commands sent over USB from the host PC and sends data back to the host PC. Data flow from the PC consists of commands for operating the board and configuring the sensors. Data flow back to the PC primarily consists of the magnetic field data from the sensors, as well as the identification register values (to allow non-responsive sensors to be found). Communication between the firmware, multiplexers and sensors is over I<sup>2</sup>C [84]. The microcontroller has only one I<sup>2</sup>C port, so data transfer from the sensors must occur sequentially. The multiplexers must be addressed to route communication to the correct sensor(s). Therefore data transfer from the microcontroller to the multiplexers consists of addresses followed by commands for the sensors. The sensors place magnetic field data in an output register, which can be read back when requested by the firmware. Communication between the PC and microcontroller is by USB bulk transfer [85]. The software and firmware can read or write data in one or two 64 byte ‘packets’, depending on the direction of data flow, which are then sent over the USB connection. Commands and data flow are shown in Figure 3.2.

The PC software provides an interface for the user to choose which commands to send to the sensor array. The software also handles writing magnetic data to file, for viewing and analysis. Data is saved as text files, with 3 files per frame (one for each axis).

### 3.2.2 Hardware structure

#### *Sensors*

The magnetic sensors used are Honeywell HMC5883L 3-axis compass ICs [86]. These each contain 3 orthogonal anisotropic magnetoresistive sensors. Gain can be set using an I<sup>2</sup>C command. Maximum gain is 1370 lsb G<sup>-1</sup> (least significant bits per Gauss) allowing fields of  $\pm 0.88$  G to be measured. Minimum gain is 230 lsb G<sup>-1</sup>, suitable for fields of  $\pm 8.1$  G). The sensor ICs have some useful supporting features – self test and read back identification register. Reading back identification register is used in this application as a simple test to check the responsiveness of the devices. The ICs have identical values stored in the identification register, so requesting the device number from each chip allows the user to identify any which are not working by comparing the received value to the expected value. If the sensor is instructed to self-test, then it applies a known current to some internal wires, causing a known magnetic field to be present. It then measures the field and outputs the result. The user can then check if the sensor is performing as required.

**Multiplexer levels**

**Figure 3.3 - Addressing each sensor sequentially using 3 tier multiplexing.**

The normal application of the sensor chips is in devices where only one is required, for example in digital compasses or mobile phones. As a result, their I<sup>2</sup>C device address cannot be set. Therefore some multiplexing is needed to address specific devices on the same I<sup>2</sup>C bus. The sensor board uses a multi-level multiplexing structure to allow communication with each

of the 256 sensors. The microcontroller's I<sup>2</sup>C bus is connected to a top level 4 channel bus switch (NXP PCA9546A [87]), which routes the I<sup>2</sup>C communication to any of 4 channels. Each of these 4 channels is connected to an 8 channel bus multiplexer (NXP PCA9547 [88]), each of which routes to 1 of 8 third level bus switches. There are thus  $4 \times 8 = 32$  third level bus switches (one for each column of switches). The third level switches (NXP PCA9548A [89]) route I<sup>2</sup>C communications to individual sensors.

Figure 3.3 shows how the 3 tiers of multiplexing can be used to address each sensor individually.

In order to communicate with the multiplexers and bus switches their device address must first be placed on the I<sup>2</sup>C bus, followed by the instruction for which channel or channels to enable. All the multiplexers and bus switches have user-settable device addresses. The microcontroller can communicate over USB to a PC.

### ***Microcontroller***

The microcontroller (PIC18F4550 [90]) is physically connected to the top tier of multiplexers via the I<sup>2</sup>C lines. It is also connected to the multiplexers' address set pins. A 20 MHz external oscillator is used for the clock. The microcontroller is also connected to the data lines of the USB output. The microcontroller can be reprogrammed using an ICD 3 [91] debugger connected via an RJ-11 socket.

### ***Power supplies***

The device runs from a regulated 3 V DC. It can be powered from a DC supply at  $> 5$  V or draw power from the USB connection.

### **3.2.3 Firmware**

The primary operations for the sensor device are contained in a function, summarised in the flow chart shown in

Figure 3.4. The important part is the switch statement which is contained in a loop, in order to poll the PC for the next command. 'Populate table of connected sensors' retrieves the first identification register value for all sensors. The values read from these registers are sent to the host PC. This provides information on which sensors are connected. Measurements are not read from sensors which have failed the identification register test. 'Read one frame of magnetic data' sends the command to trigger magnetic measurement and send the result back over USB.

Figure 3.5 shows the flow chart for this subroutine. 'Send configuration settings to sensors' sends data to the configuration registers of the sensors. Options for the configuration settings which are used in this system are the gain setting, and enabling the sensors' self-test mode. Other options which are not used in this system are averaging of measurements, and the data rate for continuous-output mode (since measurements are taken by repeatedly triggering the sensors' single-measurement mode).

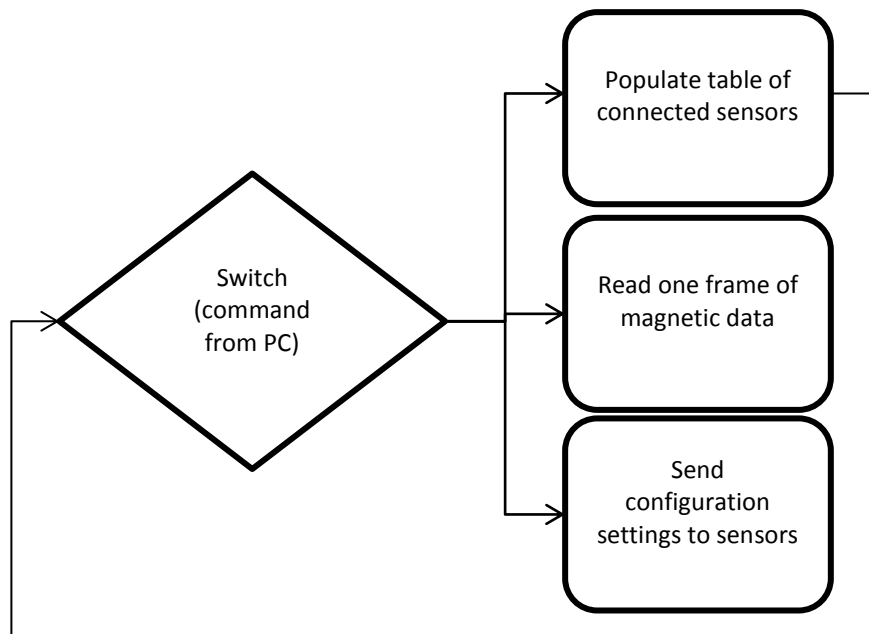


Figure 3.4 – Flow chart of top-level firmware functions.

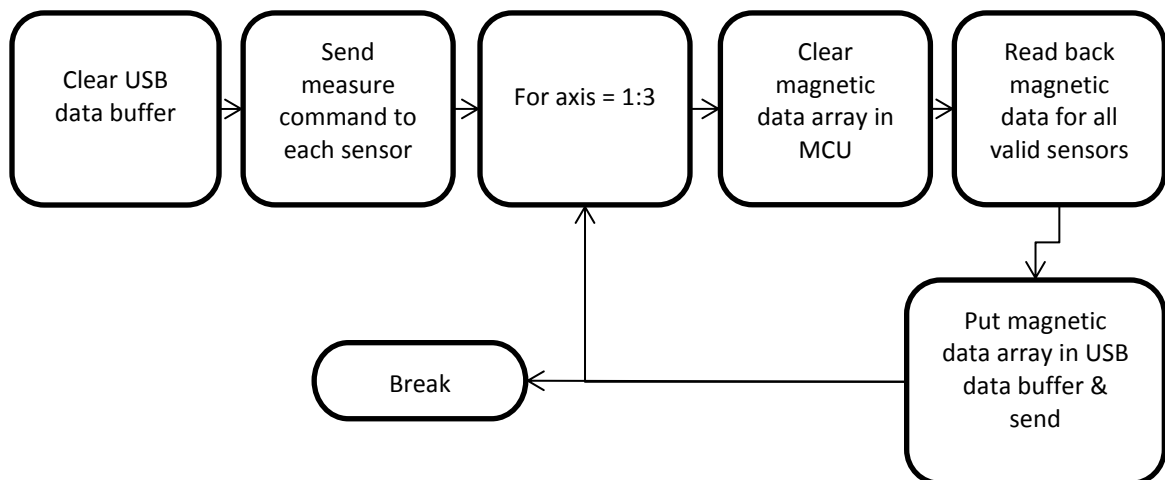


Figure 3.5 - 'Read a frame' function.

### 3.2.4 Solver

Calculating current distribution from magnetic measurements is in general an ill-posed inverse problem [72], [92]. A method of reducing problem complexity, known as special basis projection [77], is developed further for this application (see Section 4.3). A simplified system diagram is given in

Figure 3.6. Magnetic field is measured by the magnetic sensors, and partial magnetic fields are generated in a finite element simulation of the cell. If the unknown current distribution in the cell can be considered to be some linear combination,  $\xi$ , of the currents which are used to generate the partial fields, then the measured magnetic fields are also a linear combination of the simulated partial magnetic fields. By solving  $\xi = \mathbf{B}_s^{-1}\mathbf{B}$  (see (2.44)) and substituting into (2.34) the distribution of current is found. The mathematical process is covered in more detail in Section 4.3.1, but for the purpose of system definition, it is necessary to describe the structure of the solver.

The finite element model of the cell is created in Ansys Maxwell. Magnetic data is sampled at locations corresponding to those of the magnetic sensors. The cell volume is partitioned in the  $xz$  plane into a  $5 \times 4$  grid of segments. The current is set to 1 A in each segment, one at a time, with all other segment currents set to 0 A. The magnetostatic simulation is run once for each segment current so that a set of 20 partial magnetic fields is built up.

The equation  $\xi = \mathbf{B}_s^{-1}\mathbf{B}$  is solved approximately, using Tikhonov regularisation to avoid overfitting [93]. This is implemented in Octave 4.0.3, using the 'Regtools' package [69]. The resolution of the resulting current distribution 'image' is dependent on the number of segments used to generate the partial currents and fields – in this case the resolution is  $5 \times 4$ . In simulations, mean absolute error is found to depend on regularisation parameter and source current distribution but can be as low as 2.25 % for solving a uniform source distribution. Using magnetic measurements taken on a simplified resistive model of a cell, having a nearly-uniform current distribution, yields a mean absolute error of 5.66 %, indicating that the regularised solver is reasonably tolerant of typical measurement errors.

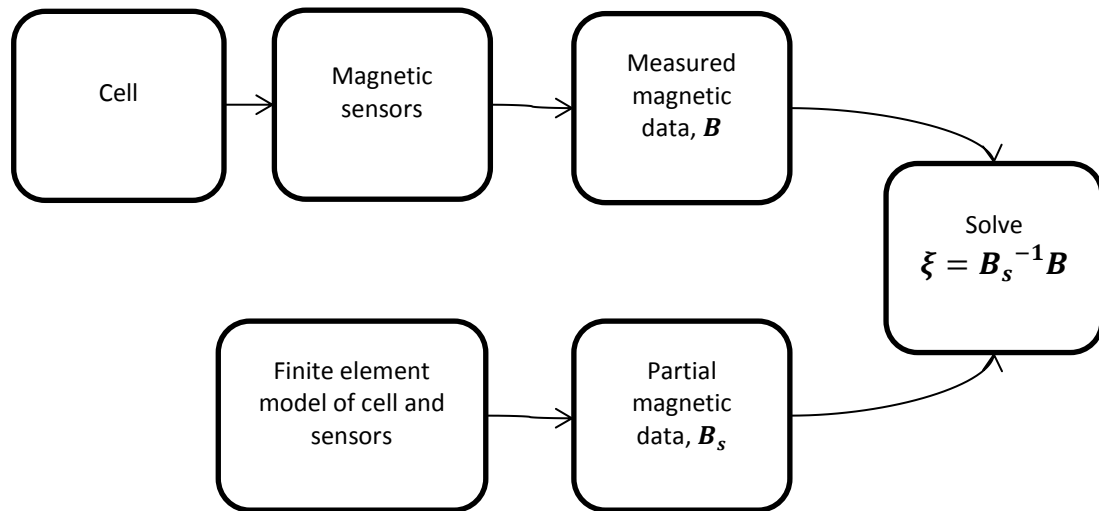


Figure 3.6 – System diagram of solver.

### 3.3 Internal Current Distribution Measurement

To verify the non-invasive magnetic imaging method, a more direct and possibly invasive method is required. Practical work is presented on two different methods which already exist in the literature – a scanning pair of reference electrodes [32], [31], and an array of magnetic cores [67].

#### 3.3.1 Reference electrode pair

The electrolyte exhibits a resistive voltage drop when a current is flowing through it. A pair of reference electrodes can be used to measure the local voltage drop, which is proportional to the current flowing past both electrodes.

Figure 3.7 shows the response of the reference electrode differential voltage to a 3 A (peak) triangular current waveform. By placing the pair at different heights in the electrolyte, the distribution of current up and down the plate can be obtained [32], [31]. Measurements were taken at 3 different reference electrode heights. A set of current pulses is passed through the cell once for each electrode position to build up a set of 3 differential voltages.

Figure 3.9 shows the 3 different reference electrode voltage waveforms, responding to 3 identical sets of current pulses. The reference electrodes used in this preliminary work are Ag/Ag<sub>2</sub>SO<sub>4</sub> types produced by Koslow Scientific. These electrodes are chloride-free, making them suitable for use with lead acid batteries [94].

In order to obtain the 3 voltage waveforms shown in

Figure 3.9, the position of the reference electrodes is altered manually, and the current pulse or set of pulses is repeated for each reference electrode position. Repeating the current pulses is not ideal as care must be taken to maintain the conditions of the cell in between repeats. Some conditions, such as temperature and state of charge, are relatively straightforward to control. However some internal conditions of the cell, such as acid stratification, are more difficult to control and may vary depending on recent cycle history.

Guo *et al.* [32], [31] used a motorised scan which allows the electrodes to be moved during the current pulse of interest, eliminating the need to repeat the current pulses. A system which scans the electrodes through multiple positions during a single current pulse does not rely on cell conditions staying constant. However, the scan time must be sufficiently fast to capture the cell state. The reference electrode voltage at a given position varies with time over the course of a current pulse (

Figure 3.9), so any variation in voltage observed while scanning the electrode vertically will be in part due to this time variation as well as spatial variation.

Figure 3.9 shows that the electrode at the top position is especially time-varying, and certainly varies significantly over the 40 s scan time reported in [32], [31].

Neither the repeating pulse method nor the motorised scanning method is entirely satisfactory. A third method is to use an array of sensors. An array of reference electrodes has been reported [54], although the size of the electrodes used here makes them impractical to place in an array. An alternative approach to creating a sensor array is to use magnetic core current sensors as the elements of the array [67], which is presented next.

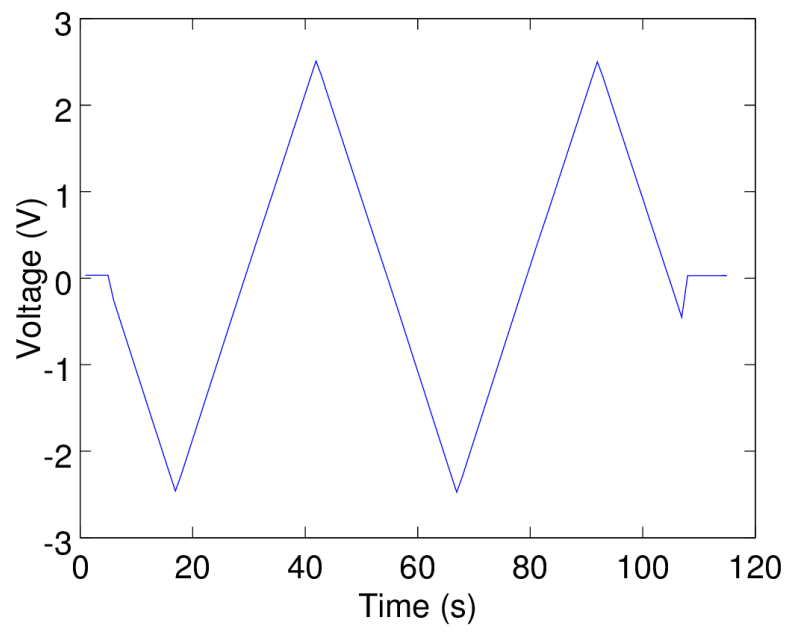


Figure 3.7 - Reference electrode response to a triangular current wave.

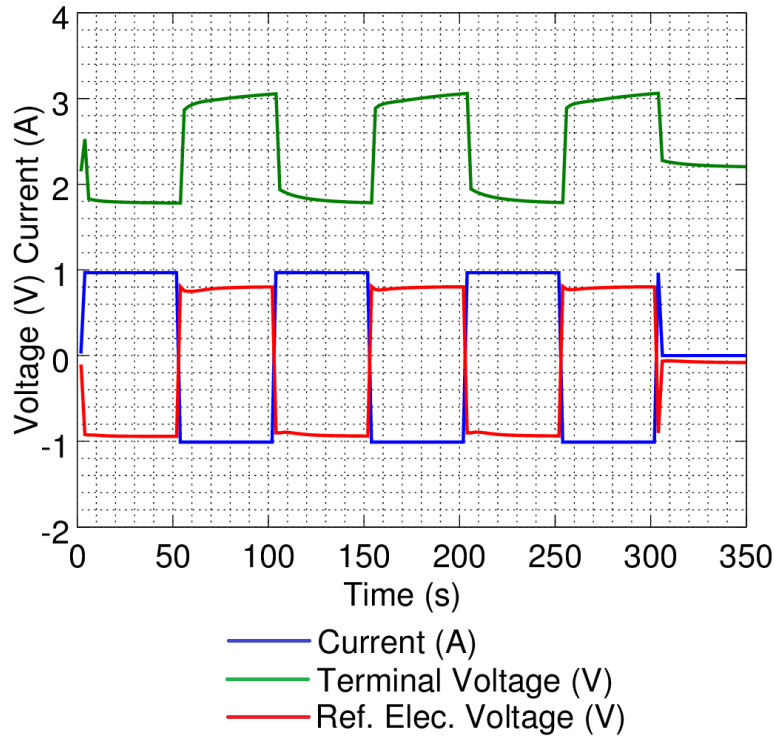


Figure 3.8 - The battery current, terminal voltage and reference electrode differential voltage (electrode in bottom position).

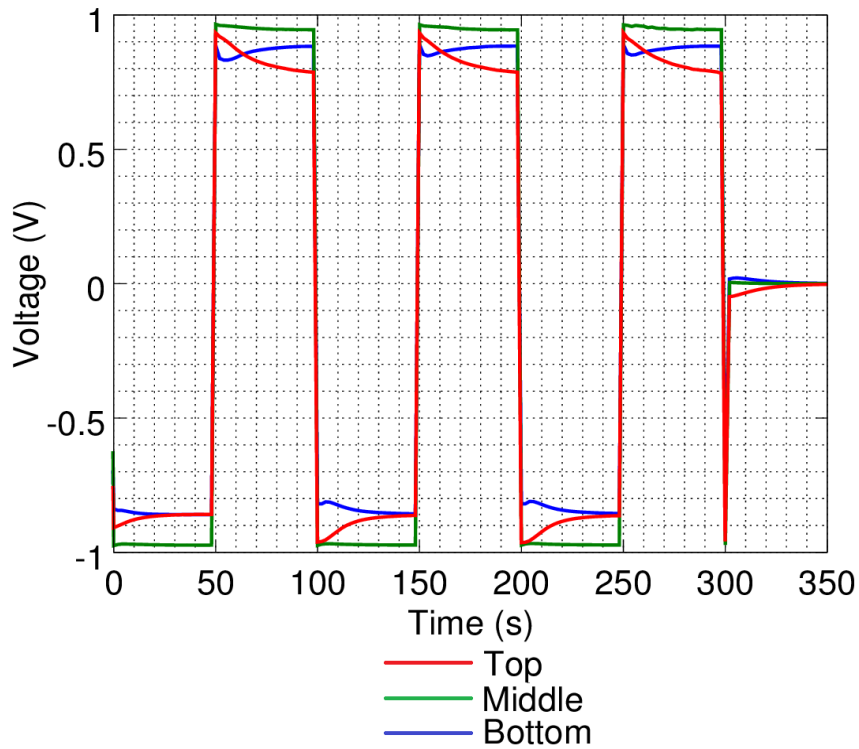


Figure 3.9 - Reference electrode differential voltages at 3 different positions.

### 3.3.2 Magnetic current sensor array

A bespoke electrolytic current sensor array based on ferrous cores and magnetic transducers is adapted for use with the test cell based on a Shield 027 battery [95] (Section 3.4.2), from a design published by Wieser *et al.* [67] and described in Section 2.2.7. The design of the sensor array is explained in detail in Chapter 5, but some relevant specifications are summarised in

Table 3.1. The sensor array is shown fitted into the cell case in

Figure 3.10. The magnetic sensors used are the same as those used in the magnetic imaging system (Section 3.2.2) and as such have configurable gain and averaging settings. The software, written for Octave 4.0.3 (Appendix III – FTS Octave Code), supports automated writing to file along with automatic file naming according to bypass switch state (the bypass switch operation and function is covered in Section 3.4.3). The sensors are interfaced using an Arduino Due, with the firmware included in Appendix II – FTS Arduino Firmware.

Property	Value
Number of apertures for current flow	20
Total available cross section area available for current flow, % of plate area	54.8
Full-scale current per segment, A	$\pm 0.139$ to $\pm 1.28$
Full scale cell current if assumed uniform, A	$\pm 2.78$ to $\pm 25.63$
Frame rate, frames per second	2.9
Typical mean absolute error on a uniform current test case, % of mean current	4.21
Averaging, number of samples per average	1 - 8

Table 3.1 – Flow-through sensor specifications.



**Figure 3.10 – Flow-through current sensor inserted into test cell case. Electrolyte can freely flow-through the white square tubes which pass through the sensor system.**

## 3.4 Cell

### 3.4.1 Initial design

A simplified cell is constructed from one pair of plates from a Yuasa YTX9-BS motorcycle battery, immersed in a 1.5 L of a 40 % concentration solution of sulphuric acid (specific gravity =  $1.312 \text{ kg L}^{-1}$ ). Off-the-shelf polypropylene containers are used for the cell case and for a bund to protect against spillage of the electrolyte (

Figure 3.12). To fit the reference electrodes in between the plates it is necessary to increase the spacing between them by making a custom mounting for the plates (Figure 3.13). The cell is made adjustable so that different plate positions can be achieved. The reference electrodes are secured by nylon bolts to the slots in the plate backing. The vertical position of each reference electrode in relation to the cell plates can be altered by loosening the nylon bolts. The guide rail/plate/reference electrode assembly can be removed from the cell, to allow safe adjustment of the reference electrodes and cell plates. The assembly is made from polypropylene and fastened with nylon studding and nuts. The cell plates are attached to the polypropylene plate backing using a commercial epoxy based grouting material (MAPEI® Kerapoxy [96]).

The Yuasa YTX9-BS has a nominal capacity of 8 Ah. Each of the 6 (2 V) cells consists of 8 plate-pairs (the concept of a 'plate-pair' is illustrated in Figure 3.11). Therefore the capacity of a cell made up of 1 plate-pair can be estimated as 1 A h. Measured capacity at 0.2 C (stop condition  $v_{cell} = 1.75 \text{ V}$ ) is in approximate agreement.

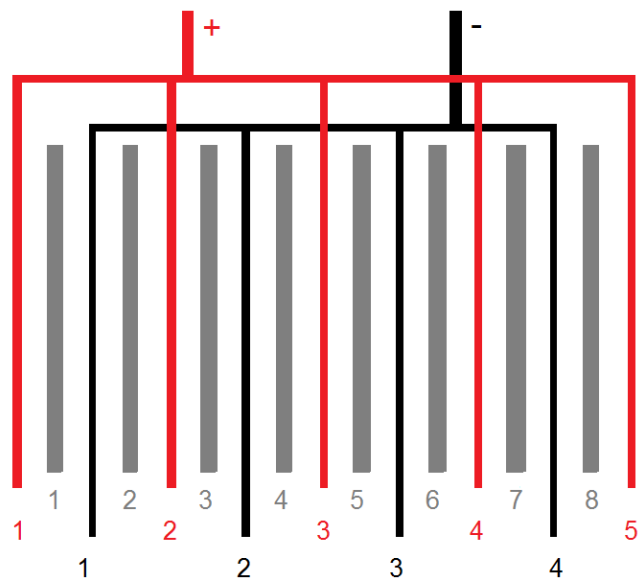


Figure 3.11 - A lead acid cell made up of 4 negative plates and 5 positive plates, giving 8 plate-pairs. Under fully charged conditions red represents the  $\text{PbO}_2$  (positive) plate and black represents the Pb (negative) plate. The absorbent glass mat (AGM) spacer material is grey.

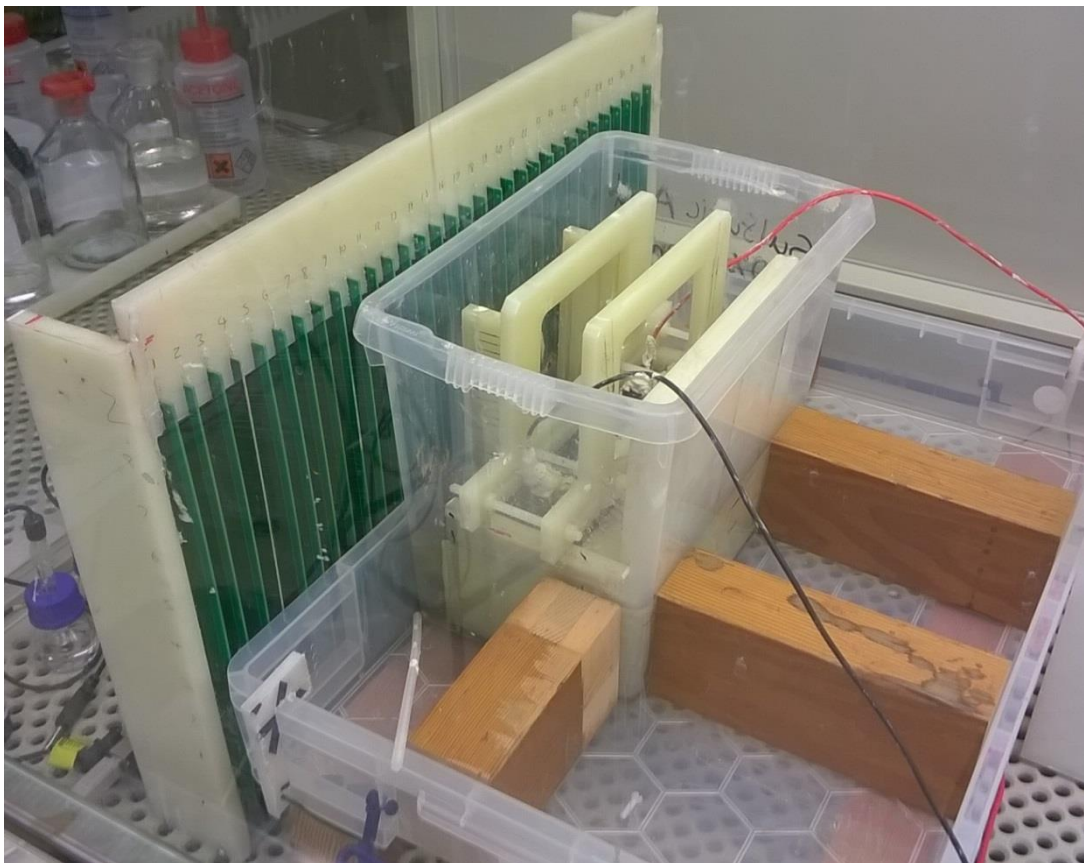
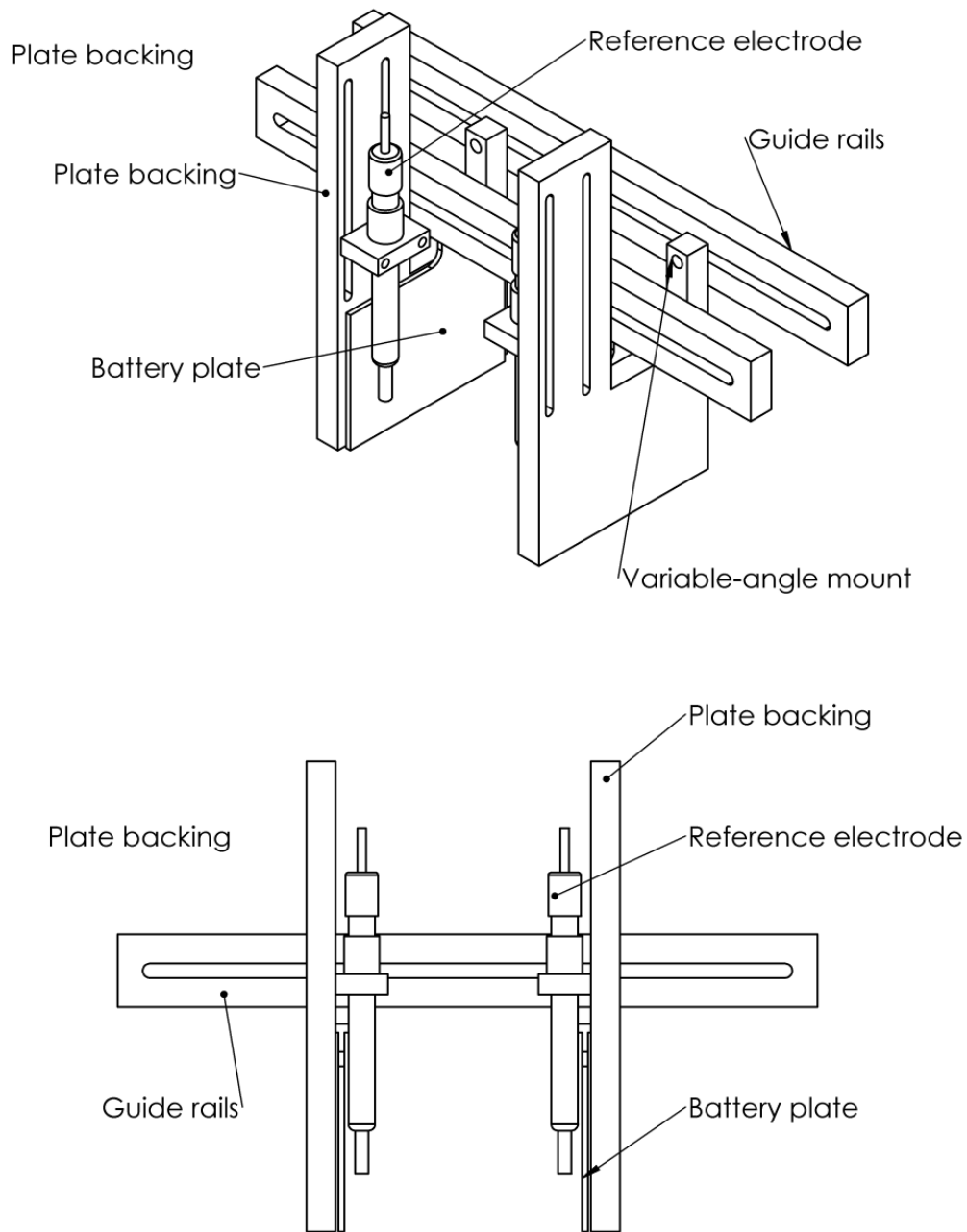


Figure 3.12 - First test cell and magnetic imaging array.



**Figure 3.13 - Arrangement of cell plates and reference electrodes.**

The freely moving terminal wires cause difficulty when modelling the cell's magnetic field. Since the magnetic field is affected by the current in the whole length of the terminal wires, and in the active load circuit, then the model should be extended to cover at least some of these. An accurate model is an essential part of the solver system (See Section 0). The difficulty with representing the terminal wires is illustrated by Figure 3.14 to Figure 3.16. Figure 3.14 and Figure 3.15 show two different options for representing a simplified version of the test cell in Ansys Maxwell. Both models cut the terminal wires short, so as to avoid creating an overly large and complicated model of the whole circuit (including current control circuit). Figure 3.14

cuts the wires off shorter than Figure 3.15. The effect of the difference between these two models and the real test cell on the resulting magnetic field is shown in Figure 3.16. The  $\mathbf{B}$  fields from each model are different, and neither model matches the measured data on all 3 components of  $\mathbf{B}$ . Therefore it appears from this test (a) that representation of the terminal wires has an effect on the  $\mathbf{B}$  data applied to the solver and (b) that at least one of the parameters or measurements in the model is wrong, and/or some complexity must be added. Adding complexity to the model is undesirable. It means there are more parameters and measurements which are subject to uncertainty, increasing sources of error in the model, and time needed to accurately design the model. In this case, insufficient dimensional data was gathered about the rest of the circuit to accurately model it all. Adding complexity also increases the computational cost of the model.

Another problem with the existing cell design is the pre-built polypropylene cell case. Its inner dimensions do not match those of the cell plates, and so it is likely that the current exhibits some fringing into the irregularly-shaped volume of electrolyte. This is another part of the cell where the current follows a relatively complex path. Finally, the nylon parts (studding, nuts and bolts) did not resist the sulphuric acid electrolyte sufficiently and many of the nylon bolts and nuts required frequent replacement.

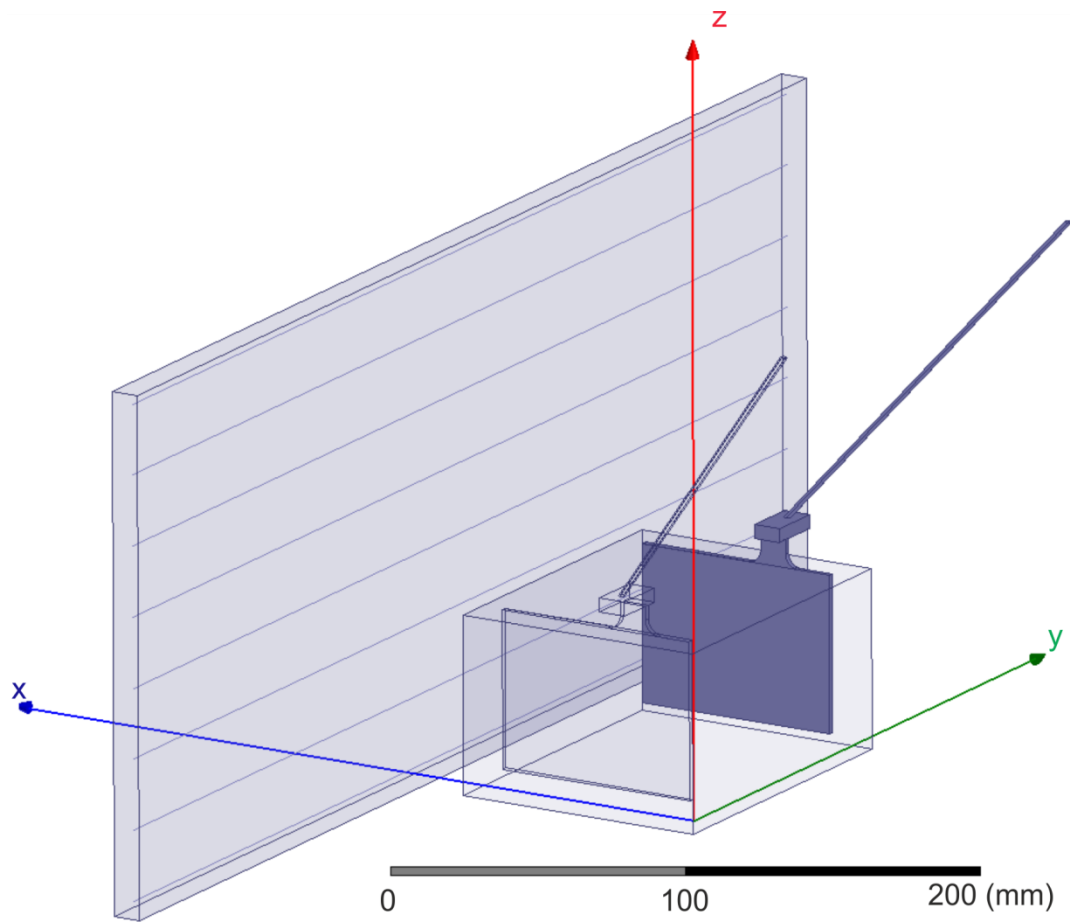


Figure 3.14 - Ansys Maxwell model of cell with short terminal wires added.

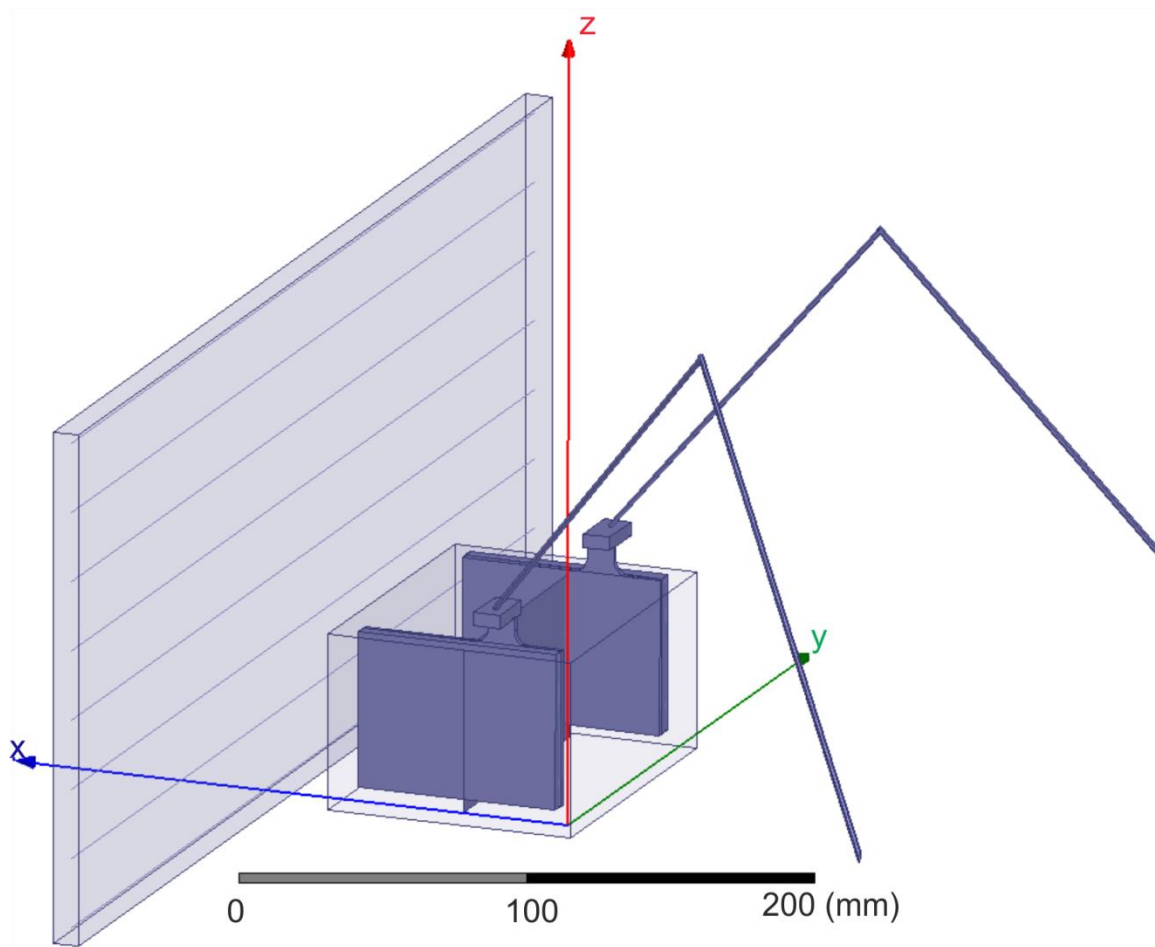


Figure 3.15 - Ansys Maxwell model of cell with longer terminal wires added.

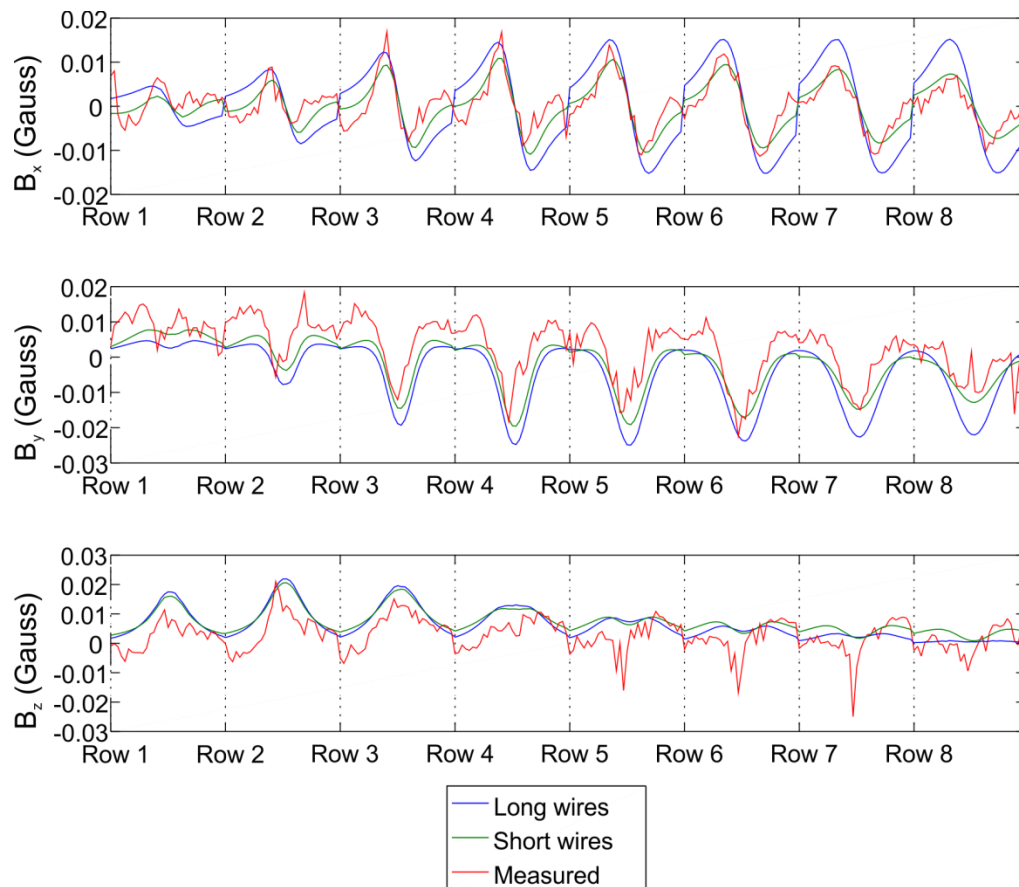


Figure 3.16 - Comparison of B field data from two simulations and a measurement.

### 3.4.2 Improved design

An updated cell is designed based on the findings from using the initial cell design. Some modifications are also necessary in order to accommodate the choice of a magnetic current sensor array rather than reference electrodes for internal current sensing. The modifications are summarised in

Modification	Notes
<b>Solid bus bars replace terminal wires (1)</b>	Cannot move freely – consistent position across measurements.
<b>Bypass switch (2)</b>	Shortens magnetic effective length of terminal wire which must be represented in model (see Section 3.4.3).
<b>Larger cell plates</b>	More current, giving stronger $B$ field. More area over which to resolve current distribution.
<b>Bespoke cell case (3)</b>	To fit cell plates, resulting in less fringing.
<b>Non-adjustable plate positions</b>	Less dimensional variables.
<b>Non-removable plates</b>	Using a magnetic current sensor array rather than reference electrodes – no adjustments to be made inside cell during operation.
<b>Recessed cell case (4)</b>	To fit current sensor array in a fixed position relative to cell
<b>Cell and sensor array fixed to wooden base (5)</b>	Reduces variation in dimensions over course of experiment

Table 3.2, and some are illustrated in Figure 3.17.

The new cell is based around a car battery rather than a motorcycle battery. This is in order to pass a larger current, in turn giving a stronger  $B$  field to be measured by the magnetic sensors. It also makes construction of the cell and the flow-through sensor more convenient as less miniaturisation is required. A Shield 027 battery [95] is chosen as it is available dry-charged (with fully formed plates and no electrolyte). The absence of electrolyte makes it relatively straightforward and safe to recover the plates to use in a test cell. After dismantling the cell using hand tools, the plate is measured as 145 mm  $\times$  104 mm. The Shield 027 has a nominal capacity of 60 A h and each cell consists of 12 plate-pairs. Therefore nominal capacity of the test cell is 5 A h. However, the 0.2 C capacity for the test cell is measured at 7.9 A h.

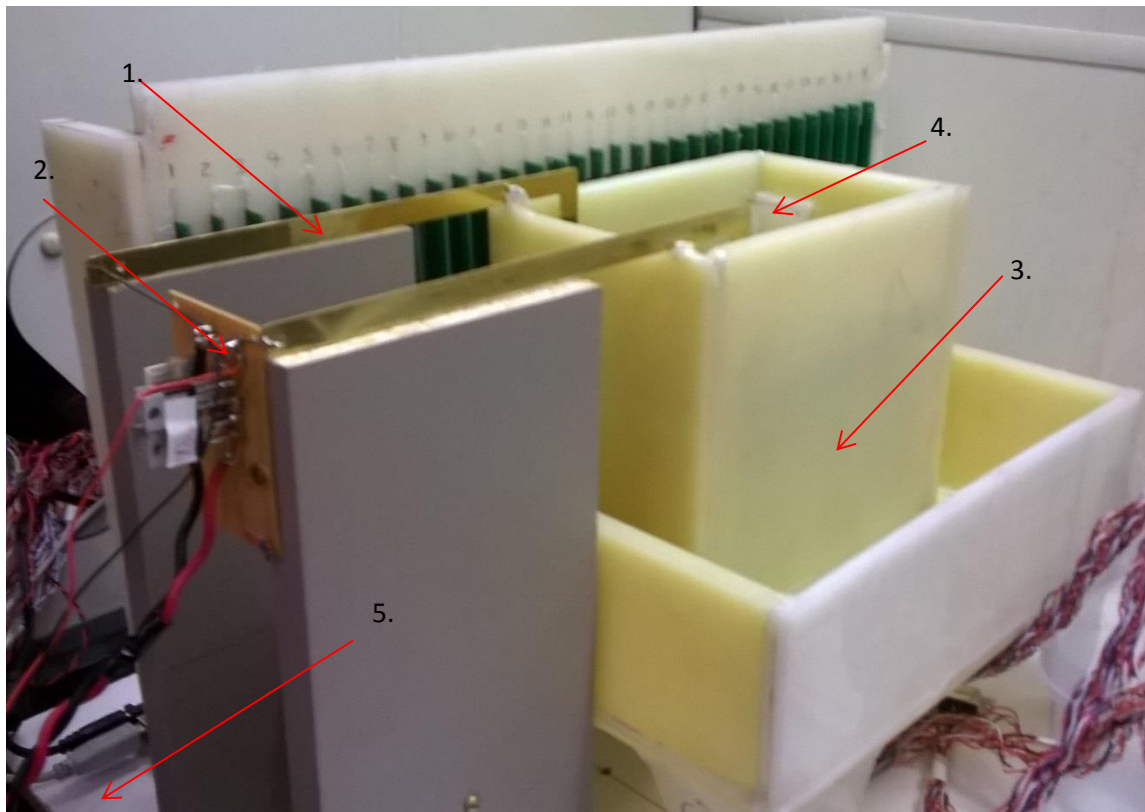


Figure 3.17 - Updated test cell with magnetic sensor array in background. Modifications are numbered where visible, according to

Modification	Notes
<b>Solid bus bars replace terminal wires (1)</b>	Cannot move freely – consistent position across measurements.
<b>Bypass switch (2)</b>	Shortens magnetic effective length of terminal wire which must be represented in model (see Section 3.4.3).
<b>Larger cell plates</b>	More current, giving stronger $B$ field. More area over which to resolve current distribution.
<b>Bespoke cell case (3)</b>	To fit cell plates, resulting in less fringing.
<b>Non-adjustable plate positions</b>	Less dimensional variables.
<b>Non-removable plates</b>	Using a magnetic current sensor array rather than reference electrodes – no adjustments to be made inside cell during operation.
<b>Recessed cell case (4)</b>	To fit current sensor array in a fixed position relative to cell
<b>Cell and sensor array fixed to wooden base (5)</b>	Reduces variation in dimensions over course of experiment

Table 3.2.

Modification	Notes
<b>Solid bus bars replace terminal wires (1)</b>	Cannot move freely – consistent position across measurements.
<b>Bypass switch (2)</b>	Shortens magnetic effective length of terminal wire which must be represented in model (see Section 3.4.3).
<b>Larger cell plates</b>	More current, giving stronger $B$ field. More area over which to resolve current distribution.
<b>Bespoke cell case (3)</b>	To fit cell plates, resulting in less fringing.
<b>Non-adjustable plate positions</b>	Less dimensional variables.
<b>Non-removable plates</b>	Using a magnetic current sensor array rather than reference electrodes – no adjustments to be made inside cell during operation.
<b>Recessed cell case (4)</b>	To fit current sensor array in a fixed position relative to cell
<b>Cell and sensor array fixed to wooden base (5)</b>	Reduces variation in dimensions over course of experiment

Table 3.2 - Modifications to initial cell design. Numbers in brackets refer to annotations on Figure 3.17.

The cell case is constructed from polypropylene sheet joined using heat welding, since most glues do not adhere strongly to polypropylene. The cross section dimensions of the electrolyte volume approximately match those of the cell plate, except for the recess where the flow-through sensor is located. Figure 3.18 shows the cell case interior. The outer of the case (shown in green) is constructed first and leak tested in a water bath. The flow-through sensor locator blocks (shown in red) are then assembled and tacked into place using heat weld. The plates rest on top of the locator blocks and are semi-permanently fastened to the case outer

using Araldite® epoxy. The epoxy adheres strongly enough to hold the plates in place, but can be easily chiselled away from the polypropylene.

Solid brass bus bars can be constructed in a simple, right angled geometry. The straight lines and right angles make them easy to draw in CAD software (Autodesk Inventor) for use in an Ansys Maxwell model. By fixing their position at the plate tab and at the end where it joins the rest of the circuit, a more repeatable position is achieved than with the wires used previously. The bus bars are attached to the cell plates using M2 brass screws (Figure 3.19).

The bund is designed to have sufficient internal volume to contain a spillage of the entire liquid content of the cell (approximately 1.4 L). It is fitted with legs which raise the cell plates to approximately mid-way up the magnetic imaging array. The cell case outer is fixed into place inside the bund using blocks of wood. The position of the bund is fixed relative to the magnetic imaging array by screwing both to a wooden base.

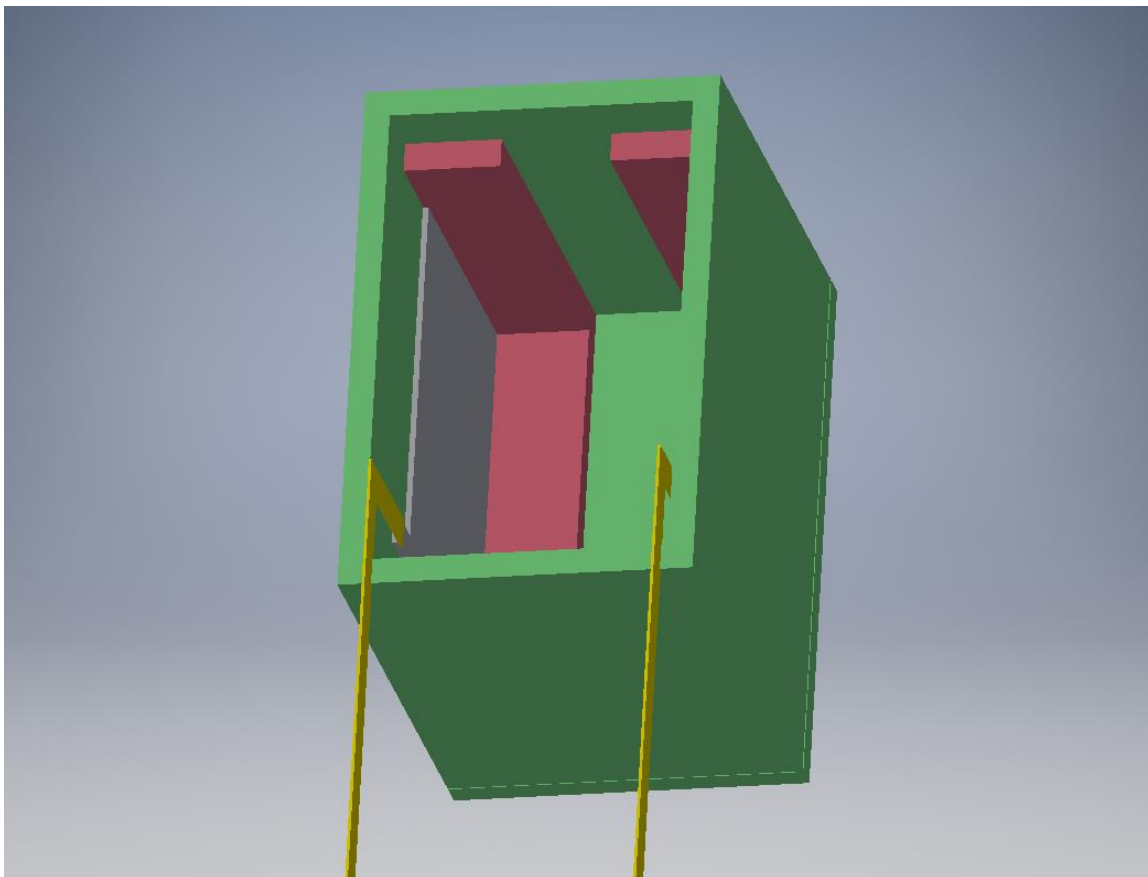


**Figure 3.18 - Autodesk Inventor drawing of the test cell. Cell case shown in green, locator blocks shown in red, negative plate shown in grey and brass terminals shown in gold.**

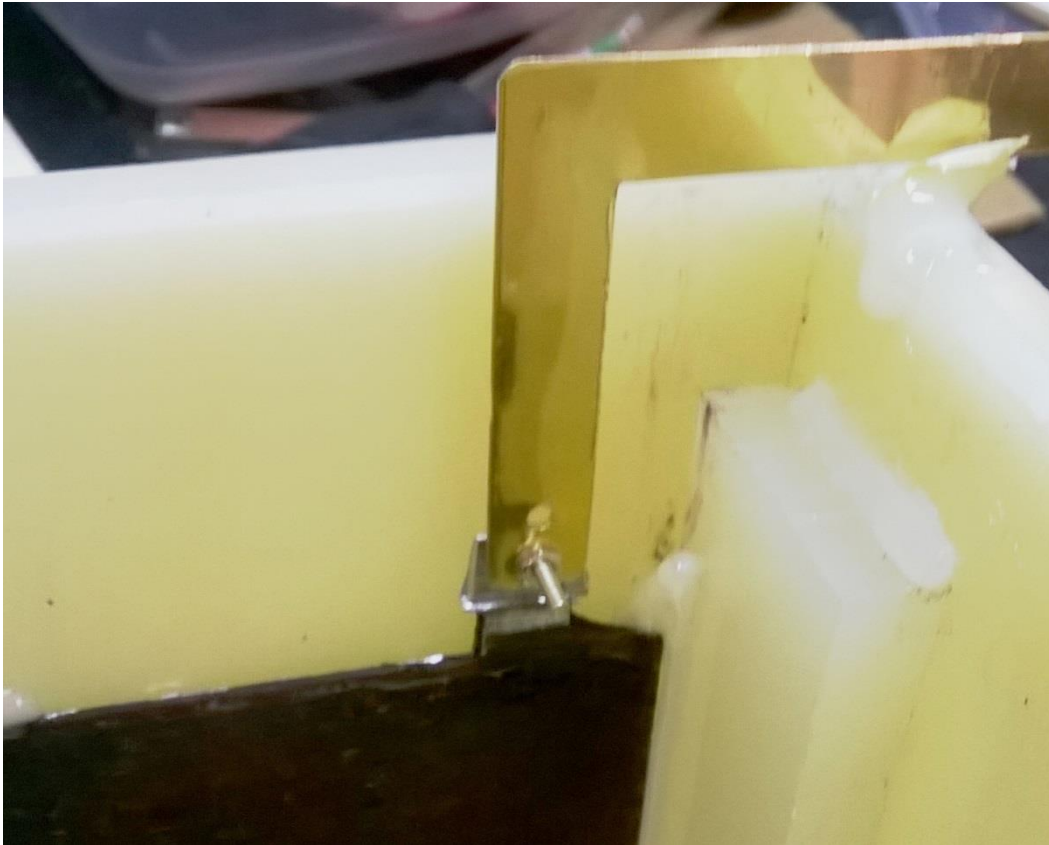


Figure 3.19 - Bus bar attached to plate tab using brass bolt and nuts.

### 3.4.3 Bypass switch

In magnetic sensing, it is desirable to eliminate the ambient magnetic field from measurements. This can be accomplished by shielding or by active cancellation [73], [74]. For removing steady-state components of the ambient field (such as the Earth's magnetic field), active cancellation is achieved very simply by subtracting a measurement of the ambient field from a measurement of the device under test. In the case of the current-carrying test cell, the current is set to 0 so that the ambient data may be recorded. Care should be taken not to disturb the position of the cell or sensors before switching on the current in the cell and taking an 'image' measurement. The forward model in this case must account for the entire path of the current that passes through the cell, including any control circuitry, but does not have to take account of the sources of ambient magnetic field. In the experiment being proposed in this chapter, a bypass switch is employed in order to obtain the ambient field readings. This further reduces the necessary scope of the forward model by subtracting out the effect of the current source and the wires linking the cell to the current source.

When taking the ambient data using the bypass method, the current from the active load is diverted from the cell rather than switched off entirely. This means that all of the  $B$  field due

to the current on the common side of the bypass switch is subtracted out as part of the dark frame. The flexible wires and active load circuit do not need to be added to the magnetic model at all, providing that their position remains constant between taking the dark frame and the image frame. The resultant current path in the system after subtraction is given by  $I_3 = I_1 - I_2$ , where  $I_1$  is the current path taken when the image frame is taken,  $I_2$  is the current path when the dark frame is taken, and  $I_3$  is the resultant current. Only  $I_3$  needs to be included in the magnetic model (providing the magnitudes of  $I_1$  and  $I_2$  are equal). Simplified circuit diagrams showing these current paths are given in Figure 3.20. SW1 is the bypass switch, a single pole dual throw (SPDT) type. The current source I represents the active load and provides a constant current.  $I_3$  is convenient to represent in Ansys Maxwell as the current is a closed loop, which doesn't pass through the problem region boundary. Figure 3.21 shows a model representing the test cell. Notice the twisted pair cable connected to the bypass switch shown in Figure 3.17 is not shown as it does not carry any resultant current after dark frame subtraction.

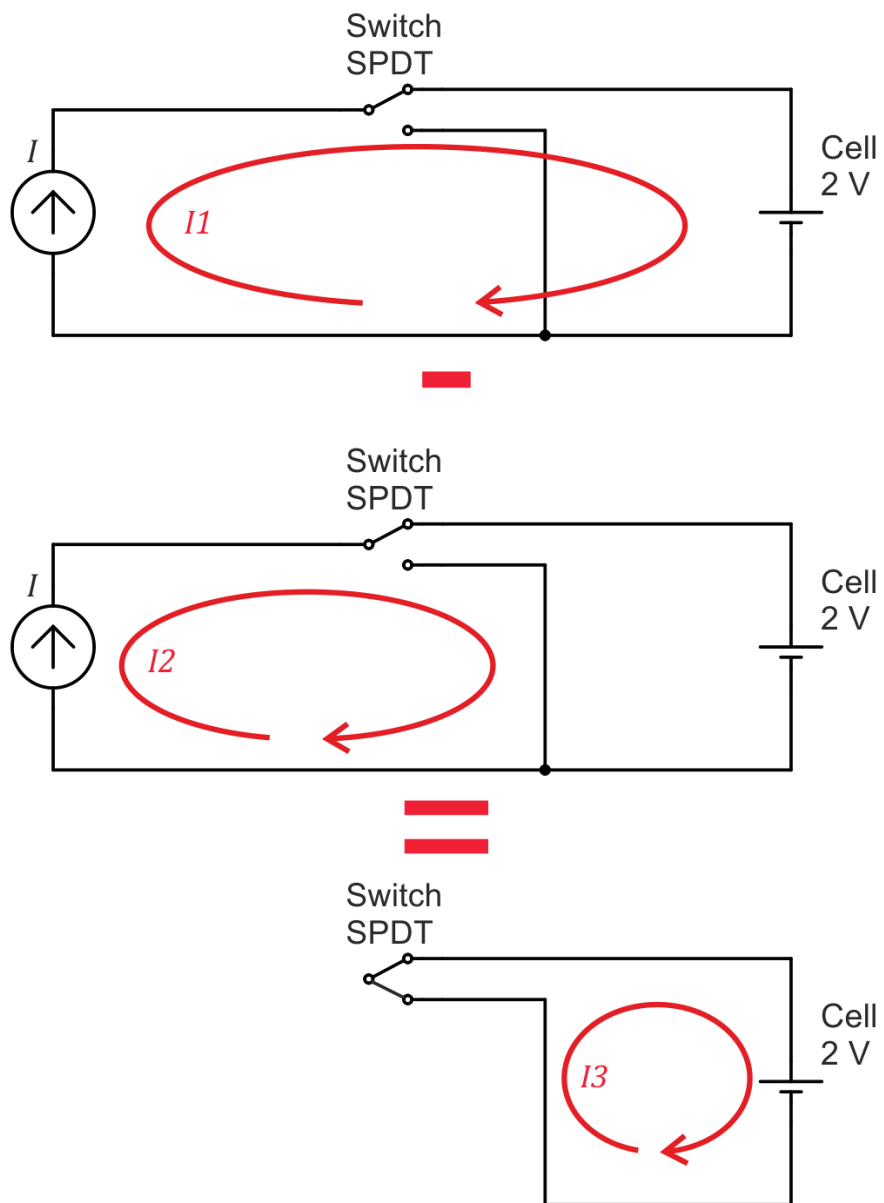


Figure 3.20 - Using the bypass switch to subtract out part of the circuit.

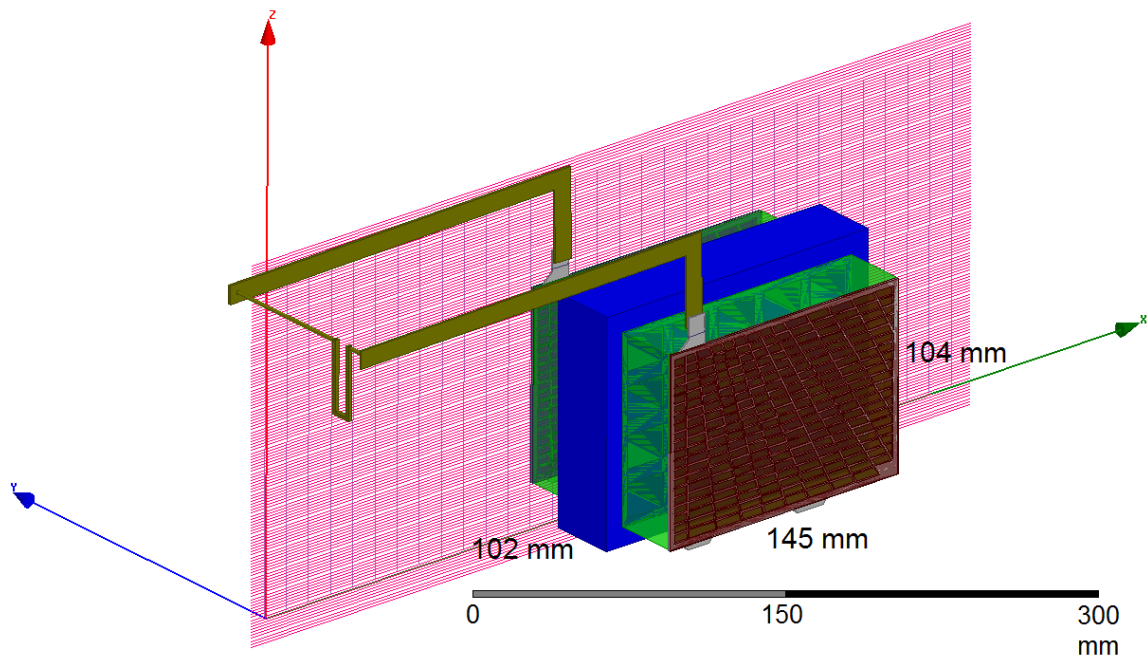


Figure 3.21 - Representation of the cell and terminal wires in Ansys Maxwell. Cell plates measure  $145 \times 104$  mm, plate separation is 102 mm

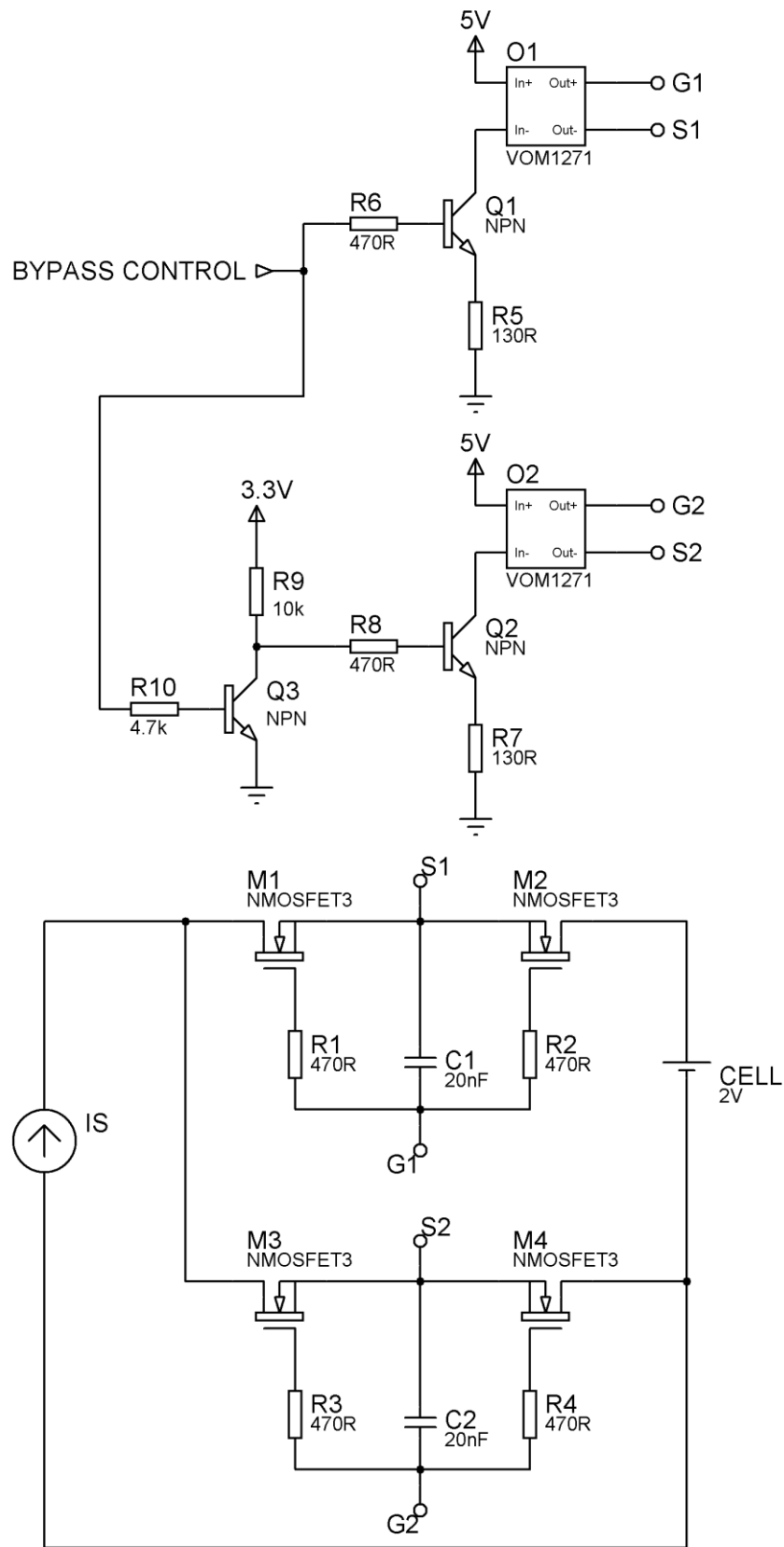


Figure 3.22 - Solid state relay circuit implemented using opto-couplers and MOSFETs.

Remote control of the switch is desirable for user safety, as it is located inside the chemical station close to the open test cell. Also, mechanically operating a switch is likely to disturb the position of the cell or the cables in between taking the dark frame and the image frame, reducing the accuracy of the resultant frame. A solid state relay is a suitable device for this. A solid state relay is preferable to an electromagnetic relay due to the presence of magnetic material in the actuator, which would have to be included in the finite element model, increasing model complexity and sources of positional errors. The solid state relay is implemented using discrete power MOSFETs, driven by opto-couplers and controlled by a microcontroller. A circuit diagram is shown in Figure 3.22.

In Figure 3.22, the MOSFETs M1 and M2 form the ‘through cell’ path, so that when they are turned on by  $v_{gs1}$  all current from the current source  $i_s$  passes through the cell. M1 and M2 are arranged back to back in series, so that their blocking diodes are facing opposite directions. This is so that they can block currents in both directions, since the cell must both be charged and discharged.  $r_{dsON}$  is approximately 2.94 m $\Omega$  per device [97].  $v_{gs1}$  is controlled by the optocoupler O1. O1 is a VOM1271 [98] MOSFET driver.  $v_{s1}$  will vary as the cell’s SoC changes, so connecting  $v_{gs1}$  to a floating potential gives reliable switching. The input to O1 is the current required to drive its internal LED, so it is connected to the current source circuit formed by Q1 and R5. When the ‘Bypass Control’ signal is high (3.3 V), Q1 will switch on and R5 has  $3.3 - v_{be1} \approx 2.6$  V across it, giving  $i_{e1} \approx i_{c1} \approx 20$  mA through the LED of O1. According to the specification of the VOM1271 this gives an open circuit output voltage of 8.7 V and a short circuit output current of 30  $\mu$ A.

M3 and M4 are the equivalent for the ‘bypass cell’ path. The operation of M3 and M4, the isolator O2 and current source Q1, R7 is identical to that for the ‘through cell’ path. Q2 is switched on by the output of Q3, which is configured as a common emitter inverter, which inverts the Bypass Control signal. The branches M1, M2 and M3, M4 are thus switched alternately.

If both branches switch on at the same time then the cell terminals are short-circuited and a large current will discharge the cell. This is avoided by introducing a time delay after switching off a branch, before switching on the other branch. This time delay happens as a result of the output characteristic of the VOM1271 (small output current, with fast turn-off circuit) and the 10 nF gate capacitance (approx.) of each MOSFET [97], represented in Figure 3.22 by C1 and C2. Figure 3.23 shows  $v_{gs1}$  (‘Through’) and  $v_{gs2}$  (‘Bypass’). Notice that the rising edges are less

steep than the falling edges, so that the point at which they cross over is  $< 1$  V, which is well below the turn on threshold voltage for the MOSFETs. The output current through the switch branches is shown in Figure 3.24. To measure the currents 2 V is applied to the switch common and a  $2.2 \Omega$  sense resistor is connected from each branch to ground. The dead time between the 'Bypass' and the 'Through' currents is due to  $v_{gs1}$  and  $v_{gs2}$  having slower rising edges than falling edges. By adding extra capacitance in the circuit in the same position as C1 and C2, the dead time can be increased if required. The dead times going from 'Bypass' to 'Through' and vice versa are not equal. This is because of incorrect design of the inverter, resulting in a base voltage at Q2 of 2.4 V rather than 3.3 V. This means less current to the input of O2 and as a result less current to charge the gate-source capacitances of M3 and M4.

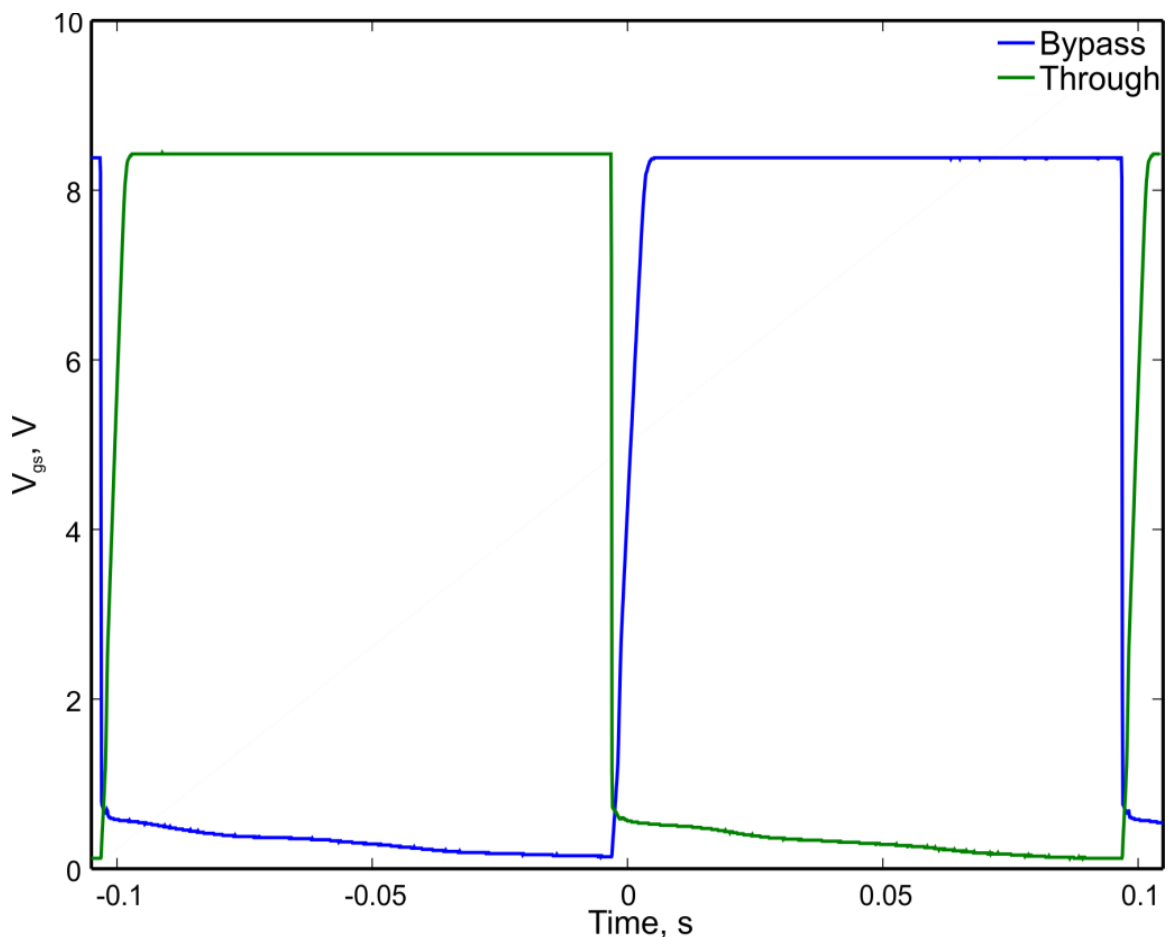


Figure 3.23 – Gate-source voltages for each branch of the dual-throw bypass switch when a 5 Hz control signal is applied.

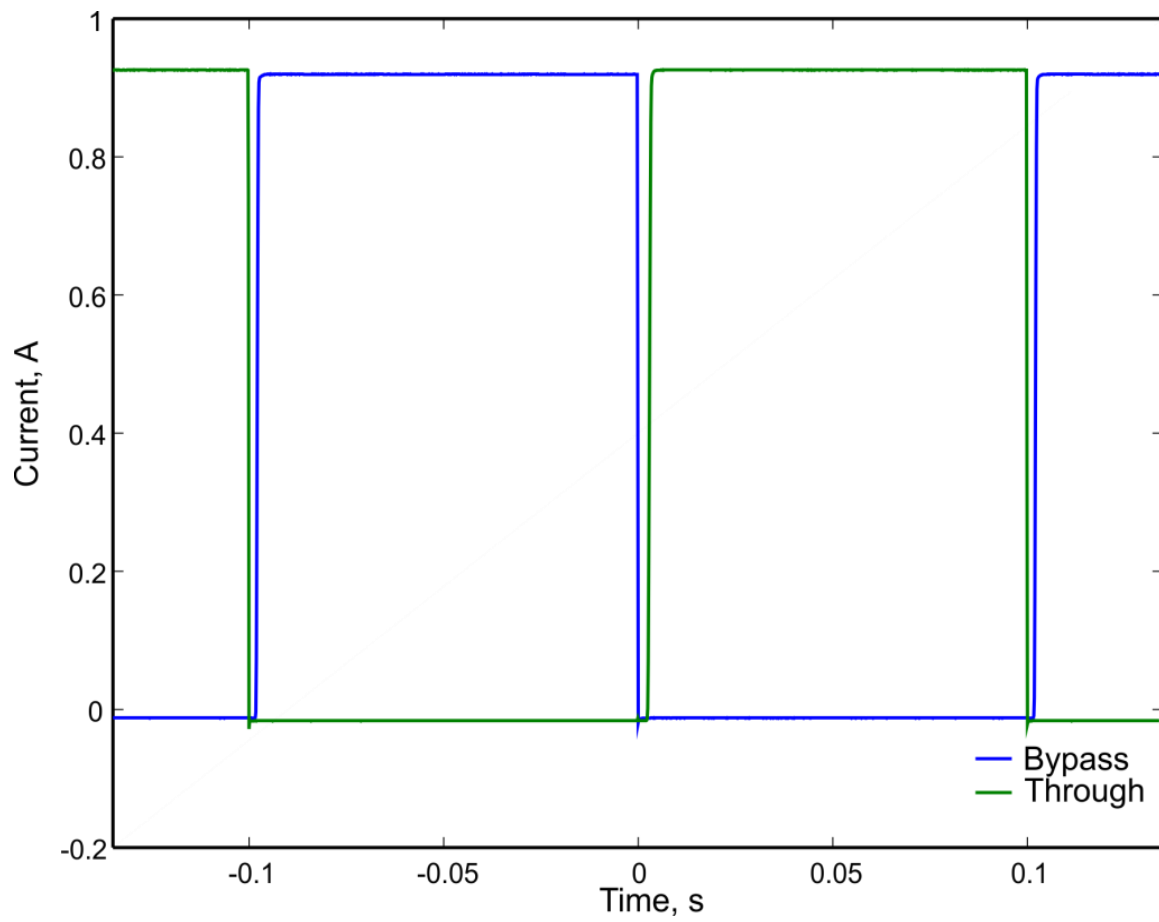


Figure 3.24 – Current through each branch of the switch when a 5 Hz control signal is applied. Current is measured using a 2.2  $\Omega$  sense resistor connected in each branch.

### 3.5 Current Control

Connecting the cell to a constant current active load allows convenient checking of current distribution data, since the segment currents must sum to the cell terminal current. Also, cancellation of magnetic field due to wire currents using the bypass switch described in Section 3.4.3 requires a constant current in order to work properly.

#### 3.5.1 Requirements specification

The desired cell terminal current is 5 A as it gives a 1 C rate relative to the nominal capacity of the cell. A preliminary test using Ansys Maxwell shows that the maximum measured magnetic field,  $b$ , from a 5 A current in the designed geometry is approximately  $2.25 \times 10^{-5}$  T, which quantises into  $\pm 52$  lsb when the HMC5883L is set to maximum gain. It is important that charging currents match the discharging currents to maintain the state of charge of the cell. In other words, the output current should have low DC offset.

#### 3.5.2 Constructed design

A controlled current active load is required to connect the cell to. Figure 3.25 shows a Class B power amplifier, with feedback taken from a current sense resistor R1, which fulfils this function. Q1 and Q2 form the output stage of the amplifier. Q1 is a TIP132 NPN Darlington pair and Q2 is a TIP137, the PNP equivalent of Q1. Q3 and Q4 form an intermediate stage to drive the bases of Q1 and Q2. To eliminate DC offset, the magnitude of the current is set by a demand signal and feedback circuit (U1 and U2) and the direction of the current through the cell is determined by a double pole double throw (DPDT) switch (Figure 3.26). The direction of current from the point of view of the amplifier does not reverse. U2 is a differential amplifier which takes its inputs from very close to the terminals of R1, so that any  $ir$  drop across interconnect resistances does not contribute to the feedback signal. U1 compares the output of U2 to  $v_{demand}$ . Since  $R1 = 0.1 \Omega$  and the differential amplifier in the feedback path has a gain of 1, the overall transconductance (output current over demand voltage) of the circuit is  $10 \text{ A V}^{-1}$ .

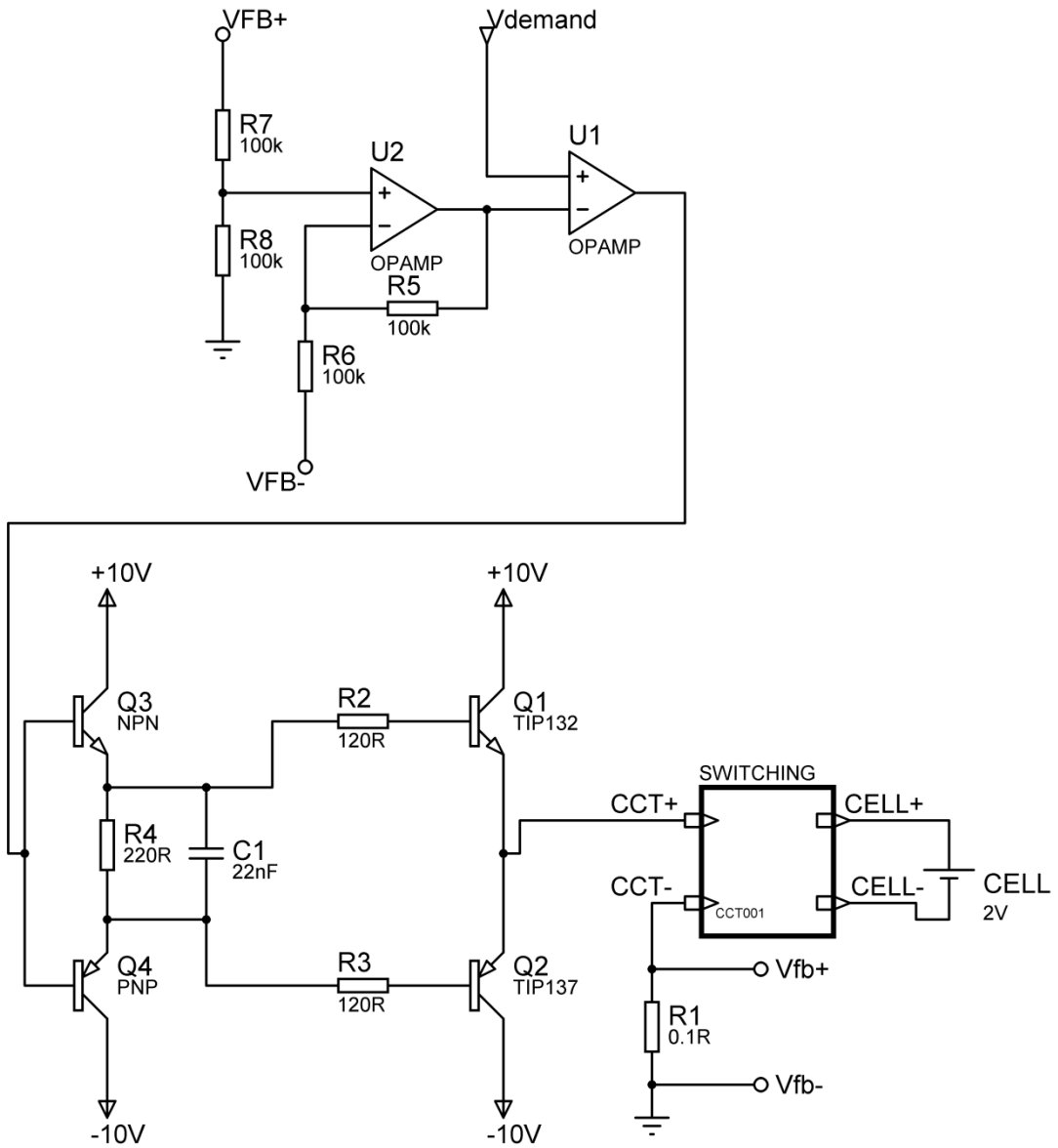


Figure 3.25 - Current controller - simplified circuit diagram.

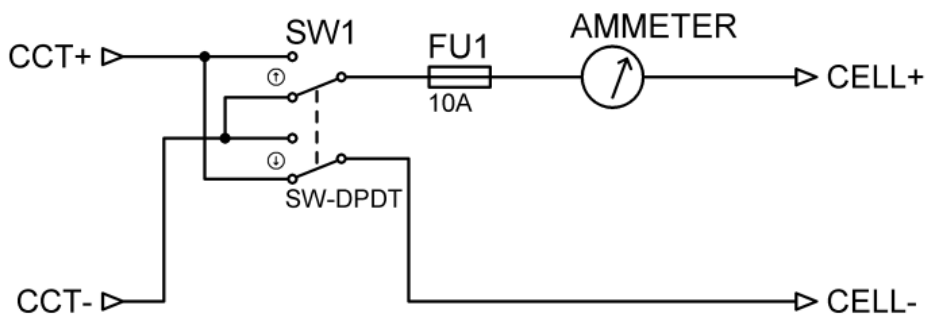


Figure 3.26 - Charge/discharge switch.

### **3.6 Summary of Chapter 3**

An experimental setup has been devised for verifying magnetic tomography-derived current distribution reconstructions. In particular, a novel solver algorithm, novel internal current distribution measurement system, bespoke test cell and current control circuit are developed and tested to be used in the overall experimental system. The experimental hardware is designed to facilitate a convenient experimental procedure as much as possible – for example an automated bypass switch is employed to control dark frame subtraction, and the internal current distribution sensors allow a nearly-instant capture of current distribution data.

## 4 Magnetic Tomography Solver Development

Some method for recovering a current distribution from magnetic field measurements is needed in order to perform a current distribution estimation using magnetic tomography. In order to proceed with this objective, it is necessary to consider the magnetostatic system (the cell and sensors) in terms of an inverse problem. This requires an appropriately designed magnetostatic model (the forward model) and a method of approximately inverting the model. Many of the design choices in the solver are determined by practical considerations, such as cell geometry, material conductances, and the sensor hardware used.

This chapter describes the process of developing a suitable regularising inverse problem solver for magnetic tomography of a lead acid battery. First, 2D models are investigated. This provides early verification of the measurement system and forward model, by allowing comparison of measured data from a known current distribution against simulated magnetic data from a model of the known current distribution. It is shown that the current distribution within a single battery plate can be considered as a 2D distribution with non-zero divergence. A 2D solver is applied to a simulated battery plate, yielding an approximate reconstruction of the current distribution within the plate. However, the reconstructed 2D plate currents are found to be insufficient for inferring the full 3D cell distribution.

The problem of current distribution within a 3D lead acid cell, particularly within the electrolyte, is then considered. Firstly, extrapolation of the electrolyte current distribution from the plate current distribution is investigated. Then, true 3D forward models are employed. A method (special basis projection) of reducing the number of variables in the problem is used and adapted for this application. It is found that this method can be used in conjunction with commercial 3D finite element software, allowing more representative forward models to be used. A final version of the solver code as used in the experiment can be found in Appendix IV – Solver Octave Code

### 4.1 Problem Definition

The current in the lead acid cell will cause a magnetic field outside of the cell. Using magnetostatics (Biot-Savart, Maxwell laws) and a model of the cell it is possible to calculate the magnetic field that expected outside of the cell. This is the forward magnetostatic problem. Taking measurements of the magnetic field outside the cell and the model of the cell to calculate the current distribution is the inverse magnetostatic problem (

Figure 4.1). Finding the solution to the inverse problem requires estimating the inverse to the magnetostatic model using regularisation, or an iterative method where solutions are guessed, put into the forward model and improved. This chapter focuses on regularised inversion of the forward model as opposed to iterative methods.

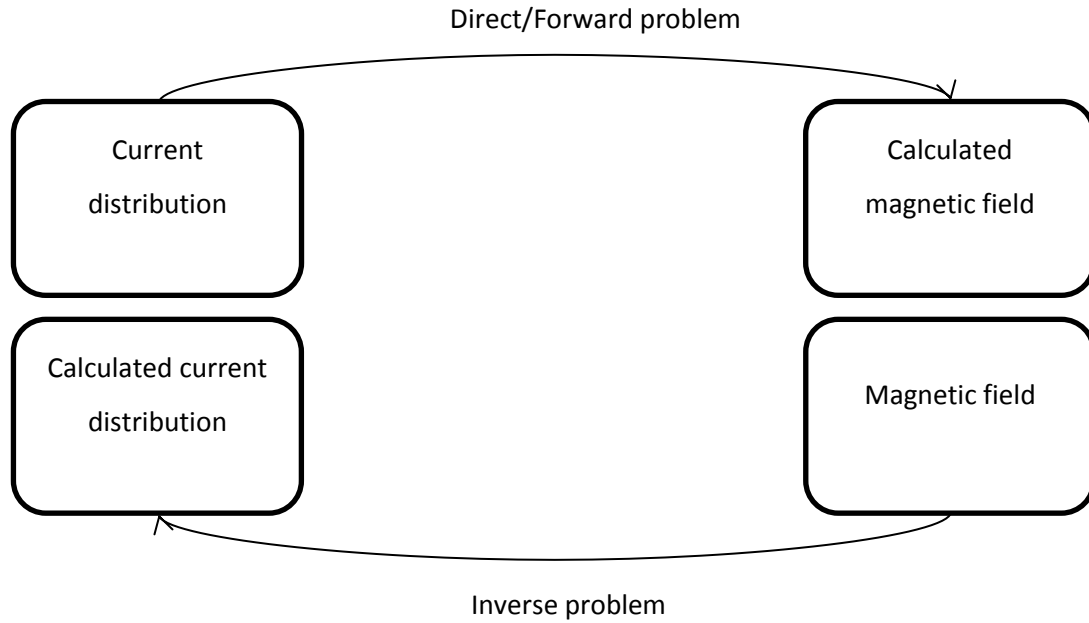


Figure 4.1 - Calculating magnetic field from current and vice versa.

## 4.2 2D Current Distributions

### 4.2.1 Gradient field

In certain special cases, information about current distribution can be extracted from magnetic field data without formally using an inverse problem method. An example of one of these special cases is shown in Figure 4.2, which shows a series of copper conductors carrying non-equal currents. The magnetic field is measured using the magnetic measurement system described in Section 3.2.2. The locations of the sensors are indicated in the diagram by the blue lines or 'Sensor Rows'. The currents are localised within the wires of the circuit, which are all arranged along either the  $x$  or the  $z$  axes. Equation (2.22) can be rewritten as (4.1) for  $\mathbf{j}_{xz}$  the coordinate system shown. Note that the  $x$  component on the rhs is proportional to  $-j_z$

$$\begin{pmatrix} j_x \\ 0 \\ j_z \end{pmatrix} \times \begin{pmatrix} x - x' \\ y - y' \\ z - z' \end{pmatrix} = \begin{pmatrix} -j_z(y - y') \\ j_x(z - z') - j_z(x - x') \\ j_x(y - y') \end{pmatrix} \quad (4.1)$$

Simulated  $B_x$  data from sensor row 4 (near the middle of the sensor array height) is plotted in Figure 4.3. The relative distribution of current among the 5 vertical wires can be discerned by inspection from the  $B_x$  data. It can be considered as a low pass filtered or “smeared” version of the discretised distribution of  $z$  currents. For example, the green plots each show a sharp peak at the location of the wire that is carrying all the current. The blue and light blue plots show a region near the middle of the sensor array where the vertical currents are non-zero. Reading the data in this way relies on prior knowledge of the direction of the currents – we know to look at the component of  $\mathbf{B}$  which is orthogonal to the direction of  $\mathbf{J}$  and the perpendicular displacement from a given sensor to the closest point in the plane in which the circuit lies. In a sense, knowledge of the ‘right-hand corkscrew rule’ forms the forward model, and some approximate inversion of the problem can be performed by simply visualising how a  $z$  direction current would affect measurements of  $\mathbf{B}_x$ .

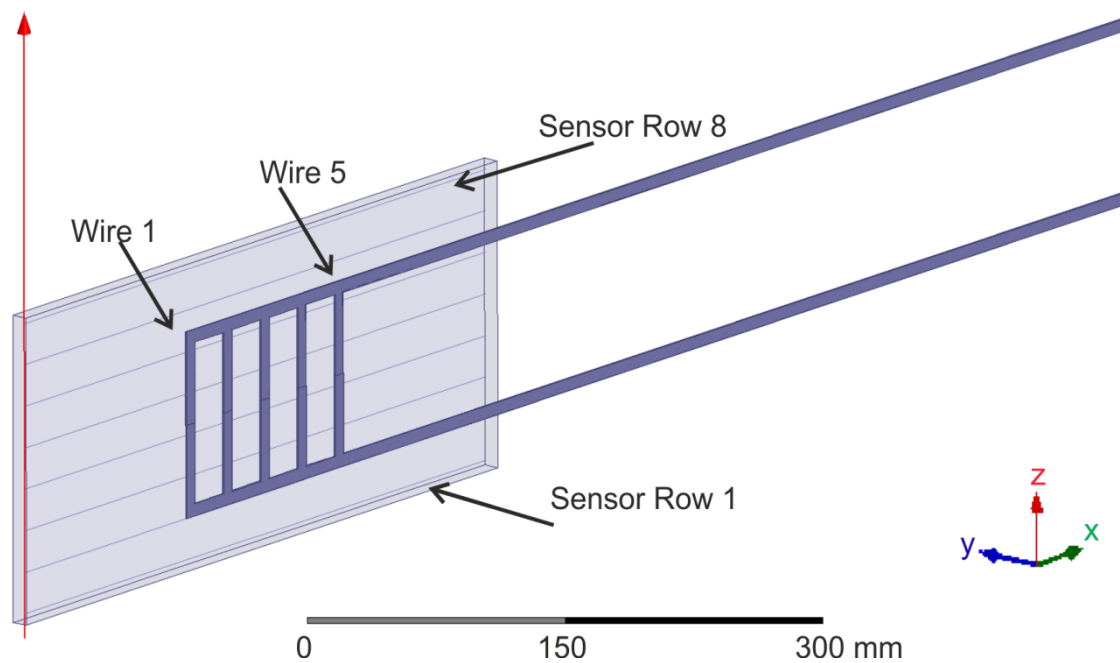


Figure 4.2 - Orthogonal 2D circuit, represented in Ansys Maxwell.

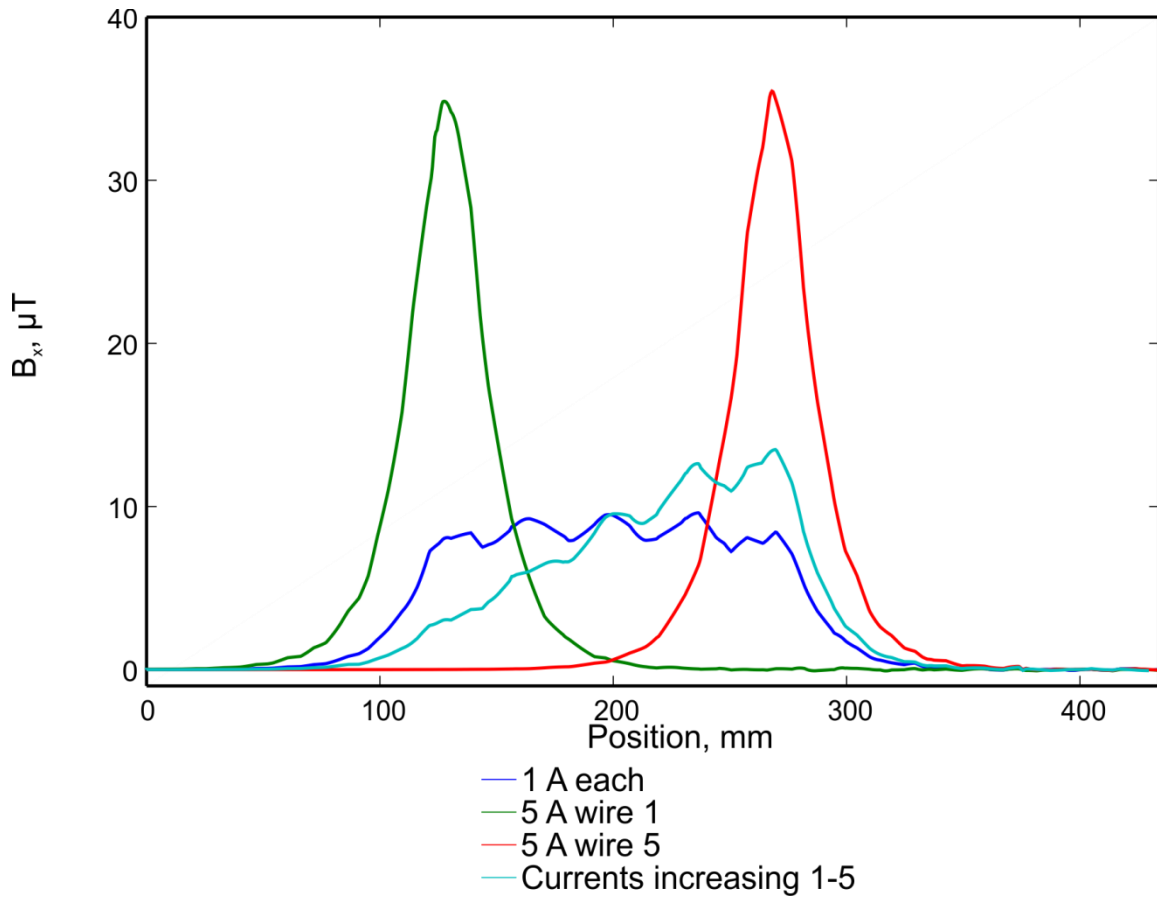


Figure 4.3 - Measured magnetic fields for 4 different current distributions.

Although the  $J_z$  components are most easily spotted by eye from the  $B_x$  data (as would be  $J_x$  from  $B_z$  data), the entire 2D current distribution  $\mathbf{J}$  can be reconstructed from any of the 3 components of  $\mathbf{B}$ , provided  $\mathbf{J}$  is non-diverging [71]. This can be shown, for the special case in Figure 4.2, again without a formal inverse problem method. Figure 4.4 shows a visualisation of the current vectors which correspond to plot 2 in Figure 4.3. Figure 4.5 shows the  $B_y$  data arranged over a  $32 \times 8$  grid in the same configuration as the sensor array. Figure 4.6 shows a plot of  $|\nabla B_y|$  over the same grid. The current distribution is the same as Figure 4.4 - all the current is passing through wire 1. The shape of the maxima in Figure 4.6 reflects the shape of the circuit, and the approximately constant magnitude along the contour is similar to the constant magnitude of current around the single-loop circuit. A more complicated, non-uniform current distribution is shown in Figure 4.7, with the resulting  $\nabla B_y$  data plotted in Figure 4.8. The magnitudes of the  $z$  currents, which increase from left to right, are reflected in the  $x$  component of  $\nabla B_y$ . Figure 4.6 and Figure 4.8 show empirically that, under certain conditions,  $B_y$  contains information about location and magnitude of currents. It is also possible to extract direction information from the  $\nabla B_y$  field for the special case of this circuit.

$\nabla B_y$  is a vector quantity (Figure 4.9), and by rotating the vectors by  $90^\circ$  anti-clockwise an image of the direction of current in the circuit is formed (Figure 4.10).

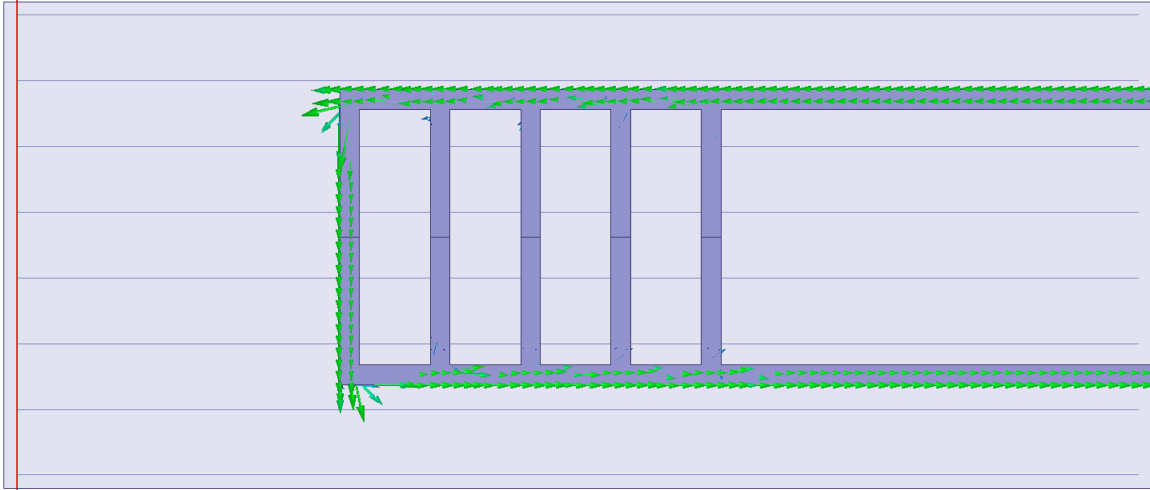


Figure 4.4 – Visualisation of 5 A passing through wire 1 only.

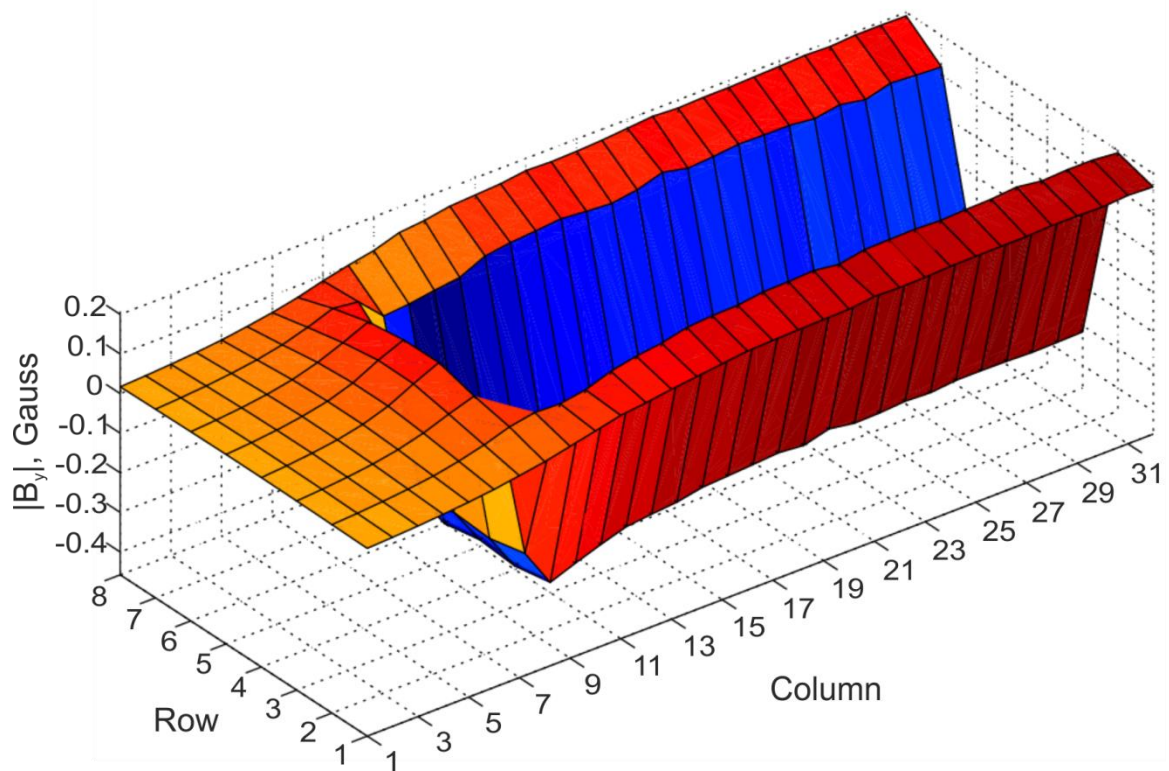


Figure 4.5 - Magnitude of  $B_y$  over sensor array locations.

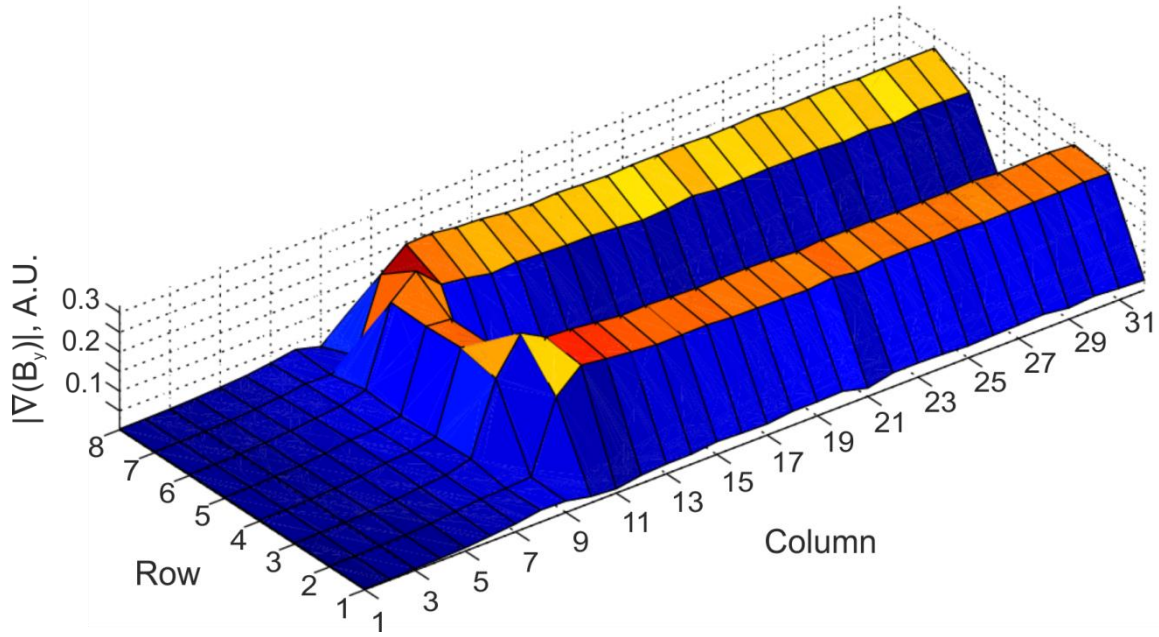


Figure 4.6 - Magnitude of  $\nabla B_y$  over sensor array locations.

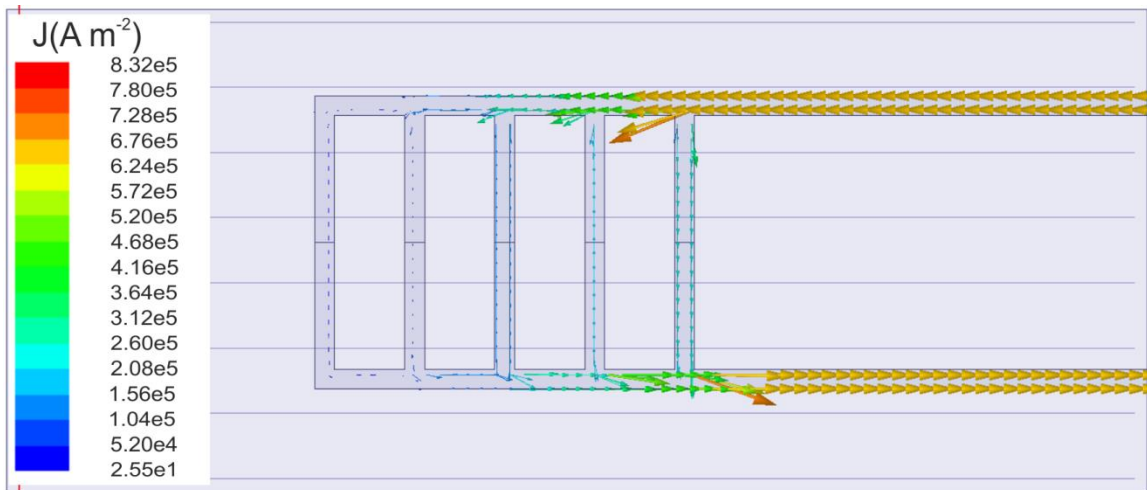


Figure 4.7 – Visualisation of the current distribution corresponding to the light blue plot in Figure 4.3

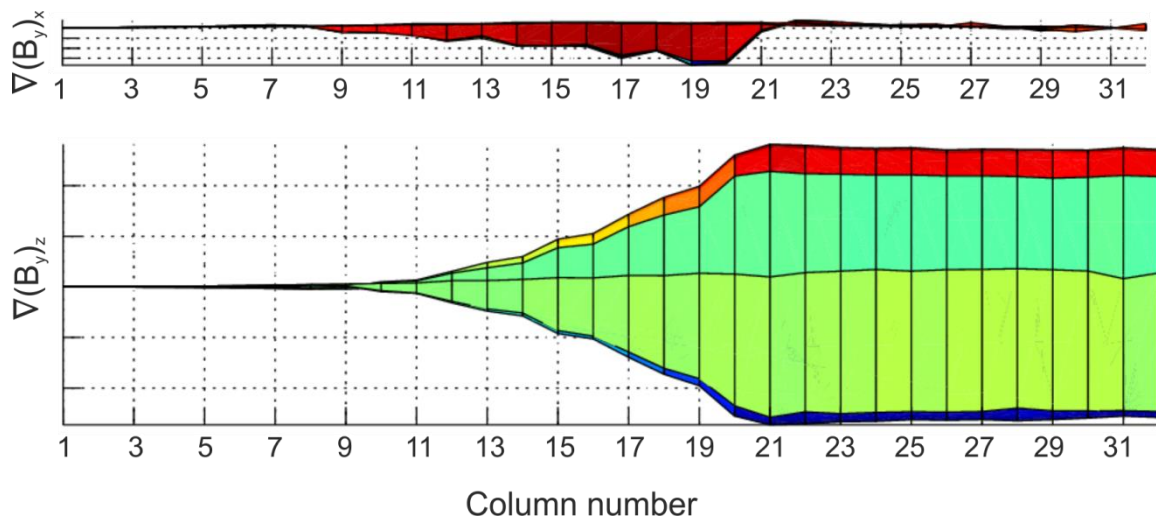


Figure 4.8 - Magnitude of x and z components of  $\nabla B_y$  for the current distribution shown in Figure 4.7.

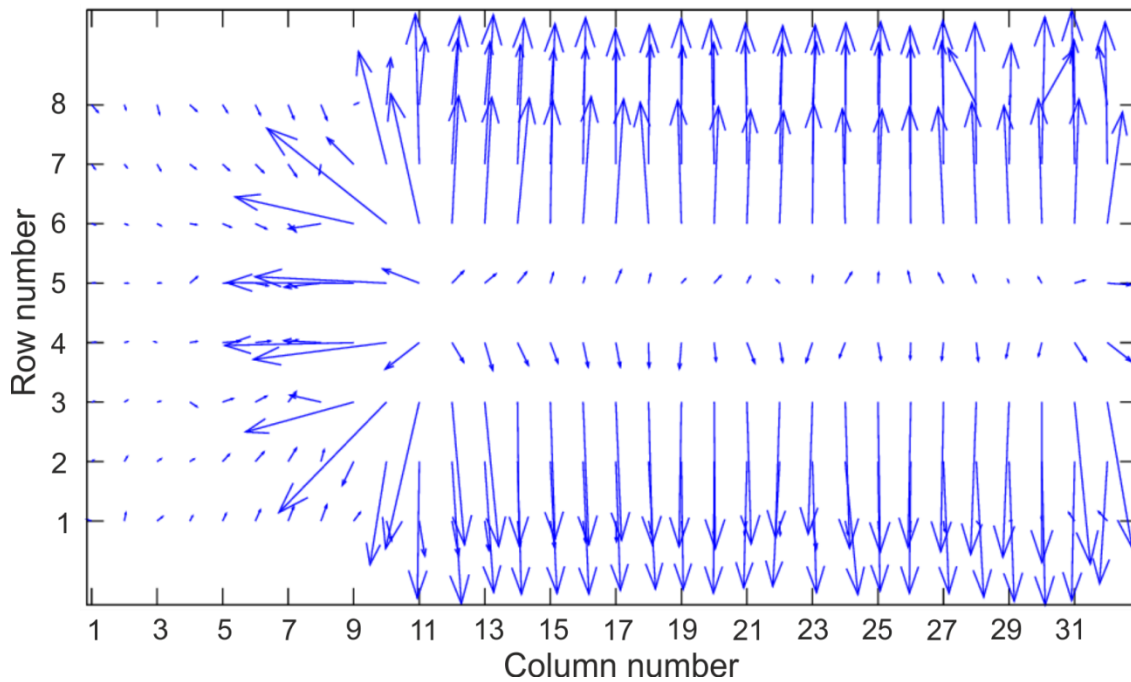


Figure 4.9 – Vector plot of  $\nabla B_y$ , from measured  $B_y$  data and current distribution from Figure 4.4.

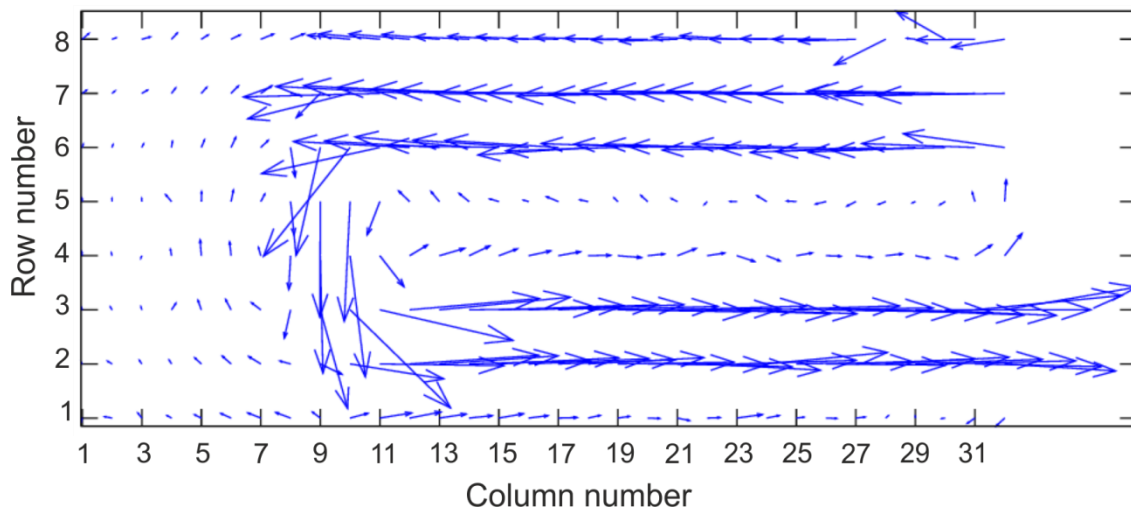


Figure 4.10 –  $\nabla B_y$  rotated through  $90^\circ$ , from measured  $B_y$  data.

However, using  $\nabla B_y$  as an estimate of  $\mathbf{J}$  is easily confounded. An example of a confounding situation is if the current distribution is uniform over an area rather than confined to relatively thin wires as in Figure 4.2 to Figure 4.10. The current distribution in the plate of a battery could be continuously distributed rather than contained in thin paths so being able to solve over such a geometry is a requirement for a battery current imaging system. Figure 4.11 shows the magnitude of a current distribution that is directed along the  $x$ -axis. Note that this current distribution has a non-zero divergence. Since the solver uses  $B_y$  only, it cannot ‘see’ any current in the  $y$ -direction, and so the current flowing from the plate to the electrolyte appears as though it is being created from a source of current flux. Current flowing from the plate to

the electrolyte appears as a current flux sink. Therefore any solver which is designed to treat the current in the cell plate as a 2D system must be able to find a unique solution even when  $\nabla \cdot \mathbf{J}_{xz} \neq 0$ . The feasibility of this is addressed in the remainder of Section 4.2.

Figure 4.13 shows the scalar field  $(\nabla \mathbf{B}_y)_z$ , which in this case does not match the distribution of magnitude of  $\mathbf{J}$  (Figure 4.11). Furthermore the rotated vector field  $\nabla \mathbf{B}_y$  (Figure 4.14) does not match the direction of  $\mathbf{J}$  (Figure 4.12). It appears as though the  $\nabla$  operator is not an adequate method of extracting current distribution information from a battery or circuit having battery-like geometry. The next step is to investigate using a formal inverse problem method.

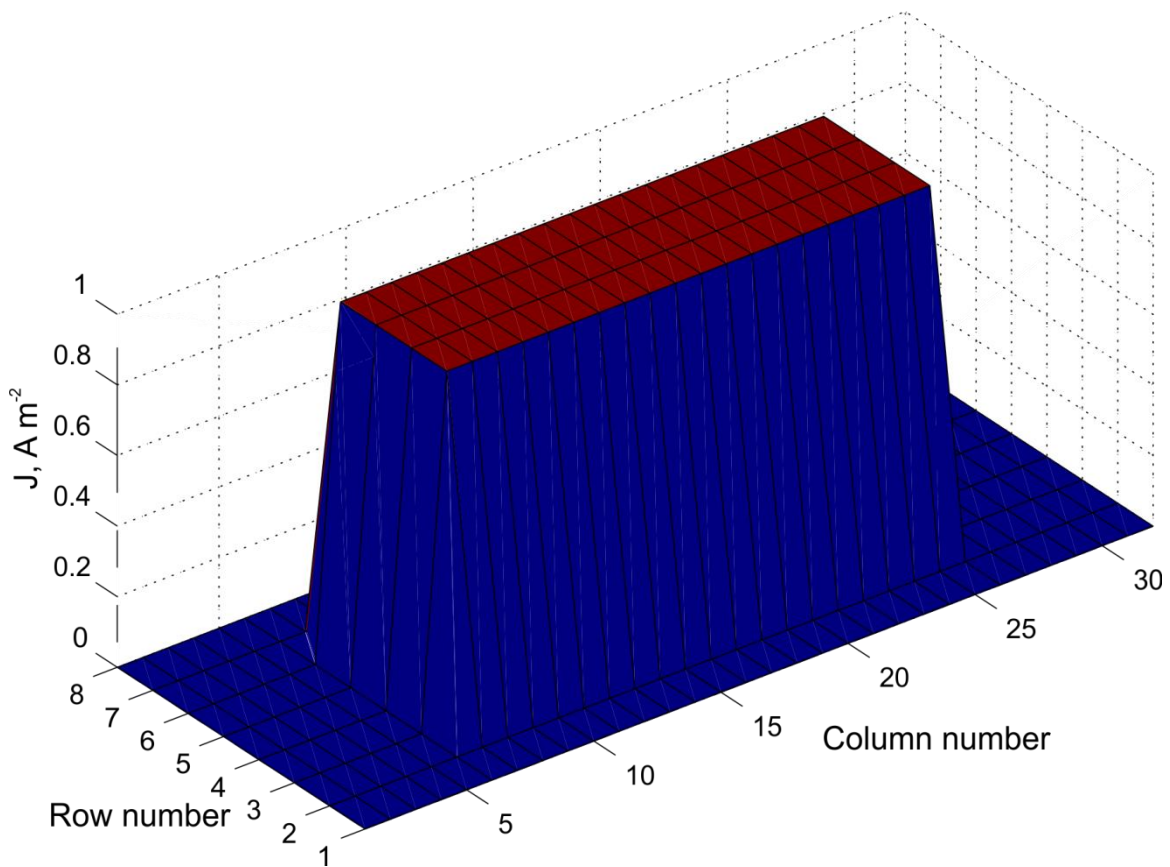


Figure 4.11 - Magnitude of simulated positive  $x$ -direction current.

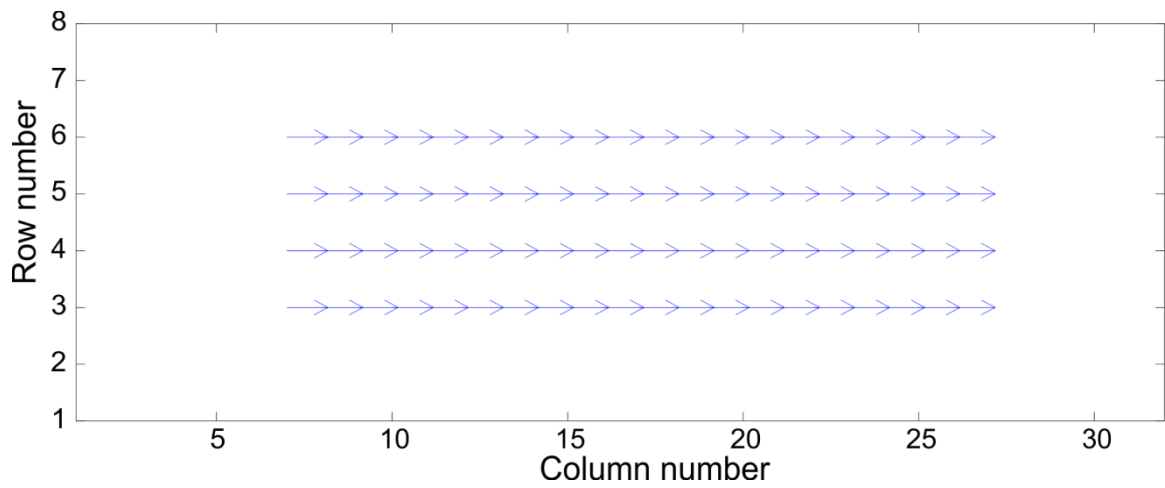


Figure 4.12 - Vector plot of simulated positive  $x$ -direction current.

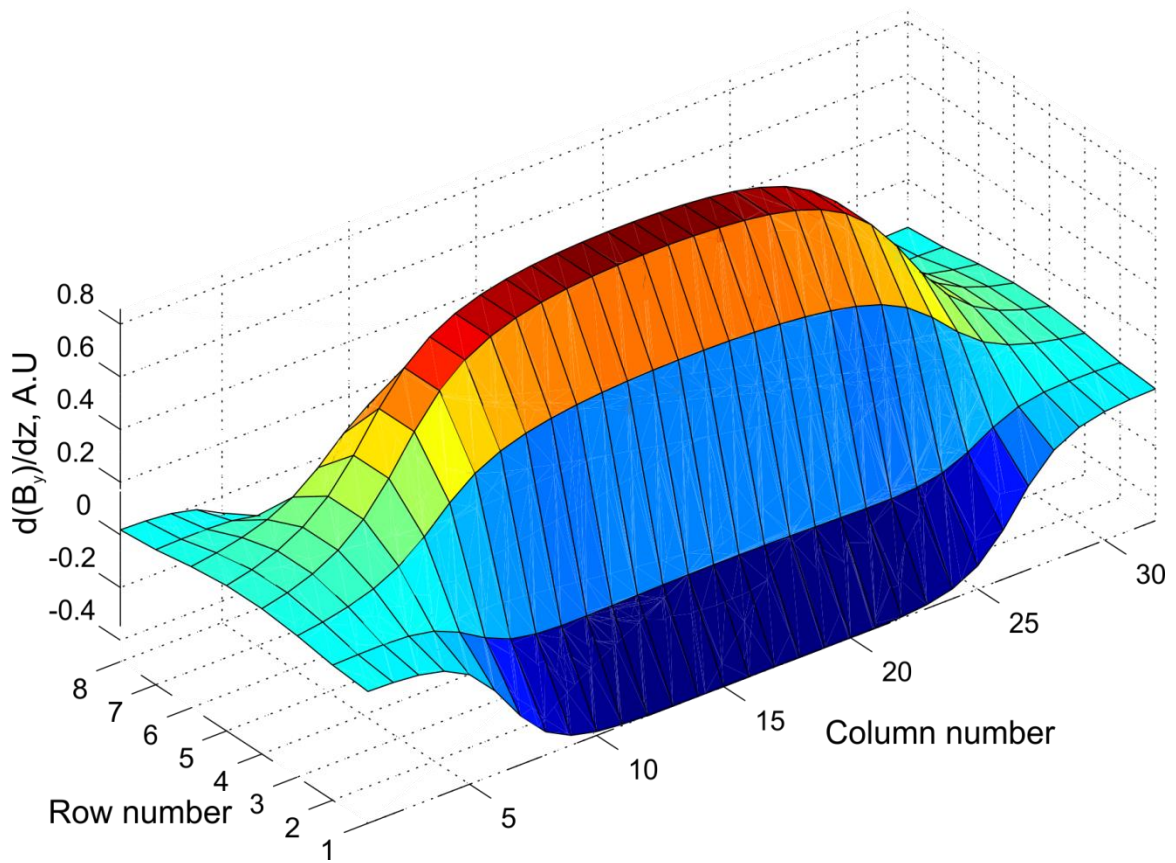


Figure 4.13 - Simulated  $(\nabla B_y)_z$  due to the current distribution given in Figure 4.11.

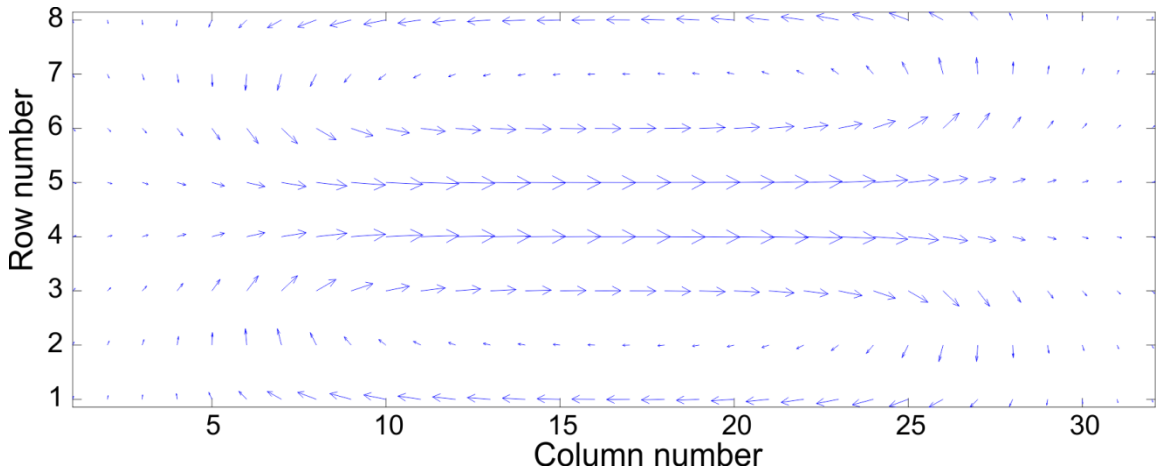


Figure 4.14 – Simulated  $\nabla B_y$ , due to the current distribution given in Figure 4.11, rotated through  $90^\circ$  to estimate direction of current.

#### 4.2.2 Matrix inversion

An inverse problem approach requires defining a forward model to couple the  $\mathbf{J}$  data to the  $\mathbf{B}$  data, and then inverting that coupling by some means. The approach taken by Hofer *et al.* [72] is to arrange all the  $\mathbf{J}$  and  $\mathbf{B}$  data into 1D vectors and then construct a matrix  $\mathbf{K}$  which couples each element of  $\mathbf{B}$  to an element of  $\mathbf{J}$ , according to (2.23)

The elements of  $\mathbf{K}$  are populated according to the Biot-Savart law for current elements and depend on the relative orientation of the current element and magnetic sensing location to which it corresponds (2.24). The forward model  $\mathbf{K}$  consists of information about the geometry of the problem – the locations of possible current elements and magnetic sensing elements. If the plane in which the current lies and the plane in which the sensing array lie are parallel then constructing  $\mathbf{K}$  is simplified as the perpendicular distance between the two remains constant. Inversion of  $\mathbf{K}$  yields the solution  $\mathbf{J}$  (2.25), where  $\mathbf{K}^{-1}$  may not have a unique solution or may be ill-conditioned, and an approximate solution may be necessary. In the following work, Tikhonov regularisation is used to approximate  $\mathbf{K}^{-1}$ .

For easy comparison with the gradient field method, 256 current element locations are defined, with the same  $x$  and  $z$  coordinates as the sensor locations, and offset in the  $y$  direction. No significant improvement over using  $\nabla B_y$  can be seen in this reconstruction, shown in Figure 4.15 and Figure 4.16. The vector field plotted in Figure 4.16 has divergence which is non-zero but not equal to that of the source distribution. This example illustrates the effect that constraining the divergence has on uniqueness when only one component of  $\mathbf{B}$  is used – the value of  $\nabla \cdot \mathbf{J}_{xz}$  ( $y$  currents) differentiates the correct solution from the incorrect reconstruction, but the model has no way of measuring  $y$  currents since  $B_y$  does not depend

on  $J_y$ . In other words the incorrect reconstruction and the original current distribution are approximately equivalent from the point of view of  $B_y$ . It is not desirable to constrain  $J_y$ , since it is (non-)uniformity of electrolyte current which is of interest in this work.

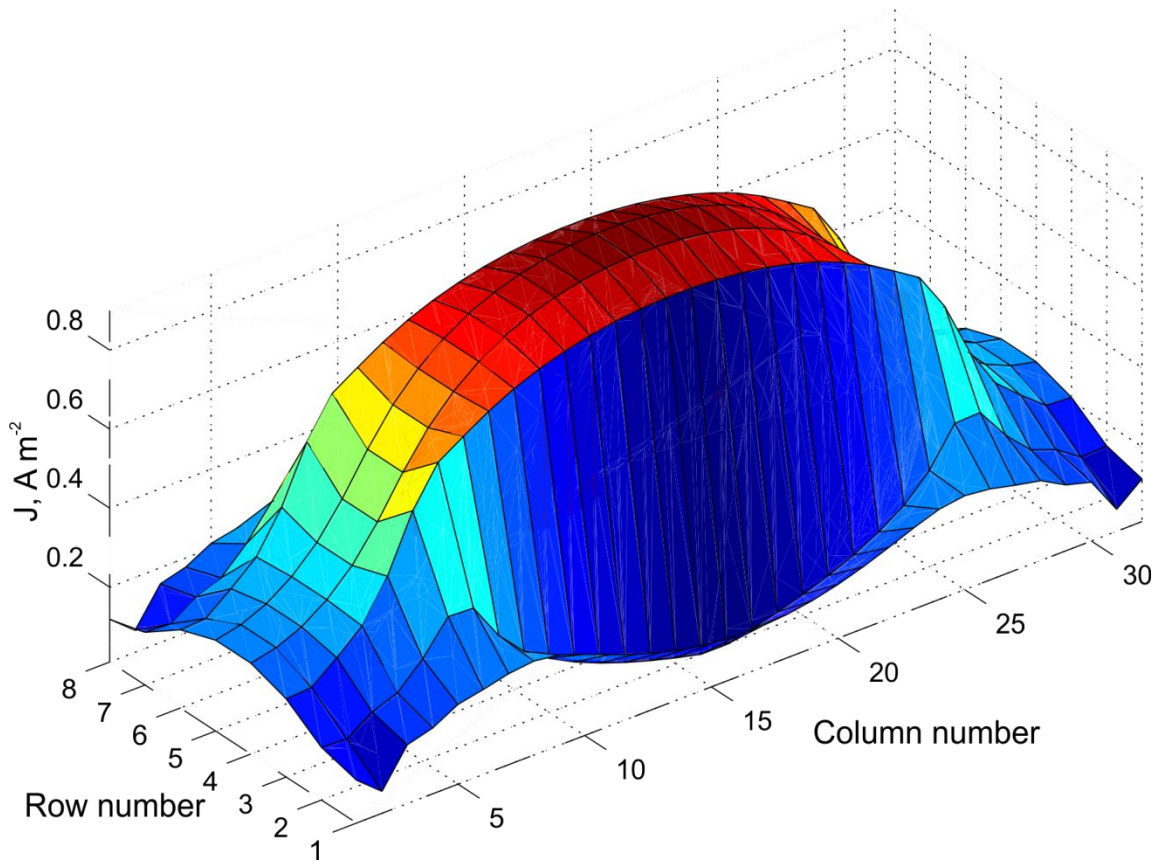


Figure 4.15 - Magnitude of reconstructed current density from the simulated distribution shown in Figure 4.11, using Tikhonov regularisation.

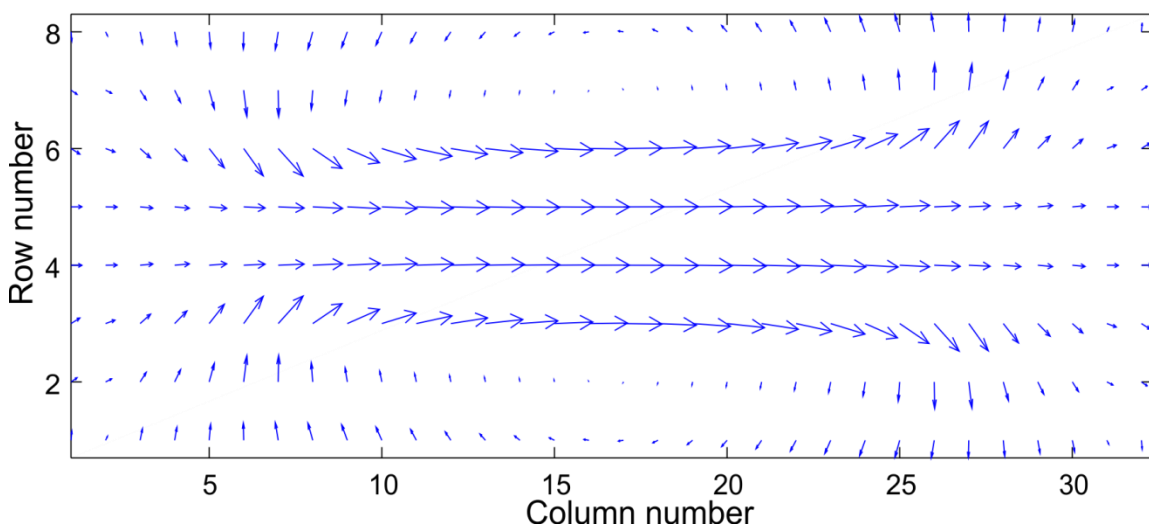


Figure 4.16 - Vector plot of the reconstructed current distribution from the simulated distribution shown in Figure 4.11 using Tikhonov regularisation.

Some other valid constraint on the 2D solution could remove the ambiguity and yield a unique solution. In this case the solution satisfies  $J_{xz} \geq 0$ , so this can be used as a constraint. It is possible to use a non-negative least squares optimisation function alongside Tikhonov regularisation in order to solve(2.25) [99]. The reconstruction of Figure 4.11 by this method is shown in Figure 4.17 and Figure 4.18. A more accurate reconstruction is obtained this time.

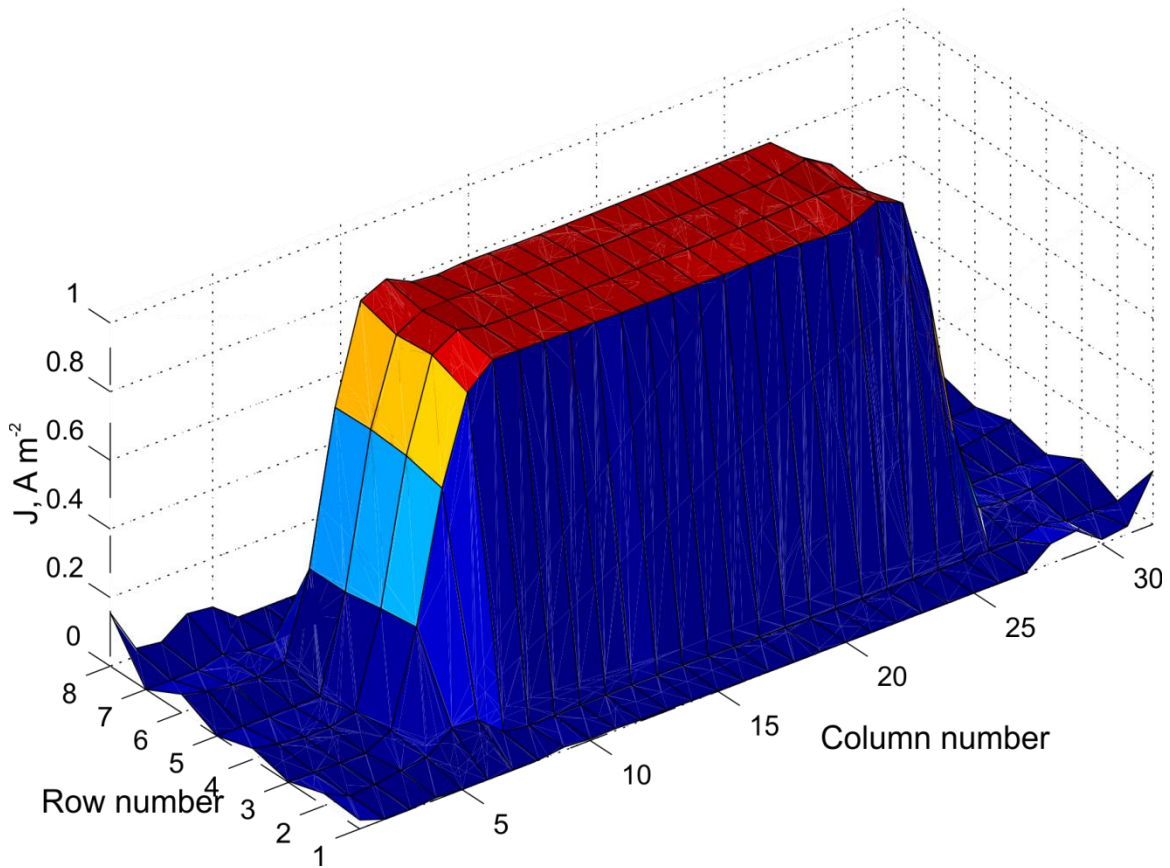


Figure 4.17 - Magnitude of reconstruction of Figure 4.11, using non-negative constrained Tikhonov regularisation

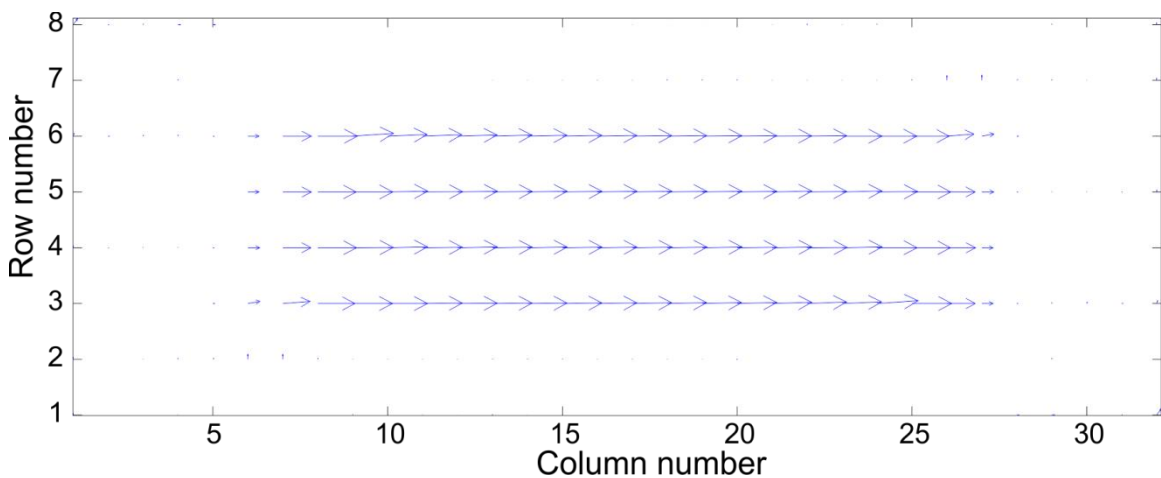


Figure 4.18 - Vector plot of reconstruction of Figure 4.11, using non-negative constrained Tikhonov regularisation

The previous example shows that non-negativity constraints make it possible to find a solution to 2D problems with non-zero divergence. The non-negativity constraint can be applied to the current flow in the plate of a battery. Figure 4.19 shows a model of a simplified cell connected in a circuit. In the plate closest to the sensor array, the current flows in the positive  $x$  and  $z$  direction since the plate tab is placed at the top right of the plate. The electrolyte current density is uniform, making the magnitude of the plate current decrease further away from the tab. Figure 4.20 shows directly sampled current density vectors. The sampled current density vectors are used as the input to a 2D forward model written in Octave. The model is then regularised and inverted to produce the reconstruction shown in Figure 4.21. The general direction of the vectors is preserved, although there are some visible errors in the top right of the plot near to where the tab is located. Since the same model  $\mathbf{K}$  is used to generate the simulated  $\mathbf{B}$  and the solution  $\mathbf{J}$ , with no measurement errors added, this is a simple problem to solve.

A more difficult problem to solve is using Ansys Maxwell to simulate  $\mathbf{B}$ , and use the forward model  $\mathbf{K}$  (written in Octave) to find the solution. The forward model in the solver is now only an approximation of the quasi-continuous Ansys model and is subject to errors due to quantisation of the current (which changes very rapidly near to the plate tab). This is a problem that would occur if a  $\mathbf{K}$  model were used to reconstruct real data. A vector plot of the solution to this, more difficult, problem is given in Figure 4.22. There is visible distortion present in this solution. Figure 4.23 to Figure 4.25 show the respective magnitudes of the sampled current density and the reconstructed current density, by both methods. Again the solution to the easy problem appears similar to the original, whereas the solution to the hard problem appears more distorted. These results indicate that a typical current distribution as found in a cell plate may be reconstructed if appropriate non-negativity constraints are applied. However, the results are much more successful when the solver model is identical to the system which has generated the  $\mathbf{B}$  data than when the solver does not include an exactly correct forward model.

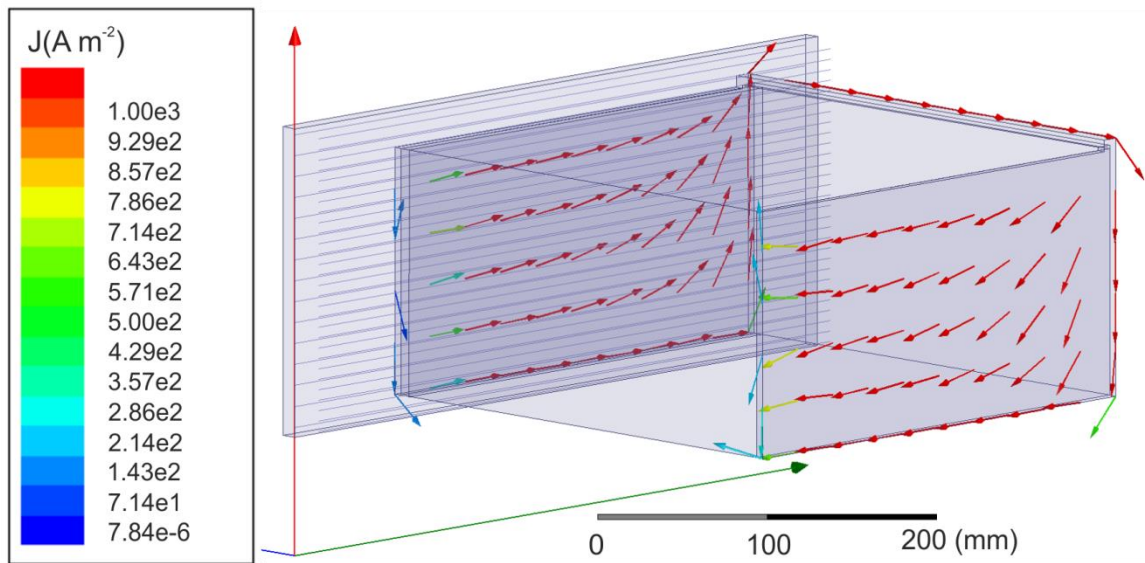


Figure 4.19 - Current flow in a cell where plate terminals are positioned in the top corner of the plates.

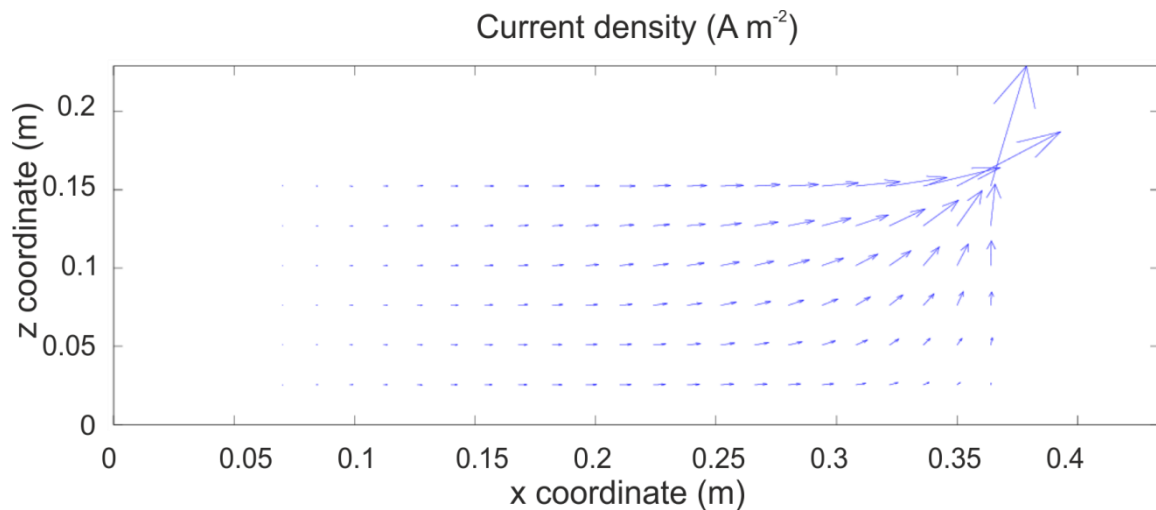


Figure 4.20 - Current density vectors in the plate, directly sampled from Ansys model.

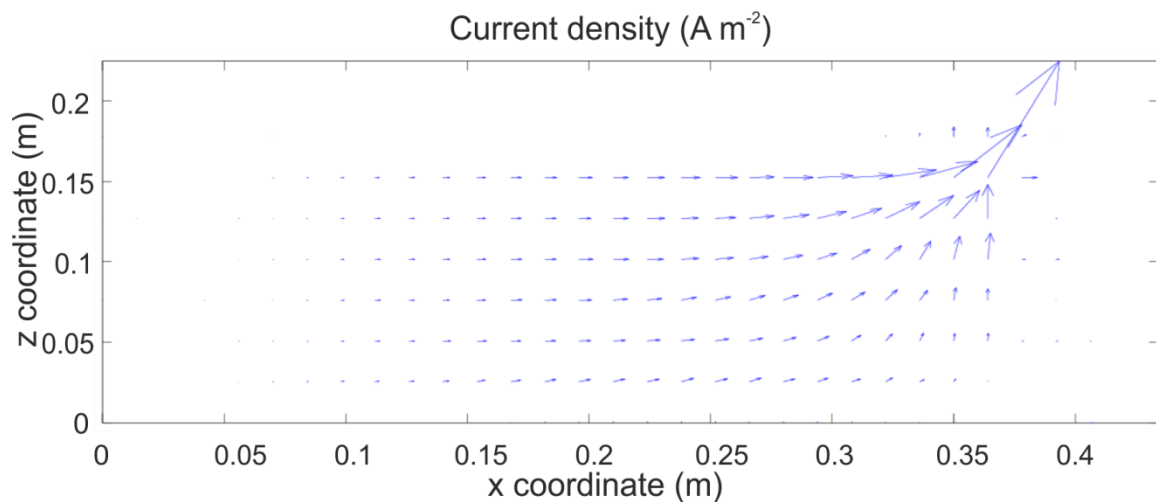


Figure 4.21 - Reconstructed current density vectors using  $J_{xz} \geq 0$  constraint, using  $B$  data derived from the  $K$  model used by the solver.

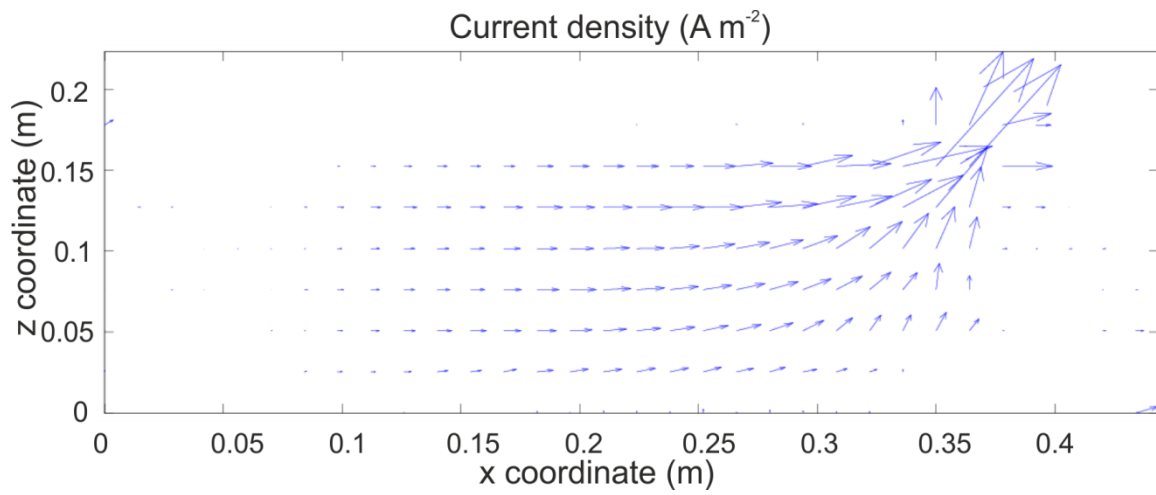


Figure 4.22 - Reconstructed current density vectors using  $J_{xz} \geq 0$  constraint, using  $B$  data from Ansys model.

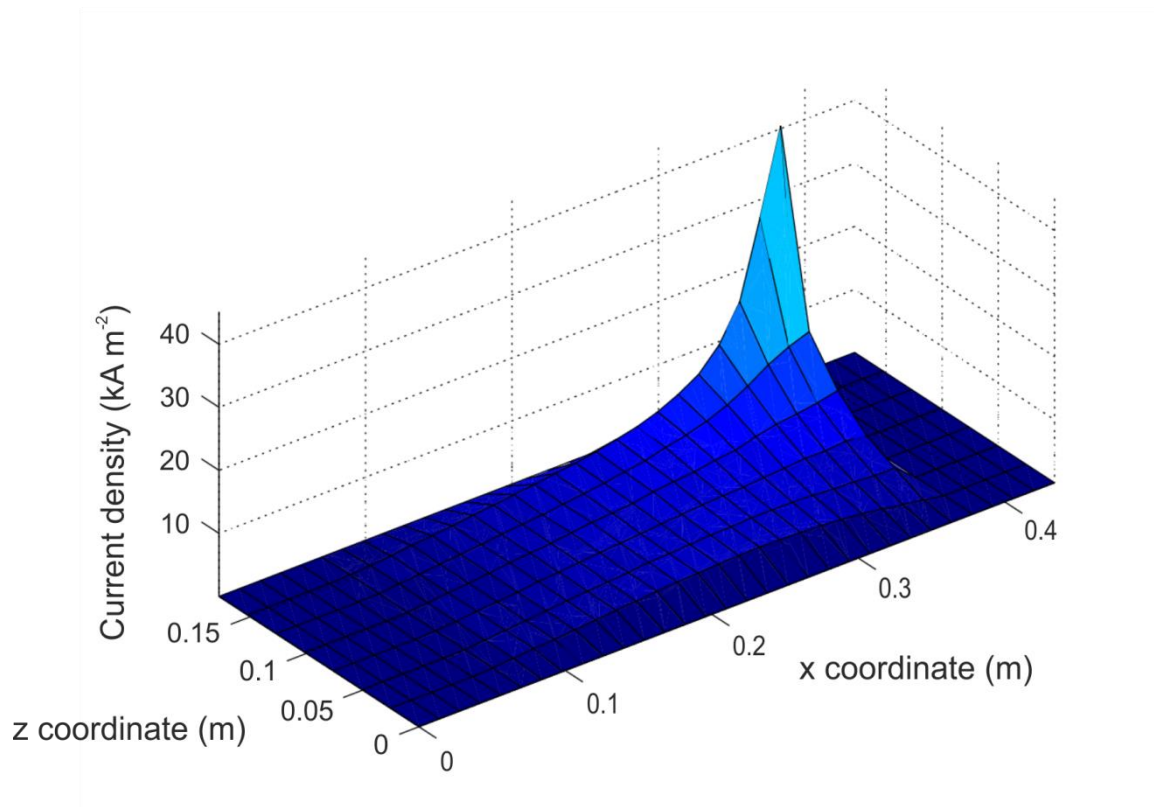


Figure 4.23 - Magnitude of current density in the plate, directly sampled from Ansys model.

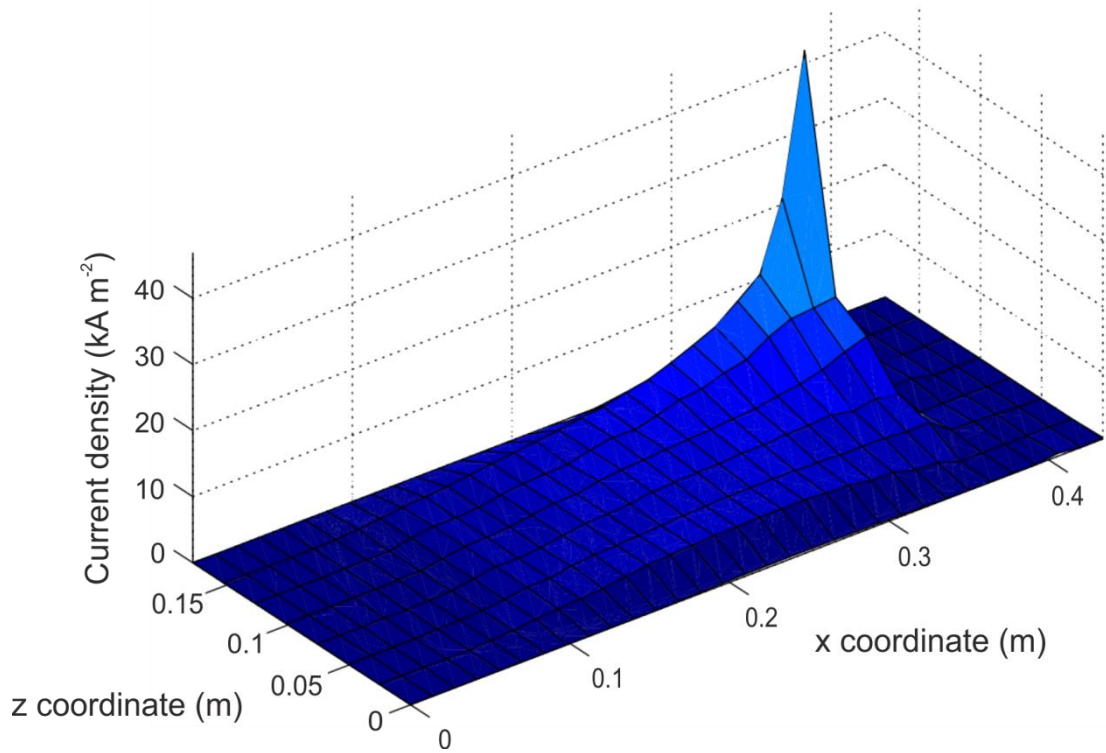


Figure 4.24 - Reconstructed current density magnitude using  $J_{xz} \geq 0$  constraint, using  $B$  data derived from the  $K$  model used by the solver.

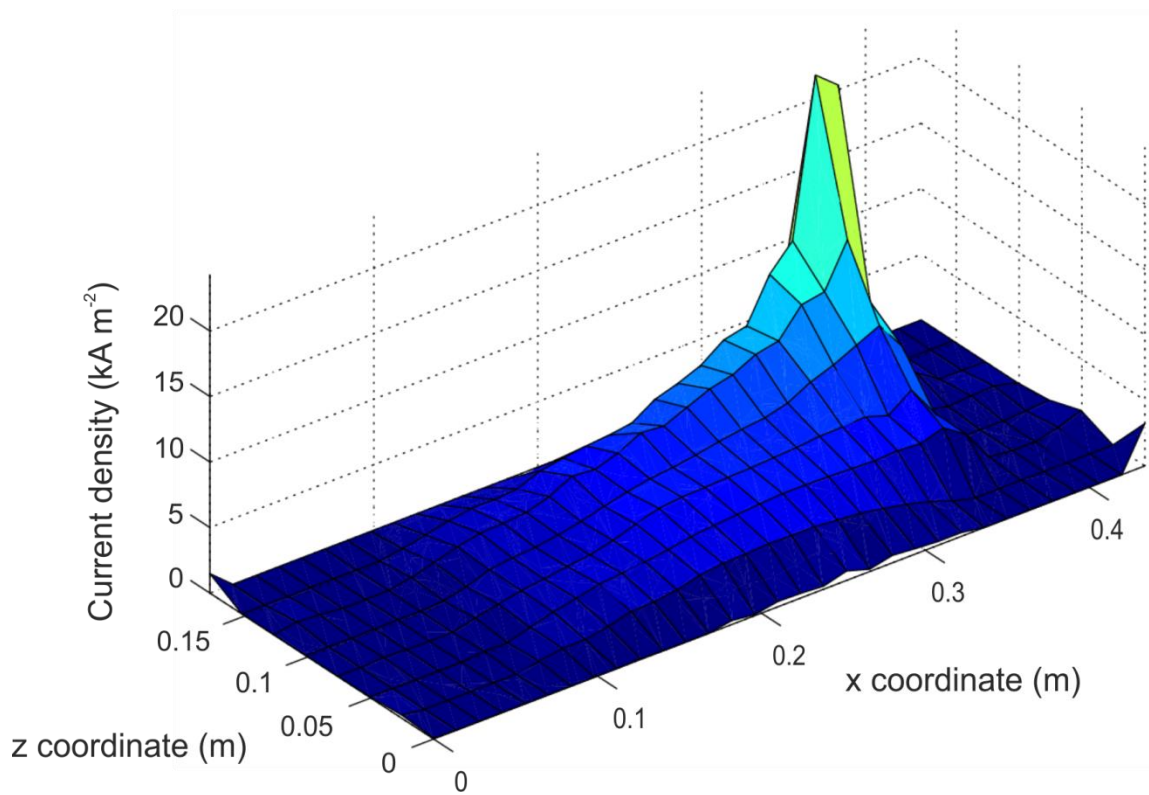


Figure 4.25 - Reconstructed current density magnitude using  $J_{xz} \geq 0$  constraint, using  $B$  data from Ansys model.

### 4.2.3 Extrapolating 3D from 2D

Section 4.2.2 describes how a magnetic imaging system may be used to estimate magnitude and direction of a 2D current distribution. The constraint that  $\nabla \cdot \mathbf{J} = 0$ , which does not apply to the 2D distribution within the cell plate, may be discarded in favour of a non-negativity constraint. The 2D distribution within the plate is of interest if the electrolyte current distribution may be extracted from it. The purpose of the solver is to find the electrolyte current distribution, which is in fact calculated from the 2D distribution using the divergence operator. The 2D solutions are useful if the divergence of the reconstructed 2D current distribution is approximately equal to the divergence of the source 2D current distribution.

First the divergence of the source current distribution (vector field shown in Figure 4.20) is calculated. The result of this is plotted in Figure 4.26. The uniform electrolyte current can be seen over much of the plate area, particularly on the left side of the plate. The left edge of the cell can be discerned as well as the left hand parts of the top and bottom edges of the cell. The right hand side, near to the cell tab, exhibits a very large divergence which does not reflect the electrolyte current. This shows that the divergence around most of the plate does reflect the electrolyte current, although care must be taken when sampling near to the tab, where the vector field changes much more rapidly. However, the divergence of the reconstruction of  $\mathbf{J}_{xz}$  bears even less resemblance to the uniform electrolyte current (Figure 4.27) even in the region of the plate away from the tab.

This suggests that the non-negativity constraint does not constrain the divergence of the solution to match that of the source. While magnitude and direction of the 2D current may be estimated with some accuracy, the solutions do not preserve the divergence sufficiently in order to reconstruct the  $y$ -direction current. This suggests that perhaps a 3D model is required, where the coupling between  $\mathbf{J}_y$  and  $\mathbf{B}_{xz}$  is included in the forward model. By modelling all 3 dimensions of the current and using all 3 components of  $\mathbf{B}$  then the ambiguity can be reduced. A zero-divergence constraint may also be applied to the 3D  $\mathbf{J}$  field.

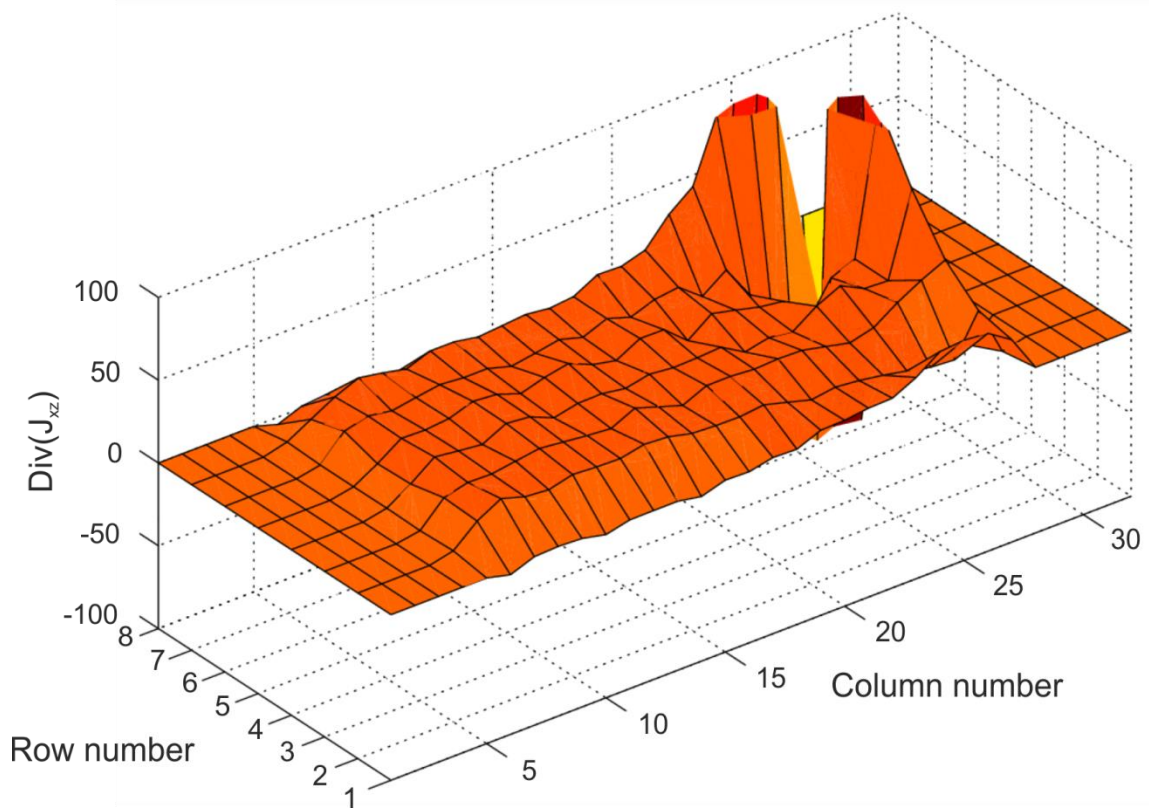


Figure 4.26 -  $\nabla \cdot J_{xz,original}$  plotted over the plate area.

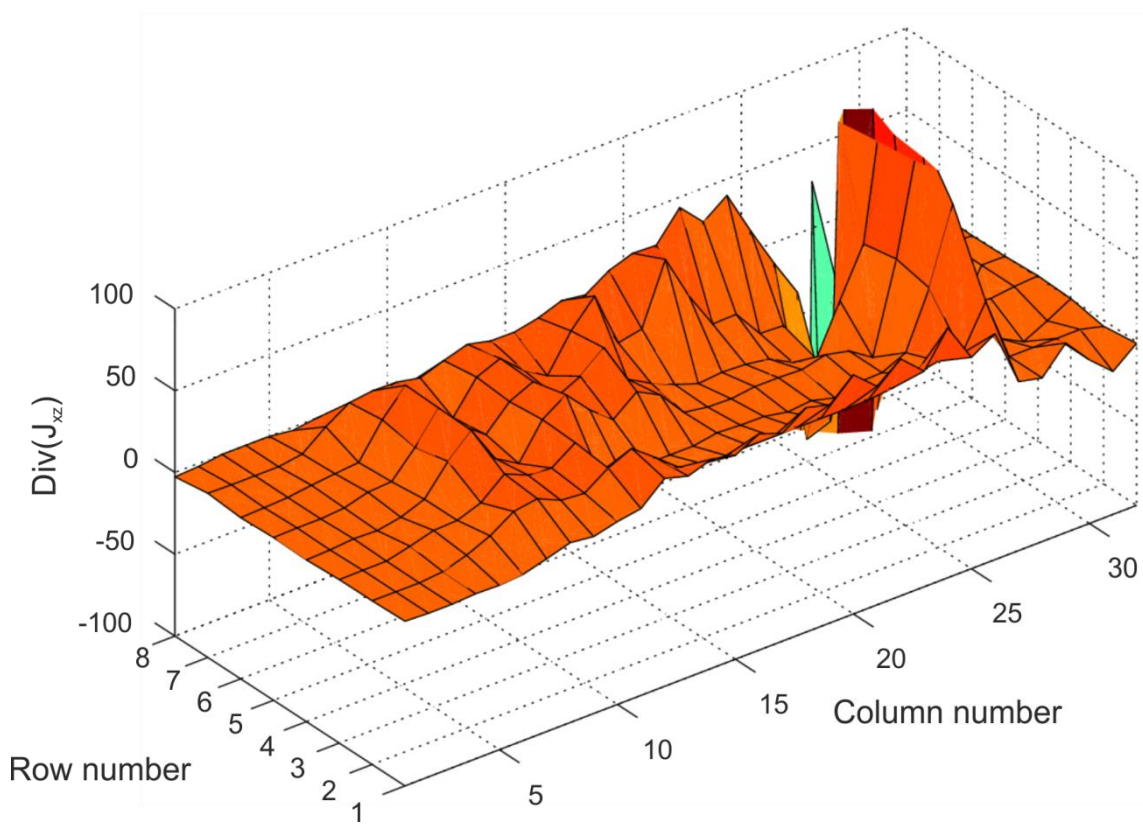


Figure 4.27 -  $\nabla \cdot J_{xz,estimate}$  plotted over the plate area.

## 4.3 3D Current Distributions

### 4.3.1 Divergence-free models and special basis projection

In a 3D model, all components of  $\mathbf{J}$  or  $\mathbf{I}$  are included and so a zero divergence constraint may be applied. The zero divergence constraint is satisfied by constructing a circuit model which the solved current must follow. Imposing Kirchoff's current law on the model ensures that there are no sources or sinks of current flux. Hauer *et al.* [77] provide two methods of constraining the current distribution to a divergence-constrained circuit model and show the beneficial effect on solution stability compared with a non-divergence-constrained solution. One of their methods, 'special basis projection', is studied in detail in this section.

In order to apply the technique, the pseudo-code algorithm presented in [77] is coded in Octave. The technique is applied to the 5-source resistor-wire problem presented in Figure 4.2. Magnetic field is sampled at locations corresponding to the sensor locations in previous simulations and real measurements. The circuit is modelled as a  $6 \times 2$  array of connected nodes (Figure 4.28), with the conductance of the 5 leftmost  $z$ -direction wires set to an arbitrary non-zero value and the one on the right hand side set to zero conductance. The  $x$ -direction wires are assigned an arbitrary conductance much greater than that of the  $z$ -direction wires. The two rightmost nodes are set as the inflow and outflow to the circuit, so that current flows into the right hand bottom node, clockwise around the circuit and out of the right hand top node.

When applied to simulated data generated in Ansys Maxwell with no noise added to either the magnetic field values or the relative position of the sensors and wires, an accurate reconstruction is obtained (see Figure 4.29). The mean absolute error (MAE) in the 5 wire currents is 0.77 %. Adding noise to the values of magnetic field strength increases error. Figure 4.30 shows the effect of increasing noise on the reconstruction error. The error for each value of noise is averaged over 20 runs. Measurement noise below 1 mG variance appears not to have a deleterious effect on error. The regularisation parameter  $\lambda$  has a small effect on  $\mathbf{I}$  (via  $\xi$  see (2.34) - (2.43)). Increasing  $\lambda$  slightly increases the error for small values of noise and slightly reduces error for large values of noise. Note that much larger values of  $\lambda$  are necessary here than in previous Tikhonov regularisations (Section 4.2.2) because the average magnitude of  $\xi$  is much larger than that of  $\mathbf{K}$ . A sensor gain of  $440 \text{ lsb G}^{-1}$  is equivalent to a resolution of  $2.27 \text{ mG lsb}^{-1}$  [86], which according to Figure 4.30 would yield an error in reconstructed current of approximately 1.4 mA.

The effect of positional errors in the system on reconstruction accuracy is shown in Figure 4.31. The range of errors considered approximately corresponds to that which would be practically achievable – 1  $\mu\text{m}$  up to 1 cm. Regularisation appears not to be beneficial over almost all values of measurement precision up to 1 cm. Taking 2 mm as a reasonable precision that could be achieved using a 1 mm graded ruler yields an error in wire currents of 4.02 %. Improving positional measurement precision much below 1 mm appears not to yield a significant benefit by this measure. However, due to the reciprocal nature of the magnetic field magnitude, the measurement accuracy is sensitive to shifts in position which increase the sensor to circuit separation. For the Ansys-generated magnetic data, the separation in the solver is set to a range of values within  $\pm 5$  mm of the true value, and the MAE is plotted for each (Figure 4.32). A minimum can be seen at 21 mm separation, and percentage MAE rises to around 15 % when separation is perturbed by 5 mm in either direction. Accurate measurement of this dimension will require knowledge of where exactly in the HMC5883L IC package are the magnetic transducers located. A set of real measurements is reconstructed (Figure 4.33), with a MAE of 2.88 % for the uniform current case, which is within the expected bounds. The MAE for a set of currents that increase from left to right is 5.65 %, which could also be attributed to positional error.

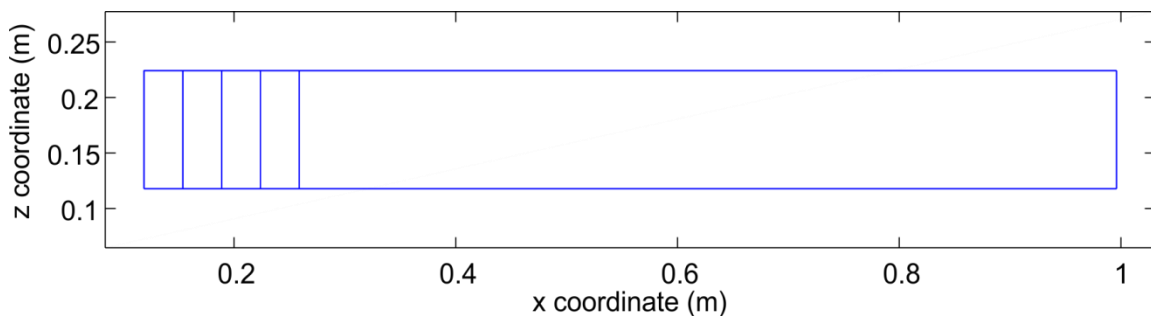


Figure 4.28 - Plot showing modelled wire network.

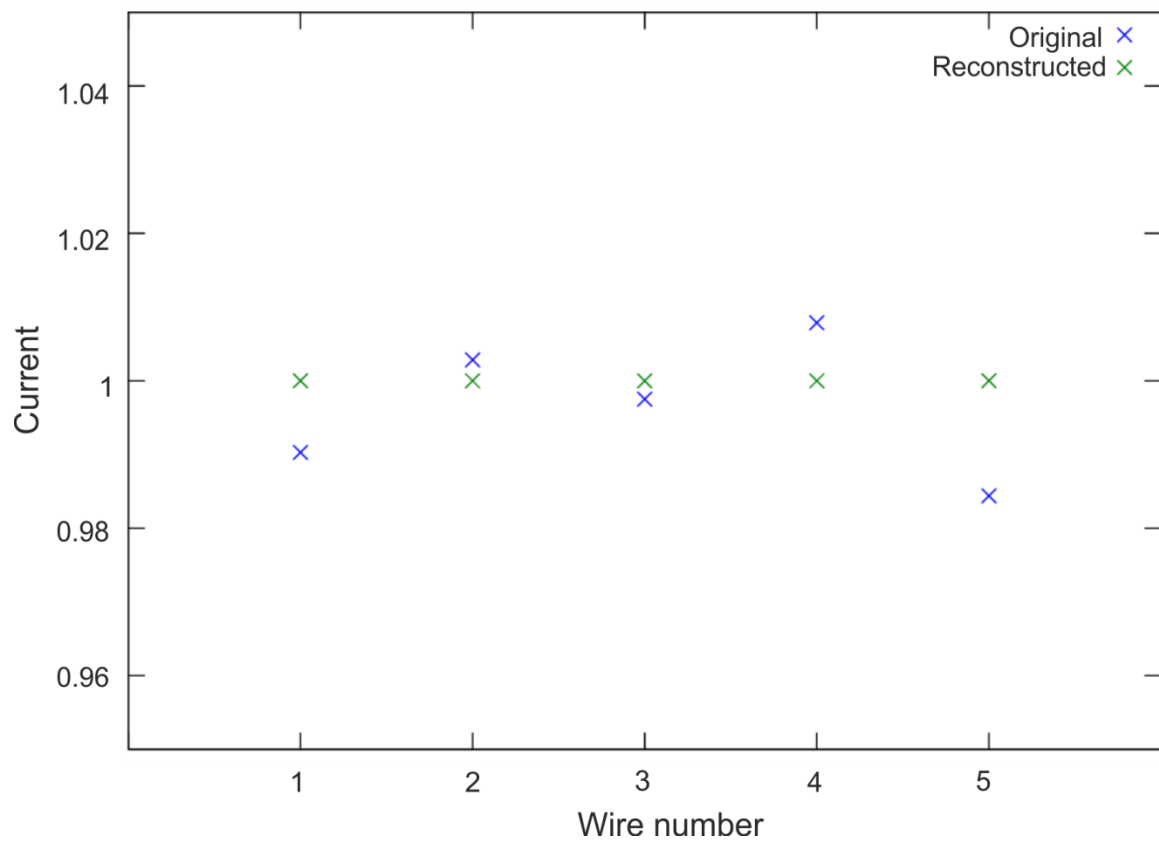


Figure 4.29 – Reconstructed (via Ansys simulation) compared with original wire currents.

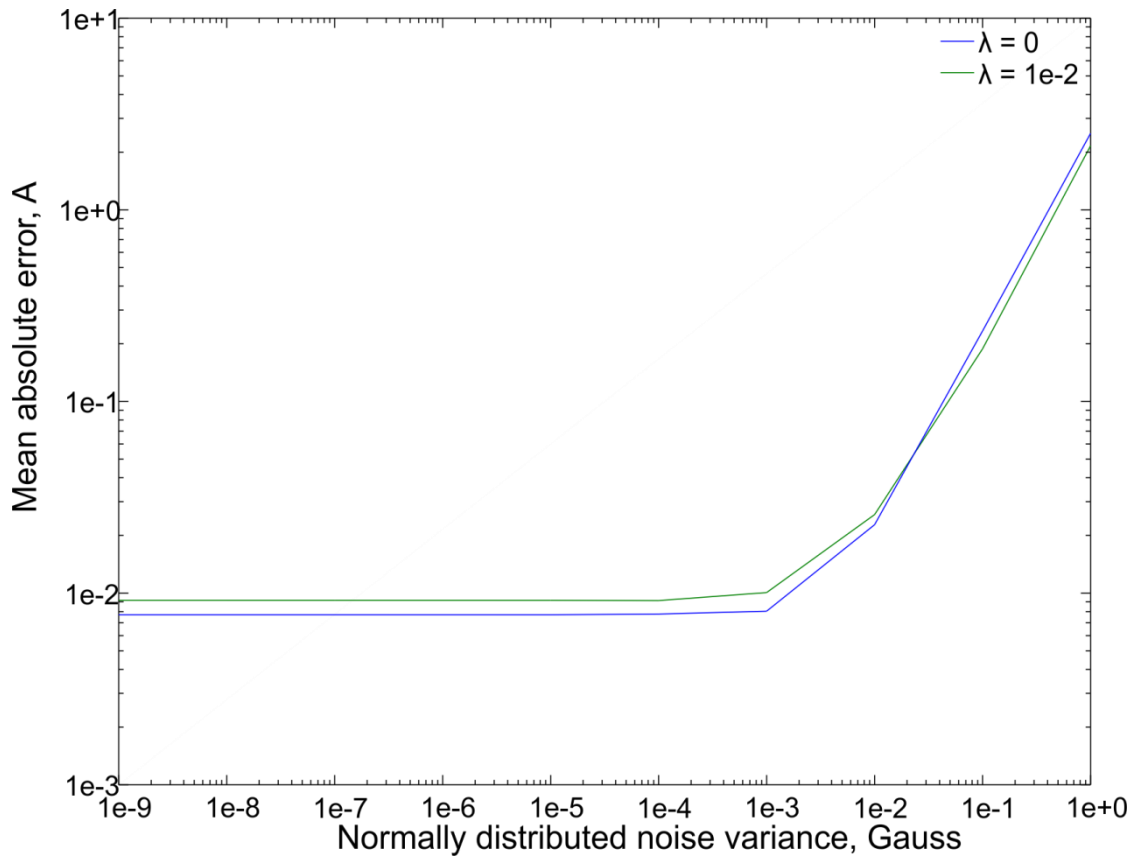


Figure 4.30 – Effect of random noise in magnetic measurements on reconstruction accuracy for two different values of  $\lambda$ .

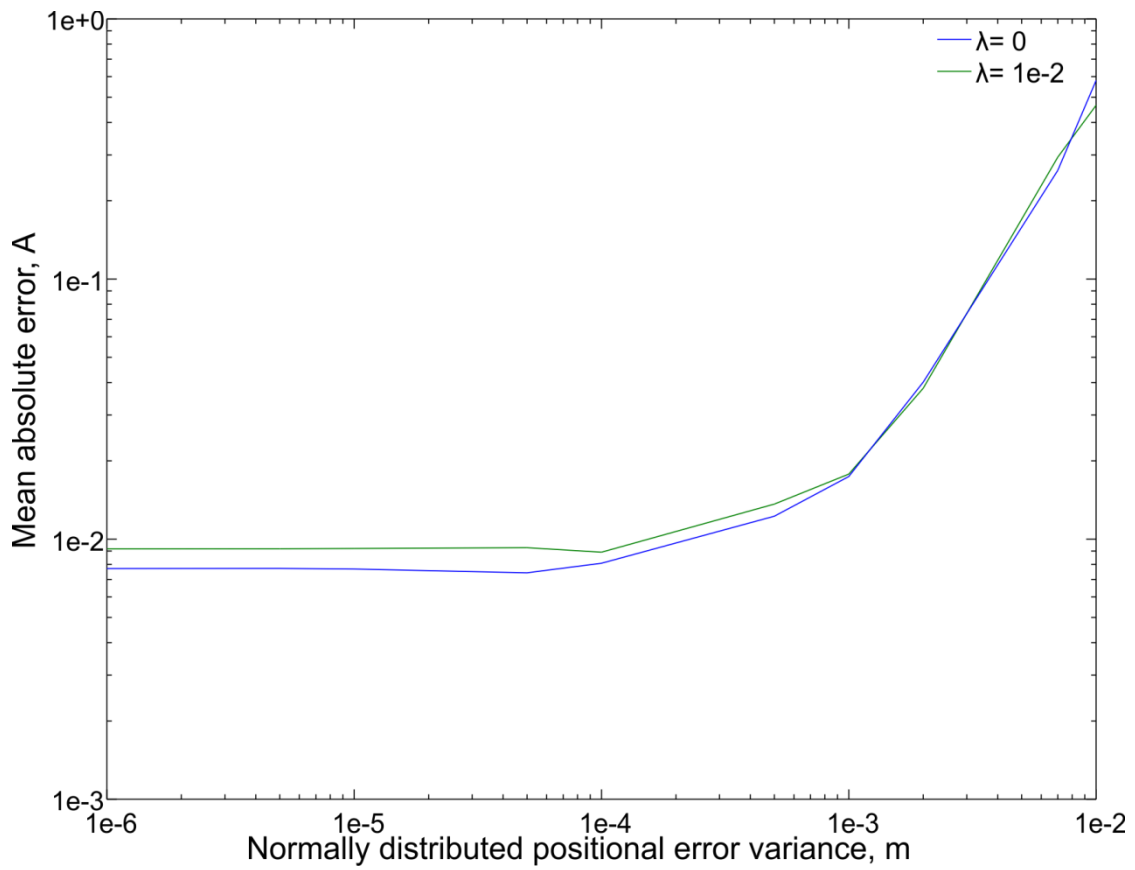


Figure 4.31– Effect of random errors in sensor position on reconstruction accuracy accuracy for two different values of  $\lambda$

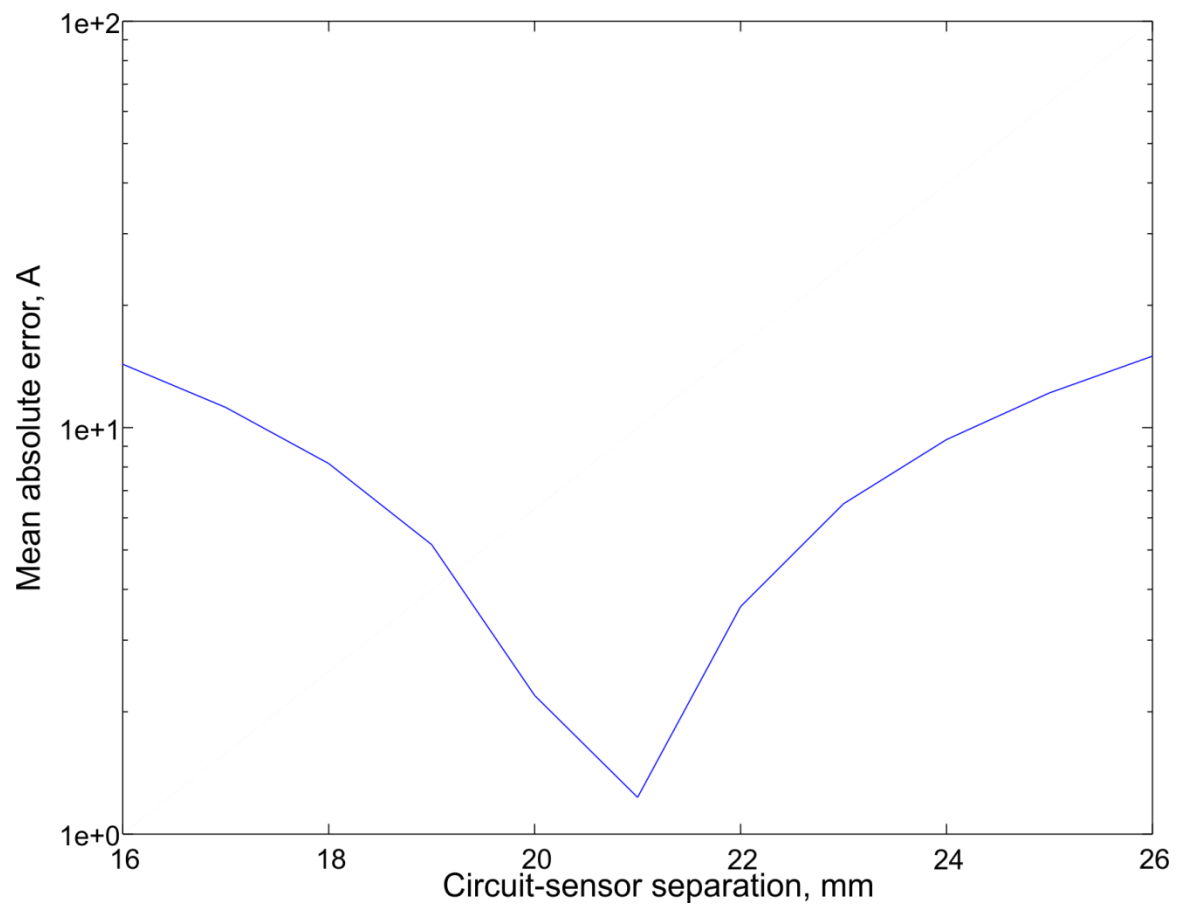


Figure 4.32 – Effect of shifting  $y$  separation on MAE.

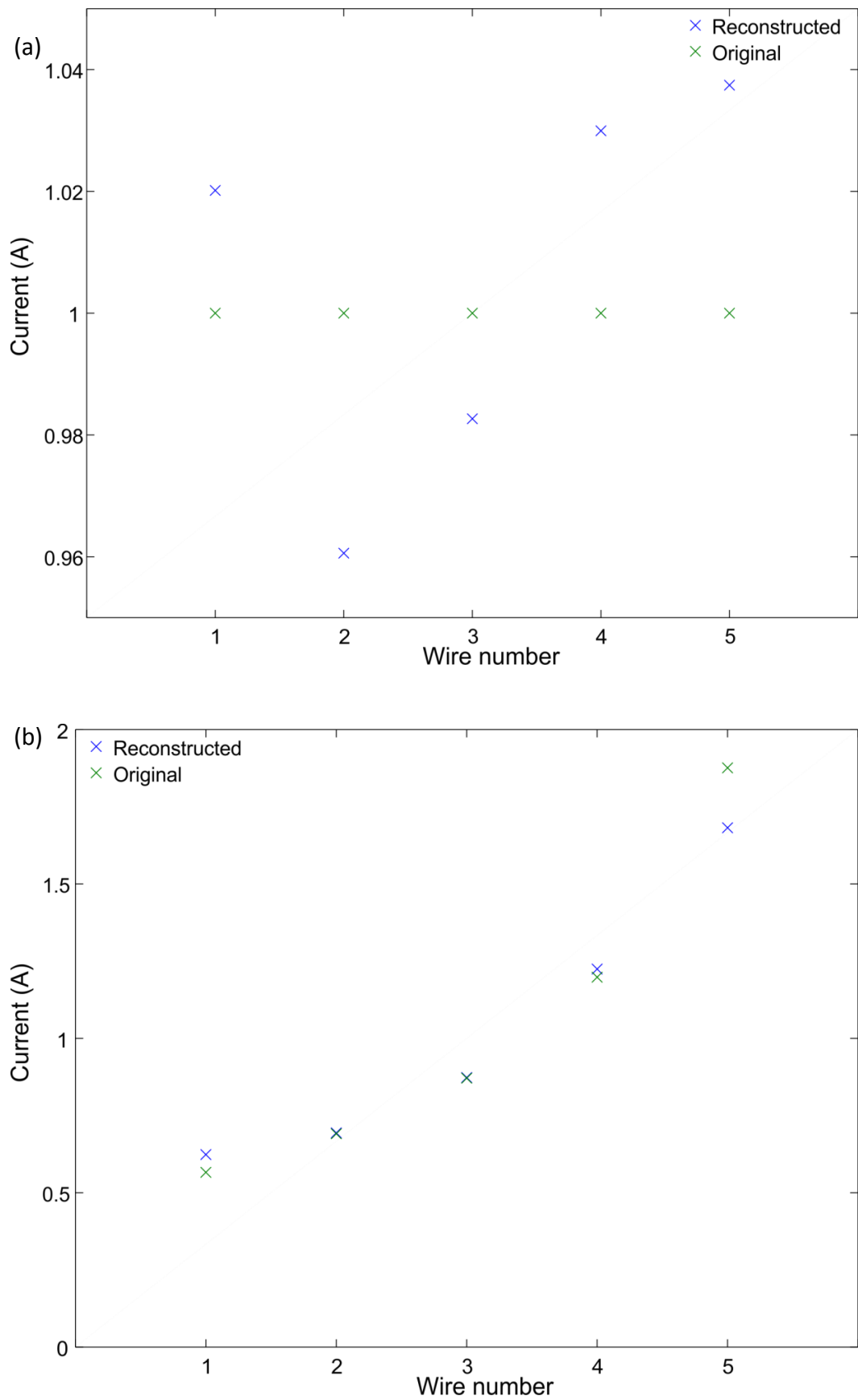


Figure 4.33 – Reconstructed currents from real measurement, (a) uniform wire currents (b) currents increasing from left right.

### 4.3.2 Simulated 3D circuit

The special basis projection method is now applied to a 3 dimensional problem. A 3D network of nodes and wires is constructed as shown in Figure 4.34. The plate is aligned with the  $xz$  plane and the electrolyte current flows along the  $y$  direction. Setting all the  $y$ -resistances to  $0.1 \Omega$  and the  $x$  and  $z$  resistances to  $500 \Omega$  yields the current distribution shown in Figure 4.35, 'Original' plot. The electrolyte current is almost uniform due to the very low resistance in the plate resulting in an almost uniform distribution of potential around the plate. Magnetic field values are taken from an array of the same dimensions as the sensor array in Section 3.2. The result is as shown in the 'Reconstructed' plot in Figure 4.35. No noise is added to the measurements or sensor positions, in order to test the model on a simple case. The reconstructed current distribution is visually very similar to the original, in contrast to the divergence or reconstructed plate current method presented in Section 4.2.3. When the  $y$ -resistances in the right hand side of the cell are set to  $3 \Omega$  (leaving all others the same as before), then the current distribution is no longer uniform. The original and reconstructed electrolyte current distributions resulting from this circuit are presented in Figure 4.36. The reconstruction visually is similar to the original as well.

The increased number of current elements and reduced spacing between elements appears to increase the susceptibility to noise compared with the 5-wire circuit presented previously. Measurement noise and positional noise are added in varying amounts and the resulting mean absolute errors in the current element values are presented in Figure 4.37 and Figure 4.38 respectively. Regularisation appears to have a much stronger effect than in Figure 4.30 and Figure 4.31, possibly due to the fact that the solution  $\xi$  for the 5 wire problem has relatively few elements, as do the other components of the coupling between the solution and the measurements such as the magnetostatic model  $\mathbf{K}$  and the circuit model  $\mathbf{T}$ . On the other hand, for the 3D problem the solution vector and coupling matrices are generally larger giving more degrees of freedom.

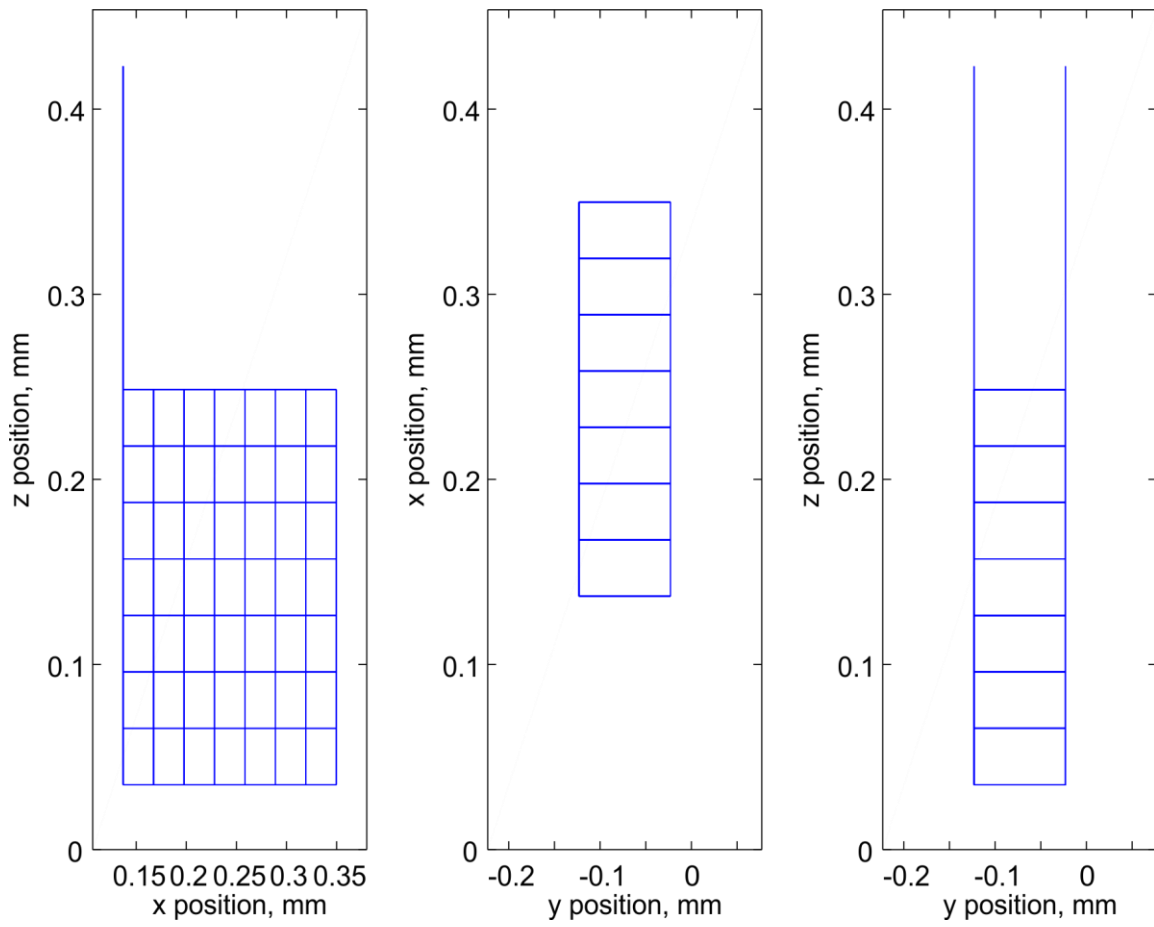


Figure 4.34 – 3D network used to represent a typical pair of plates, electrolyte and terminal leads.

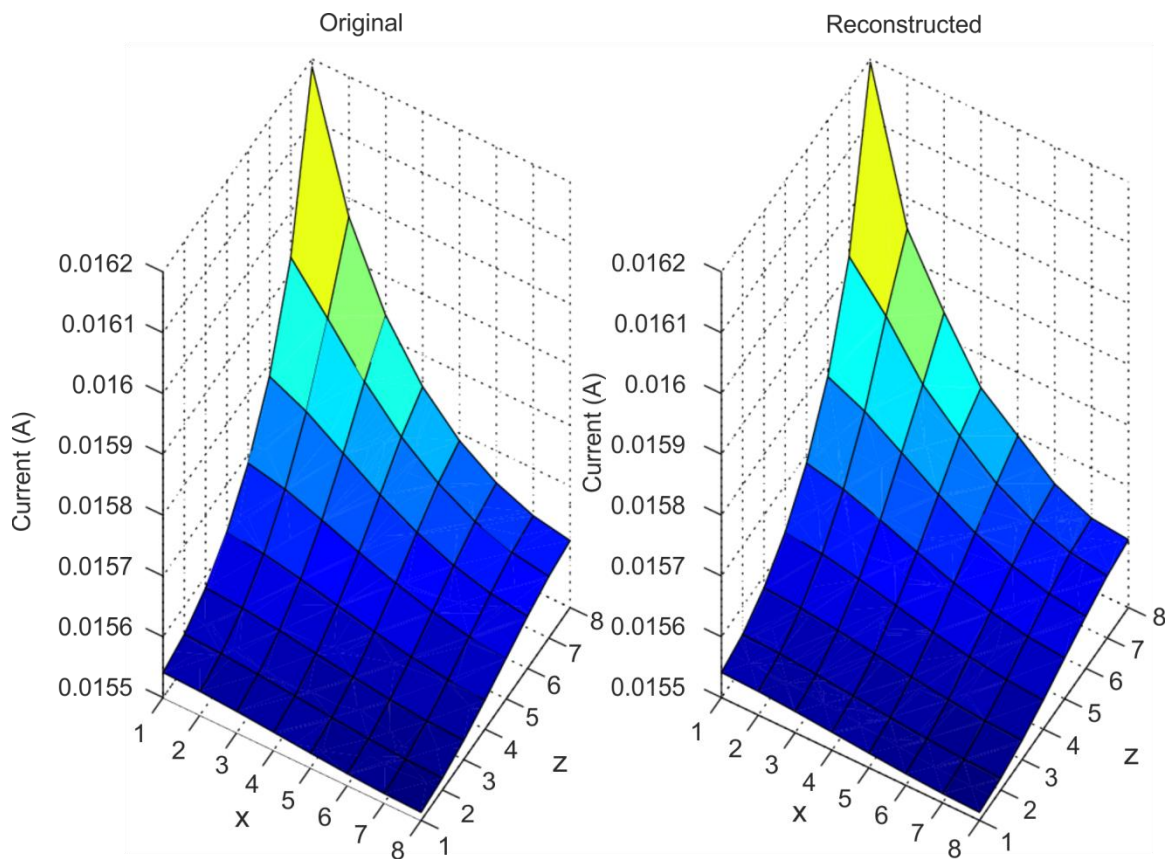


Figure 4.35 – A nearly uniform electrolyte current distribution and its reconstruction.  $\lambda = 1e^{-4}$ .

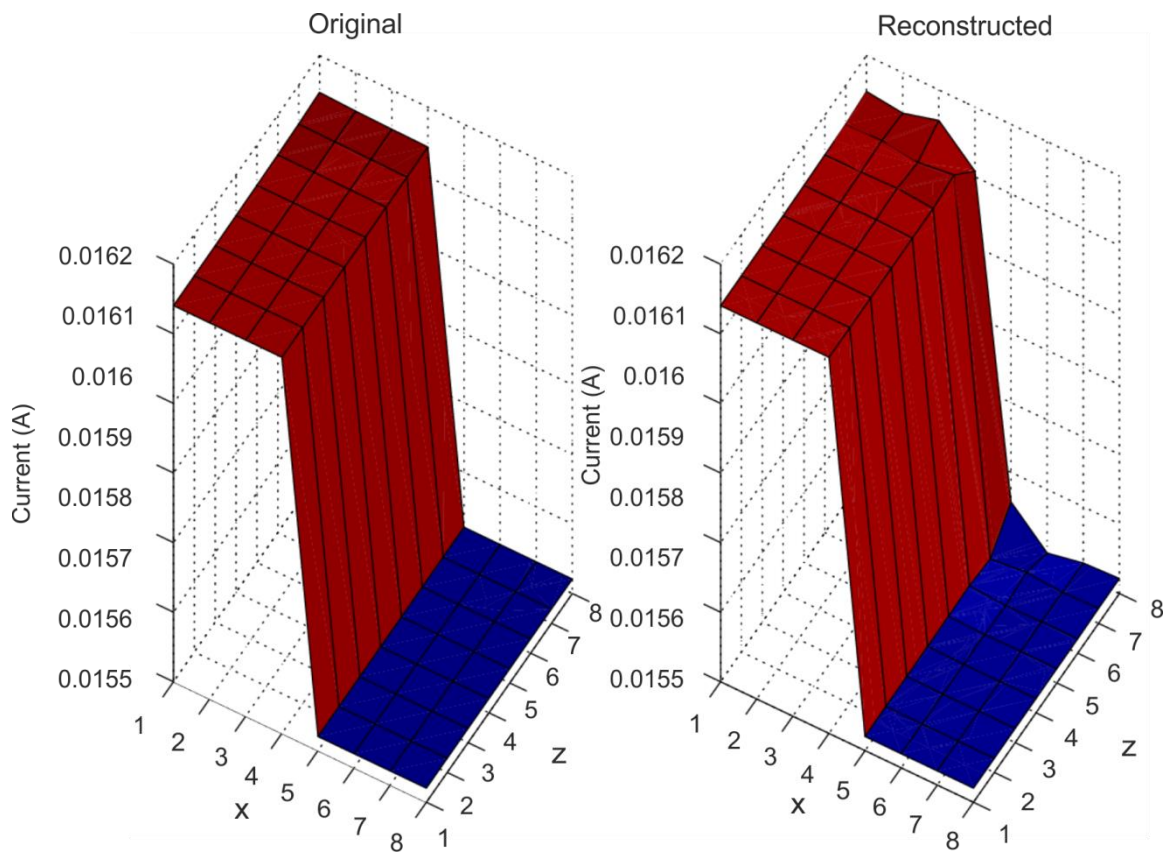


Figure 4.36 – A simple non-uniform current distribution and its reconstruction.  $\lambda = 1e^{-4}$ .

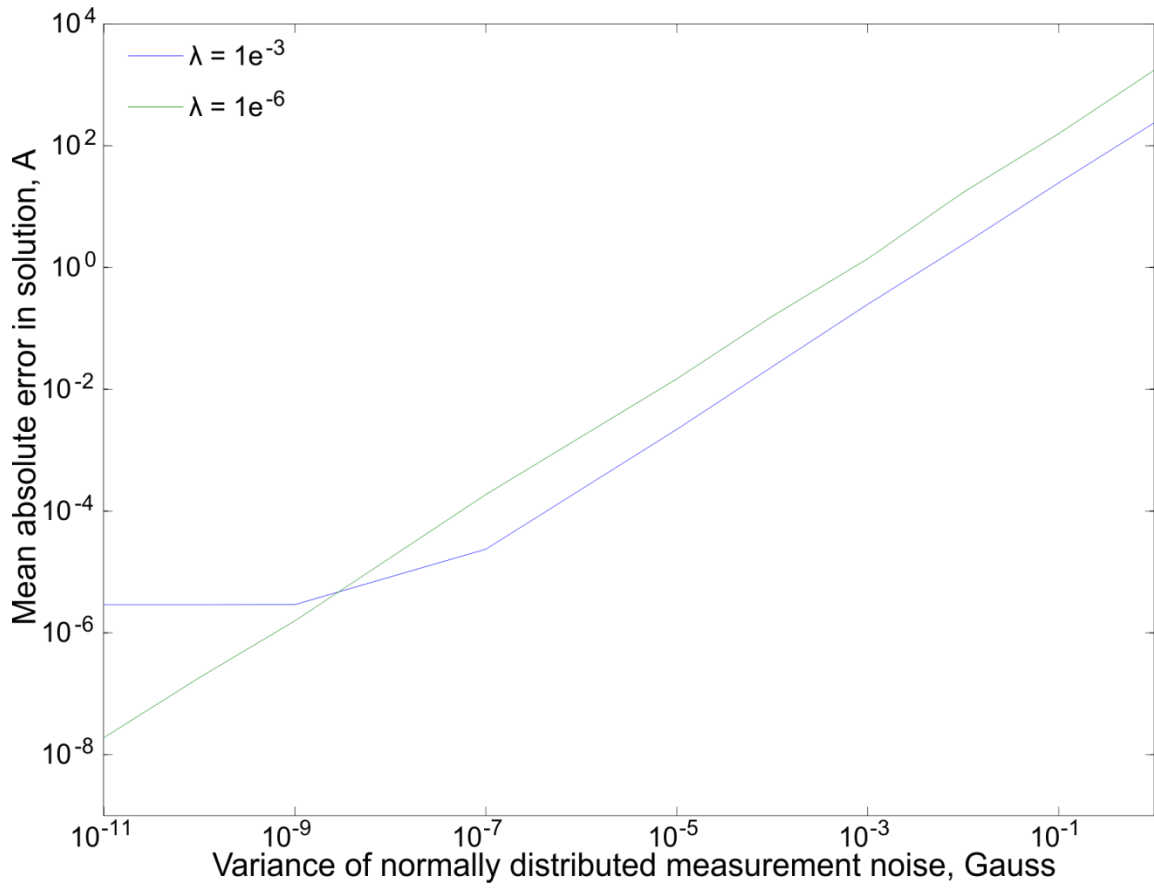


Figure 4.37 – MAE in current elements vs variance of random magnetic measurement noise, for two values of  $\lambda$ .

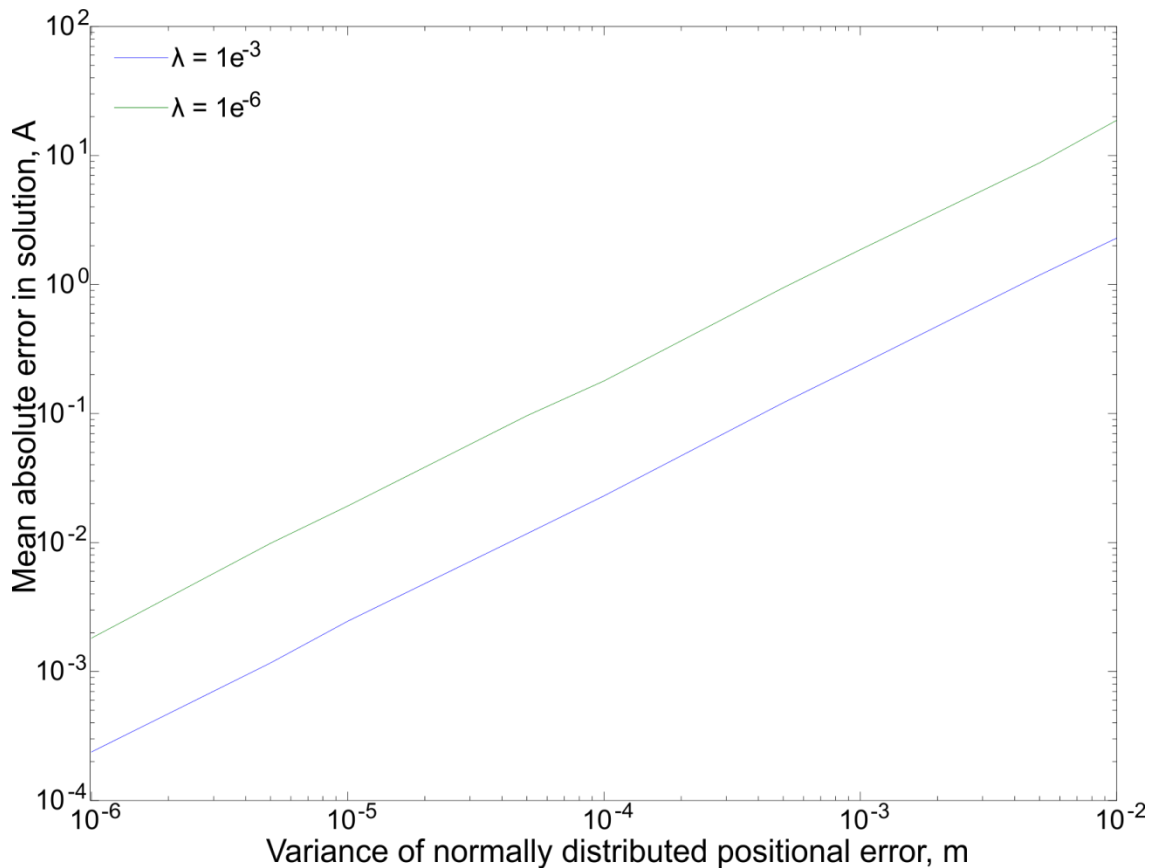


Figure 4.38 – MAE in current elements vs variance of random measurement noise, for two values of  $\lambda$ .

### 4.3.3 Using existing finite element software

The solution of the problem by special basis projection does not involve inversion of the magnetostatic forward model  $\mathbf{K}$ . Instead it approximates on the one hand the unknown current distribution as a linear combination of some partial current distributions, and on the other hand the measured magnetic field as a linear combination of some partial magnetic field distributions (see [77] or Section 2.3.1). The partial magnetic fields can be calculated from the partial current distributions externally to the solver algorithm, allowing the use of sophisticated commercial finite element software, such as Ansys Maxwell. There are a few advantages to using finite element software. Firstly, it allows the electrolyte to be divided into volume segments, rather than approximating the electrolyte as an array of arbitrarily thin wires as in Section 4.3.2. Secondly, it allows more complex, realistic geometry to be defined than is possible in the rudimentary wire model utilised in the previous section. It is straightforward to input the geometry using the built in graphical editor, or import parts created using 3D drawing software. Thirdly, it is possible to divide the electrolyte into a relatively coarse grid (which is solved more rapidly) and still obtain realistic current and magnetic distributions. The current can take realistic diagonal paths through the plate volumes

since the Ansys model is quantised on a variable-size mesh, tailored to the cell geometry. Finally, magnetic materials may be included in the finite element model, with either a constant magnetic permeability or a non-linear  $bh$  curve. This permits the use of magnetic core current sensors for verification of the current distribution measurements (See Chapters 3 and 5).

The partial currents and magnetic fields are obtained by dividing the electrolyte volume into a regular grid drawn parallel to the plates. For example, the electrolyte may be divided into a  $5 \times 5$  grid of equally-sized electrolyte volumes. The current in one small volume is set to a nominal constant value (in the  $y$  direction) and to zero in all the other volumes, the model is solved and the magnetic field data is exported. Then the next electrolyte volume is set to the nominal current density and the previous one set to zero along with the others. This is repeated until all the partial electrolyte currents and their accompanying partial magnetic fields have been considered. In practice it is more convenient to just draw one partial electrolyte volume and shift it around the original electrolyte volume. Figure 4.39 shows the first (a) and last (b) position of the partial electrolyte. The process of moving the partial electrolyte, solving the model and exporting data can be controlled via a Visual Basic macro script and takes between 20 minutes and 5 hours for a  $5 \times 5$  grid (depending on meshing and solution settings). This process needs to be performed once for a given cell design.

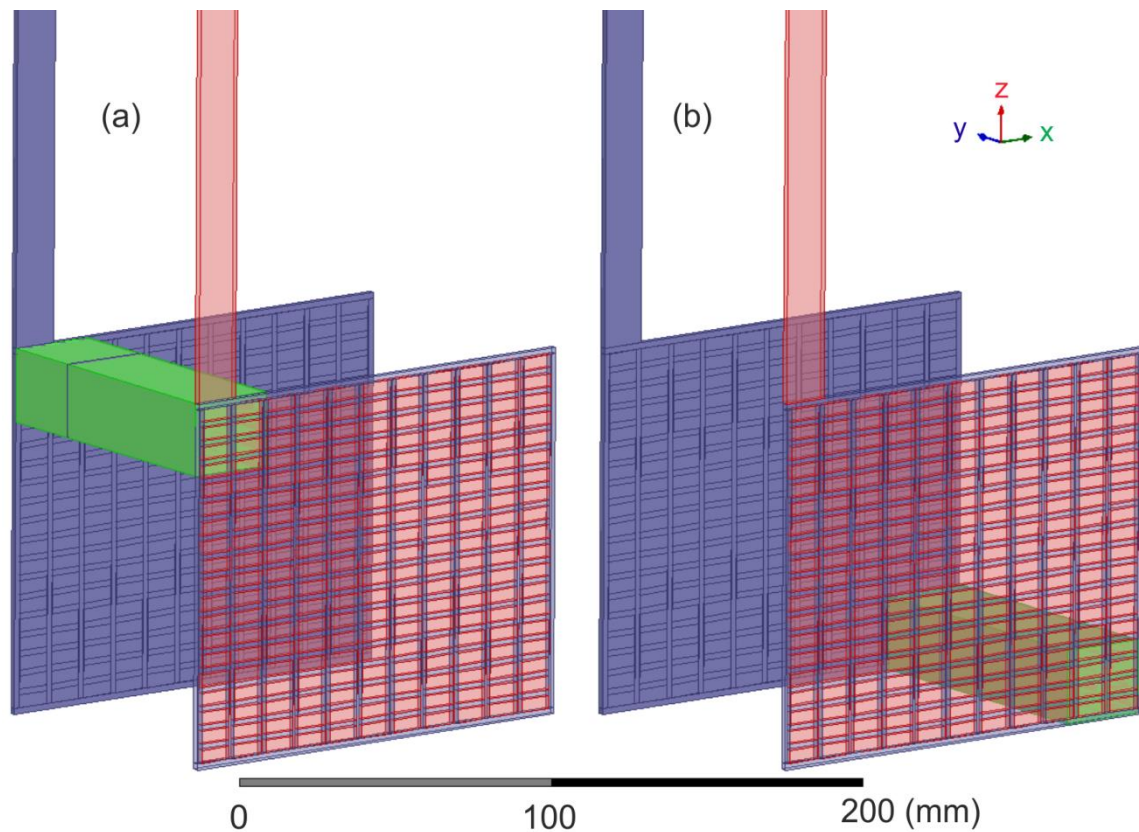


Figure 4.39 – Two positions of the partial electrolyte when the electrolyte volume is divided into a  $5 \times 5$  array.

Initial reconstruction results using a  $5 \times 5$  grid are presented in Figure 4.40. There is an artefact near to the terminal wire. Reconstruction of a step-changing distribution is given in Figure 4.41. The solutions do not match the original data as closely as when the wire-mesh model is solved (Figure 4.35 and Figure 4.36), but since the finite element software is superior to a wire mesh model for describing a real cell then this may be a necessary trade-off. The time taken to fetch the partial magnetic field data, the ‘measured’ data, and solve for  $\xi$  is less than 1 s. If a varying current distribution in a constant geometry is being measured, this time can be reduced further by not reloading the partial magnetic fields each time.

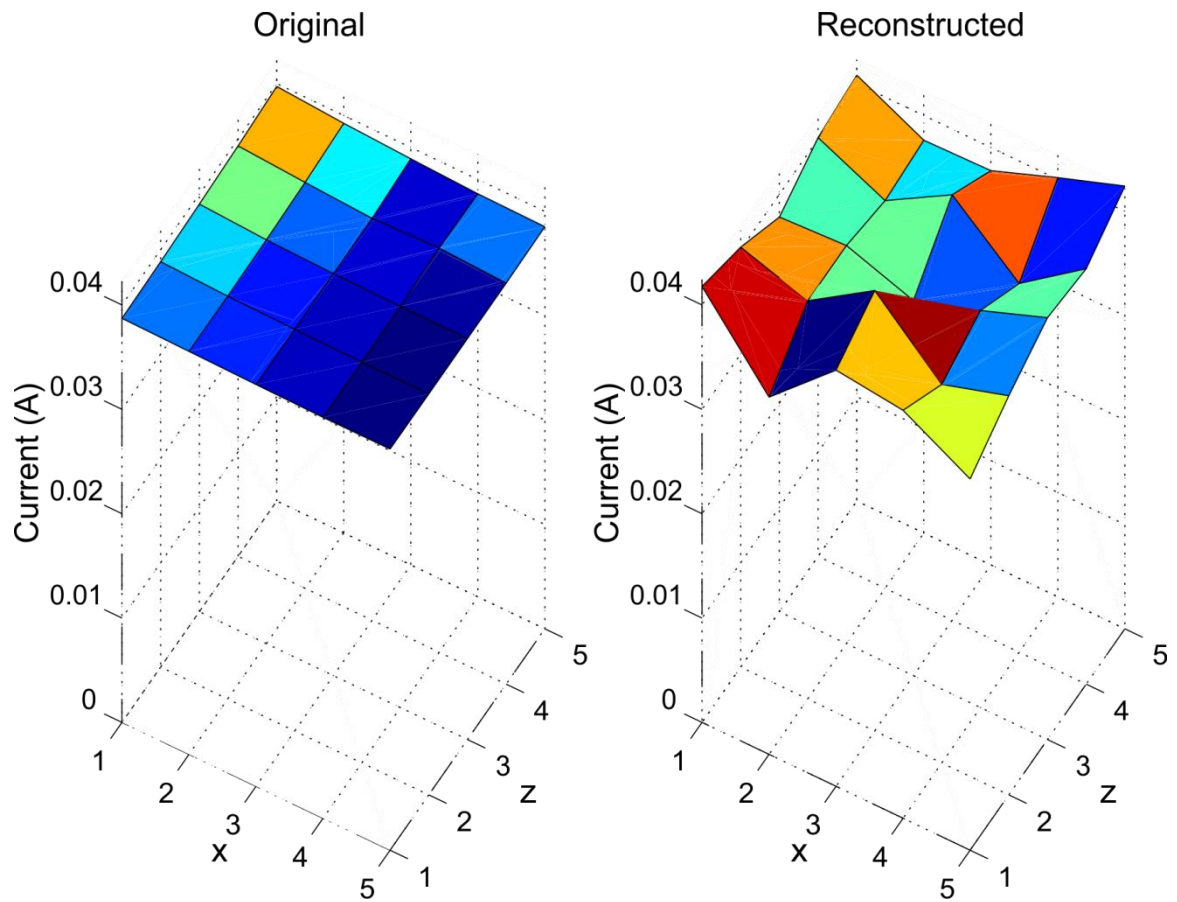


Figure 4.40 – Reconstruction of a uniform current distribution over a  $5 \times 5$  grid.

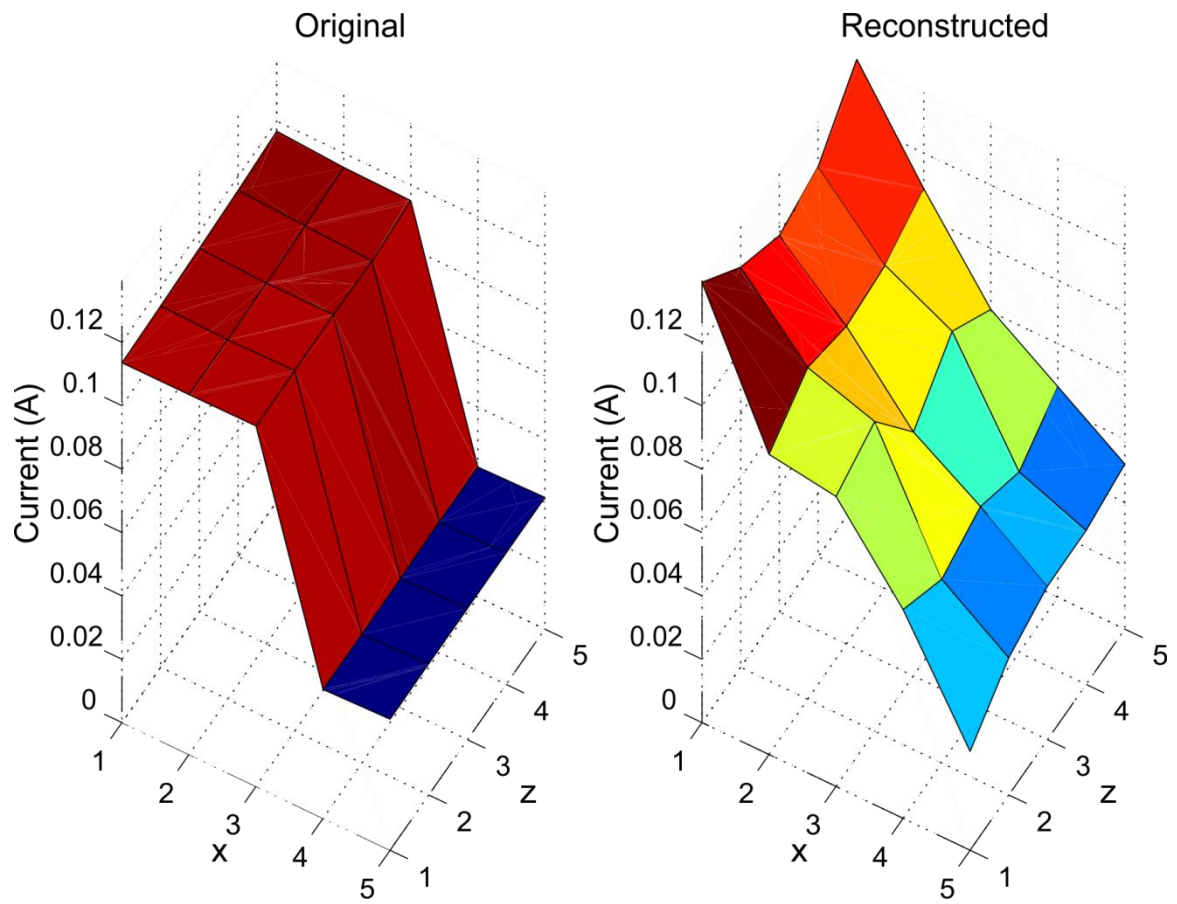


Figure 4.41 – Reconstruction of a step-changing current distribution over a  $5 \times 5$  grid.

#### 4.3.4 Extending the basis to include plate resistance variation

The SBP method requires an accurate model of the cell conductance (2.32) in order to produce a good solution. An accurate conductance model of a real cell may, however, not be available and so the performance of the solver under this condition is investigated. To generate the simulated measurement data all  $[r_x, r_y, r_z]$  are set to  $[0.1, 10, 0.15] \Omega$ . These values are chosen such that  $r_y$  dominates, resulting in a nearly-uniform current distribution. Then, partial fields data are generated with the correct value of  $\mathbf{R}$ . This results in good agreement with the original current distribution. This can be seen by comparison of the plots 'Original' and 'Correct' in Figure 4.42. Next, partial fields data is generated where all  $[r_x, r_y, r_z]$  are set to  $[0.1, 10, 0.1] \Omega$ .  $r_y$  is still much greater than  $r_x$  and  $r_z$ , so the source current distribution is not changed greatly, but the reconstruction appears highly non-uniform ('Incorrect' plot, Figure 4.42).

A way to proceed in spite of an unknown in the resistance distribution is to extend the basis, by generating partial fields data for a range of possible values of  $\mathbf{R}$ . In this case, the 'unknown' value of  $R_z$  can be replaced by a maximum and a minimum expected value of  $R_z$ . First, 64 partial fields are generated for  $[r_x, r_y, r_z] = [0.1, 10, 0.1] \Omega$ , then 64 more are generated for  $[r_x, r_y, r_z] = [0.1, 10, 0.2]$ . The solver can then find the weighting of all 128 partial fields to generate a solution. The result of this method is shown in the 'Extended' plot on Figure 4.42.

The results show that very accurate reconstructions are possible using a special basis projection solver when no errors are present. However, the forward model used to generate partial fields must be carefully designed to match the cell under test, in order to avoid errors in reconstruction. Some tolerance can be built into the solver by extending the basis. In the example given, an error is present in only one variable in the model and so only 2 sets of  $p$  partial fields are necessary to account for it. The number of partial fields scales as  $2^q p$  for  $p$  unknown  $y$  currents and  $q$  unknown model parameters, so extending the basis over many variables quickly becomes computationally expensive.

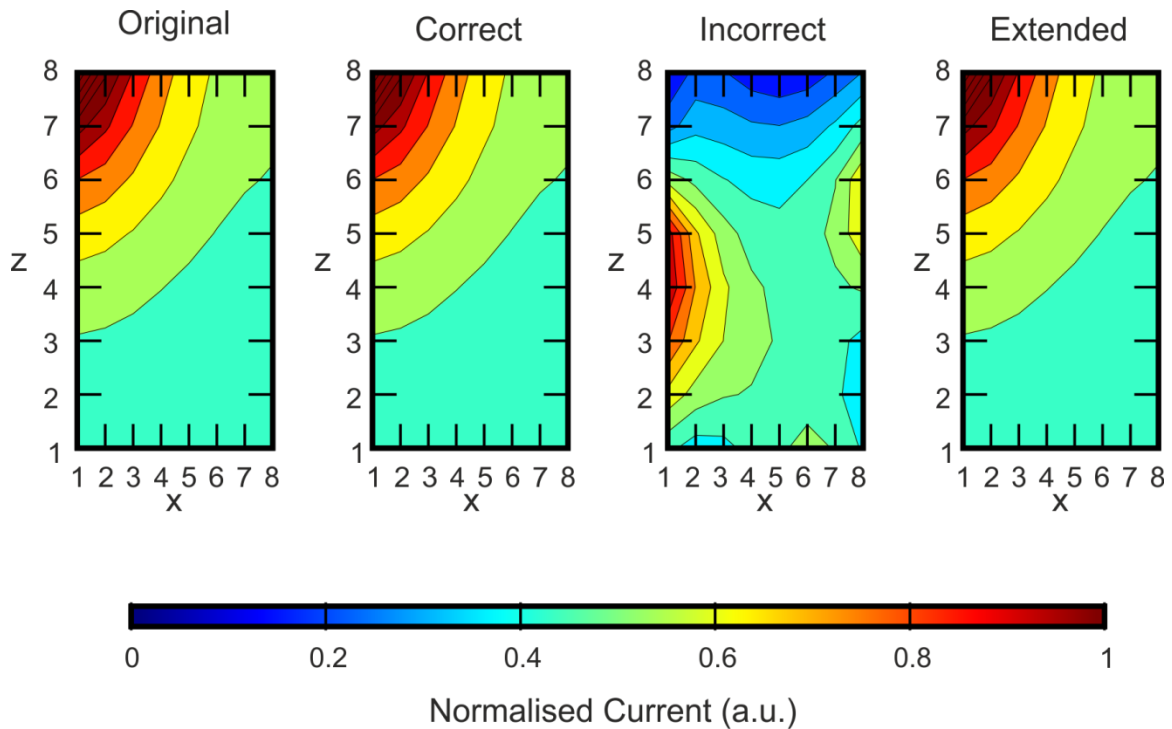


Figure 4.42 – An almost uniform current distribution ('Original'), and 3 reconstructions, classed by the basis used to solve. 'Correct' basis uses the same branch resistances in the solver as in the model under test. 'Incorrect' basis uses incorrect branch resistances in the solver. 'Extended' basis uses 2 sets of partial data, each with a different  $R_z$  value to allow some flexibility in the solver.

As a result of the computational cost, this method is best suited to cases where the plate resistance can be defined with a minimum of parameters. In this case all wires in the  $x$  direction have resistance  $r_x$  and all wires in the  $z$  direction have resistance  $r_z$  so specifying the ratio between them is enough to define the path which current will choose to take through the plate. Sunu and Burrows [27] found when measuring the grid members that they are not regular. However if the resistance of the grid members is known, then an extended basis could be used to account for any change in resistance in the active mass over the discharge cycle. To test this idea, a model of the cell using Sunu and Burrows' grid measurements is constructed, with the spaces in between filled with the Ansys default lead material model (conductivity,  $\sigma = 5 \times 10^6 \Omega^{-1} \text{m}^{-1}$ ) (Figure 4.43). Two sets of partial fields are also modelled, one where the plates are made of solid lead, one where the grid model is used but filled in with a low-conductivity material ( $\sigma = 83 \Omega^{-1} \text{m}^{-1}$ ). Neither of these models used to generate the partial fields use accurate representations of the plate resistance in the cell to be solved. As a control, partial fields are also generated from a 'correct' model of the plates. Figure 4.44 shows example current reconstructions for correct, incorrect and extended bases at  $\lambda_r = 1$ . This illustrates the kind of distortion that can result from an incorrect grid model in the solver, and how an extended basis reduces this distortion. Figure 4.45 shows the same set of reconstructions at  $\lambda_r = 4$ . These over-regularised solutions appear closer to the original distribution than the  $\lambda_r = 1$  solutions. The mean absolute errors of the 6 solutions are given in

Table 4.1.

Figure 4.46 shows the MAE against  $\lambda_r$  plot for the solutions generated by the 2 incorrect sets of partial fields, the extended basis consisting of both incorrect sets of fields, and the correct set of partial fields. The MAE against  $\lambda_r$  curves for both the correct and extended partial fields are very similar. This suggests, in this case, that knowing the exact conductivity of the material pasted into the plate grids is not necessary in order to obtain a good solution, if an extended basis method is used. The value of  $\lambda_r$  at which the minima for the correct and extended fields

occur is lower than  $\lambda_r$  at the minima for the incorrect grid solution, meaning that a solution using the value of  $\lambda$  given by the L-curve would be better than if either incorrect set of partial fields were used (in other words, the incorrect partial fields require over-regularising in order to provide a good solution). The extended basis solutions have minimum MAE of 2.25 % for a uniform source distribution and 22.5 % for a step-changing source distribution.

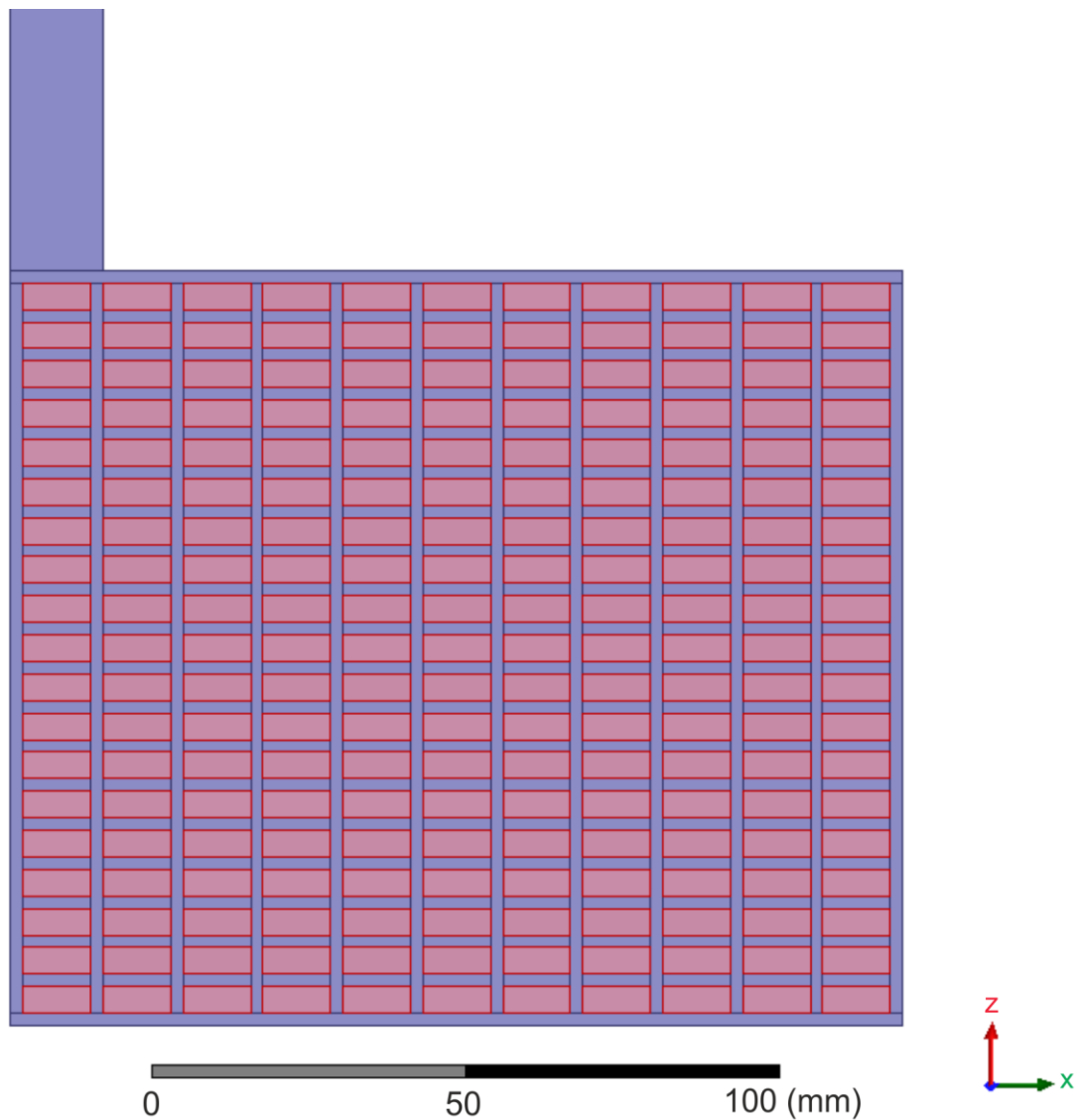


Figure 4.43 – Geometry of the grid used to assess the effect of non-uniformity of the resistances in the grid members.

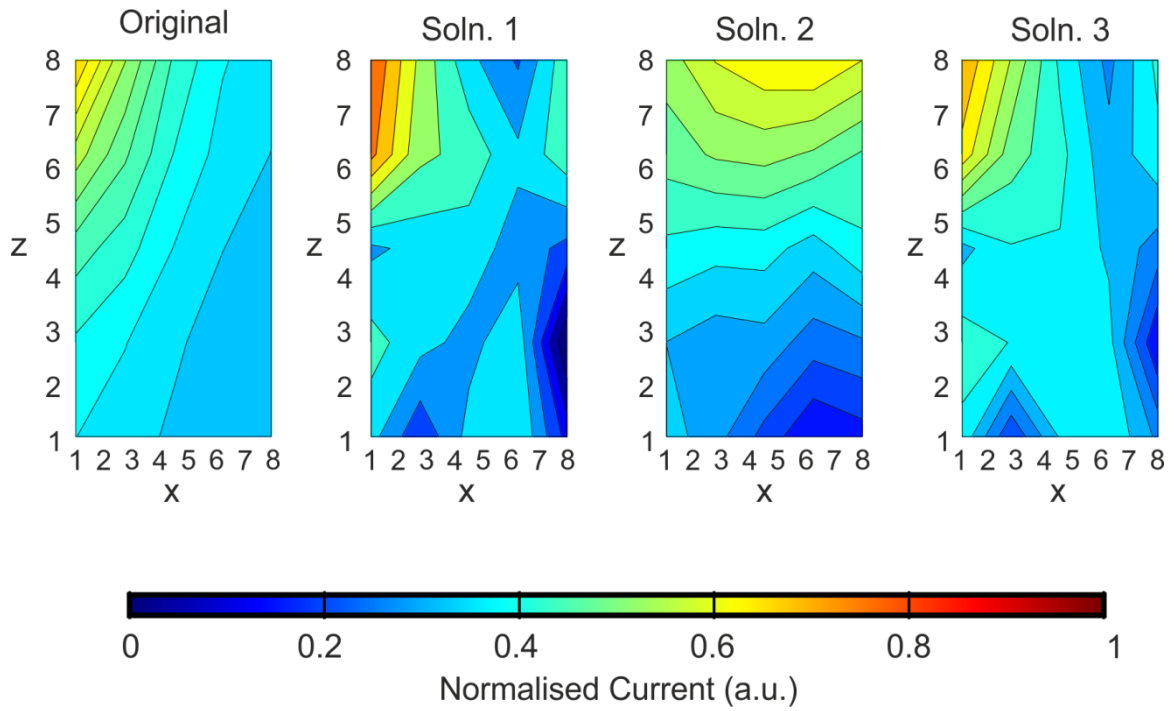


Figure 4.44 - Reconstructions of a uniform current distribution using Ansys as the forward model. Solution 1 uses a correct grid to generate the partial fields and a standard basis. Solution 2 uses an incorrect grid model for the partial fields. Solution 3 uses a correct grid model and a basis which is extended over a variable conductivity in the paste material.  $\lambda_r = 1$ .

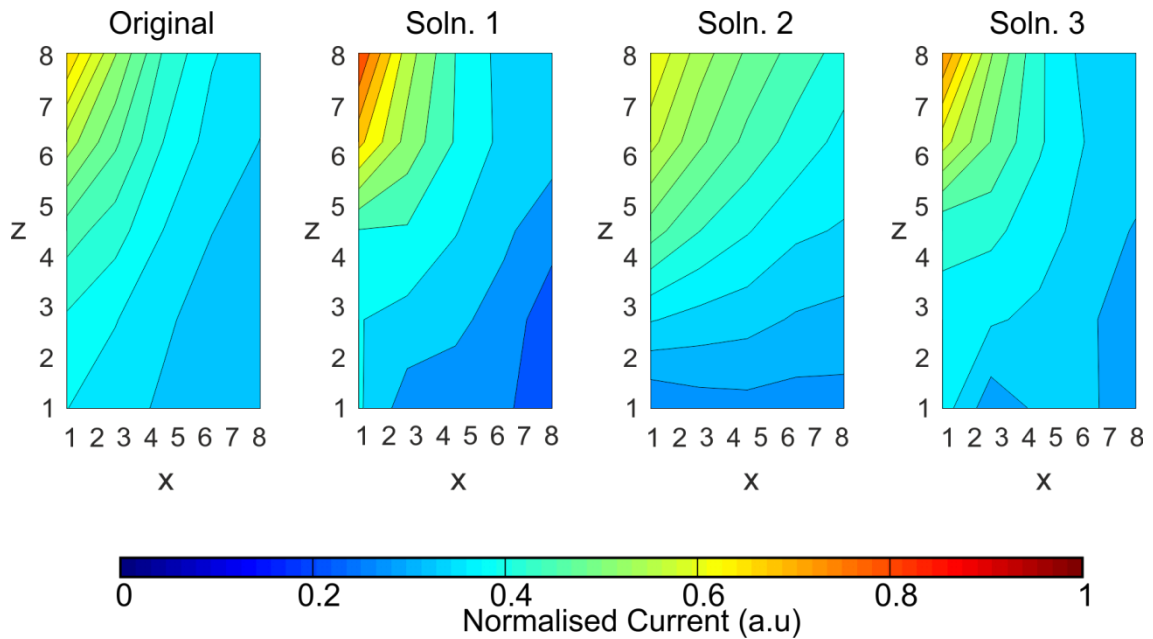


Figure 4.45 - Reconstructions of a uniform current distribution using Ansys as the forward model, solution numbers same as Figure 4.44.  $\lambda_r = 4$ .

	1 – Correct grid and active mass in solver	2 – Grid represented as uniform material	3 – Correct grid, basis extended over active mass conductivity
Mean absolute error, % of mean absolute value of $\xi$ ; $\lambda_r = 1$	23.16 %	24.23 %	13.68 %
Mean absolute error, % of mean absolute value of $\xi$ ; $\lambda_r = 4$	9.53 %	9.01 %	4.71 %

Table 4.1 – Values of mean absolute error for the 3 solution types and 2 values of  $\lambda_r$  shown in Figure 4.44 and Figure 4.45.

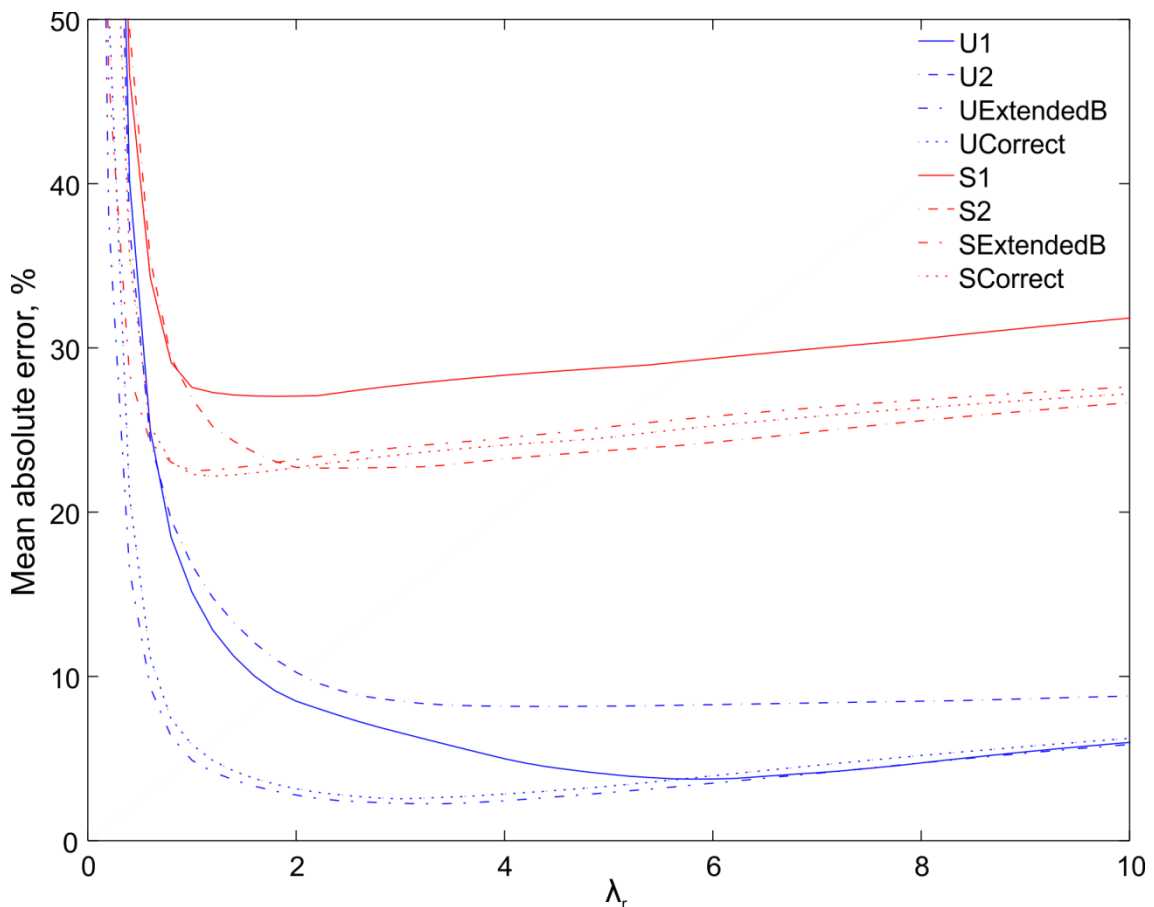


Figure 4.46 – MAE against relative regularization parameter. U1 and S1 use a solid lead model of the plates to generate partial fields, U2 and S2 use a grid model of the plates with low conductivity material in the gaps. UCorrect and SCorrect use the grid model with lead in the gaps (same as in the cell being solved). UExtendedB and SExtendedB use an extended basis consisting of set of partial fields 1 and set of partial fields 2.

#### 4.3.5 Real 3D circuit

To be practically useful the solver must be robust enough to solve the 3D inverse problem for real measurements. A  $5 \times 5 \times 2$  node circuit (Figure 4.47) is constructed which represents 2 parallel plates connected by an electrolyte separated into 25 segments. Resistance along each  $x$ - or  $z$ -direction branch (*i.e.* in the plane of the plate) is nominally  $0.1 \Omega$ , resistance along the

$y$ -direction branches is  $10 \Omega$ . The magnetic imaging system is described in Section 3.2.2. The geometry of the circuit is chosen as it can be represented by a model similar to that shown in Figure 4.34, but having fewer  $y$  direction branches. A standard basis and an extended basis solver (where  $r_z$  is allowed to vary between  $0.1 \Omega$  and  $0.2 \Omega$ ) are tested. For comparison, a reconstruction using simulated data is also made.

**Examples of reconstructions from the real magnetic data are given in Figure 4.48. Clearly the reconstructions using real measurements (MO and MO2) are less accurate reconstructions than a simulated-only problem with the same resistor values (OO). The region of high current density in the right of the region is reproduced more visibly in the extended basis case (MO2, see Section 0 for an explanation of extending the basis) than in the standard basis (MO). These observations are in agreement with measurements of mean absolute error with respect to the original current distribution (**

Table 4.2) – neither MO or MO2 are as accurate as OO, but MO2 is slightly better than MO. The improvement in performance that is seen when using an extended basis model may be due to non-ideal resistors and interconnects in the circuit being accounted for in the solver.

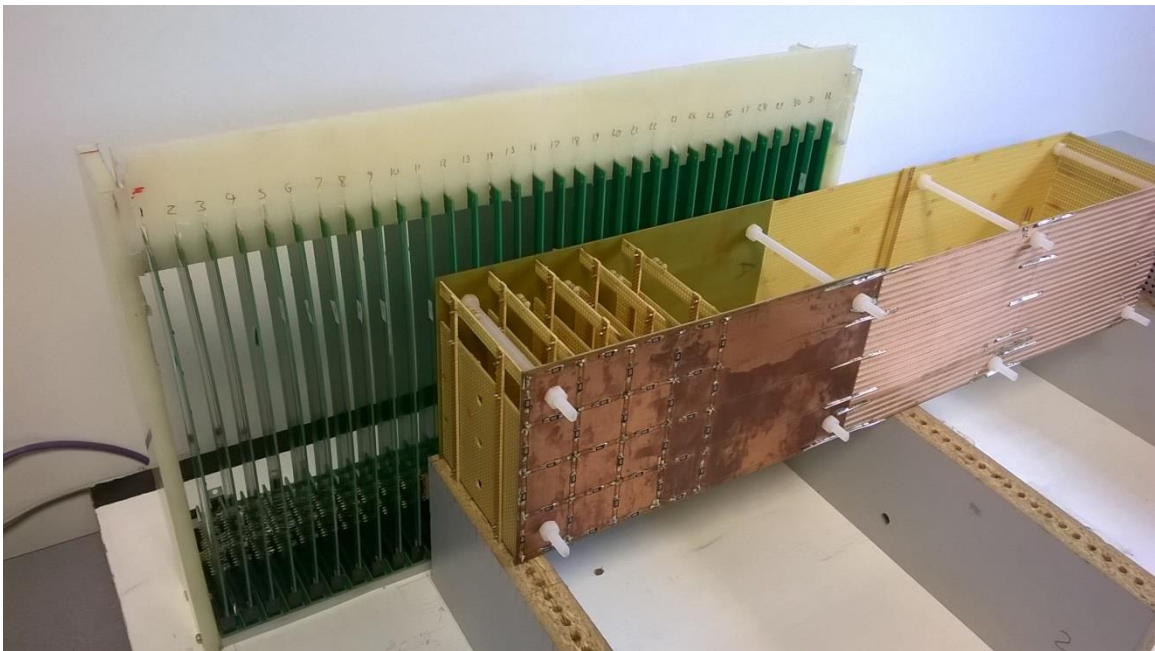


Figure 4.47 - 3D resistive circuit and magnetic sensor array used to test solver with real measured data.

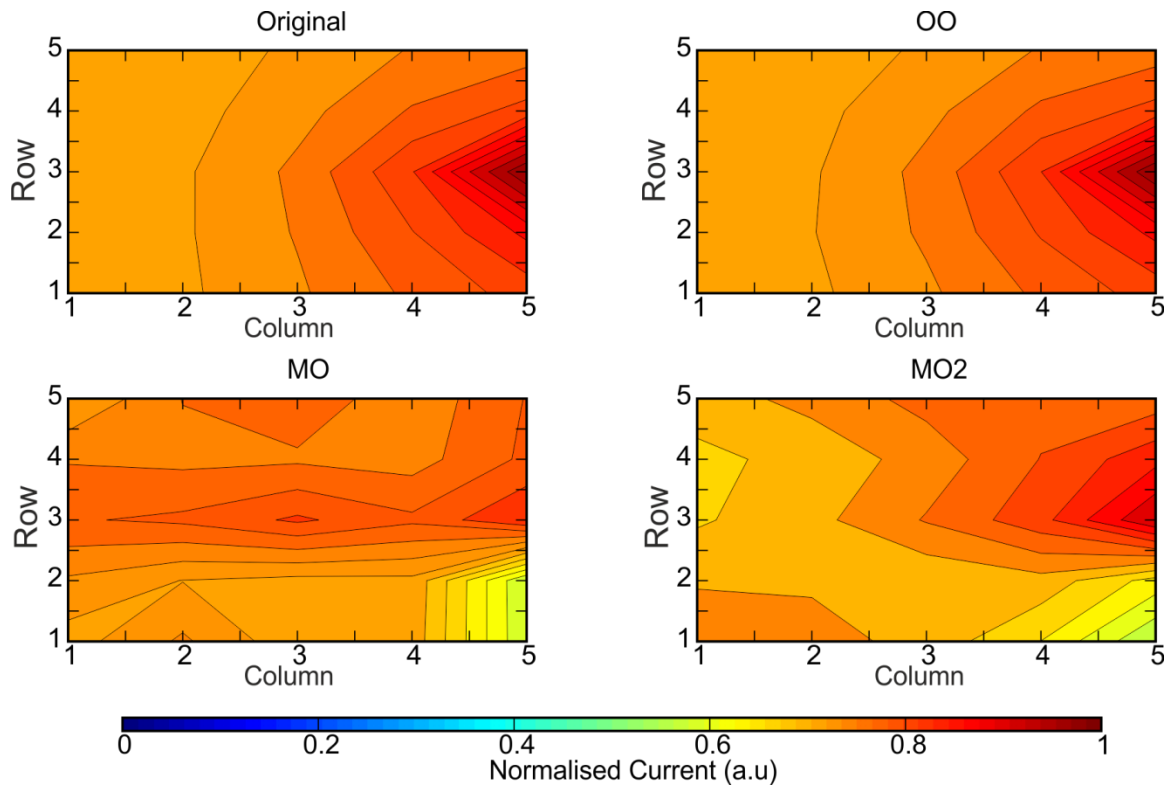


Figure 4.48 – A comparison between an original current distribution and its reconstructions. OO = partial fields generated in Octave to solve a simulated distribution. MO = partial fields generated in Octave to solve for real magnetic measurements. MO2 = extended basis generated in Octave to solve for real magnetic measurements.

	OO	MO	MO2
Mean absolute error, % of mean absolute value of $\xi$	0.14 %	8.10 %	5.66 %

Table 4.2 – Mean absolute error of the 3 different problem types shown in Figure 4.48.

#### 4.3.6 Using measured data as the basis

The idea of using an external finite element program as the forward model in the SBP method can be taken further, to use real measurements to construct the basis. Rather than simulating the partial currents and magnetic fields, the 3D resistor circuit is modified such that only one of the  $y$  direction wires is connected at a time and magnetic measurements are taken for each individual  $y$  direction wire. The advantage of this method is that any irregularity in the plate resistances, circuit or sensor positions, the sensor gain, and the position of the terminal wires is accounted for (as long as care is taken to place the sensors and circuit in the same position each time). It may not be feasible to implement this method on a real lead acid cell, but it gives some more insight into the sources of error in the magnetic imaging system.

A comparison of the performance of the solver using measured partial magnetic fields against the solver using simulated partial magnetic fields is made by plotting percentage MAE against

regularisation parameter (Figure 4.49). Real measured uniform and step-changing current distributions are solved.

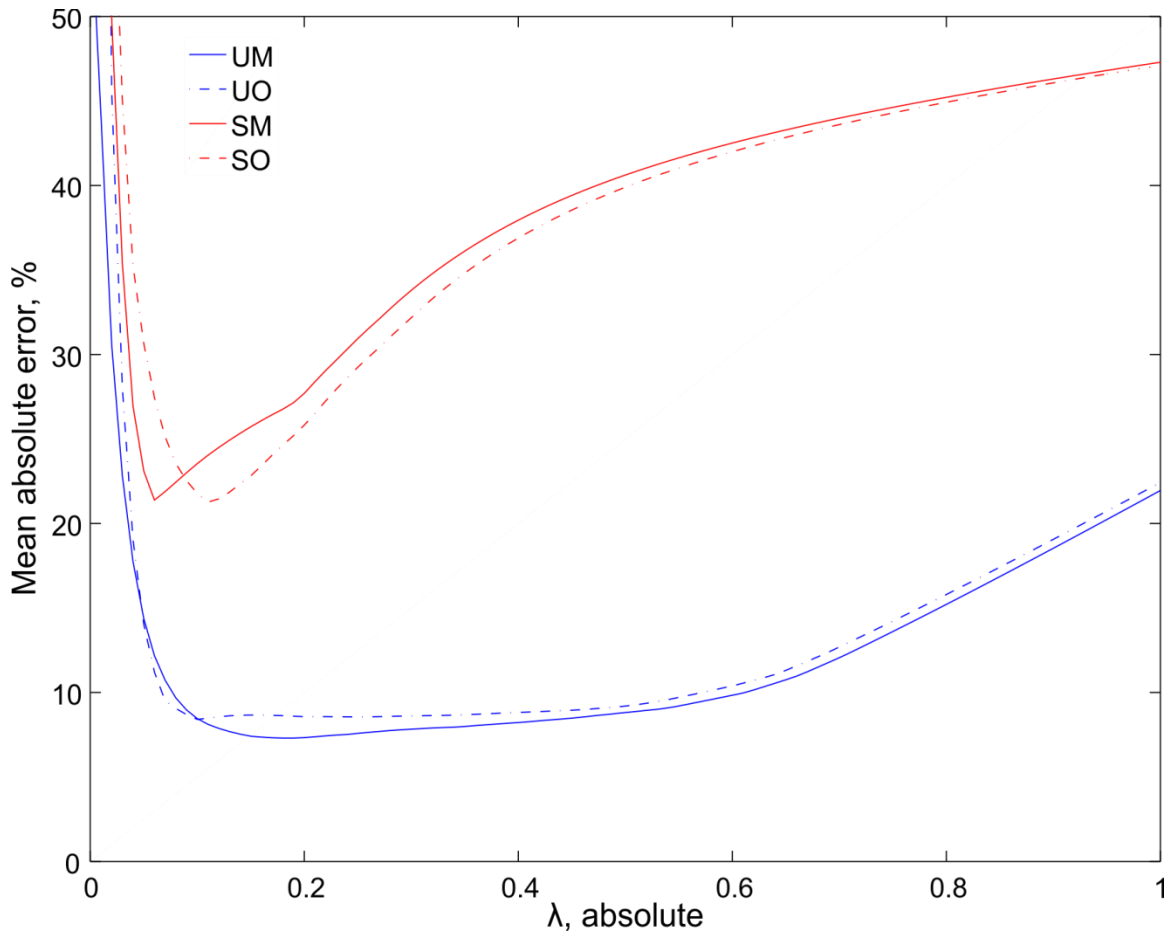


Figure 4.49 – Percentage MAE against regularisation parameter for uniform (U) and step-changing (S) problems, solved using measured (M) or simulated (O) partial magnetic fields.

Since the circuit consists of known resistors, it can be modelled accurately to generate simulated partial currents. Therefore the advantage of using measured partial fields to solve the real current distribution problem is (a) eliminating positional errors in the sensor array *e.g.* due to warped PCB mounting and (b) eliminating repeatable errors due to the sensors, such as non-ideal sensor gain. The reduction in minimum (best) MAE appears to be modest (see

Table 4.3). This suggests that the effects of the positional errors are small in this case.

Problem type	Best MAE, measured partial $B$	Best MAE, simulated partial $B$
Uniform	7.302 %	8.408 %
Step-changing	21.385 %	21.263 %

Table 4.3 – Minimum MAE against problem type and method of obtaining partial fields.

A comparison between the measured basis method and an entirely simulated problem of the same geometry is shown in Figure 4.50. For convenience of plotting, regularisation parameter  $\lambda$  is plotted here as a multiple of the corner found by the L-curve method, as the parameter required for the simulated problem is approximately  $10^4$  times less than that for the measured problem. The poor performance of the measured partial data in

Table 4.4 suggest that any discrepancy between the simulated and measured performance could be due to some time-varying error, or error in positioning the circuit in between successive partial field measurements.

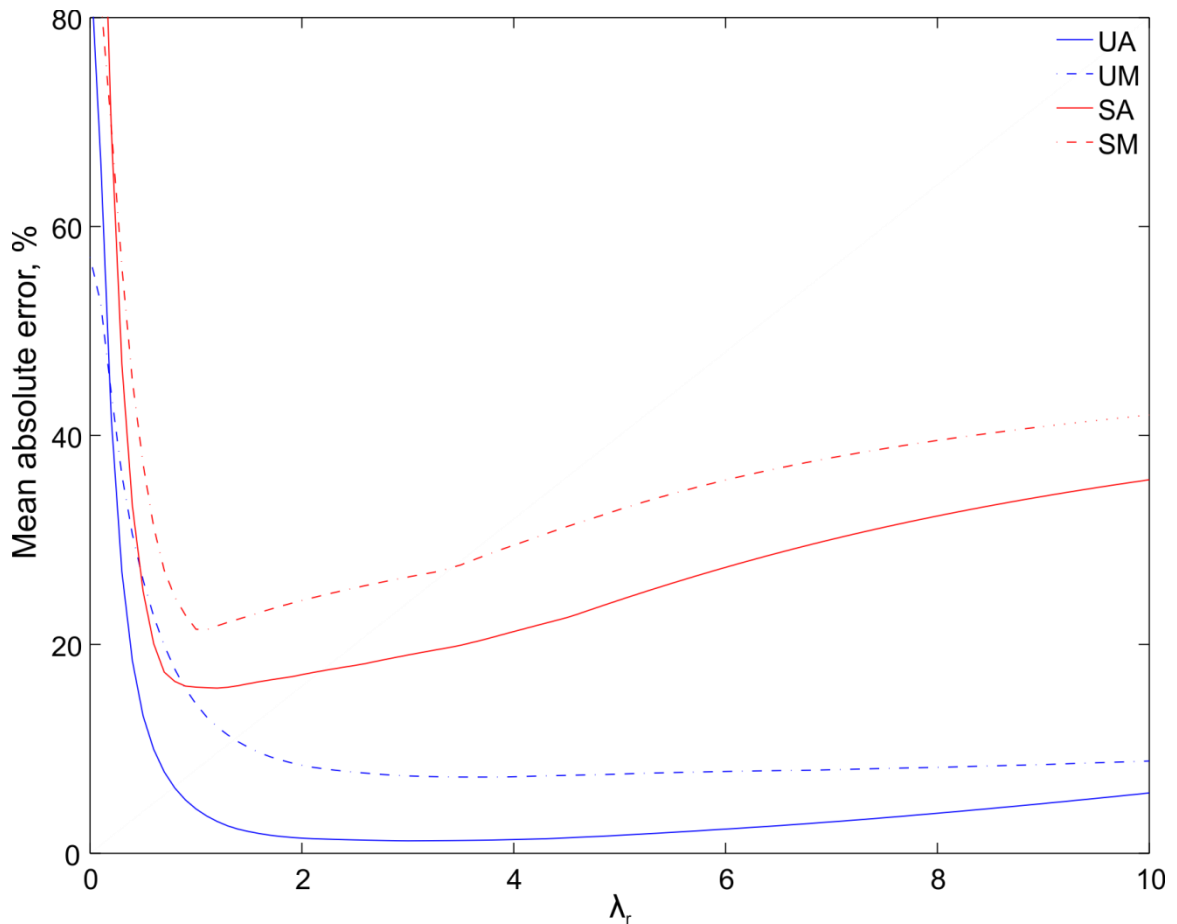


Figure 4.50 – Mean absolute error against relative regularisation parameter size, comparing the simulated data problem against measured data problem.

Problem type	Best MAE, simulated problem data and partial data	Best MAE, simulated problem data and partial data, quantized	Best MAE, measured problem data and partial data
Uniform	1.198 %	2.01 %	7.302 %
Step-changing	15.820 %	16.381 %	21.404 %

**Table 4.4 - Minimum MAE against problem type for simulated and measured problems.**

The results in Table 4.4 show that there is a significant difference between the simulated and measured problems in terms of MAE. Quantizing the  $\mathbf{B}$  field data for the simulated problem by the same amount as is done in the analogue to digital converter of the magnetic sensor (set to a resolution of  $2.27 \text{ mG lsb}^{-1}$ ) increases the best MAE for the simulated problem by a modest amount, but is not enough to entirely explain the error present in the measured data.

#### 4.3.7 Alternative sensor placements and increased resolution

An arrangement of sensors covering 6 sides of a box which encloses the cell under test is also simulated. This arrangement is shown in Figure 4.51. The spacing in between the cell and sensor box faces is set to 20 mm on all sides (the same as the  $y$  direction spacing for the 2-dimensional sensor array previously described). Since decreased sensor spacing is also a potentially interesting modification to the sensor array, the performance of the ‘box’ and the ‘flat’ arrangements will be compared across a range of sensor spacing distances. The cell is first represented by a wire grid (Figure 4.51) rather than a quasi-continuous resistive model. A quasi-continuous model is then simulated (results presented in Figure 4.57).

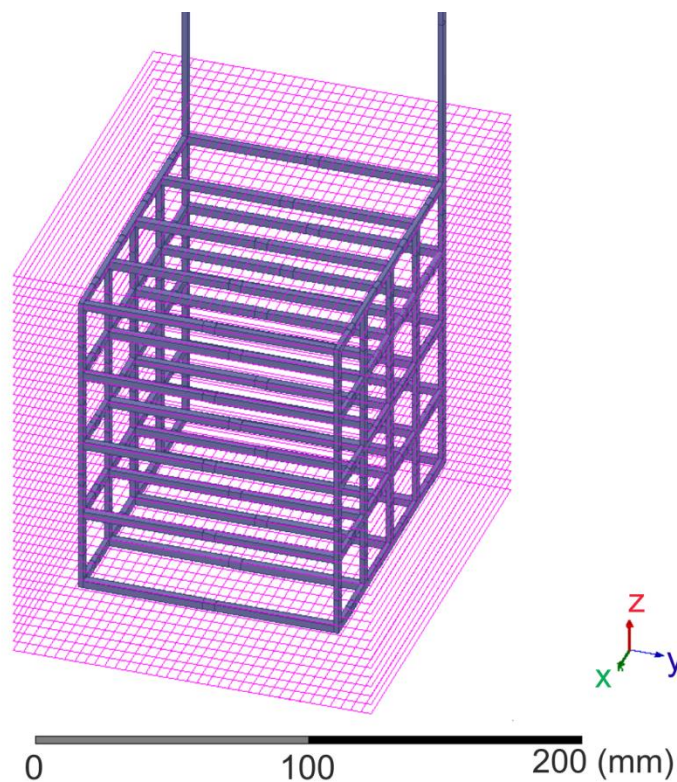


**Figure 4.51 – Sensors arranged in a box around the wire grid cell model, sensor positions indicated by pink lines**

A comparison between the solver performances with the two sensor arrangements is shown in Figure 4.52. The rapidly spatially varying field around the terminal wires causes simulation

errors in the magnetic field in this region and therefore care must be taken to exclude any sensor positions which are too close to the wires. To avoid the erroneous readings near the terminal wires the top face of the sensor box is excluded, leaving 5 remaining sides forming an open box shape around the cell. The sensor separation is 8 mm vertically and horizontally for both arrangements. The plate resistances are known and uniform. The box of sensors appears to give a smoother reconstruction of the uniform current distribution than the flat sensor array here. Reconstructions of the uniform distribution are made with a range of sensor spacing distances for both the box and the flat arrangements. Figure 4.52 shows the reconstructions from the two arrangements. Once again, the 'box' arrangement gives solutions which appear smoother, but some distortion can be observed for the coarser sensor spacing. The spacing in the real sensor array is 14 mm in the  $x$  direction and 25.4 mm in the  $z$  direction, so the 16 mm and 32 mm spacing distances are of most interest in these figures. It appears that increasing resolution causes smoother reconstructions of a uniform current distribution for both the 'flat' and the 'box' arrangements. The mean absolute errors in solving these problems are presented in Figure 4.53. Plots UF and UB show the mean absolute error when reconstructing the uniform problem using 'flat' and 'box' geometry. Despite the apparently smoother reconstructions given by the 'box' geometry, the two arrangements perform very similarly across all but the most coarse sensor spacing, where the flat geometry gives a smaller error. For the non-uniform (step changing) problems, the flat geometry performs better across all sensor spacing distances tested.

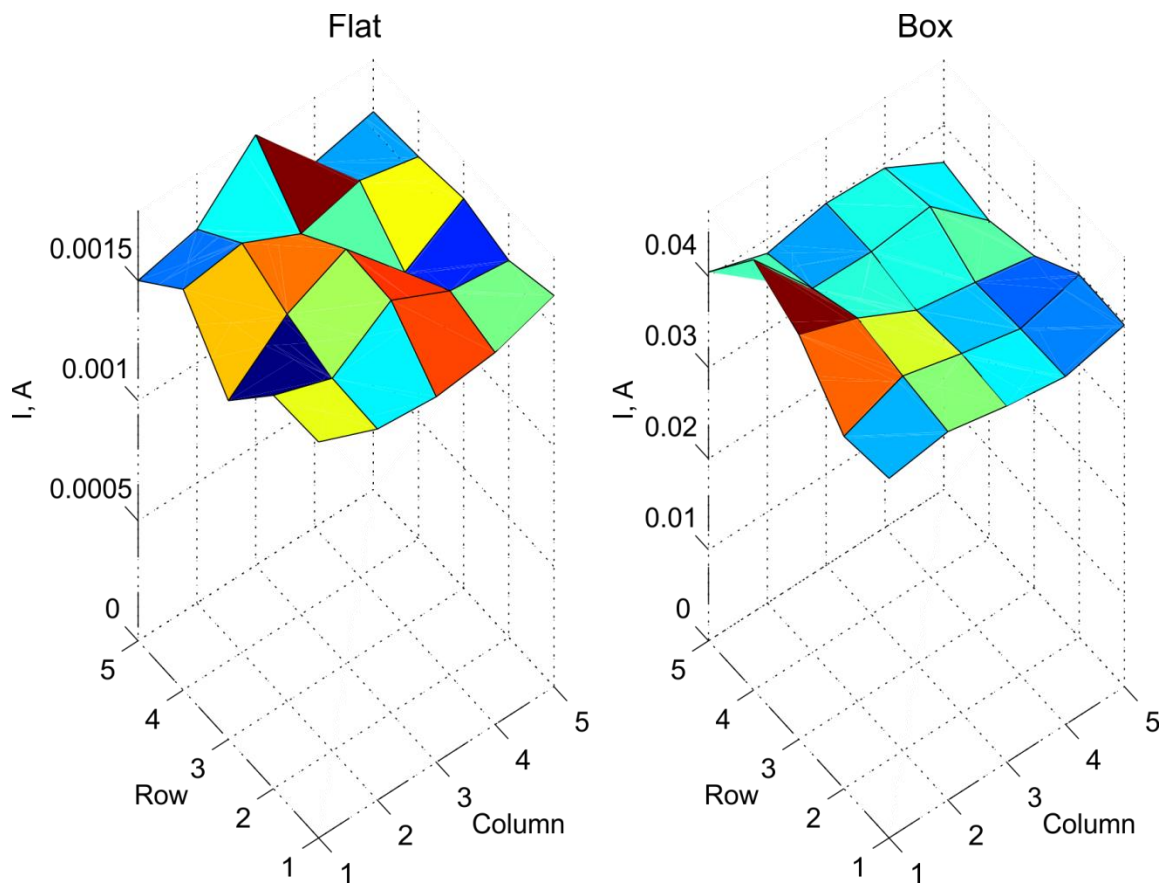
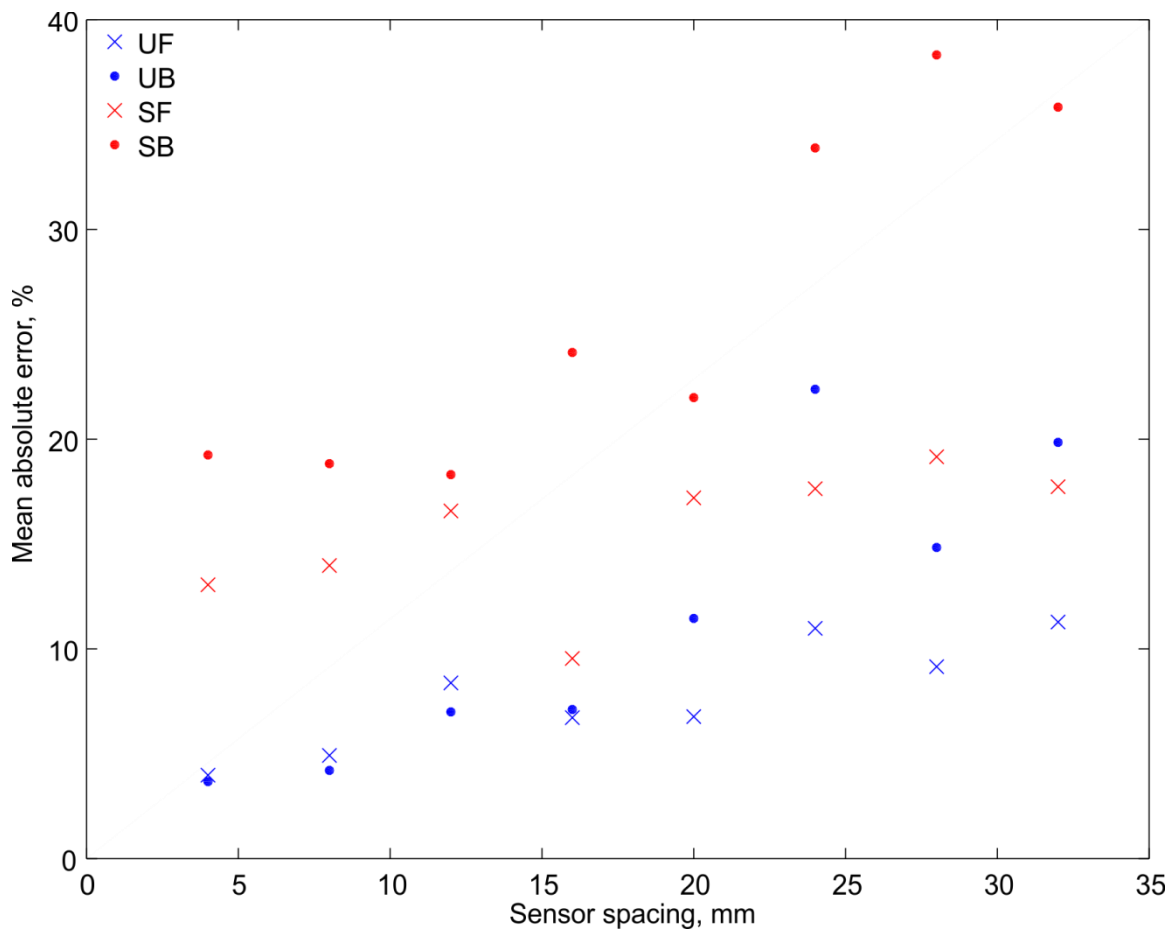


Figure 4.52 – Reconstruction of a uniform distribution using 2-dimensional sensor array (left) and a 5-sided sensor 'box' (right), sensor spacing = 8 mm (ie, finer than the real sensor array).



**Figure 4.53 – Comparison of the mean absolute error against sensor spacing, for uniform problems (UF, UB = uniform flat, uniform box respectively) and non-uniform problems (SF, SB = step changing flat, step changing box respectively).**

Application of special basis projection to the lead acid cell problem involves dealing with incorrectly modelled plate resistances. Incorrect plate resistances are tested for the ‘flat’ and ‘box’ arrangements, again attempting to reconstruct the uniform and the step changing current distributions. Inspection of Figure 4.54 suggests that the ‘box’ arrangement provides a better reconstruction, with less of the saddle shape present than in the reconstruction using the flat arrangement of sensors. Figure 4.55 shows the mean absolute error for uniform and non-uniform problems, ‘flat’ and ‘box’ arrangements. This time the ‘box’ arrangement provides smaller errors than the ‘flat’ arrangement across all sensor spacing distances below approximately 20 mm. A possible reason for the poor performance at the largest sensor spacing could be the relatively smaller faces of the sensor ‘box’ compared to the flat sensor array, meaning that an insufficient number of sensors are present on each face when the spacing becomes larger.

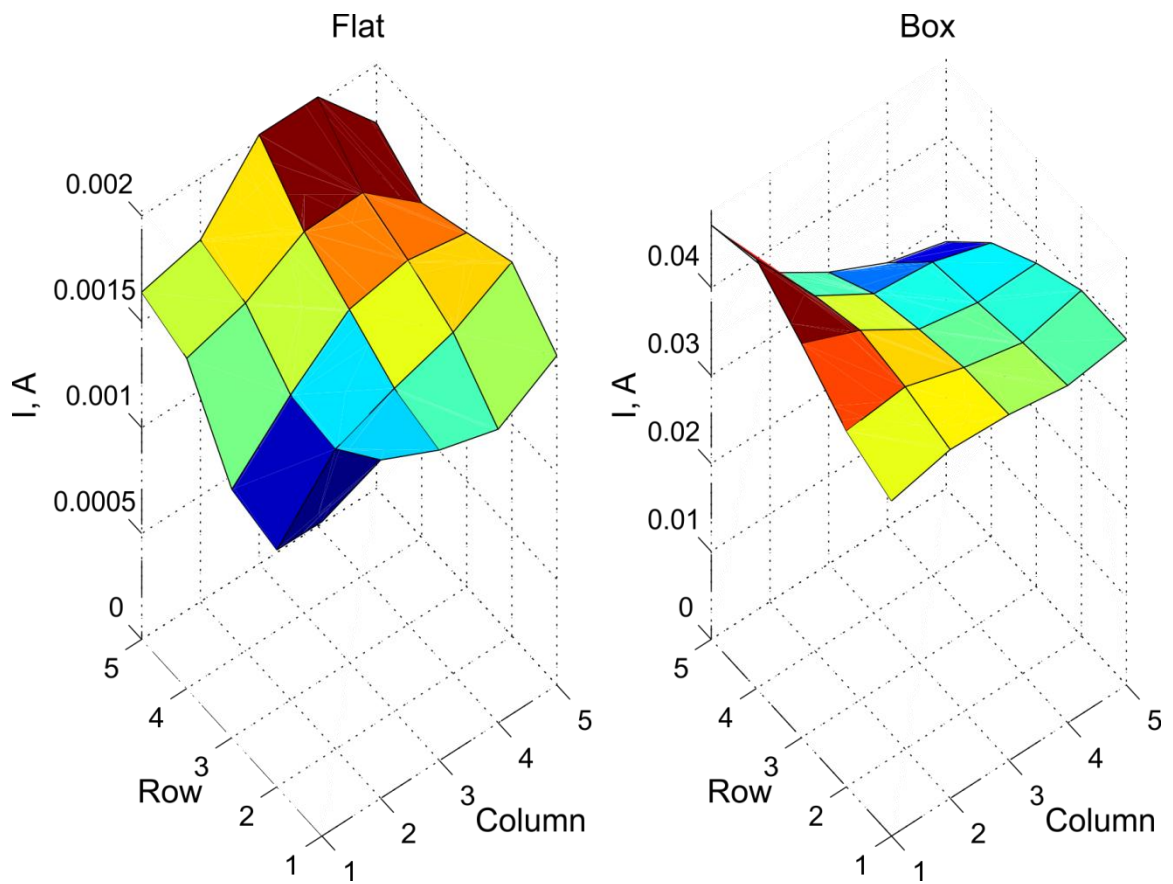


Figure 4.54 - Reconstructions of the uniform current distribution using two different sensor arrangements, where plate resistances are not known correctly. Sensor spacing = 8 mm.

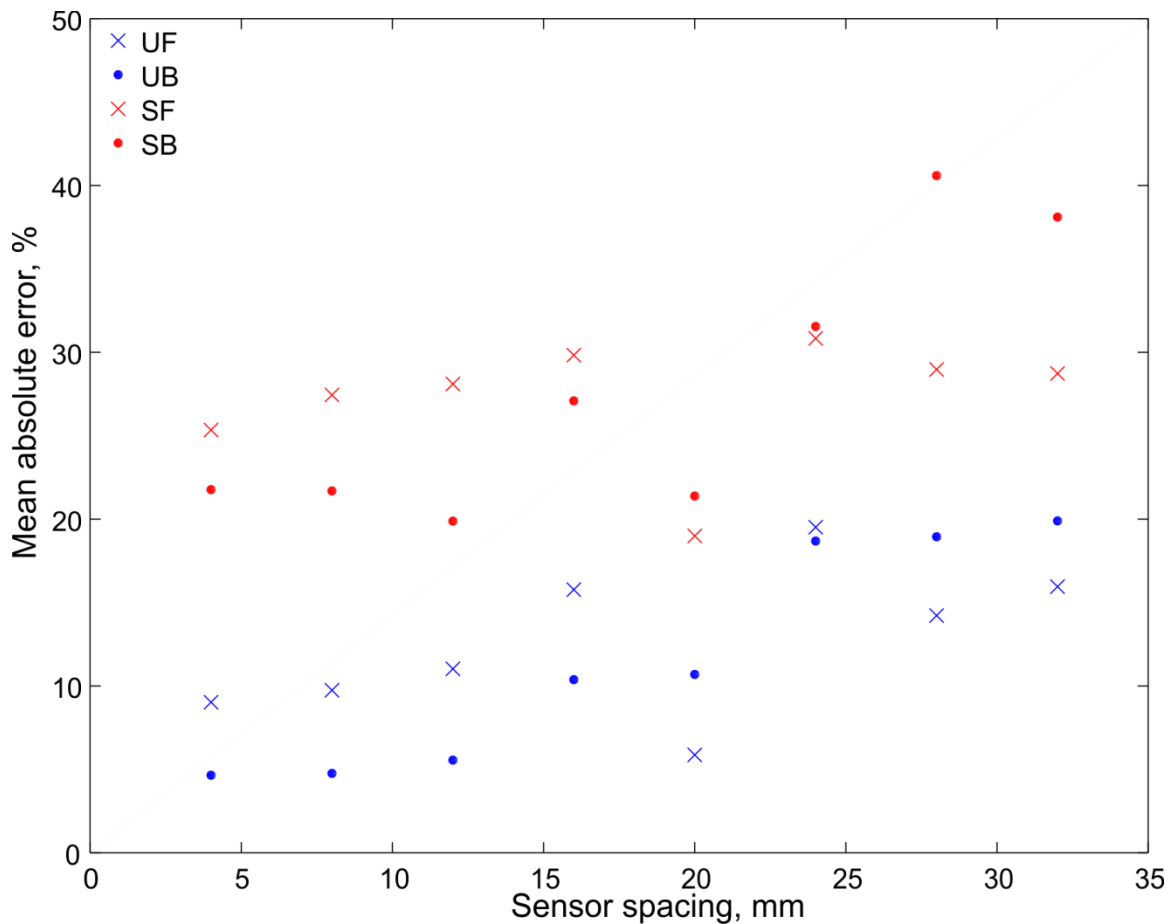


Figure 4.55 – Mean absolute error against sensor spacing for uniform flat (UF), uniform box (UB), step changing flat (SF), step changing box (SB).

It is likely that a quasi-continuous finite element Ansys model may be used rather than a wire mesh Octave model. The quasi-continuous model has been described previously but a diagram is included here for ease (Figure 4.56). Figure 4.57 shows the mean absolute error against sensor spacing and sensor arrangement (flat or box) and current distribution (uniform or step changing). The plate resistance is known to the solver. Contrary to the results for the discrete resistor wire model (Figure 4.53), the 'box' arrangement of sensors outperforms the 'flat' arrangement over all sensor spacings and on both current distributions. Furthermore, the difference in MAE between the finest (4 mm) and coarsest (32 mm) sensor spacing is only  $(15.944\% - 11.697\%) = 3.64\%$  for the 'box' of sensors on the step change problem. For the flat sensor arrangement the corresponding difference in MAE is  $(29.146\% - 15.343\%) = 13.803\%$ . These results suggest that when designing a sensor arrangement, if total number of sensors were constrained, then it would be worthwhile positioning the sensors around the cell in a box rather than using a flat array of sensors.

To evaluate the performance of the quasi-continuous model when plate resistance is not known, a model of the plates based on that in [27] is again used. The partial currents and magnetic fields are generated using a model where the plates are assumed uniform, and the simulated current and magnetic field to be solved are generated using the non-uniform grid model. Figure 4.58 shows the percentage MAE for uniform and step-changing problems solved by flat and box sensor arrangements. Again the uniform distribution is solved more accurately than the step changing one. On the uniform problem, MAEs below approximately 10 % are achieved with the 'box' arrangement for sensor spacings below 20 mm. MAEs below 20 % are achieved for all sensor spacings with the flat arrangement. Interestingly the flat arrangement appears to outperform the box arrangement on the step-changing problem, although both are quite poor at between 37 % to 50 % MAE.

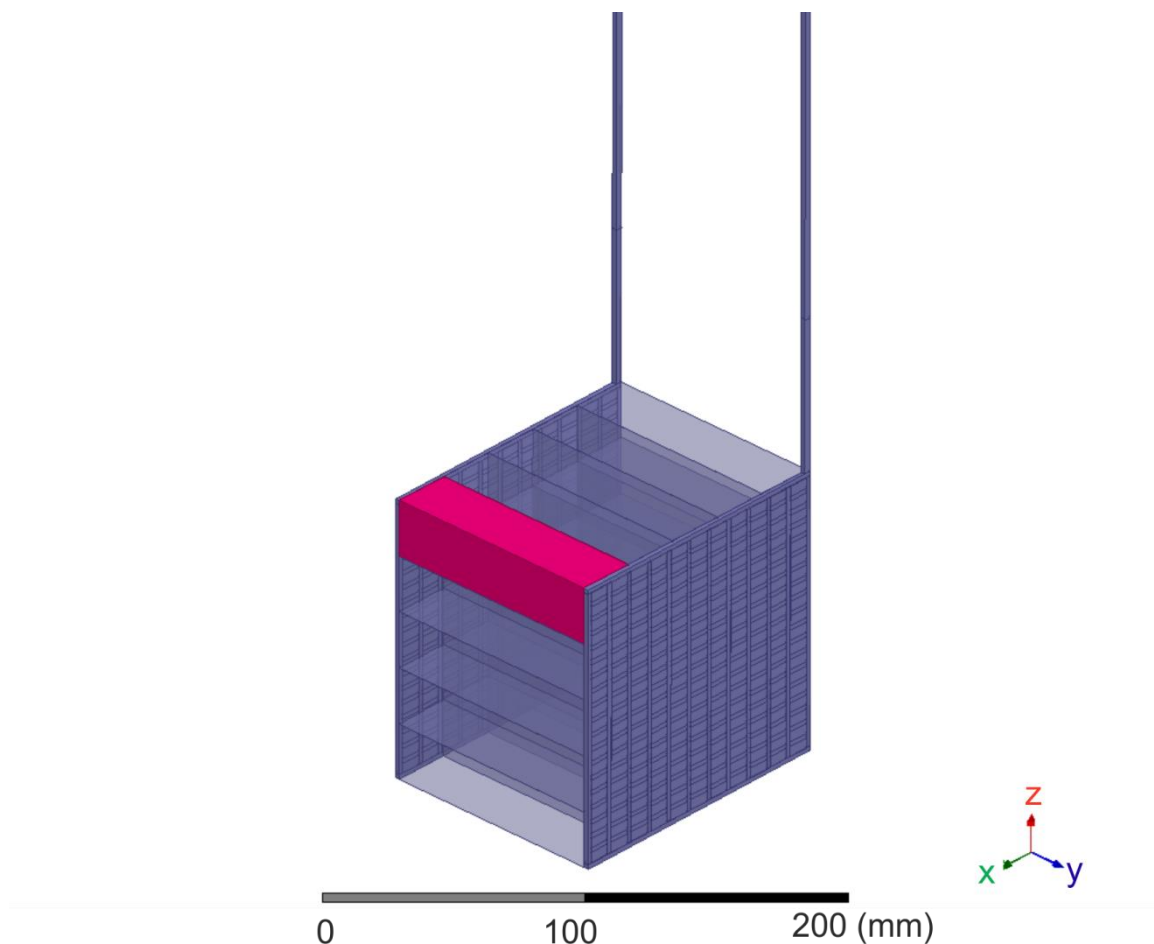


Figure 4.56 – Cell with electrolyte divided into 25 segments with first segment highlighted.

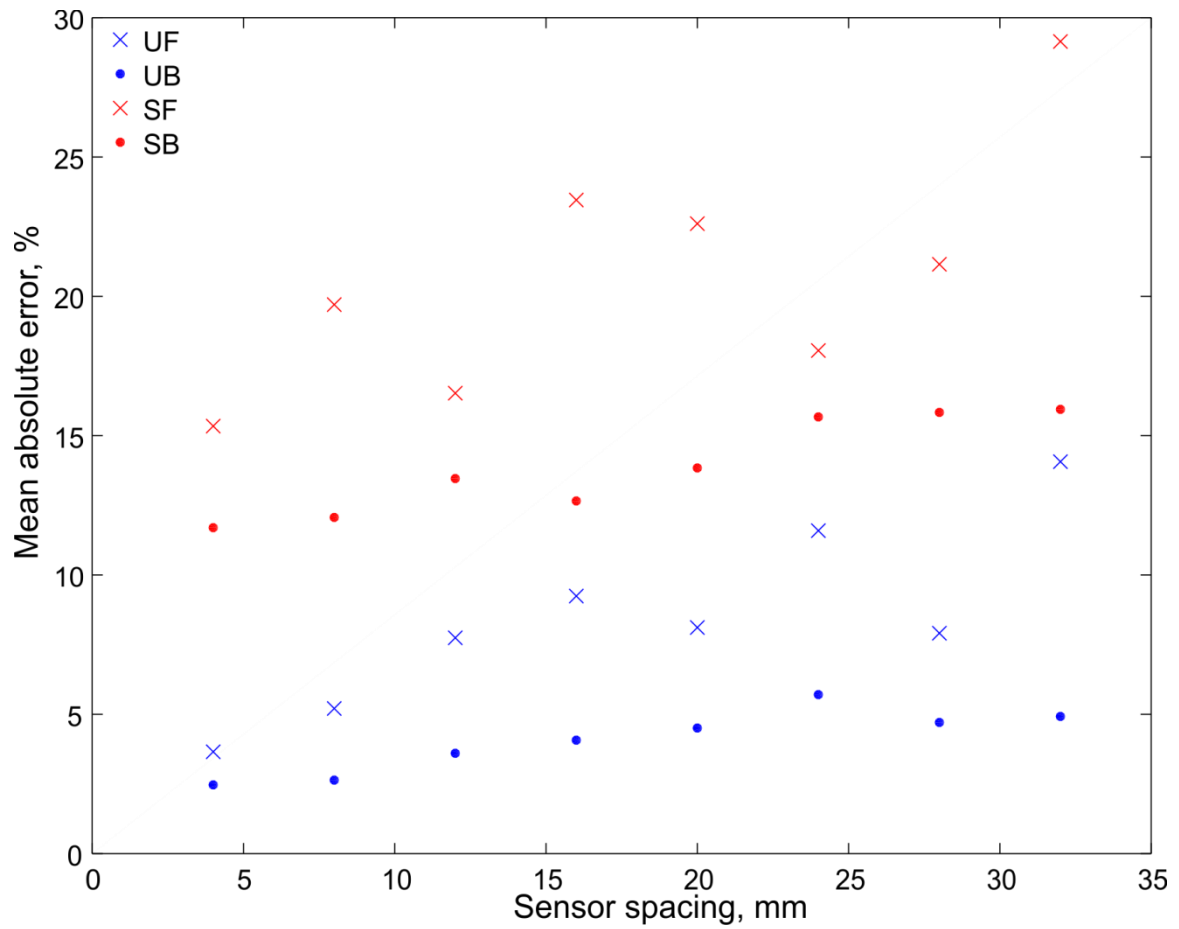


Figure 4.57 – Mean absolute error against sensor spacing for uniform flat (UF), uniform box (UB), step changing flat (SF), step changing box (SB). Quasi-continuous model.

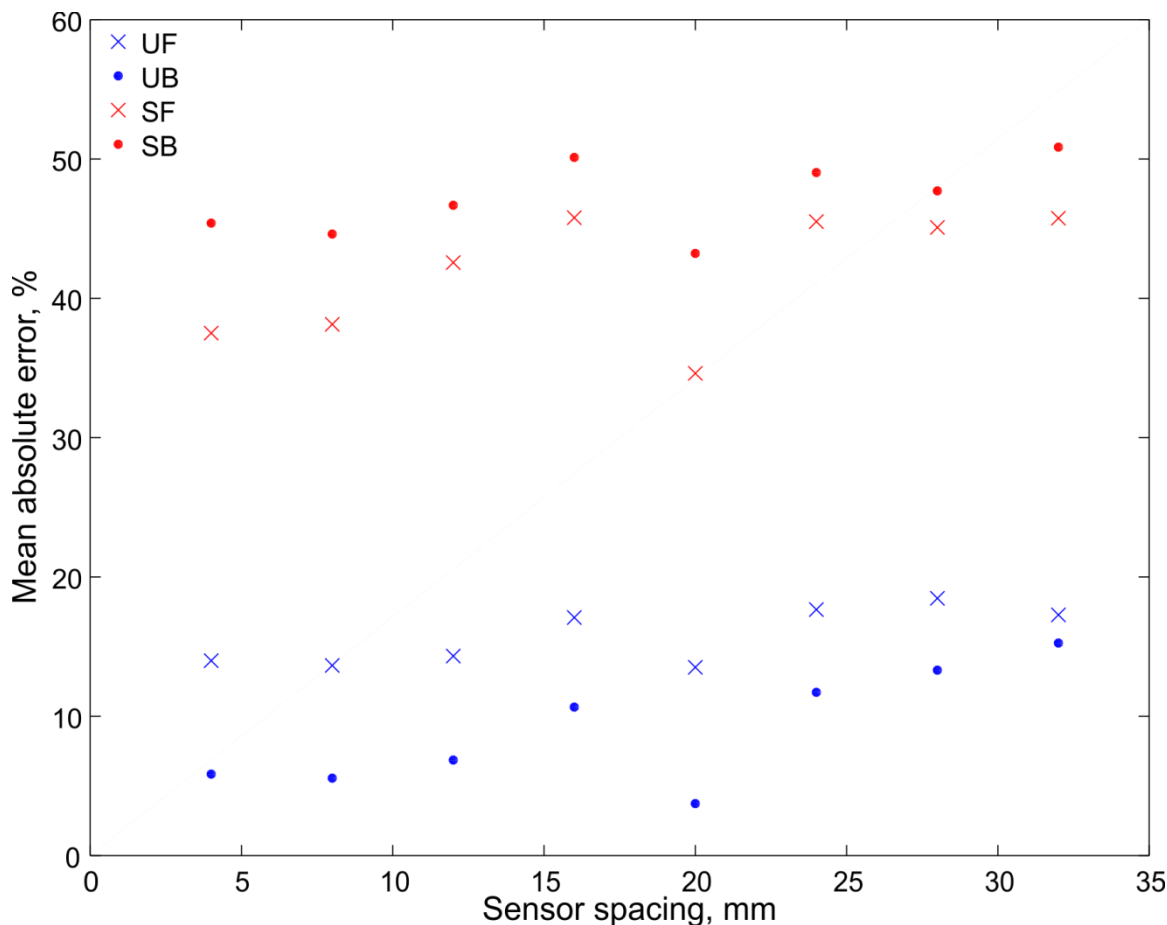


Figure 4.58 - Mean absolute error against sensor spacing for uniform flat (UF), uniform box (UB), step changing flat (SF), step changing box (SB). Quasi-continuous model, where partial currents are generated using an (incorrect) uniform plate model, and the problem data is generated using a non-uniform grid model of the plates.

#### 4.4 Summary of Chapter 4

The inverse of the coupling between a current and the magnetic field near to it has been explored from a practical perspective. Appropriate constraints applied to the forward model were found to be very important for obtaining an accurate reconstruction of the current distribution in a circuit having battery-like geometry. A 3D circuit model where the electrolyte currents are partitioned and treated as independent was found to be useful for reconstructing the electrolyte current distribution.

It has been shown that a 3D circuit model may be replaced with a 3D finite element model, allowing better representation of the cell geometry and materials than in a basic resistive circuit model. This incurs a computational cost and was not solved as accurately as a 3D circuit model, but it is likely that the practical considerations of being able to model a real cell outweigh these disadvantages.

The conductance distribution of the cell may be unknown. It has been shown that some uncertainty in the model may be compensated for by employing an extended basis, where a complete set of partial currents and magnetic fields was generated for the limits of each variable in the conductance distribution. Results were reported for a 3D circuit model where the ratio  $r_x/r_z$  is variable, and a finite element model where the conductance of the cell 'active mass' material is variable.

The solver and existing magnetic sensor array were combined to solve the current distribution in a 2D and a 3D circuit, showing that the solver is sufficiently robust for the measurement errors which occur in practice. Finally, alternative sensor placements were simulated which identified some cases in which the existing sensor array layout may be improved upon.

## 5 Development of Flow-Through Sensor

In this chapter an instrument is described for the invasive method of measuring the current distribution in a lead acid test cell. A more direct method of measuring electrolyte current distribution than magnetic tomography is required for verification of the magnetic tomography system. This sensor is designed to serve that purpose. The rest of the hardware setup used with this instrument is presented in Chapter 3, and the experimental method is described in Chapter 6.

Prior to the design of this instrument some preliminary work using a pair of reference electrodes was completed and this may be found in Section 3.3.1. However the use of reference electrodes was not suitable to provide conclusive agreement or disagreement with an experimental magnetic tomography system. The method using reference electrodes yields spatially resolved voltage measurements with this system by imposing repeated current pulses on the cell, with the electrodes in a different vertical position each time. A measurement is taken with the electrodes in the first vertical position. The electrodes are then moved vertically to the second vertical position and a second current pulse of the same magnitude and duration to the first is applied. This process continues for as many positions as desired, with a trade-off between spatial resolution and avoiding unwanted fatigue effects showing in the measurements due to repeated pulsing. A system which can instantaneously measure current distribution without having to repeat the pulses would allow measurements to be temporally and spatially resolved. This is desirable in a system such as a lead acid cell, which consists of time-varying processes of varying length, such as diffusion of ions and electrolyte stratification.

A promising system to achieve a simultaneous spatial measurement is to use an array of magnetic cores and sensors, with apertures through which ionic currents can pass. This type of system was first used for studying electrochemical cells by Wieser *et al.* [67]. In this chapter, alternative core designs are investigated in order to maximise electrolyte flow area and provide consistent magnetic field for a given current. The array of cores and sensors is integrated with a PC using a microcontroller so that measurement data may be rapidly saved, allowing current distribution measurement that is resolved in both space and time.

## 5.1 Simulation of Single Transducer

A derivation of the approximate magnetic field in the airgap is given in 2.2.7. A 2D finite element simulation, using FEMM, is used to test this approximation. Figure 5.1 shows a model consisting of a pure iron core with airgap and a copper conductor. Surrounding these materials is air. The current density is  $1 \text{ MA m}^{-1}$  and the area of the copper is  $1 \times 10^{-6} \text{ m}^2$ , giving a total current of 1 A. The airgap is 0.2 mm. According to (2.13) this gives a magnetic field strength,  $h$ , in the airgap of  $5000 \text{ A m}^{-1}$ . Figure 5.2 shows  $h$  as a colour plot. Magnetic field strength,  $h$ , is mostly concentrated in the airgap (simulated maximum is approximately  $4960 \text{ A m}^{-1}$ ) with some fringing above and below the airgap.

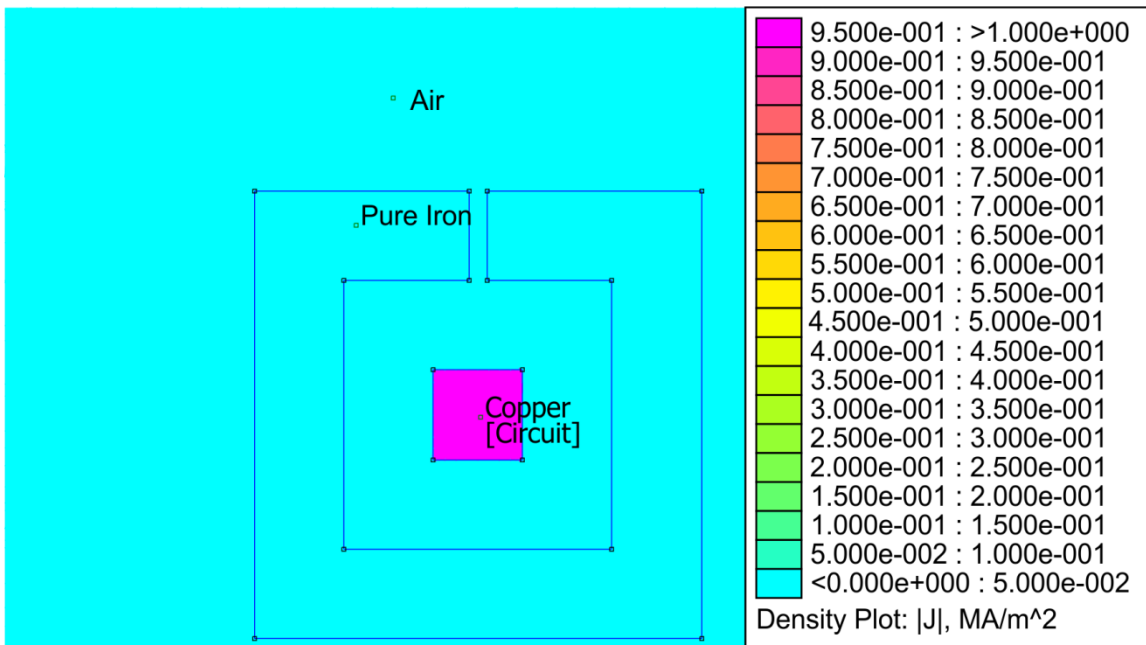


Figure 5.1 – 2D magnetostatic simulation (FEMM), showing current density through centre of magnetic core.

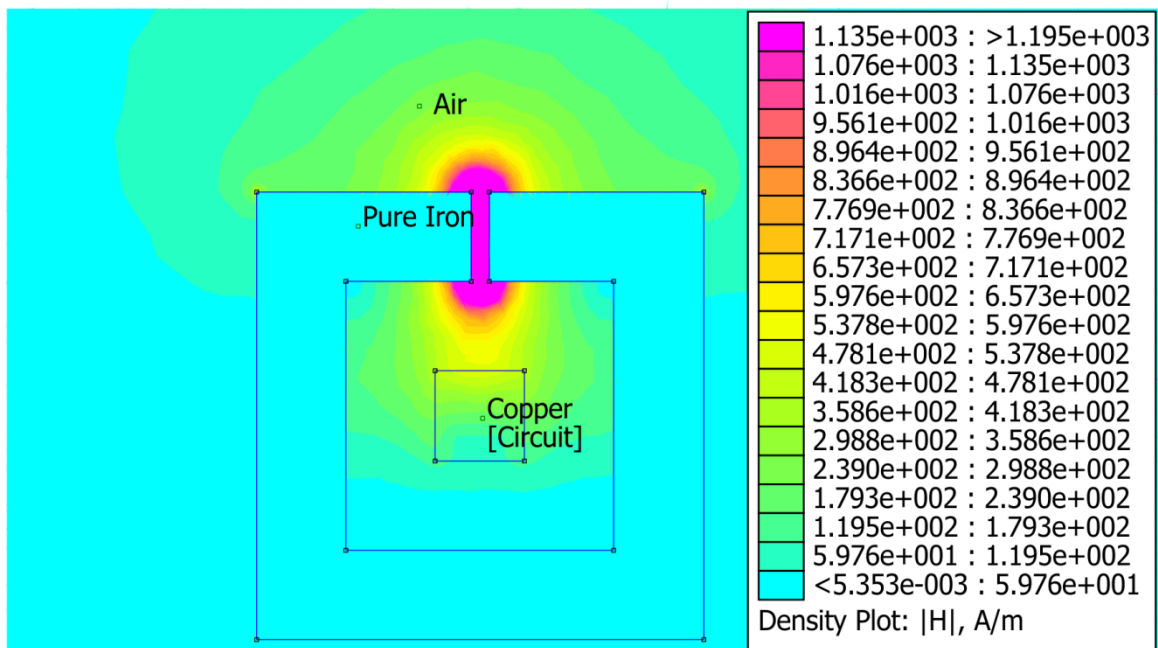


Figure 5.2 - Colour plot of magnetic field strength in magnetic core and airgap due to current density shown in Figure 5.1.

## 5.2 Design Development

### 5.2.1 Core layout

The design reported by Wieser *et al.* requires some re-design in order to be suitable for use with automotive lead acid cell plates. Their current distribution sensor is used with a large polymer electrolyte fuel cell with electrode measuring 190 mm × 304 mm, which they split into a 5 × 8 grid, so that each sensor may be up to 38 mm × 38 mm. To study the cell taken from the Shield 027 battery (plate size 144 mm × 104 mm) with segments of this approximate size would yield a 4 × 3 grid of segments. To achieve any higher resolution some miniaturisation is required.

In order to maximise aperture area for a given segment size, a rectangular core shape is proposed rather than the toroidal cores reported in the literature. A bespoke core is also necessary to obtain a good fit with the pre-built cell plates under test. A wire eroder may be used to cut custom shapes from laminated electrical steel (Cogent M330-35A [100], [101]). Wire eroding electrical steel is a commonly used technique in the construction of electrical machines, and so constructing the cores in this way can be performed to a good standard by an appropriately trained technician. Cutting ferrite, by contrast, was found to be difficult due to its brittleness. Figure 5.3 shows some of the important dimensions when fitting a rectangular core grid to the cell plate. The total available aperture area is the area of one

aperture multiplied by the number of apertures. The iron cores and any required electronics in the sensor are likely to be susceptible to corrosion by the sulphuric acid electrolyte and so some lining of the inside of the apertures is necessary. The thickness of this lining will affect the aperture dimensions. The thickness of the core will also affect aperture size. The core may be designed with variable thickness. Aperture area may be further increased making the external dimensions of the core greater than those of the plate, so that some (but not all) of the outer frame of the core overlaps with the plate area.

Some overlap between the plate and the core's outer frame is retained, in order to ensure that the apertures are each placed centrally within the cross section of an electrolyte segment. For example, if the inner horizontal members have a thickness  $c_h$ , then an aperture on the top row will lose  $c_h/2$  from its height due to the inner horizontal member below it. The outer horizontal members are then overlapped by  $c_h/2$  as well, to ensure that they have the same effect on aperture dimensions as the inner horizontal apertures. The segmentation of the cell's cross section area is shown in Figure 5.3 – notice that all apertures have the same area, all segments have the same area, and all apertures are centralised with a plate area segment.

For apertures centred over plate segments, the aperture dimensions  $w_{aperture}$  and  $h_{aperture}$  are given by (5.1) and (5.2), where  $w_{plate}, h_{plate}$  are the width and height of the cell plate,  $c_v, c_h$  are the thicknesses of the inner vertical and horizontal core members, and  $c_{plastic}$  is the thickness of the plastic lining used to protect the inside of the cores. For a given plate width and segmentation,  $w_{aperture}$  is maximised by minimising  $c_v$  and  $c_{plastic}$ . The same argument applies to  $h_{aperture}$ . However,  $c_{plastic}$  is constrained by available materials and construction methods.  $c_h$  is constrained by the width of the sensor that is inserted into the airgap;  $c_v$  may be thinner than  $c_h$  as it does not contain the magnetic sensor, but it must have sufficiently low reluctance for the magnetic circuit to focus the field effectively.

As a first approximation, an acceptable fraction of plate area to be obscured by the sensor array is taken to be < 50 %. The sensor size (Section 5.2.3) yields  $c_h = 5$  mm, and a conservative value of  $c_v$  may be taken as 3 mm. A suitable plastic lining (Sections 5.2.5 - 5.2.6) is identified, having a thickness of  $c_{plastic} = 1.5$  mm. A segmentation of  $n_{columns} = 5$  by  $n_{rows} = 4$  yields  $w_{aperture} = 23$  mm and  $h_{aperture} = 18$  mm according to (5.1) and (5.2), which gives an aperture area of  $414 \text{ mm}^2$  each, or  $8280 \text{ mm}^2$  in total, out of a total plate area of  $15080 \text{ mm}^2$ . Therefore 54.9 % of the plate area is available for current to flow through.

$$w_{aperture} = \frac{w_{plate}}{n_{columns}} - c_v - 2c_{plastic} \quad (5.1)$$

$$h_{aperture} = \frac{h_{plate}}{n_{rows}} - c_h - 2c_{plastic} \quad (5.2)$$

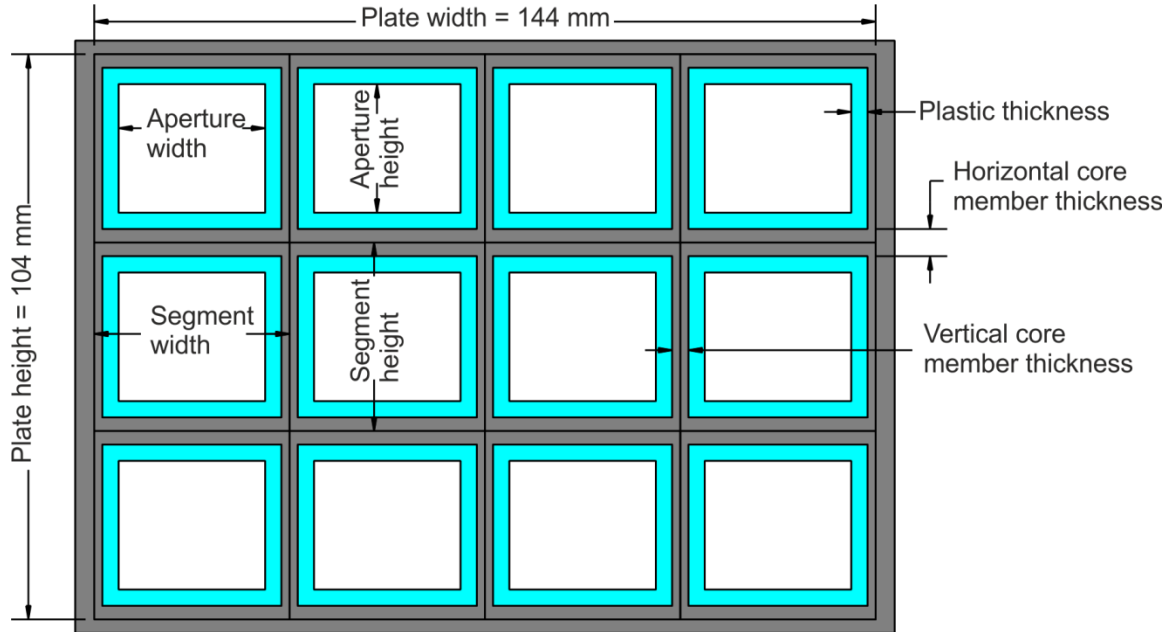


Figure 5.3 - Fitting rectangular aperture cores over the Shield 027 plate.

The grid of cores may be divided in a number of ways. Firstly, each aperture could have its own core, each arranged in the  $xz$  plane. The effective core thickness from the point of view of the aperture size is comprised of two of the single core thicknesses plus a gap in between in order to reduce magnetic flux leakage between adjacent cores (Figure 5.4). Aperture size and/or core thickness may be increased by overlapping the cores, offsetting them in the  $y$  direction (Figure 5.5). In order to overlap the cores along both their horizontal and vertical sides, they must be arranged into 4 layers, increasing the size in  $y$  of the sensor assembly.

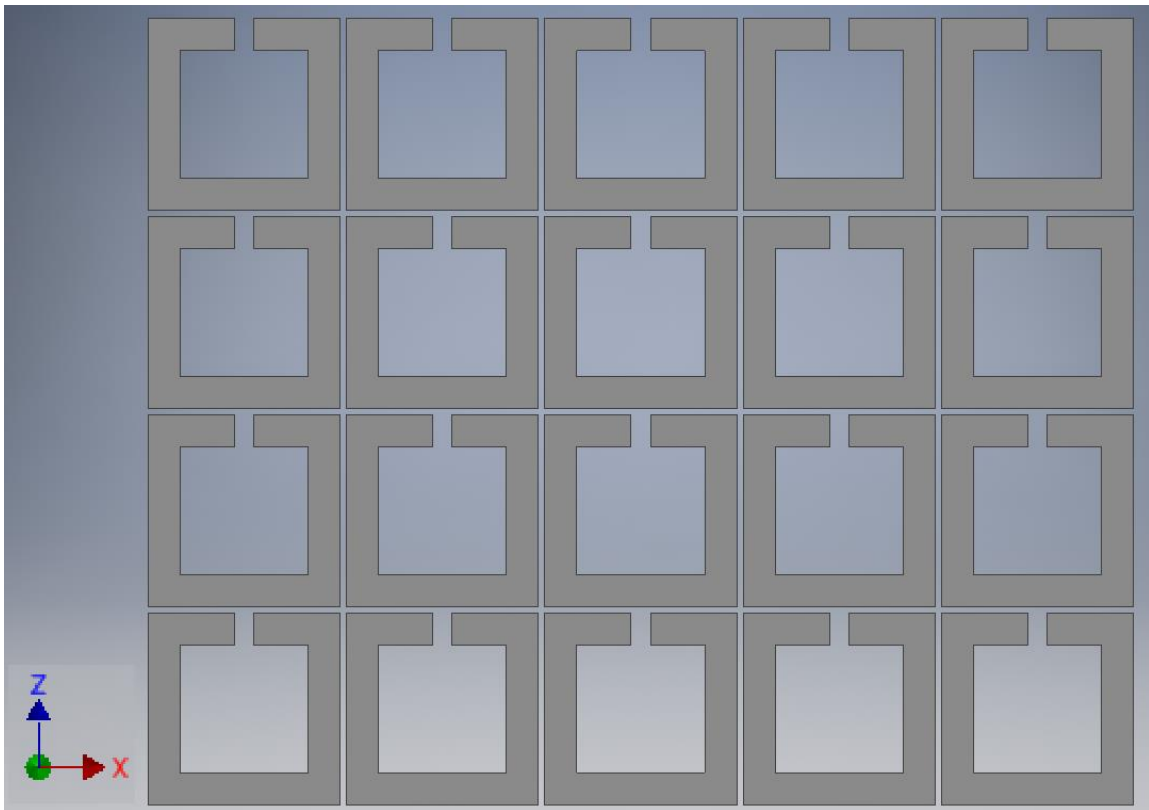


Figure 5.4 –  $5 \times 4$  grid of single rectangular cores, not overlapped.

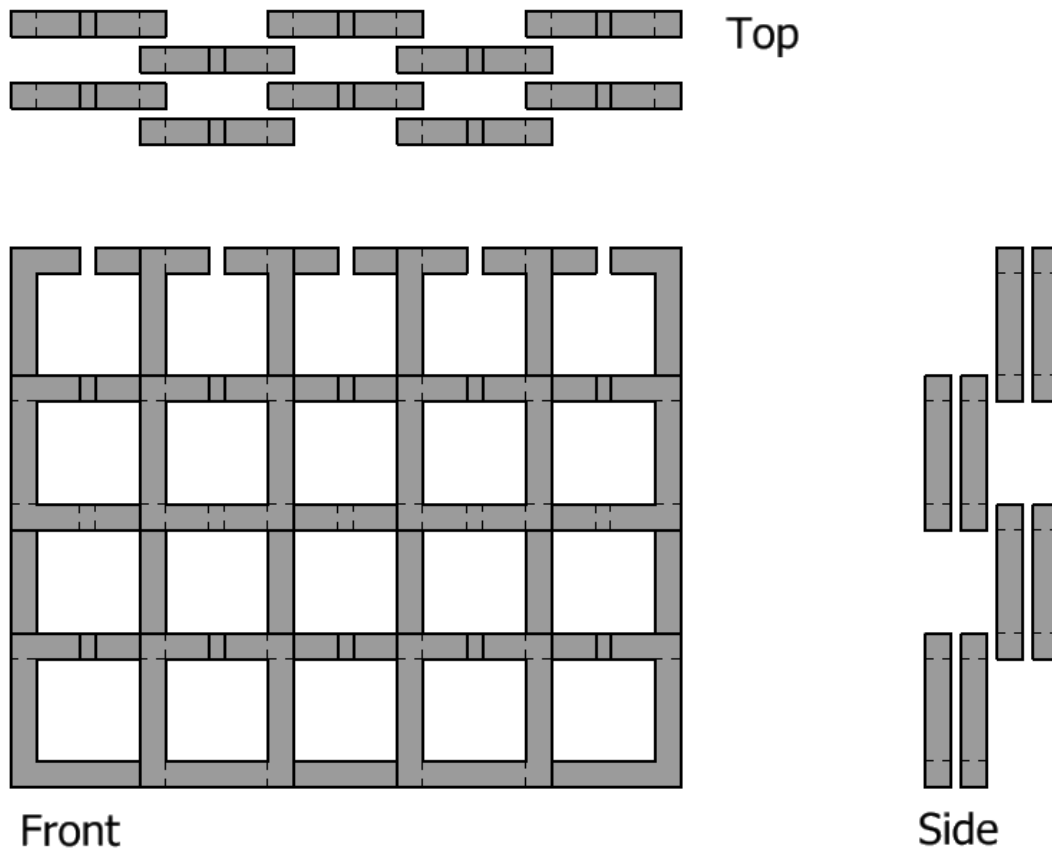


Figure 5.5 - 5 × 4 grid of single rectangular cores, overlapped.

A second option is to combine rows of cores. These rows can either be arranged in-plane (Figure 5.6) or overlapped (Figure 5.7). The vertical members of the cores are 'shared' between adjacent apertures which saves space in the  $x$  direction. Overlapping the horizontal members saves space in the  $z$  direction also, at the expense of thickness in  $y$ . Only two layers are required, so the effect of overlapping on the  $y$  size of the sensor assembly is less than when single cores are used. A further method of arranging the cores is to make the inner vertical members and inner horizontal members shared, combining all of the core segments into one piece in the same plane (Figure 5.8). This has an even smaller  $y$  dimension than the combined rows design.

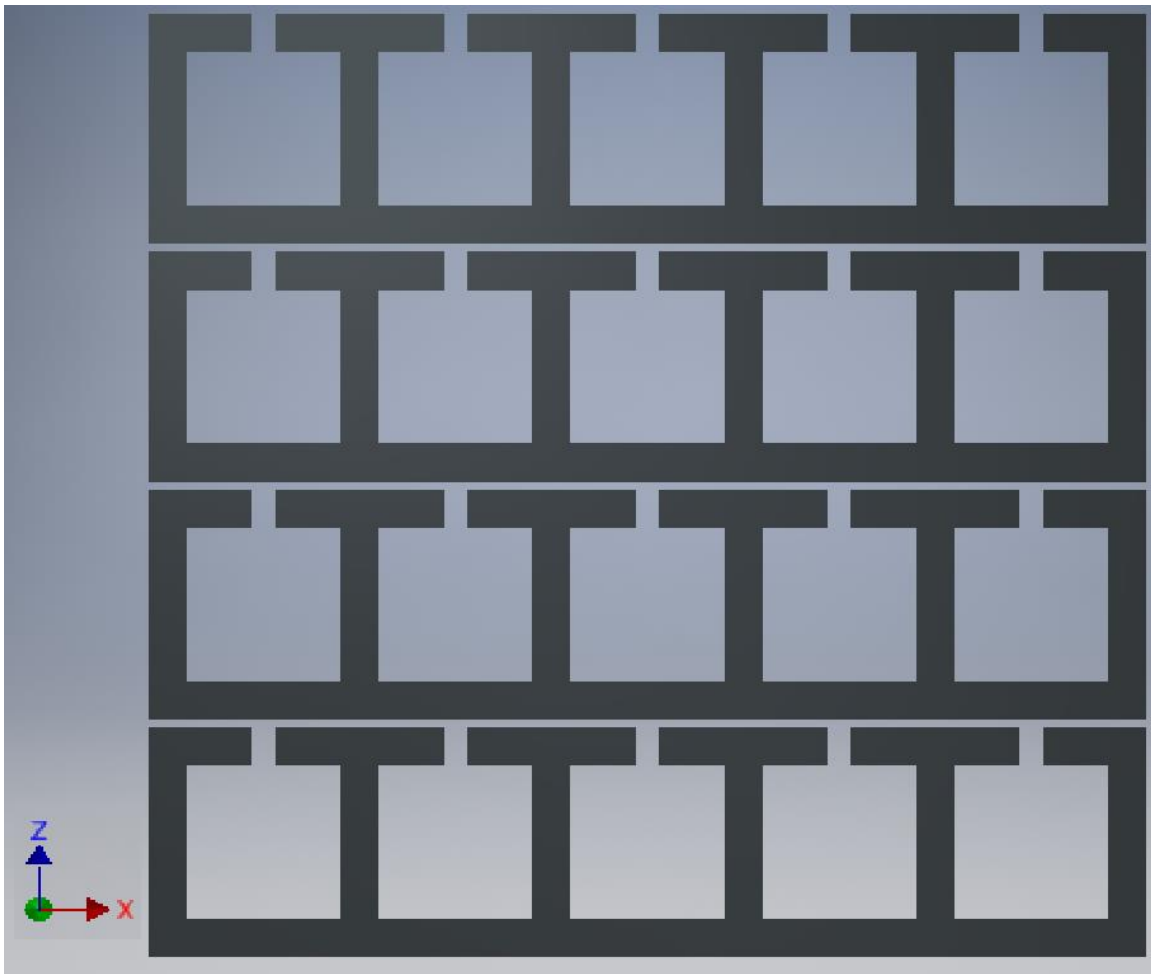
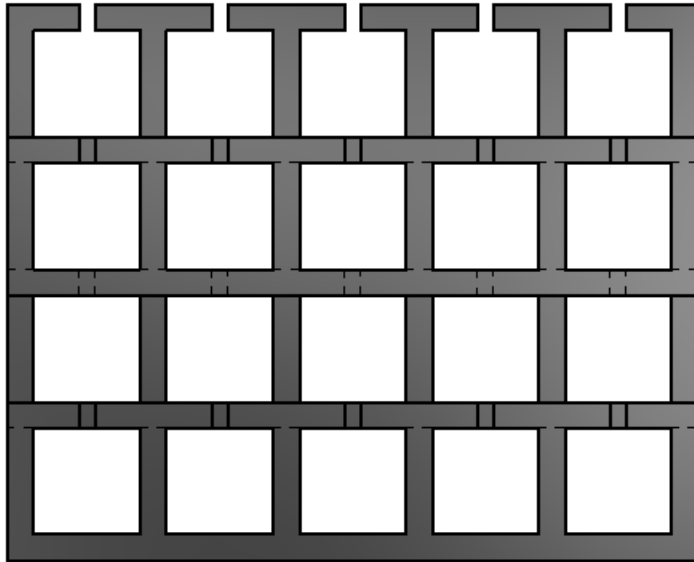


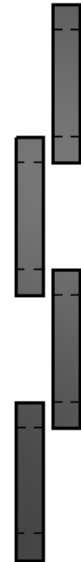
Figure 5.6 - Grid of cores, with rows combined, not overlapped.



Top



Front



Side

Figure 5.7 - Grid of cores, with rows of core segments combined. Rows overlapping.

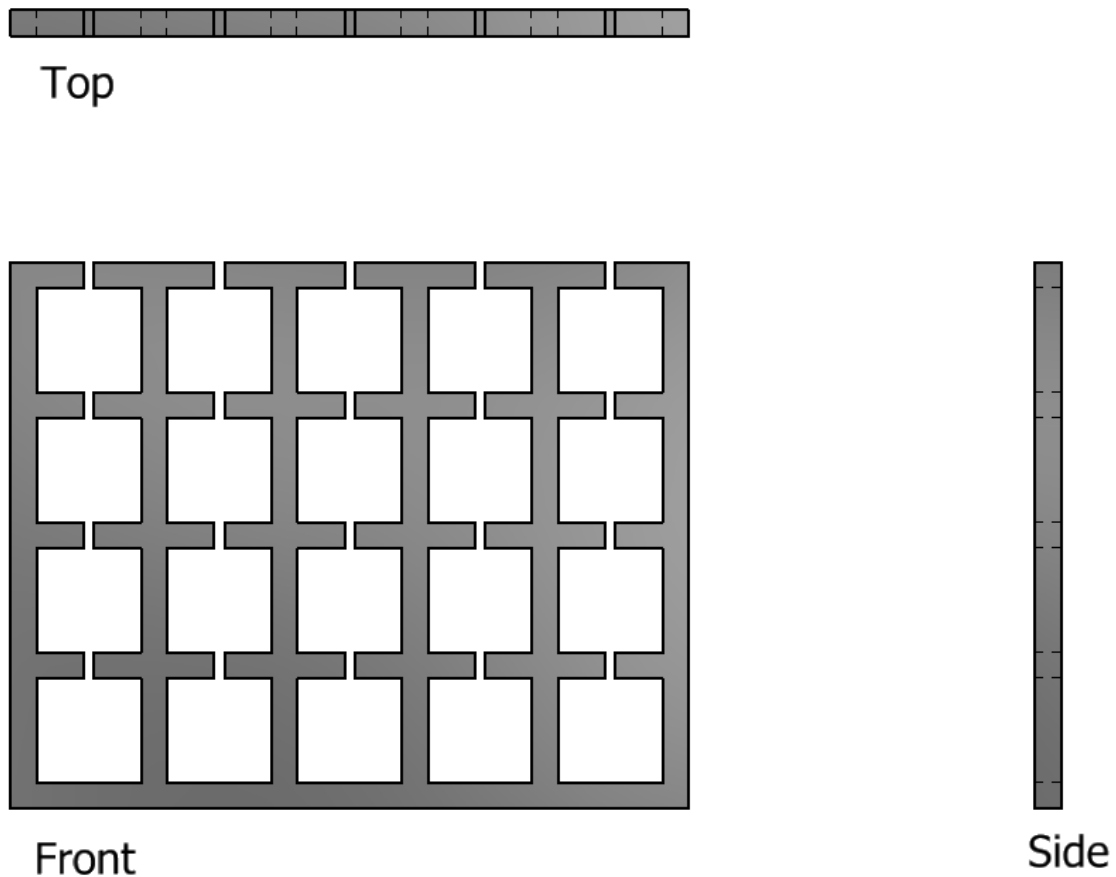


Figure 5.8 - Core segments combined into one piece.

The geometry of the combined core design is most desirable as it can fit into cells with smaller plate separation. Conversely, the individual cores design requires a greater plate separation and most likely a more complicated mounting system to hold the 20 separate cores. However, the way that flux is shared amongst the cores is different for the three core designs. The currents above and below a given aperture contribute to the flux passing the airgap above that aperture, resulting in a distribution of magnetic field strength values around the 20 airgaps which is not uniform, even when a uniform current is applied. Figure 5.9 shows an Ansys Maxwell model of the 'individual core' system in a test cell based on the Shield 027. This model is also created for the combined row and fully combined core designs. An arbitrary uniform current is passed through the cell and  $h_x$  is sampled in the centre of each airgap.

The results of this test are given in Figure 5.10. None of the distributions of magnetic fields are uniform. Compensation is required to convert the magnetic field readings to accurate current data, for all of the core designs proposed. The degree of non-uniformity,  $h_{x,max}/h_{x,min}$ , of the three samples varies with core design (

Table 5.1). The individual cores design exhibits the smallest degree of non-uniformity. The row cores design has slightly greater degree of non-uniformity, indicating more flux leakage from adjacent current segments. The combined core design exhibits a much larger degree of non-uniformity, as the core effectively forms one magnetic circuit around which flux from any of the current segments may flow.

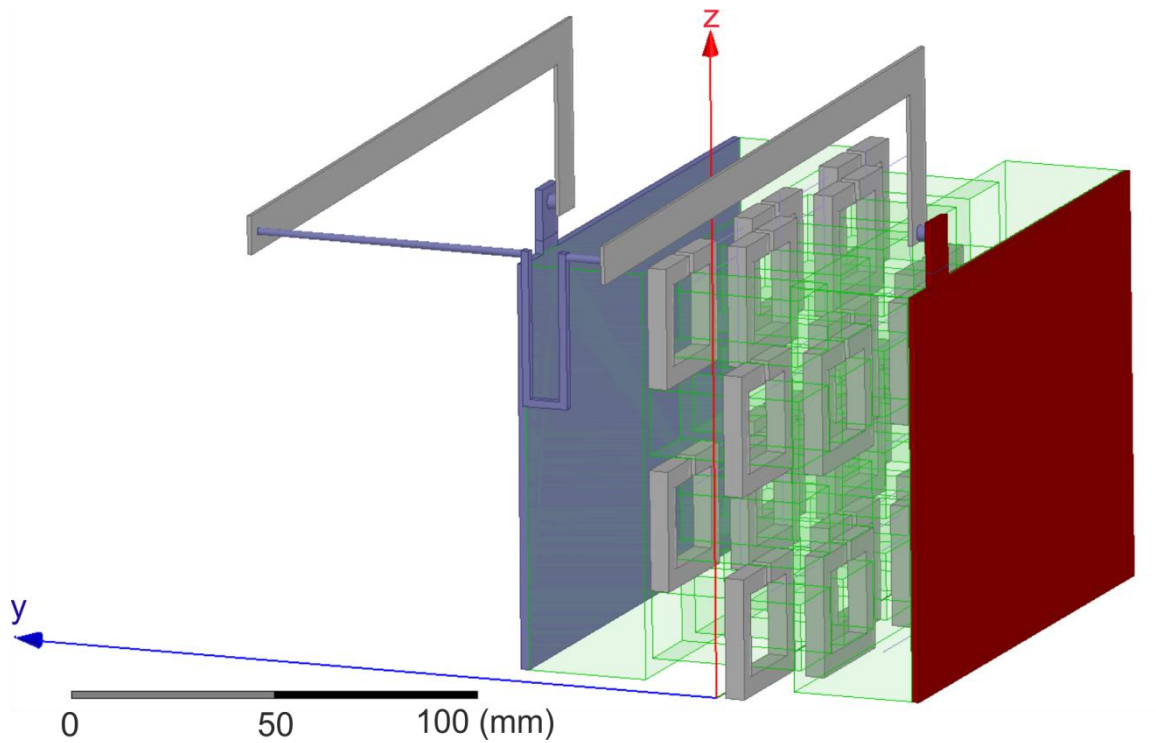


Figure 5.9 - Ansys Maxwell model to simulate magnetic field readings for a given current distribution. Individual core design shown.

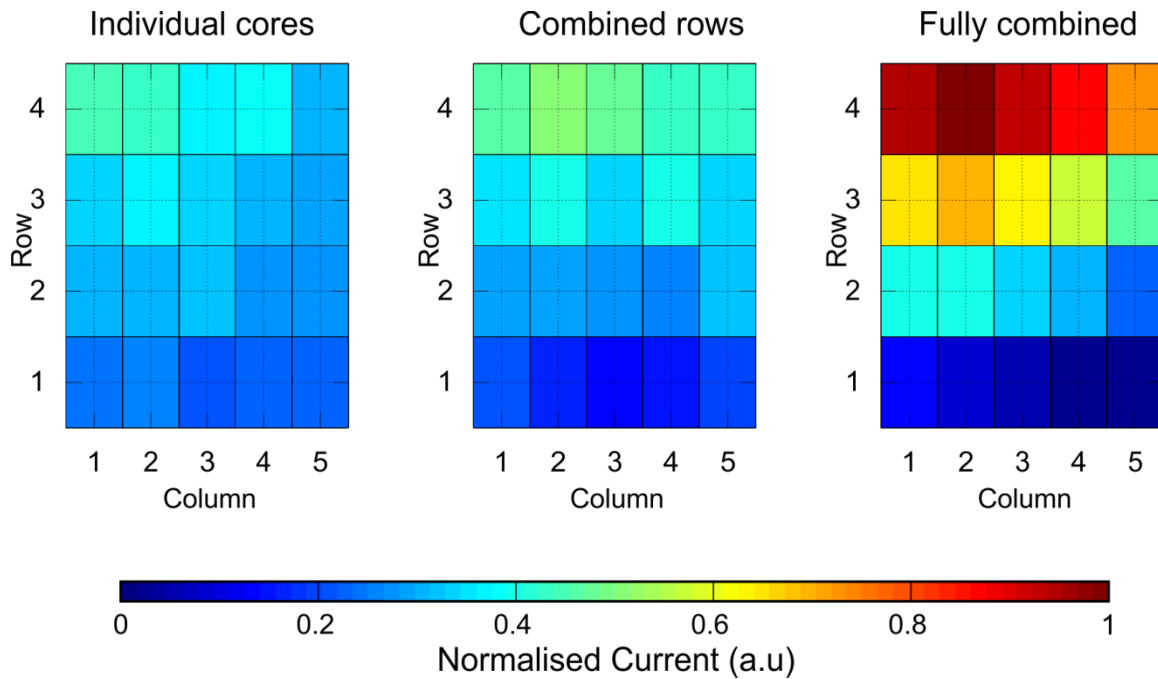


Figure 5.10 - Simulated response of airgap fields to a uniform cell current.

	Individual	Combined rows	Fully combined
Degree of non-uniformity, $h_{x,max}/h_{x,min}$	2.12	3.67	45.30

Table 5.1 – Degree of non-uniformity of the three sets of magnetic measurements shown in Figure 5.10.

This difference between the combined core design and the other two may be understood in terms of ideal magnetic circuit models. Assuming that the row cores are separated sufficiently, then each row may be considered an independent circuit, where  $p$  aperture currents,  $I = [i_1, \dots, i_p]$  are represented by magnetomotive forces  $[F_{m,1}, \dots, F_{m,p}]$ , and the airgaps each have equal reluctance  $S$ . Figure 5.11, left hand side, shows a 2 aperture row of cores as an ideal magnetic circuit. Magnetic flux is caused by a non-zero value of  $F_{m,1}$  (which in turn is caused by the current flowing through the left hand aperture,  $i_1$ ). The flux takes a path through Airgap 1, through the middle vertical core member and back to the bottom node of  $F_{m,1}$ . Since the middle vertical member forms a ‘short circuit’ (a low reluctance path), none of the flux due to  $i_1$  passes through Airgap 2. Sensors mounted in either airgap respond only to the current flowing through their corresponding aperture, or in algebraic form  $\phi_n = \frac{F_{m,n}}{S}$ .

On the right hand side of Figure 5.11 is an ideal magnetic circuit model of a  $2 \times 2$  combined core array. Considering again the case where only  $i_1$  (and therefore also  $F_{m,1}$ ) is non-zero, we see that the resulting flux now is split equally between Airgap 1 and Airgap 3, since they each

present an equal reluctance and are arranged in parallel. The middle vertical core members again ensure that no flux passes to Airgap 2 and Airgap 4. If we then consider the case where only  $i_3$  is non-zero, the flux must pass through Airgap 3, through the inner vertical core member to the bottom, then right to left along the bottom horizontal core member before returning through  $F_{m,1}$  (which has zero reluctance by analogy with a zero-impedance voltage source), to the negative side of  $F_{m,3}$ . By tracing these flux paths we see that the flux,  $\phi_3$ , passing through Airgap 3 is equal to  $\frac{F_{m,3}}{S} + \frac{F_{m,1}}{S}$ , while  $\phi_1 = \frac{F_{m,1}}{S}$  only. This means that  $|\phi_3| > |\phi_1|$  and therefore also  $|h_3| > |h_1|$  for a uniform current distribution, where  $i_1 = i_3$ .

Having not too great a value of  $h_{x,max}/h_{x,min}$  is desirable as it allows the use of a set of sensors each with the same gain. An integrated sensor such as the HMC5883L (see Section 5.2.3), has gain which is variable between 230 lsb  $G^{-1}$  (least significant bits per Gauss) and 1370 lsb  $G^{-1}$ , approximately a factor of 6, which is less than the  $h_{x,max}/h_{x,min}$  of the combined core design measurements. Operating different sensors at different gain settings in order to measure a uniform current complicates the control of the sensor system and reduces the ability to alter the overall gain of the system. For example, if the top row of sensors is set to minimum gain and the bottom row of sensors set to maximum gain, then there is no ‘headroom’ to increase or decrease the gain of all sensors in order to measure a cell current that is smaller or larger respectively. It appears that the row cores design offers a compromise between uniformity of measurements and size/complexity of mounting system.

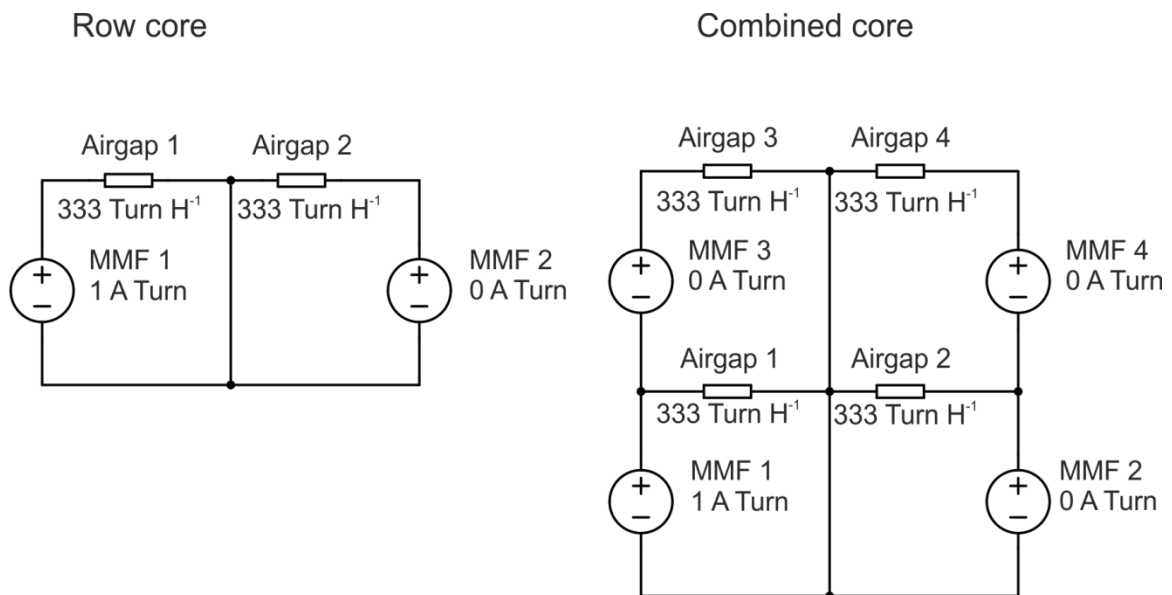


Figure 5.11 – Idealised magnetic circuit models of the row core and combined core designs, for an array size  $2 \times 2$ .

## 5.2.2 Leakage Compensation

Figure 5.10 and

Table 5.1 show that the raw magnetic data from sensors in each of the airgaps does not reflect the current distribution accurately. To compensate for this, the magnetic measurements  $\mathbf{B}$  and current segments  $\mathbf{I}$  may be treated as a linear system coupled by  $\mathbf{K}_{core}$  (assuming (2.12) holds, *i.e.* that the airgaps dominate the reluctance around the cores). This linear system is given by (5.3) and **Error! Reference source not found.**). In a similar manner to the special basis projection technique,  $\mathbf{K}_{core}$  may be constructed using Ansys Maxwell simulations by setting each element  $n = (1 : 20)$  of  $\mathbf{I}$  to 1, one at a time with the other elements set to 0, and taking the resulting  $\mathbf{B}$  as the  $n^{th}$  column of  $\mathbf{K}_{core}$ . This method ensures that all current-carrying features of the test cell may be taken into account without having to analytically create the coupling  $\mathbf{K}_{core}$ . (5.3) may then be solved for  $\mathbf{I}$  for a given set of magnetic measurements, using matrix manipulation functions in Octave.

$$\mathbf{B} = \mathbf{K}_{core}\mathbf{I} \quad (5.3)$$

$$\begin{bmatrix} b_{x1} \\ \vdots \\ b_{x20} \end{bmatrix} = \begin{bmatrix} k_{1,1} & \cdots & k_{20,1} \\ \vdots & \ddots & \vdots \\ k_{1,20} & \cdots & k_{20,20} \end{bmatrix} \begin{bmatrix} i_1 \\ \vdots \\ i_{20} \end{bmatrix} \quad (5.4)$$

Note that for an ideal current sensor system (*i.e.*, one that requires no compensation) with 20 current segments and 20 sensors, the coupling  $\mathbf{K}$  would be an identity matrix multiplied by the inverse of the airgap length, so that the magnetic field in each airgap is proportional to the current in the corresponding segment only. A comparison between an ideal coupling (for a 3 mm airgap) and the simulated coupling is given in Figure 5.12. The two matrices are similar, but not equal. This is why the raw data shown in Figure 5.10 (combined rows) is nearly, but not quite, uniform.

Figure 5.13 and Figure 5.14 show the result of compensating the raw data by calculating  $\mathbf{I} = \mathbf{K}_{core}^{-1}\mathbf{B}$ , for a uniform and a step changing current distribution respectively. The degree of non-uniformity,  $i_{max}/i_{min}$ , of the uniform reconstruction is 1.34, *i.e.* the reconstruction is more uniform than the raw  $h_x$  data. The step changing current can be identified visually from the plot.

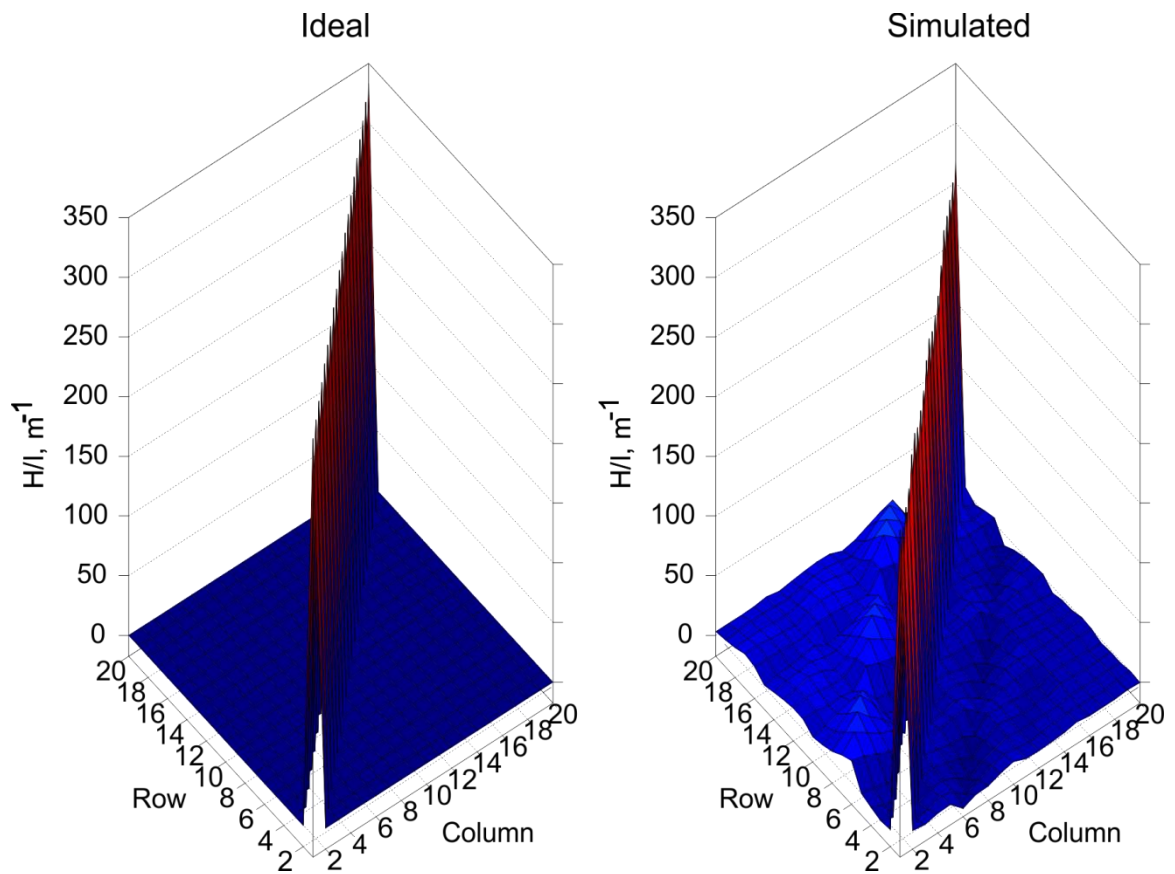


Figure 5.12 - Identity matrix (ideal sensor system) and the  $K_{core}$  matrix.

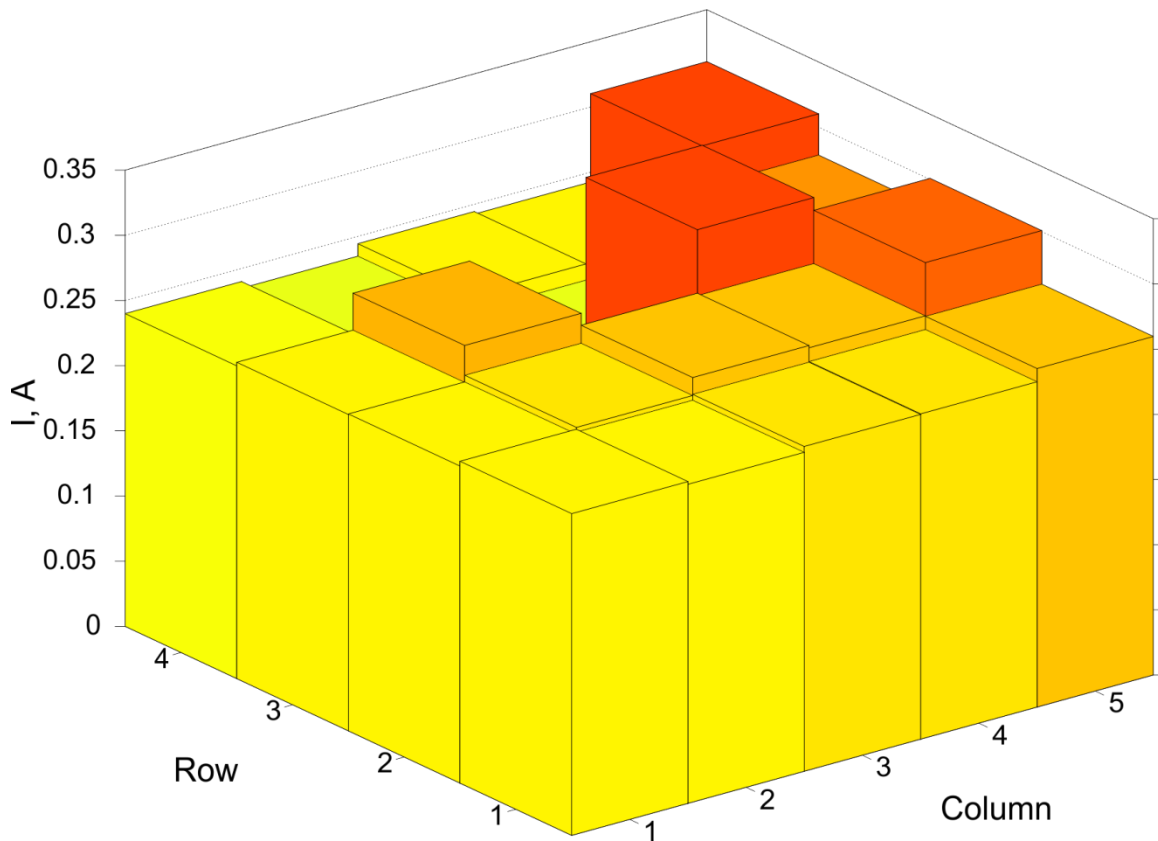


Figure 5.13 - Reconstruction of uniform current.

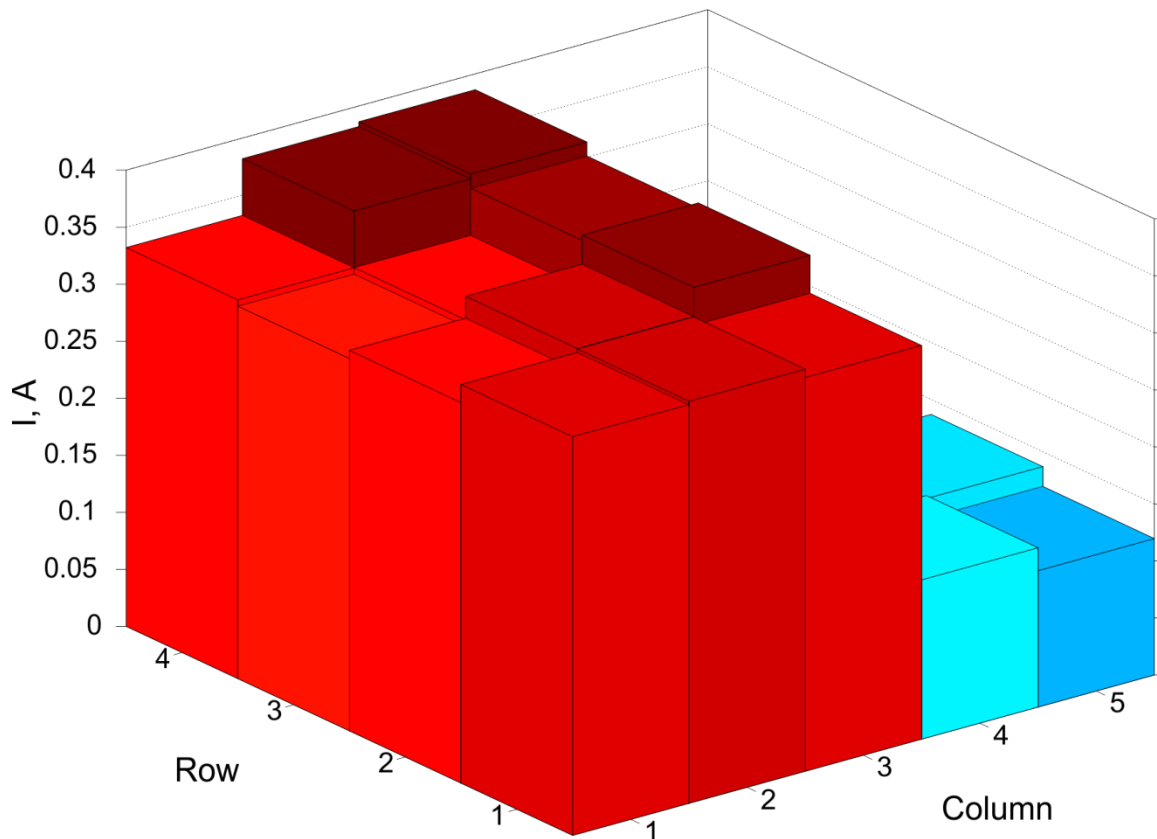


Figure 5.14 - Reconstruction of step changing current.

As well as differences between the  $h_x$  measurements taken at the centre of each airgap, the variation in  $h_x$  with  $x$  position within each airgap should be considered. Figure 5.15 shows plots of  $h_x$  against  $x$ , for each row of cores. The pulses in the plot correspond to the locations of the airgaps, since the magnetic permeability of the core material is sufficiently high that  $\mathbf{h} = \mathbf{b}/\mu \rightarrow 0$  inside the core material. The tops of the pulses are not flat, rather they vary with  $x$  position inside the airgap. In order to get consistency between the measurements, the  $x$  position within the airgap must be consistent. This is trivial when working with simulations, but becomes a potential problem if simulations are used to produce a leakage compensation matrix to be used with experimental measurements.

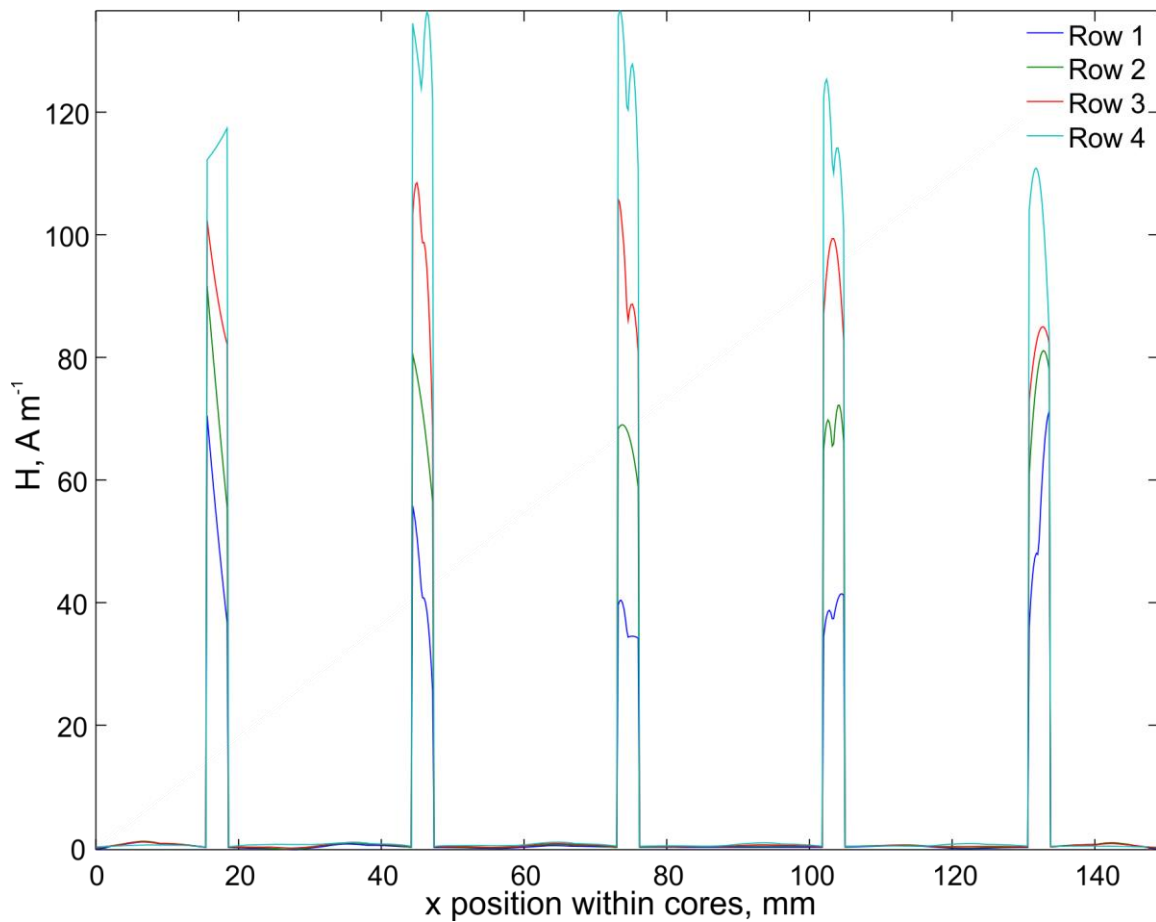


Figure 5.15 - Variation in  $H_x$  along the  $x$  dimension in each row of airgaps.

Any error in the position of the sensor within the airgap may be cancelled by using measured data to create a leakage compensation matrix. However, generating partial currents is not convenient with an electrochemical cell. An alternative is to use a resistive circuit having similar geometry to the target cell to be tested. The model shown in Figure 5.16 can be constructed from copper clad board, cut to size and shape, and a set of 20 resistors and wires (see Section 5.3.3 for implementation of this in practice).

Table 5.2 shows the error between this model and the more accurate distributed model shown in Figure 5.9. The calculated mean absolute errors show that there is no significant loss of solution accuracy when using the thin wires model to calculate the leakage compensation matrix to be used with a distributed current distribution. The reconstruction error when using the (incorrect) thin wires model for the compensation data is actually slightly smaller than when using the (more correct) distributed model.

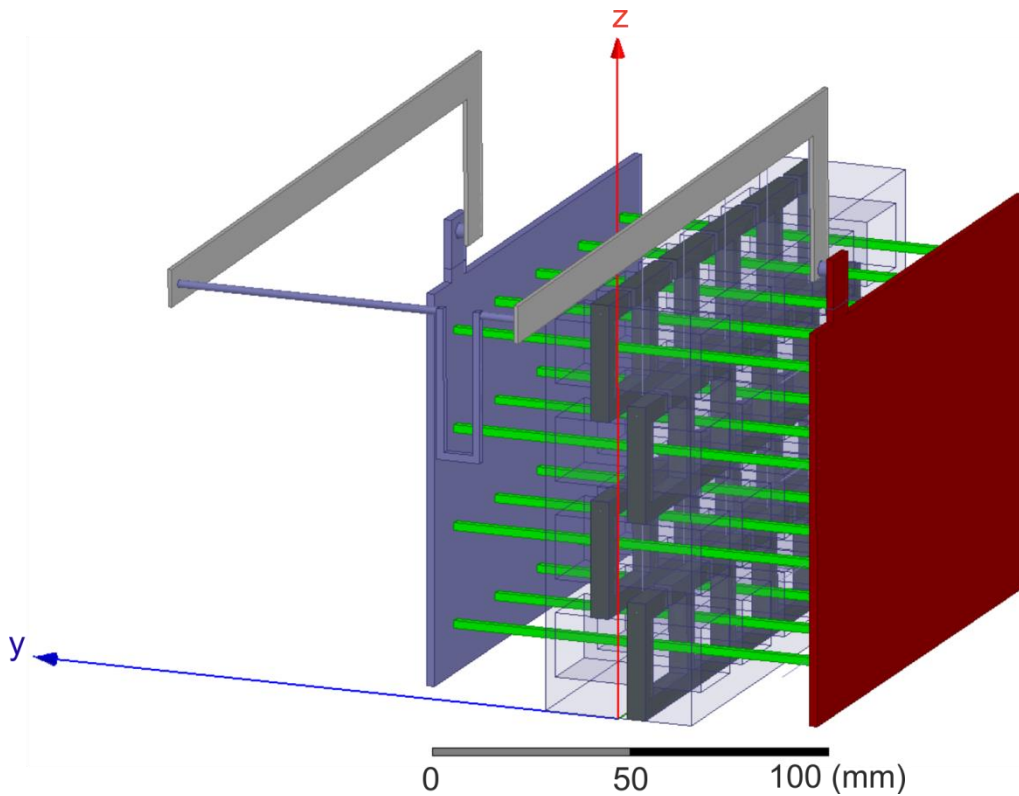


Figure 5.16 – Thin wire version of test cell.

Source distribution	$\ H_{x,wires} - H_{x,dist}\ $	$\ I_{r,dist} - I_{s,dist}\ $	$\ I_{r,wires} - I_{s,dist}\ $
Uniform	6.04 %	7.15 %	6.07 %
Step-changing	5.54 %	5.68 %	5.64 %

Table 5.2 – Percentage mean absolute error between (1) H data from wires model and H data from distributed model, (2) source I data from a distributed model and reconstruction from a distributed model, (3) source I data from a distributed model and reconstruction from a wires model.

### 5.2.3 Sensor choice

The thickness of the core impacts upon the overall aperture area available for ionic current to pass through. A minimum thickness for the core around the airgaps is set by the size of the sensor used, and so a compact sensor design is required. Neglecting leakage effects, rearranging (2.13) for  $i$  and substituting  $b = \mu_0 h$  gives an expression that tells us the current that can be measured for a given sensor and airgap size (5.5). Taking  $b$  as the full scale measurement value of a given sensor yields the full scale current that can be measured by the sensor and airgap combination. This is useful for checking an upper limit on the current that

can be measured, which may be remedied by increasing airgap length or choosing a less sensitive sensor.

$$i = \frac{l_{air} b}{\mu_0} \quad (5.5)$$

Alternatively, the sensor gain may be substituted into (2.13) to yield the sensor output for a given current. For a sensor with an analogue output this is given by (5.6) where  $A_v$  is the sensor gain in  $V T^{-1}$ . For a sensor with digital output (5.7) is more appropriate, where  $A_{lsb}$  is the sensor gain in  $lsb T^{-1}$ . This is useful for identifying where a sensor/airgap combination is not sensitive enough. If the airgap is constrained by the sensor thickness then this may only be remedied by replacing the sensor for a more sensitive or smaller one.

$$v_{out} = \frac{A_v \mu_0 i}{l_{air}} \quad (5.6)$$

$$lsb_{out} = \frac{A_{lsb} \mu_0 i}{l_{air}} \quad (5.7)$$

Most sensor packages are smaller along one dimension shown as 'thickness' in Figure 5.17. In order to maximise sensitivity it is assumed that the airgap should be sized to the thickness as it will result in the shortest possible airgap. Therefore the  $\mathbf{b}$  field will be aligned as shown in Figure 5.17. Any sensors which do not measure  $\mathbf{b}$  along this axis are not suitable for this application.

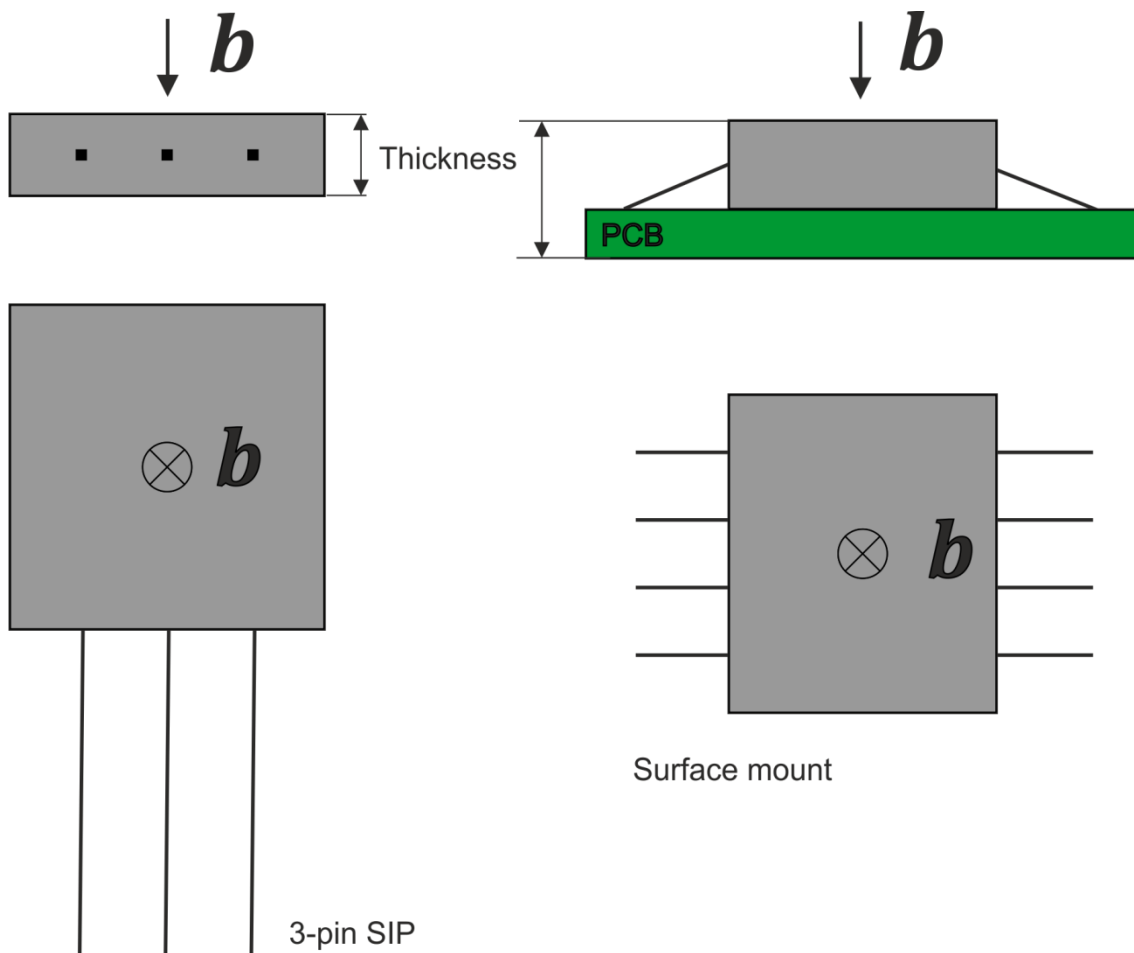


Figure 5.17 – Two common packages for compact magnetic sensors and required sensitivity axis.

Table 5.3 gives a comparison of some commercially available magnetic sensors by size and sensitivity. The A1309 and A1309 Hall effect sensors both give a small airgap due to not needing to be mounted to a PCB, as they are not surface mount components. A small airgap would increase  $b_x$  and  $h_x$  in the airgap, increasing sensitivity. However, for the 5 A system, both sensors are likely to yield small output voltages which may be susceptible to noise.

The LSM303 and HMC5883L both have adjustable gain in an appropriate range, although the HMC5883L has a better (higher) maximum sensitivity, allowing full scale current measurements at terminal currents as low as 2.58 A. They, as well as the FXOS8700CQ, are system-on-chip devices which can be read and configured over I<sup>2</sup>C. This allows them to be incorporated into a robust and flexible digital system design, in contrast with the analogue output signal from the A1309 sensors. Taking these factors into account the HMC5883L was chosen. Since the system is to be operated at 5 A at all times, the maximum gain setting is redundant with a 2 mm airgap. Increasing the airgap to 3 mm yields a full scale terminal

current of 3.86 A to 42 A which is still within useful range but has the advantage of more tolerant assembly due to some clearance between the sensor assembly and the airgap. Although the terminal current will not exceed 5 A, the headroom to measure higher segment currents is useful when measuring non-uniform current distributions.

Sensor	Package	Size ( $l \times w \times c$ ), minimum airgap in bold	Magnetic measurement range (Full scale terminal current (5.5), per 20 segments @ minimum airgap)	Reading at 5 A/20 segments (5.6), (5.7)
ST Microelectronics LSM303 [102]	LGA-14 surface mount	5 mm × 3 mm × <b>2 mm*</b>	± 1.3 G to ± 8.1 G (± 4.13 A to ± 28.01 A), depending on gain setting	1712.17 to 361.28 lsb, depending on gain setting
NXP FXOS8700CQ [103]	QFN	3 mm × 3 mm × <b>2 mm*</b>	± 12 G (38.20 A)	1570.80 lsb
Honeywell HMC5883L [86]	QFN	3 mm × 3 mm × <b>2 mm*</b>	± 0.88 G to ± 8.1 G (± 2.58 A to ± 28.01 A), depending on gain setting	2151.99 to 361.28 lsb, depending on gain setting
Allegro A1309KUA-9-T [104]	3 pin SIP	4 mm × (3 mm + leads) × <b>1.5 mm</b>	± 222 G (± 537.59 A)	18 mV
Allegro A1308KUA-1-T [104]	3 pin SIP	4 mm × (3 mm + leads) × <b>1.5 mm</b>	± 1538.46 G (± 3721.78 A)	2.68 mV

*\*1.2 mm thick IC + 0.8 mm thick PCB*

**Table 5.3 - Comparison of magnetic sensors.**

The HMC5883L is a surface mount component which must be mounted to a PCB. The PCB design is an important part of the system, as the size of the airgap in the z direction depends on the width of the PCB. Figure 5.18 shows the circuit diagram for the PCB breakout. Figure 5.19 shows the PCB layout used as the breakout board for the HMC5883L, measuring 13.7 mm × 4.7 mm (Figure 5.20). This aspect ratio is chosen since the length of the board does not affect aperture area. The circuit diagram is based on the application note in the sensor's datasheet [86] and the Sparkfun HMC5883L breakout board [105], although a useful addition which is not included in this revision would be a diode to protect against reversing the power rails due to connecting the power supply incorrectly.

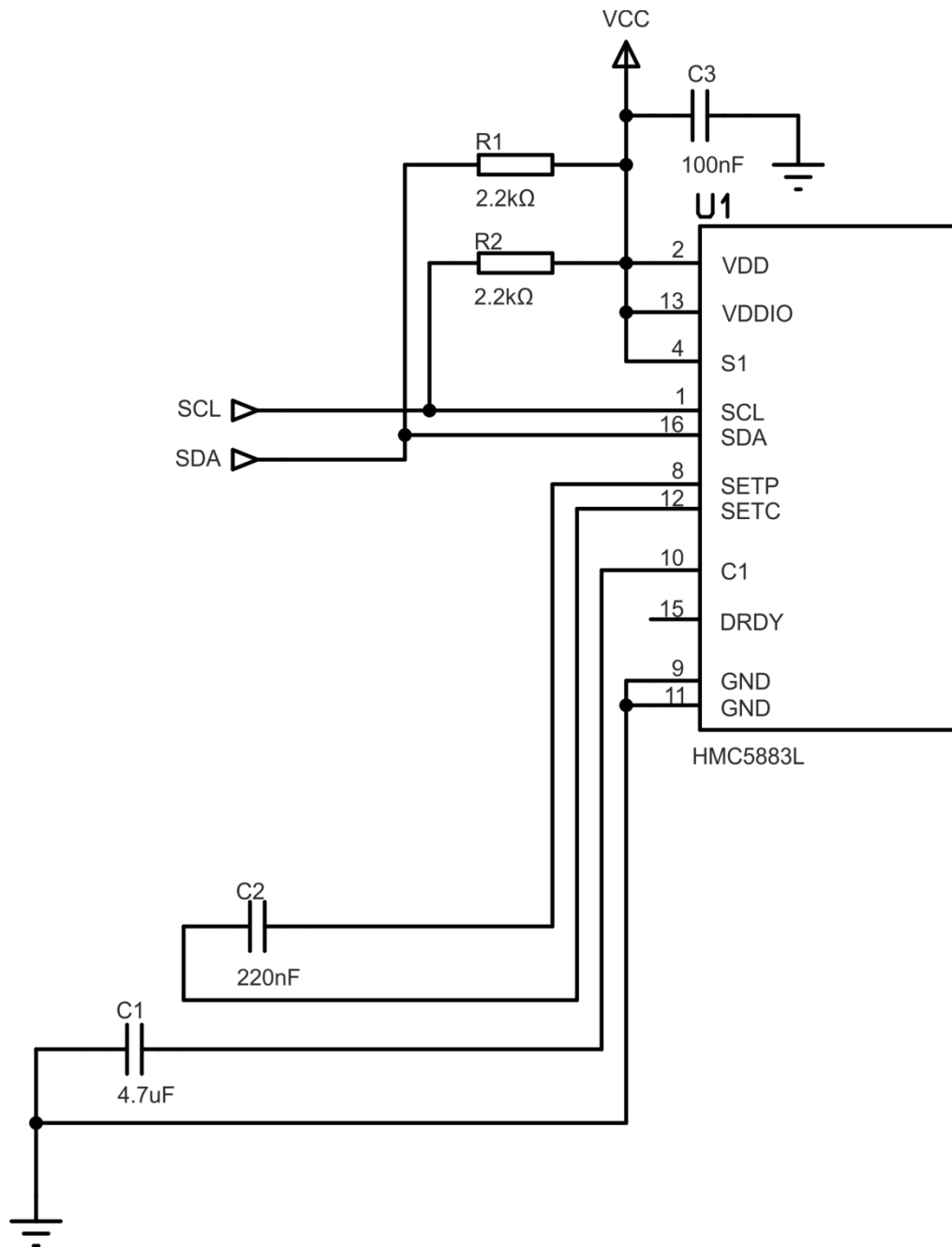


Figure 5.18 - Circuit diagram of sensor breakout board.

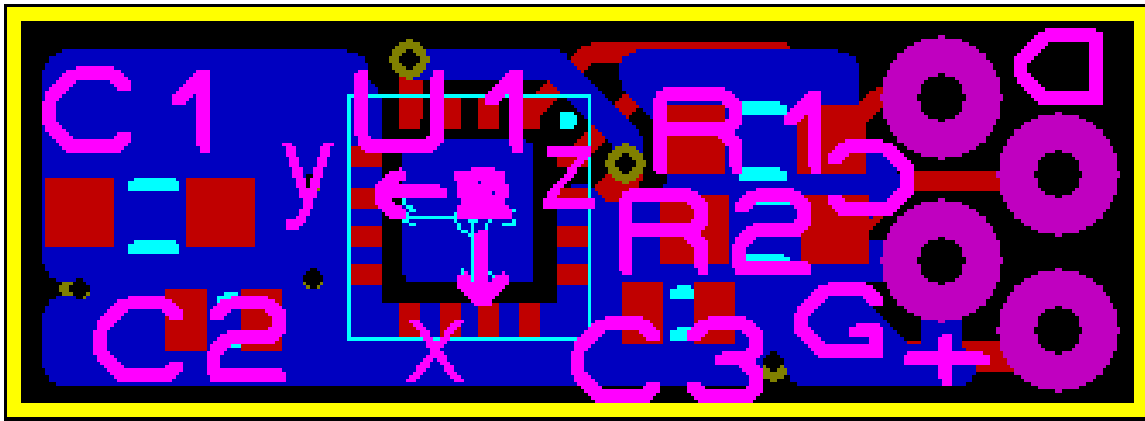


Figure 5.19 - PCB layout of HMC5883L breakout.

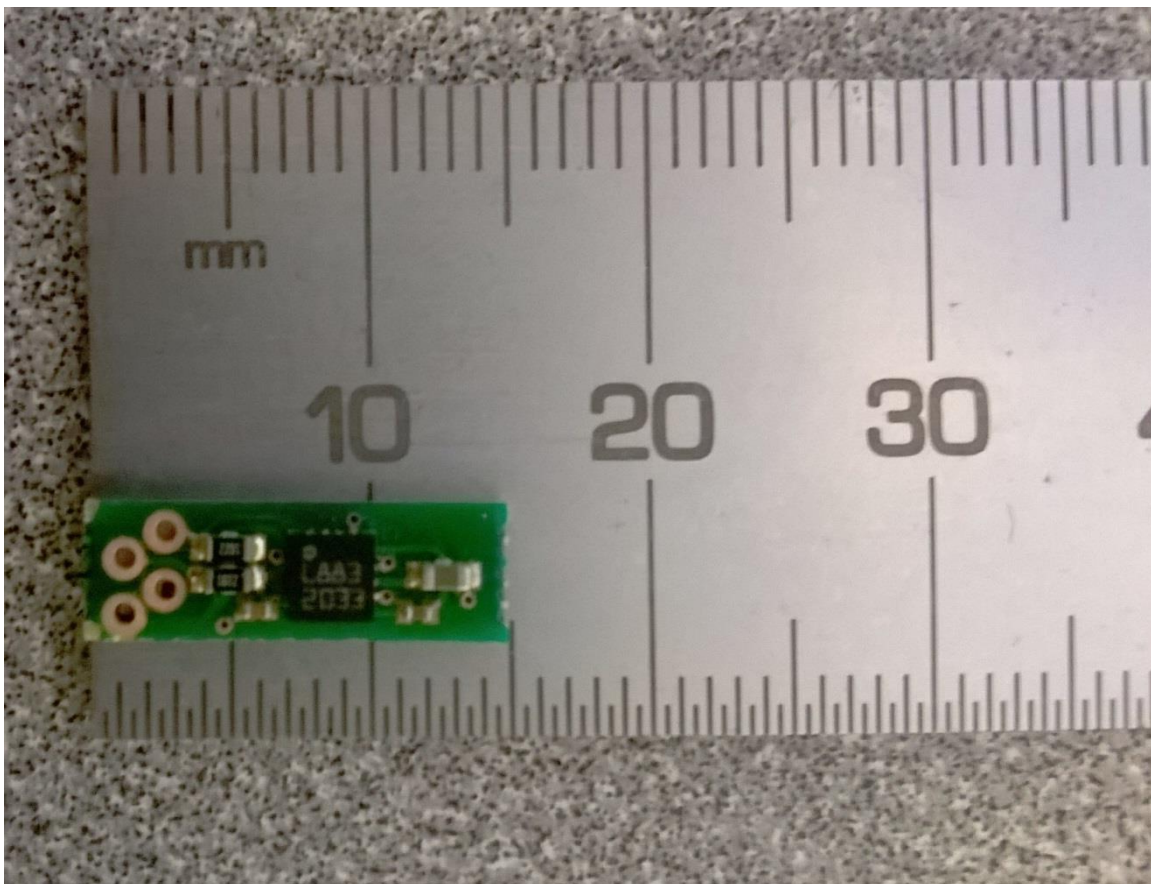


Figure 5.20 - Sensor mounted to breakout board.

#### 5.2.4 Fitting the Core to the Sensors

Using the sensor and PCB described in Section 5.2.3 allows an airgap dimension in the  $z$  direction of 5 mm. Therefore the upper horizontal member of the core must also have a thickness of 5 mm, assuming rectangular apertures. Since the cores are to be overlapped along their horizontal edges, there is no advantage (in terms of aperture size) to making the lower horizontal members any less than 5 mm. The outer vertical members are to be overlapped

outside of the plate area, so their thickness (in the  $x$  direction) does not affect aperture size at all. 5 mm is chosen for the thickness of these members. The lowest and uppermost horizontal members of the cores are designed to overlap the cell plate by 2.5 mm. The leftmost and rightmost vertical members overlap the cell plate by 1.5 mm. Figure 5.21 shows a dimensioned drawing of the arrangement of the 4 core pieces.  $y$  direction thickness of the cores is 8 mm, to minimise the overlap with the PCBs while allowing access to the solder holes for the wire connections to each PCB. A thicker core should result in less fringing, at the expense of increasing the  $y$  dimension of the assembly. The sensor and PCB assembly is measured as 1.84 mm, with the PCB measuring 0.89 mm. An airgap length close to the thickness of the sensor + PCB would leave the sensor close to one side of the airgap. The airgap length is set to 3 mm which puts the sensor approximately at the centre (Figure 5.21 Detail A). However, the location of the sensor's  $B_z$  ( $B_x$  in the working coordinate system) transducer within the integrated circuit package is unknown and so there is approximately  $\pm 0.45$  mm error in the  $x$  position of the sensing location and  $\pm 1.5$  mm error in the  $yz$  position. This uncertainty may be cancelled out by using measured data to form the compensation matrix (see Sections 5.2.2 and 5.3.3).

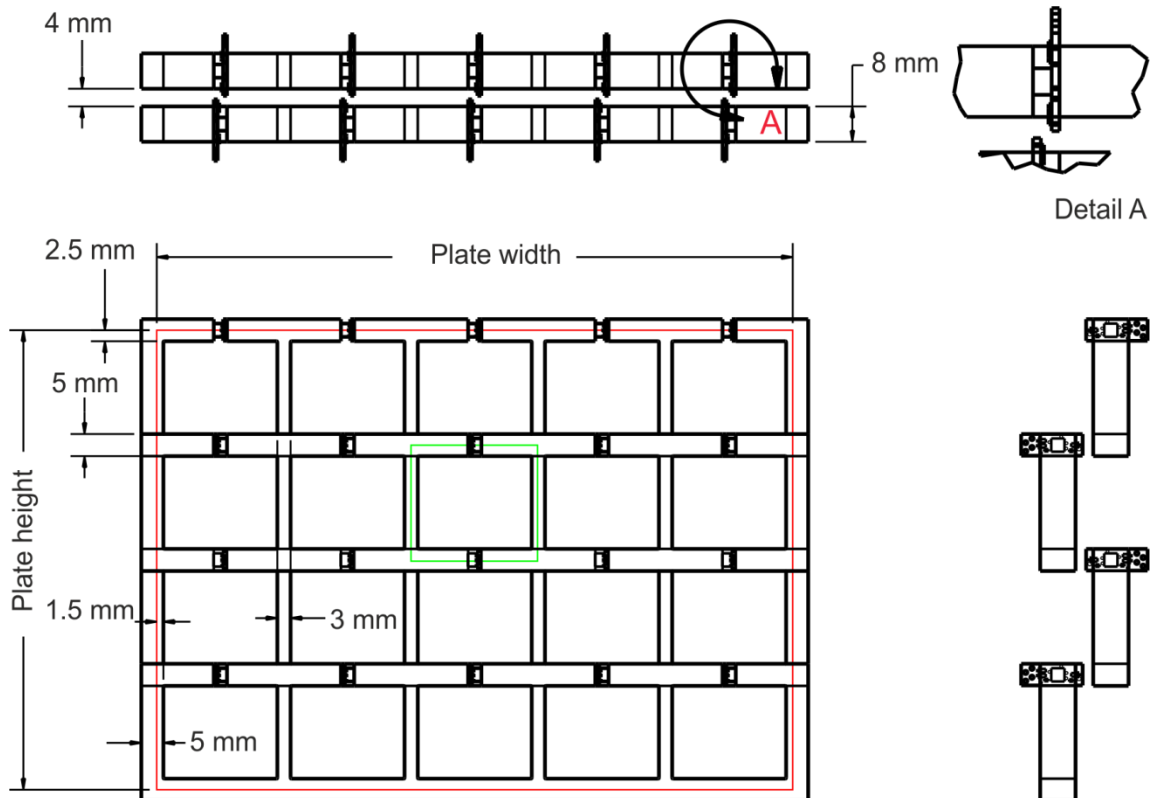


Figure 5.21 – Dimensioned drawing of cores showing overlap with other cores. Plate area outline in red, one segment outlined in green.

### 5.2.5 Chemical resistance testing

The sensors and cores must be protected from corrosion by the electrolyte. The cores also need to be held in place. Therefore a frame and protective case are needed. Polypropylene is used for the cell case (Section 3.4.2), but it requires heat welding to join it. The heat welding equipment available leaves a weld seam approximately 3 mm wide and also causes warping when used on material less than approximately 3 mm thick. Any material used to line the inside of the core apertures should be as thin as possible in order to maximise the available aperture size. Solvent welded PVC is a possible alternative. PVC is also more suited to being cut using machine tools than PP (as it is harder and less elastic), as well as being commonly available in a range of profiles as an architectural material. Before adopting the new material, some chemical resistance tests are conducted. The test involves submerging samples in 40 % concentration (by weight) sulphuric acid for 14 days, weighing the samples before and after and inspecting for any discolouration afterwards.

The PVC did not discolour over the course of the test. Some weight change was seen. The proportionally greatest weight change was seen with the PVC L section, which lost 0.1 g out of 4.8 g initial weight (2.08 %). The solvent weld did not discolour and the joints made using it maintained their integrity. However the sample of L section with a patch of solvent weld painted on did exhibit warping. This may be due to the relatively large quantity of solvent weld applied to the thin (1.5 mm) plastic sample. The Araldite® epoxy discoloured but maintained adhesion to the PVC. Potting compound proved too brittle to be used as an adhesive or thin coating. This is unlikely to be due to acid corrosion as it is specified as a chemically resistant product [106], it is more likely that it is not suited to being applied as a glue or paint.

<b>Material</b>	<b>Weight before</b>	<b>Weight after</b>	<b>Visual check</b>
<b>PVC 12 mm thick</b>	23.1 g	23.0 g	No change
<b>PVC L section 2 mm thick</b>	4.9 g	4.8 g	No change
<b>PVC L section + patch of potting compound</b>	9.5 g	9.4 g	Potting compound is brittle and flakes off
<b>PVC L section + patch of solvent weld</b>	5.5 g	5.5 g	Some warping of PVC
<b>PVC L section + patch of Araldite epoxy</b>	6.9 g	7.0 g	Yellowing of Araldite
<b>PVC joined using epoxy potting compound</b>	9.5 g	9.5 g	Potting compound is brittle and flakes off
<b>PVC joined with solvent weld</b>	10.1 g	10.1 g	No change
<b>“ “</b>	25.2 g	25.2 g	No change
<b>PVC L section joined using solvent weld</b>	9.1 g	9.1 g	No change
<b>PVC L section joined with solvent and coated with potting compound</b>	9.8	10.0 g	Potting compound is brittle and flakes off

**Table 5.4 - Results of 14 day soak of various samples in 40 % sulphuric acid.**

### **5.2.6 Plastics design and construction**

PVC and solvent weld is shown to be a suitable material for constructing the sensor casing. In order to hold the cores in place, a ‘frame’ is made from 12 mm thick PVC. The frame is made from 4 pieces which glue together using solvent weld. The bottom piece and the side pieces of the frame have 5 mm deep recesses machined into them (Figure 5.22), so that the 5 mm thick external members of each core may be housed with no overlapping. The width of the sensor case is 21 mm wider than the plate and extends 9.5 mm below the bottom of the plate due to the over-sized cores and the thickness of the frame material in the 5 mm deep core recesses. This extra size is accommodated by a recess in the cell case (Section 3.4.2). The frame is taller than necessary so that some space above the top core (core 4) is left for wiring, and also to keep the top of the sensor case above the electrolyte fill level. The core recesses are deeper than the cores in the y direction in order to leave space for the wiring to the sensors. A pair of PVC end pieces (Figure 5.23) fit onto the front and back of the frame once the cores are in place. The apertures in the end pieces are approximately the same size as the apertures in the cores themselves, so that pieces of square tube can be inserted through the both end pieces and the core apertures. The aperture size of the sensor system is then given by the internal dimensions of these square tubes. Figure 5.24 shows the CAD model of the assembled system, with the front end piece not shown in order to show the cores inside. The square tubes can be made from two interlocking lengths of ‘L’ section PVC, with a thickness of approximately 1.5 mm. This gives an aperture size of 22.8 mm × 18 mm.

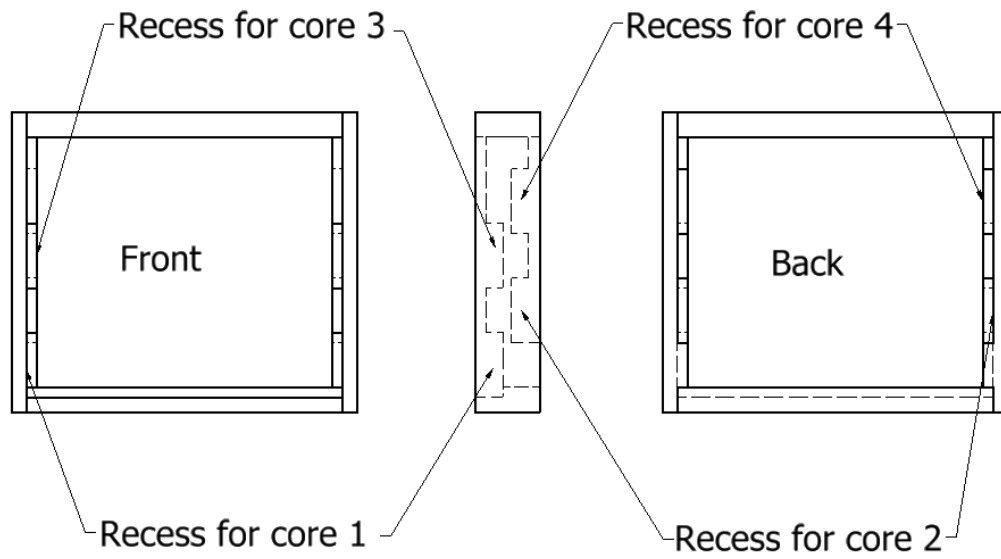


Figure 5.22 – Sensor case – 'frame' part, showing glued joints.

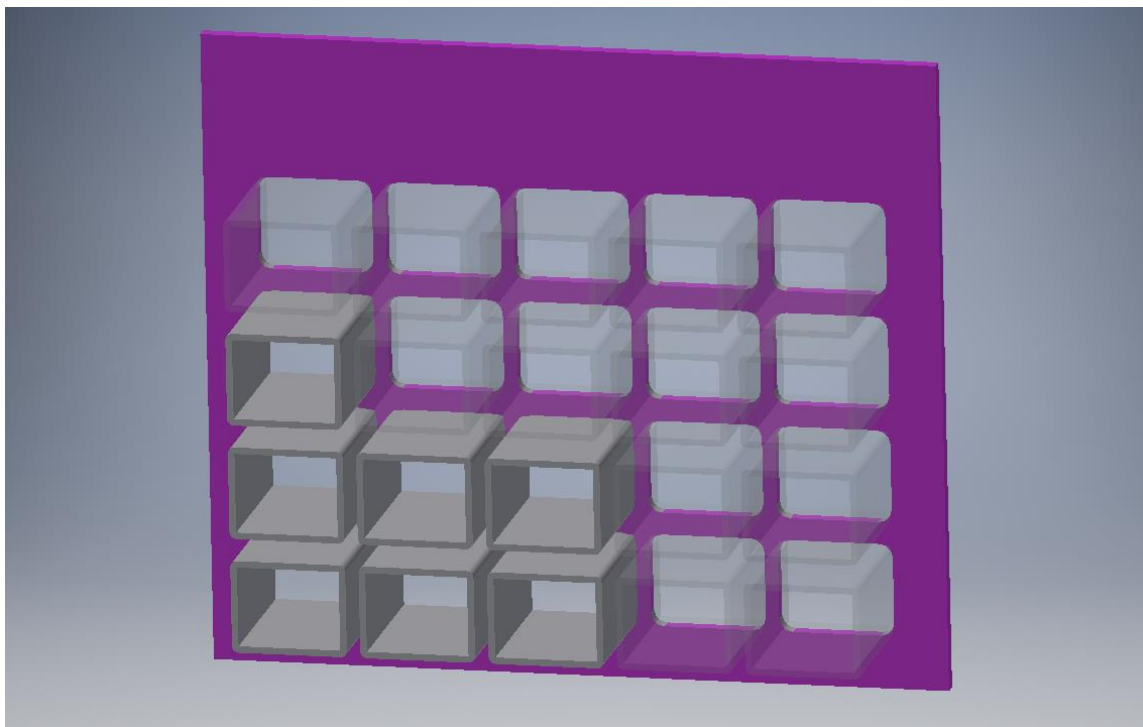
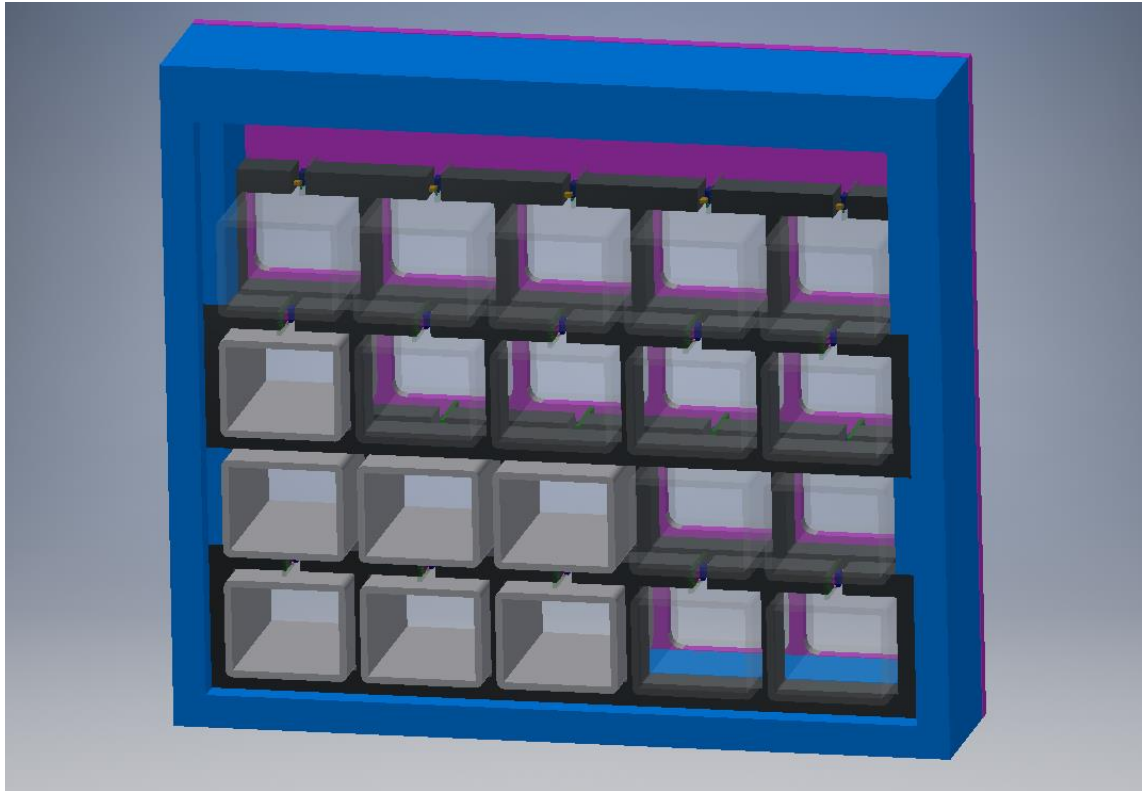


Figure 5.23 -Sensor case end piece (purple) and square tubes (grey).



**Figure 5.24 - Complete unit, front piece not shown. Frame part in blue, steel cores in dark grey.**

After machining the frame and end pieces, assembling and leak testing the square tube pieces and attaching wires to each sensor PCB, the assembly is dry fitted to check the wiring pattern (Figure 5.25). The sensors are aligned in their airgaps and fixed with Araldite®. The 4 frame pieces are fixed using solvent weld and then the end pieces are fixed with the square tubes in place. Finally the square tube pieces are fixed in place. The solvent weld does not gap-fill particularly well so the seams are reinforced with Araldite® to ensure the case is leak proof (Figure 5.26). The inside of the case is filled with potting compound under vacuum to further protect the internal parts against leaks.

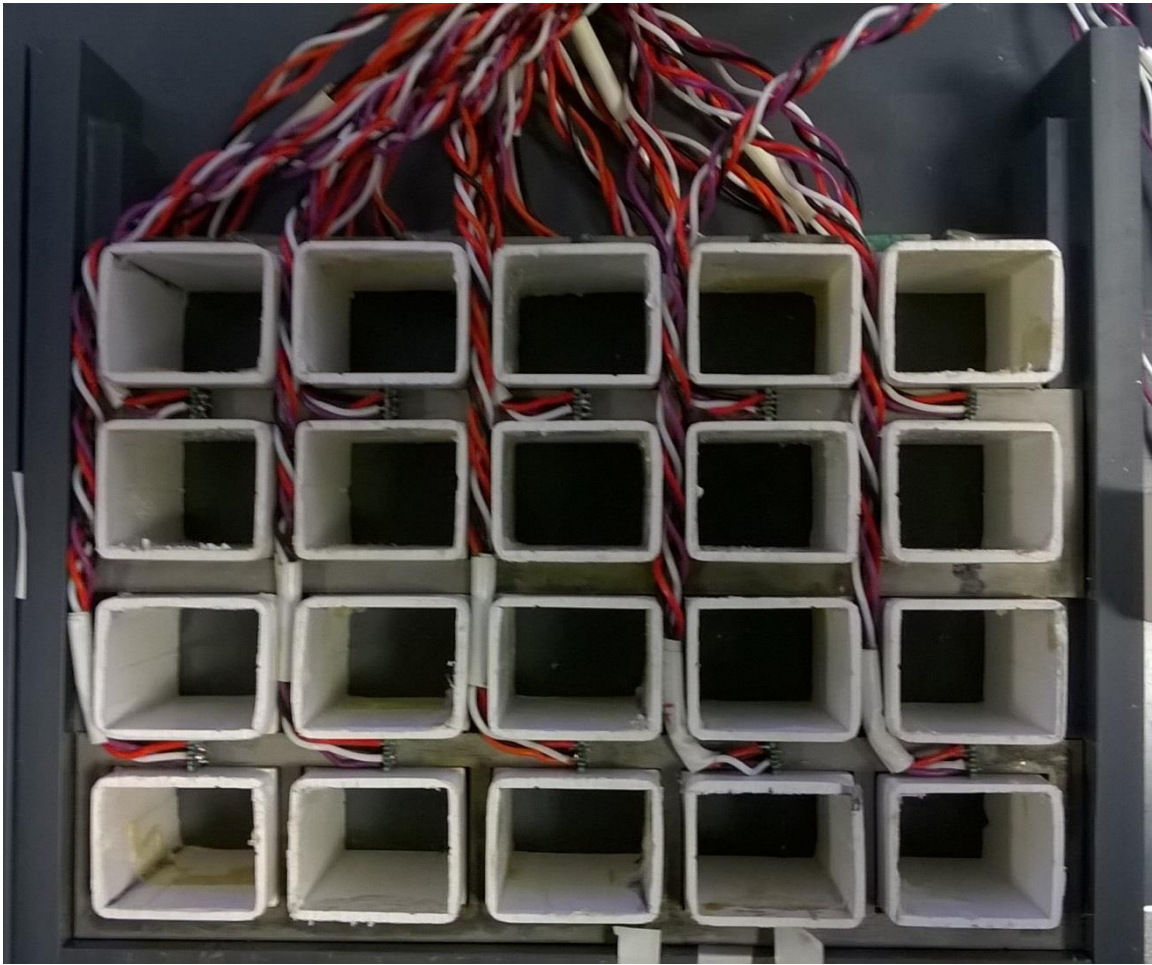


Figure 5.25 - Photo of wiring.

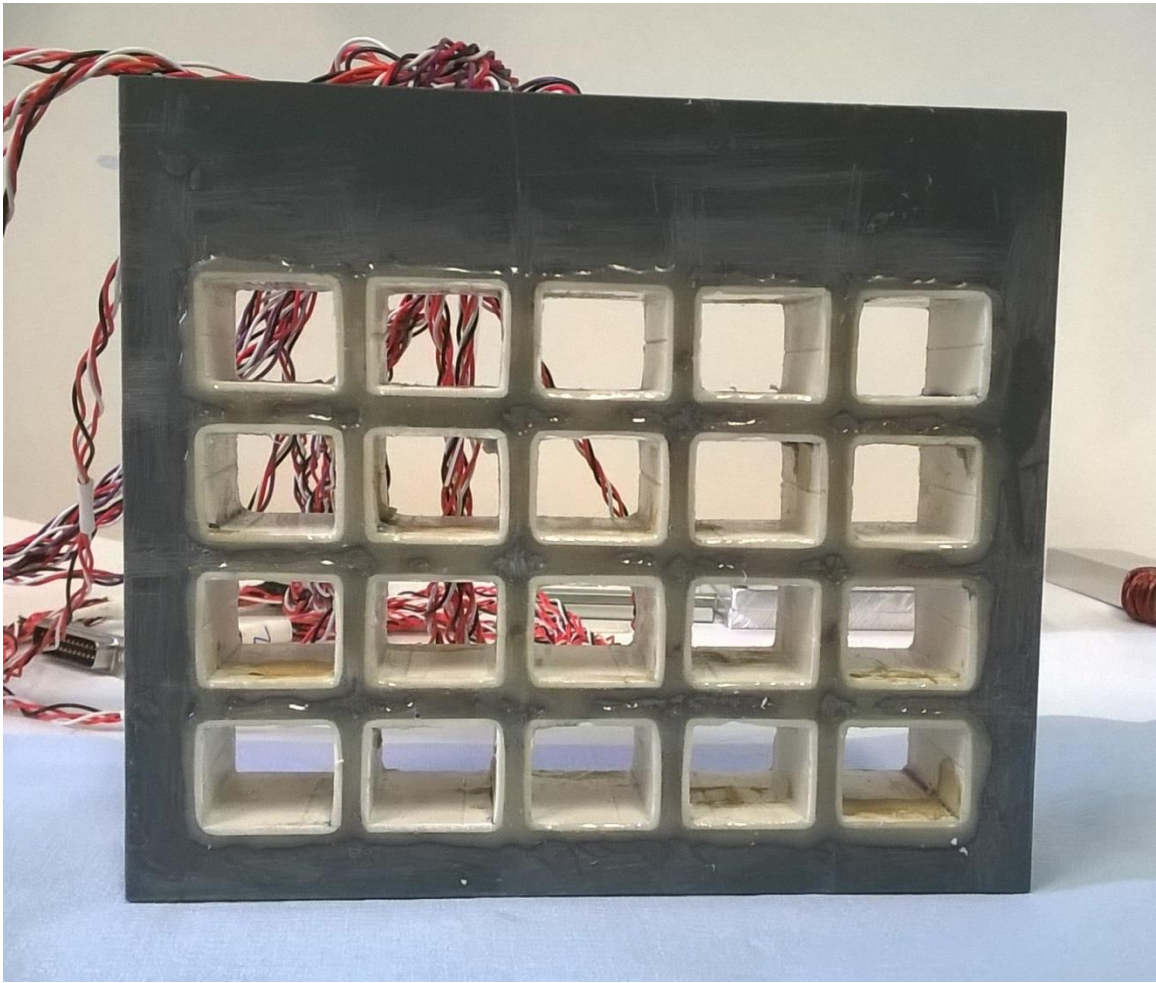


Figure 5.26 - Photo of Araldite®-reinforced seams.

## 5.3 System Integration and Testing

### 5.3.1 Multiplexing and firmware

The above section describes how the array of sensors and apertures may be arranged and constructed. In order to control and use the set of 20 individual magnetic sensors, some supporting systems are required. Figure 5.27 shows the top level system diagram. The system shares many similarities with the magnetic imaging system described in Section 3.2. The sensors used are HMC5883L, which support communication of data and commands over I<sup>2</sup>C. I<sup>2</sup>C supports addressing but the HMC5883Ls all have an identical hardware address which is not user-configurable. Therefore multiplexing is required. Controlling the multiplexing and sensors is an Arduino Due microcontroller. The microcontroller supports I<sup>2</sup>C communication to the multiplexers and sensors, and also serial communication over USB, to the host PC. The user can save the data received by the PC as well as set configuration settings at the PC which are transferred to the sensors.

The firmware (Figure 5.28) is primarily a switch-case statement which depends on the command received over serial from the PC, and loops round to receive a new command once the case instruction has been executed (see Appendix II – FTS Arduino Firmware). Five sensor functions are implemented, plus the toggle control for the bypass switch (Section 3.4.3). The one-byte character command 'i' selects the 'read sensor ID' subroutine. This reads back the contents of identification register A from each sensor to be saved on the microcontroller and also sends it back to the PC for the user to inspect. This register contains the byte 0x48. Reading this value back is a useful way to check which sensors are connected. The sensor IDs are read during setup as the list of connected sensors is used in other subroutines. The command 'r' reads the contents of the configuration registers for each connected sensor and sends it back to the PC. The two 8-bit configuration registers determine the gain, self-test mode, multiple-reading averaging and data rate for continuous-measurement mode (only single-measurement mode is implemented in this system). Command 'w' receives configuration data from the PC and writes the new data to the configuration registers. Command 't' triggers a single measurement. After taking a measurement the sensors save the data to their output register for reading later. Due to the multiplexing, each sensor receives this command sequentially. Finally, command 'f' fetches/reads the data from each sensor and sends it back to the PC. In case of an illegal command received from the PC, the character 'K' is

sent to the PC. The firmware is implemented in Arduino programming language, which is based on C.

The multiplexing is implemented using  $7 \times$  PCA9546A 4-way I<sup>2</sup>C switches (Figure 5.29). 8-way switches are available and could be used to reduce component count, but the 4-way switches have pins of larger pitch, which make hand-soldering a prototype easier. Each MUX has its own select line (MA0:MA6) and assigns an I<sup>2</sup>C hardware address to each one of its 4 I<sup>2</sup>C outputs.

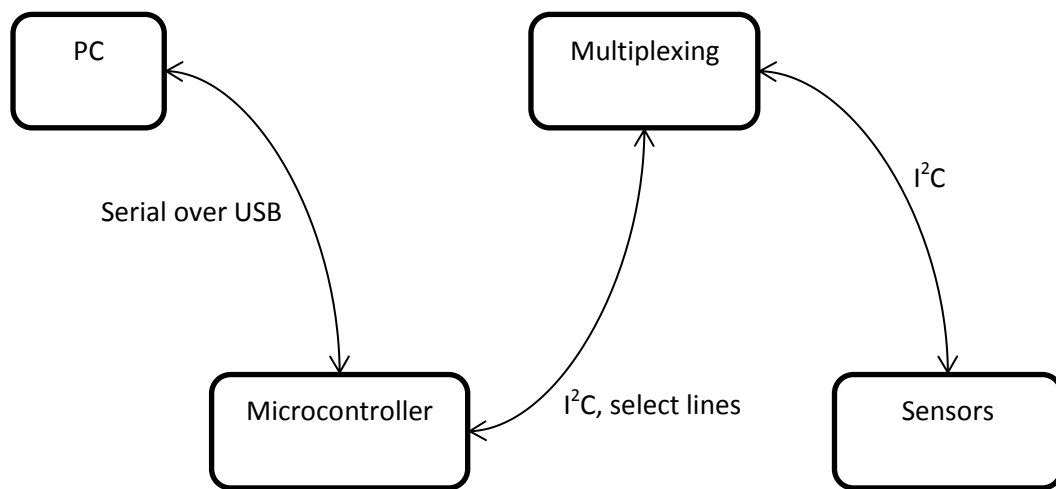


Figure 5.27 – Top level system diagram/flow chart.

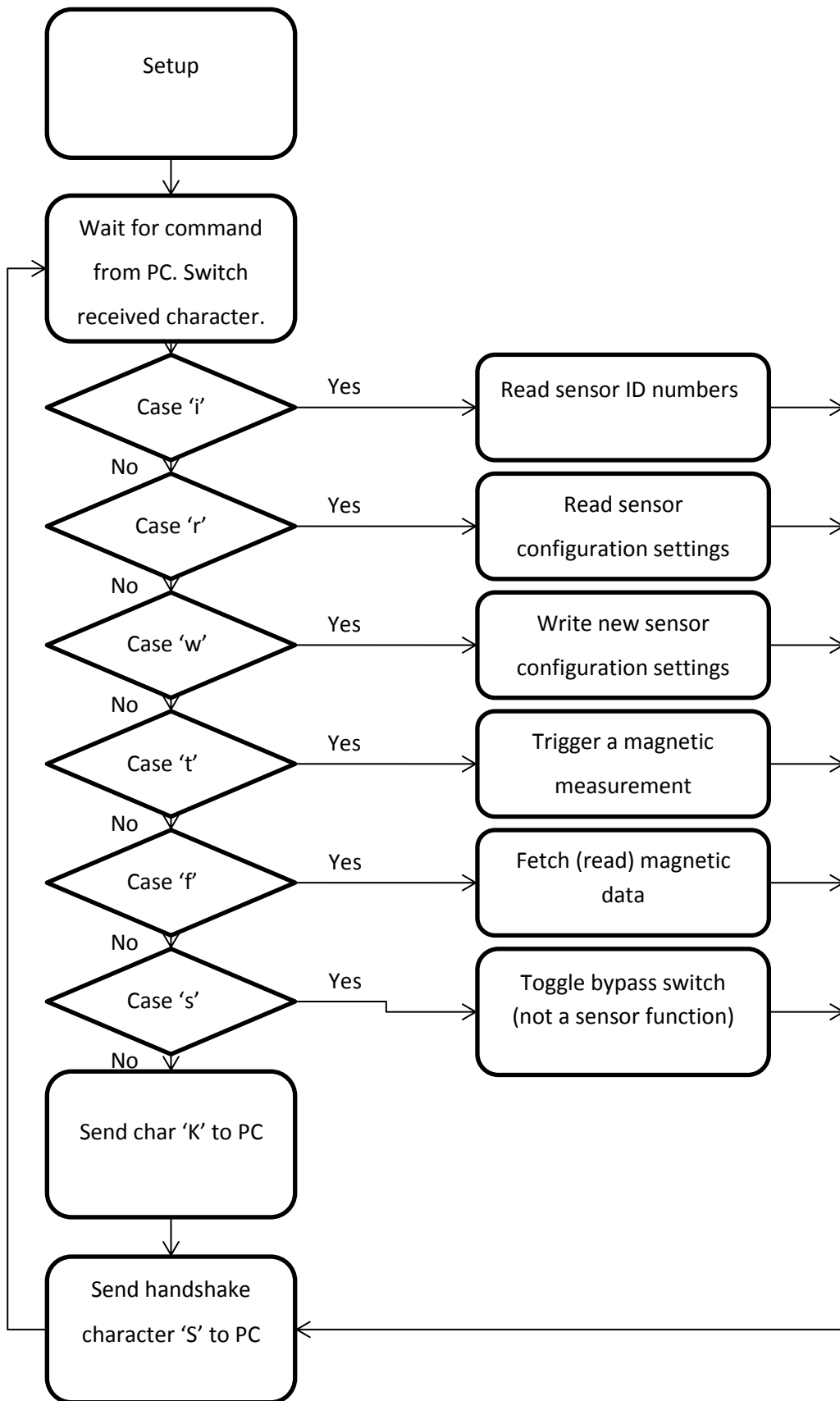


Figure 5.28 - Firmware flowchart.

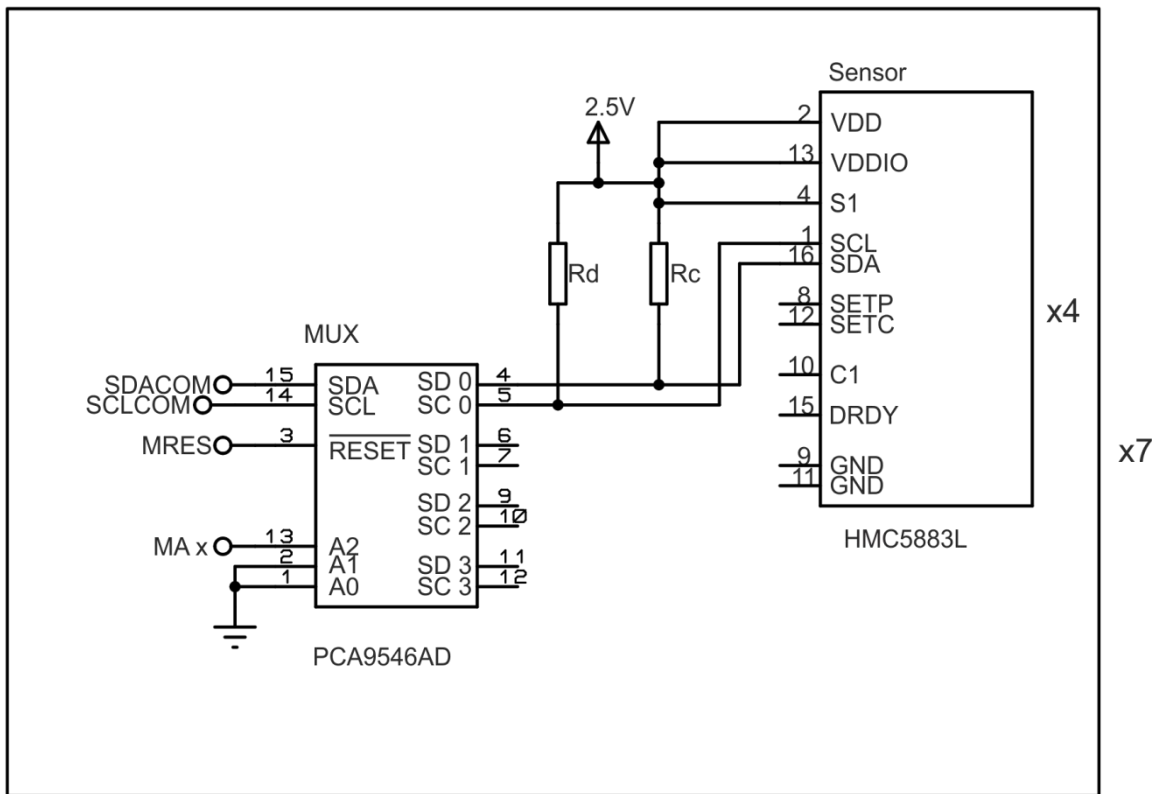
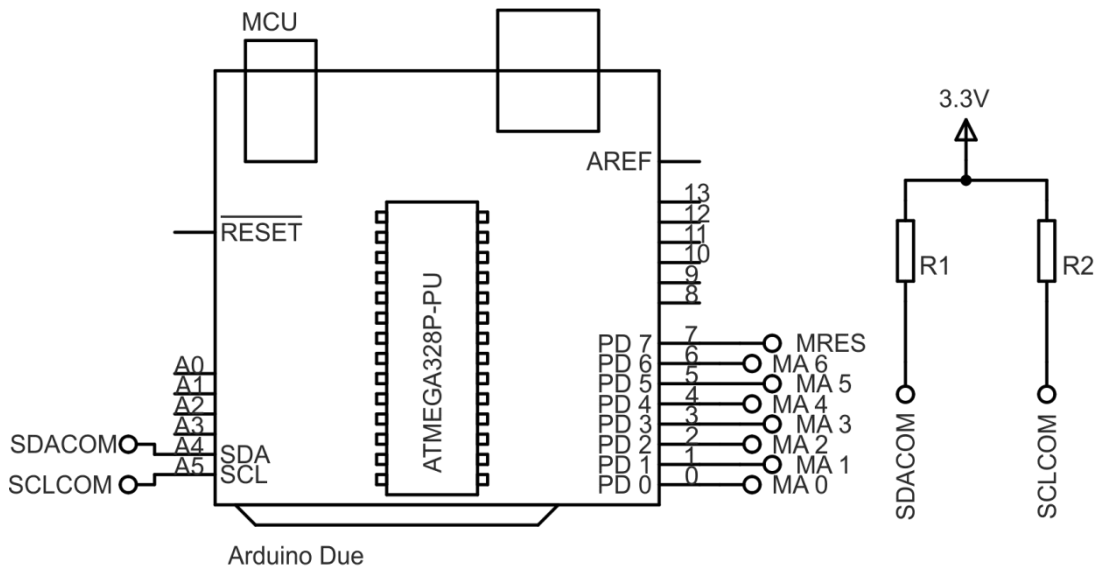


Figure 5.29 - Multiplexing circuit diagram.

### 5.3.2 Software

The purpose of the software is to convert user-readable input to single-byte commands for the multiplexers and sensors, and to read back and then save or display the magnetic data or configuration settings from the sensors. See Appendix III – FTS Octave Code for .m files. During setup the serial channel is opened to communicate with the microcontroller, the handshake character is read from the microcontroller and the identification register is read. The bypass switch is also initialised to the ‘bypass’ setting. A switch statement is used which mirrors the

firmware program, although some extra cases are added containing some useful combinations of functions. The input to the switch statement is generated using a graphical menu. The menu is shown in Figure 5.30, and the switch statement is shown as a flow chart in Figure 5.31. Synchronisation between the PC and the microcontroller programs is maintained by reading the handshake character before beginning any of the subroutines.

The options 'multiple readings' and 'auto readings' (cases 4 and 8) result in either a set number of readings to be taken, or for readings to be taken repeatedly for a set number of seconds. Each reading is saved to its own sequentially-numbered file, along with a timestamp, the ID list and configuration data. The difference between 'multiple' and 'auto' readings is that the latter controls the bypass switch as well as the sensors and names the files according to the state of the bypass switch as well as numbering them sequentially. The bypass switch (Section 3.4.3) controls whether a 'dark' frame or an 'image' frame is being taken, so automatic file naming according to bypass switch state allows dark frame subtraction to be performed.

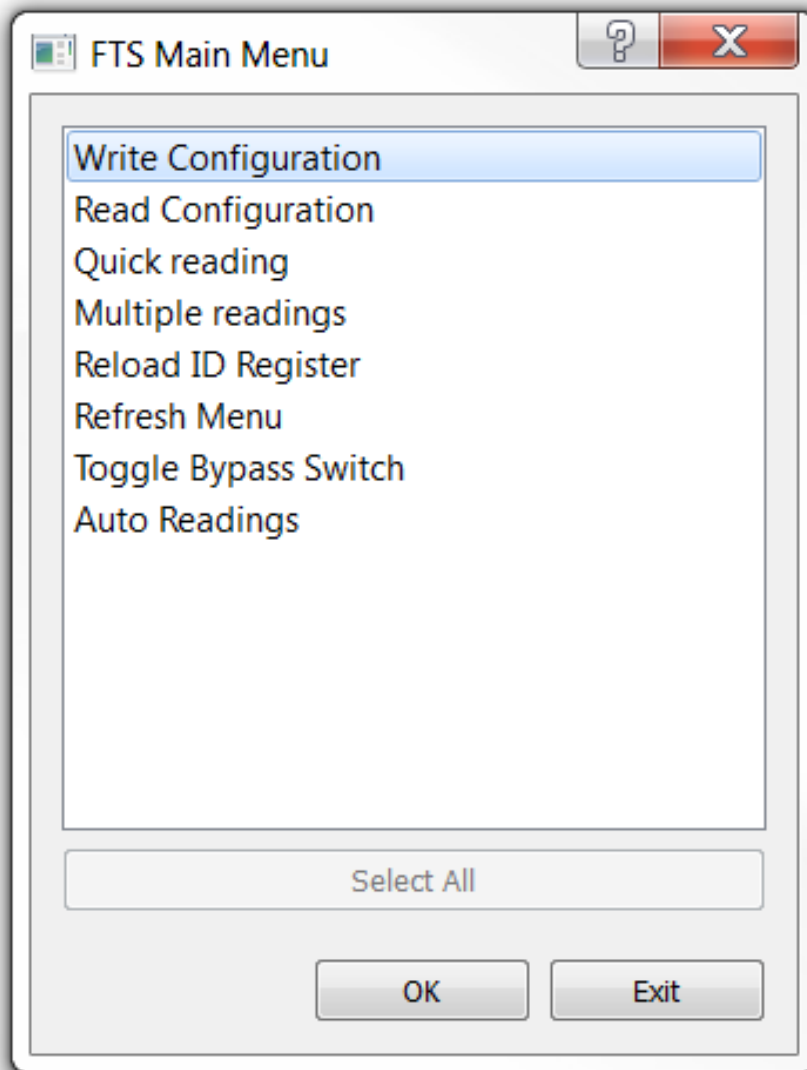


Figure 5.30 - Main menu of the FTS software.

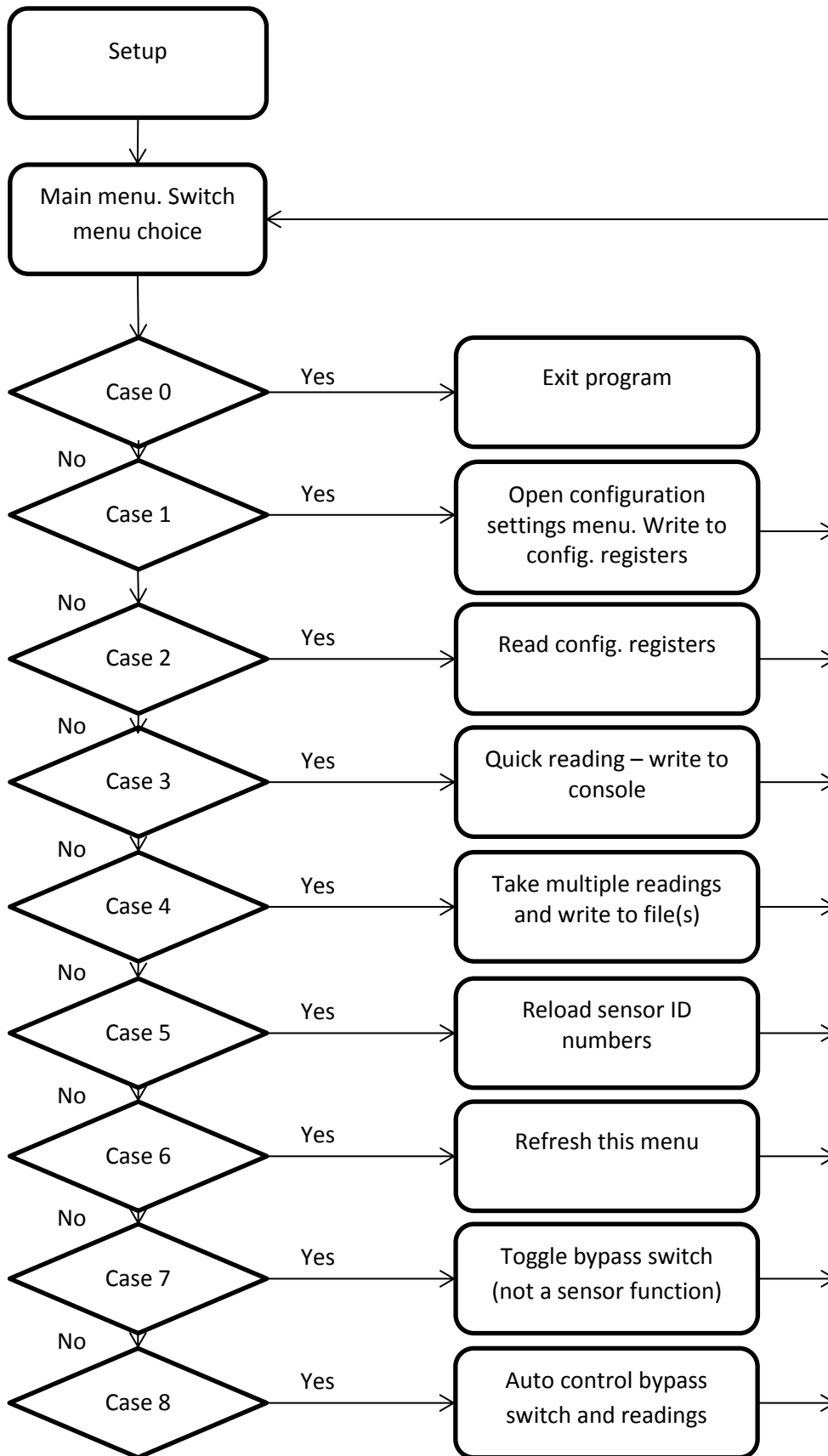


Figure 5.31 - Flow diagram of Octave software.

### 5.3.3 Verification and calibration

An initial verification test is conducted by applying a current through a single wire passing through multiple core apertures. Figure 5.32 shows some example data from this setup. The left hand plot shows the magnetic sensor data, scaled to give units of  $A\ m^{-1}$ . The data does not pass through the origin, possibly due to ambient magnetic field. This offset is easy to remove by subtraction, giving the plot on the right hand side. The zero-offset sensor data is given alongside an ideal predicted set of data (dotted line). The gradient of the measured data does not match the predicted data, nor is it consistent between sensors. This is to be expected, since no account is taken of the current-carrying wire's geometry.

The simulation results in Figure 5.10 show that there is an effect on the airgap magnetic field from currents outside of the core aperture, and therefore a model of the currents through and around the sensors is necessary to compensate for this leakage effect. The effect of circuit/cell geometry on measurements is further illustrated by manually agitating the current-carrying wire while measurements are being taken, for a constant current. The magnetic measurements are presented in Figure 5.33 along with magnetic data from a constant current in a stationary wire. Moving the wire clearly affects the sensor readings, whereas for the stationary wires the readings are not strongly time-varying.

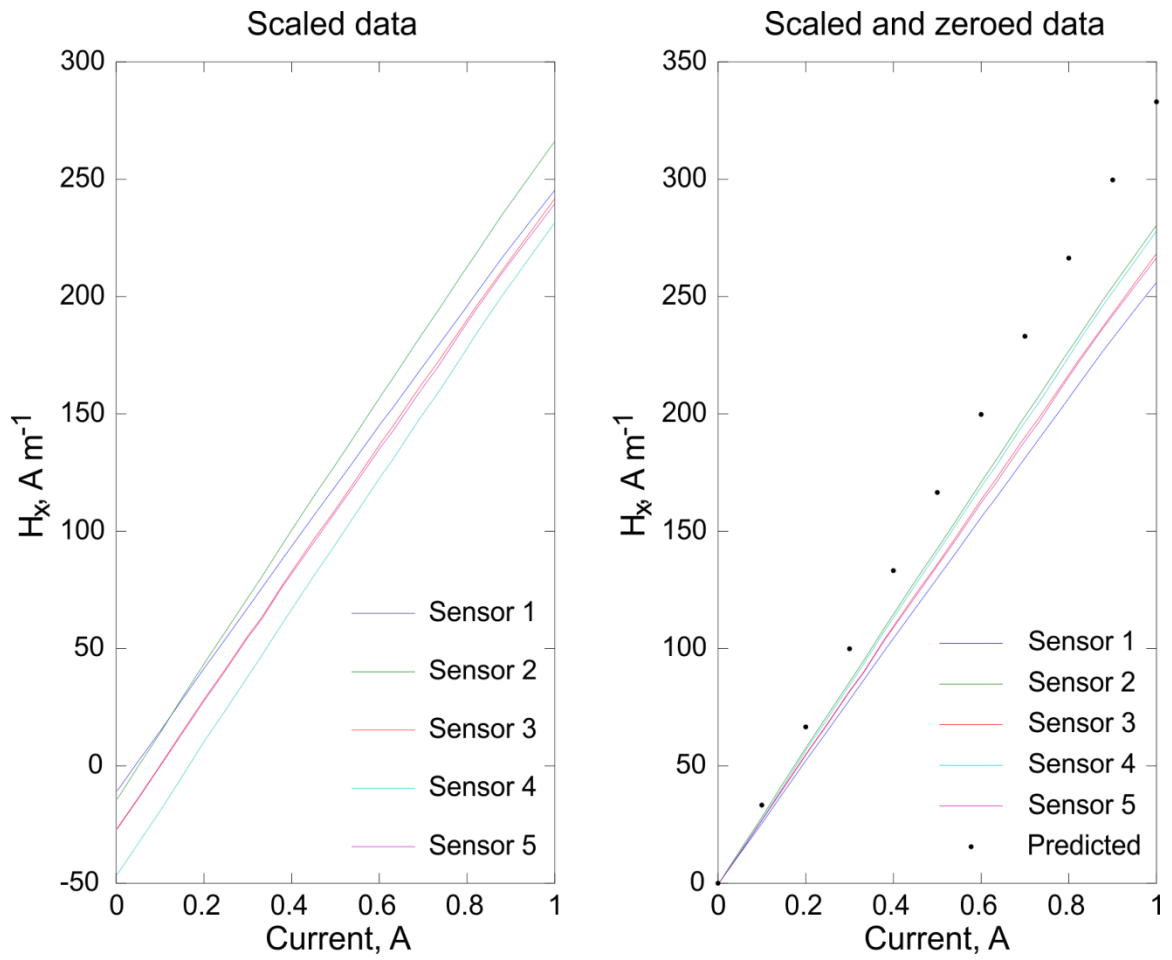


Figure 5.32 -  $h_x = \text{sensor data} / (\text{sensor gain} \times \mu_0)$  versus current for an arbitrary wire geometry. Right hand plot has been forced through the origin. Dotted line shows ideal behaviour based on airgap length.

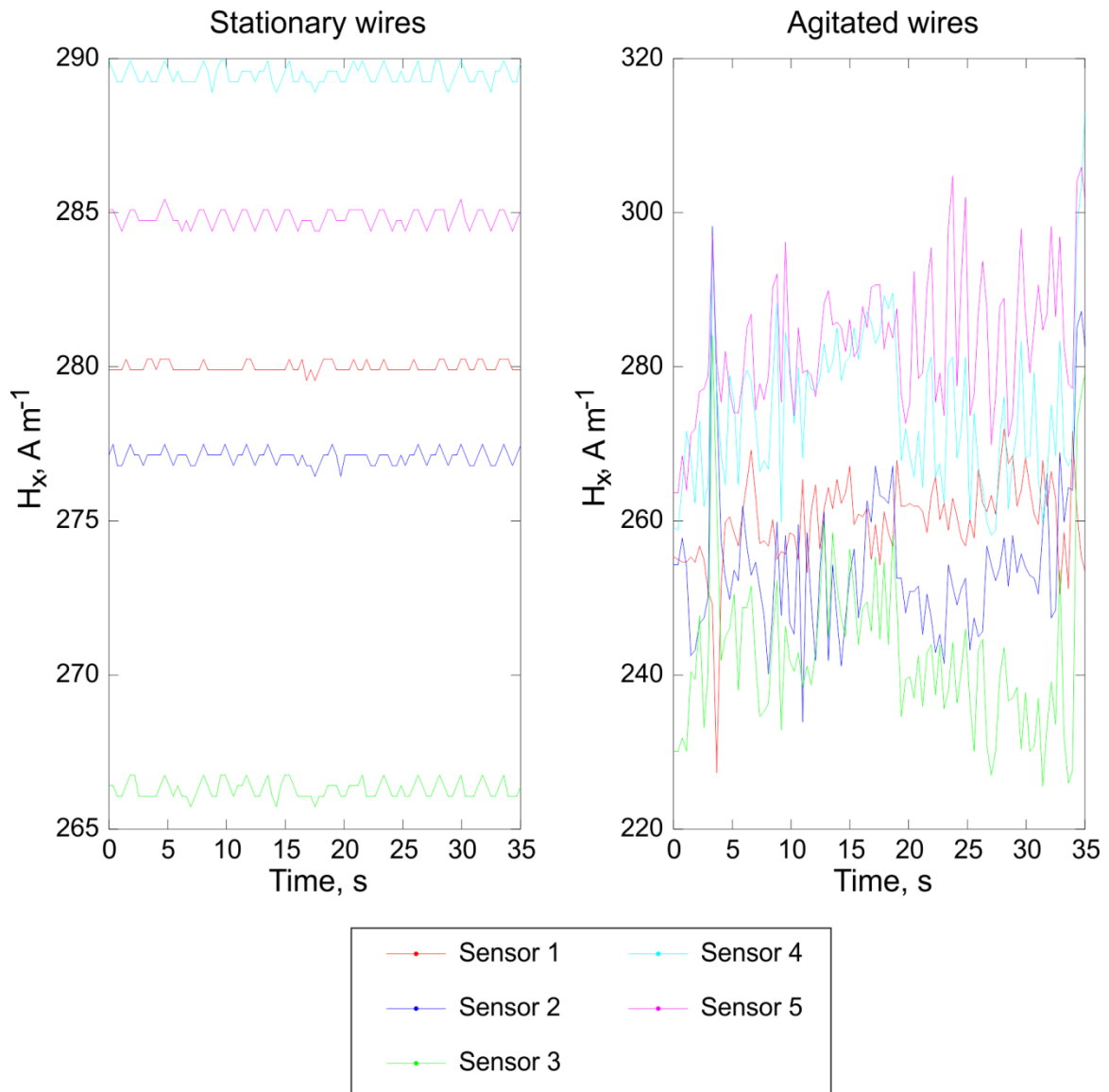


Figure 5.33 – The effect of agitating the current-carrying wire geometry on magnetic measurements taken when a current of approximately 1 A is passed.

The results shown in Figure 5.32 and Figure 5.33 agree with the results of Sections 5.2.1 and 5.2.2 in that the geometry of the circuit/cell under test is causing a non-ideal sensor response to segment currents. In order to compensate for ‘bleed’ effects between cores and the effect of terminal and plate currents on readings, a leakage compensation matrix is required. In order to cancel out effects of position of the sensor within the airgap, measured data is used to construct the compensation matrix. One of the replica plates used to assemble the resistive cell model is shown in Figure 5.34, and the resistors and wires used to simulate the electrolyte are shown in Figure 5.35.

The resulting  $K_{core}$  matrix is shown in Figure 5.36 along with the ideal coupling, a scaled identity matrix  $kI$ . As with the simulated compensation matrix,  $K_{core} \cong kI$ . Compensated measurements of a uniform and a step-

changing current distribution, using the resistor wire model, are given in Figure 5.37. The mean absolute errors are presented in

Table 5.5. Mean absolute errors are smaller than in the simulated-only case, possibly since the finite element solutions are approximate. The system operated at approximately 2.9 frames per second during this test.



Figure 5.34 – Copper-clad board cut to match Shield 027 plate dimensions. Holes for ‘electrolyte’ wires are numbered 1-20. Plate tab is at top left, terminal may be screwed to the tab.



Figure 5.35 –  $10\ \Omega$  resistors used to simulate the electrolyte.

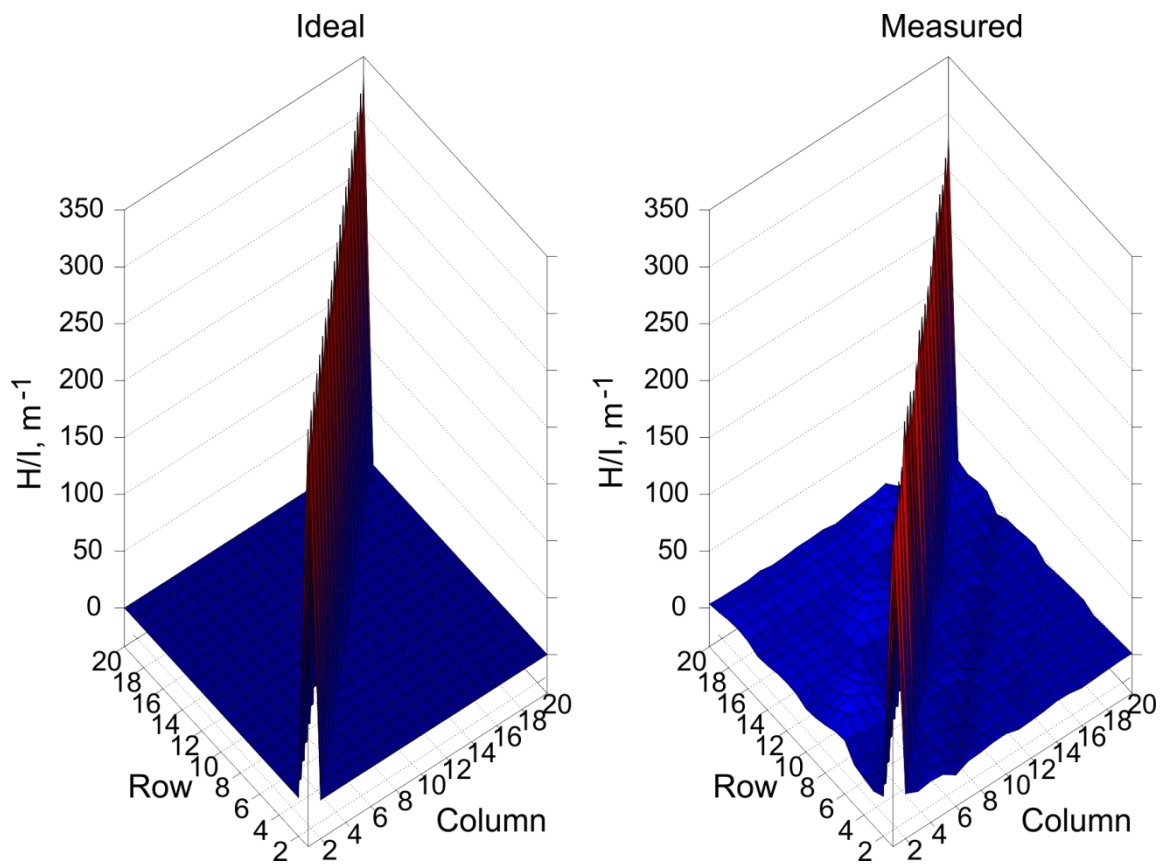


Figure 5.36 - Identity matrix (ideal sensor system) and the measured  $K_{core}$  matrix.

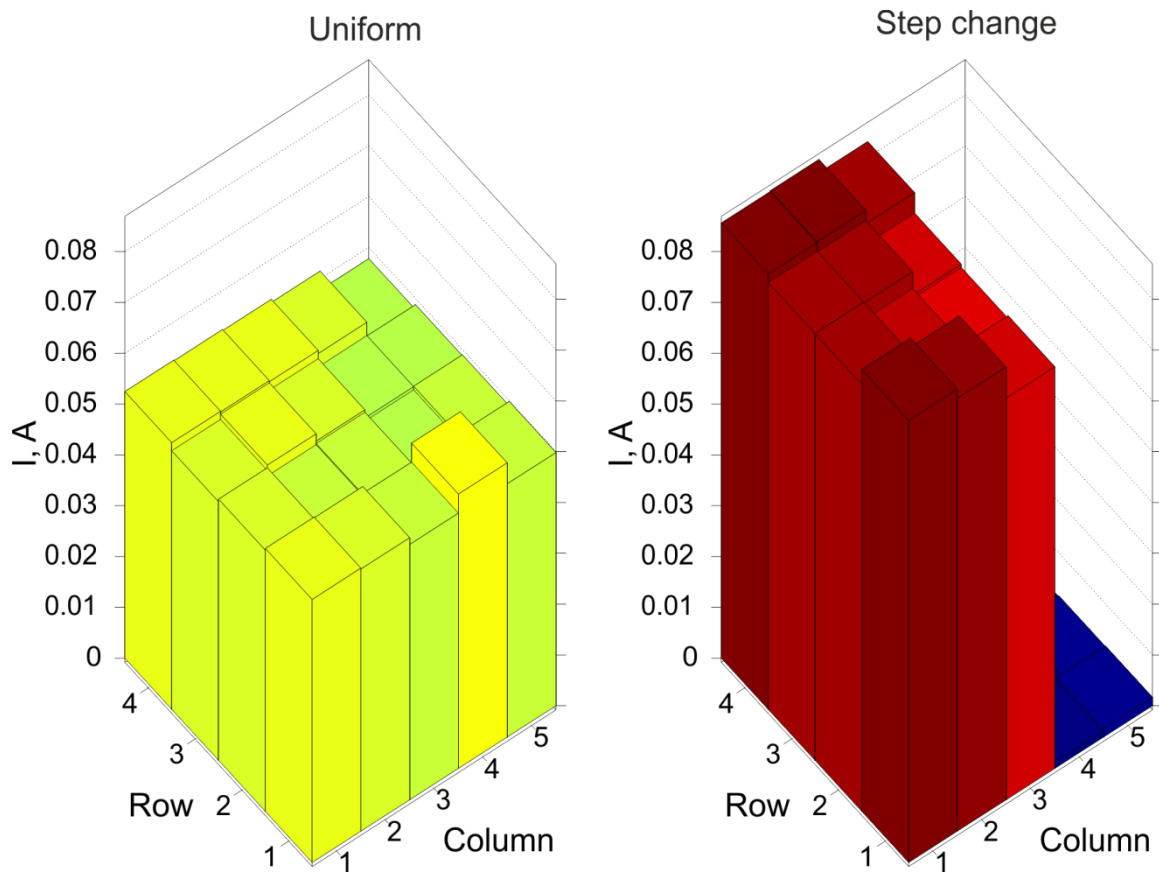


Figure 5.37 – Reconstruction of uniform (left) and step-changing (right) current distributions, from real measurements.

Source distribution	$\ I_s - I_r\ $
Uniform	2.65 %
Step-changing	4.21 %

Table 5.5 – Mean absolute error of the two reconstructions in Figure 5.37.

## 5.4 Summary of Chapter 5

An existing current distribution measurement system, based on ferrous cores and magnetic sensors, is re-designed for use with a lead acid test cell made from automotive battery plates. The layout of cores is novel in this application, and is designed around the cell plate dimensions so as to maximise the available cross-section area through which the cell electrolyte may pass. The fabrication of custom made cores is enabled by the use of laminated electrical steel, which is a novel material in this application as well. The magnetic field strength in the airgap of a given core is found to be dependent on currents other than the current which passes through the aperture of that core. This behaviour is explained in terms of a coupling matrix  $\mathbf{K}_{core}$ , which may be constructed by measuring partial currents and then used to reconstruct current distribution to within a reasonable error margin. The validity of a compensation matrix generated using a thin wire model for solving a distributed current, such as that in the volume of electrolyte in a test cell, is shown by simulation. This finding means that measured partial current data may be obtained using a resistive wire circuit in order to construct  $\mathbf{K}_{core}$ . The sensor and core array is incorporated into a user-controllable system which can configure the sensors as well as read magnetic data to file. By integrating the bypass switch control with the sensor system, magnetic measurement files may be labelled according to whether they are 'dark' or 'image' frames.

## 6 Experimental Verification of Magnetic Tomography System

This chapter describes the method and results of an experiment designed to verify the current distribution estimations produced using the magnetic tomography system. The hardware and solver algorithm necessary for the experiment have been described in previous chapters. The magnetic tomography system consists of an array of magnetic sensors (see Section 3.2) and a solver algorithm (Section 3.2 and Chapter 4) which estimates current distribution in a test cell (Section 3.4.2) from the magnetic measurements. These current distribution estimations are compared with the results from a flow-through sensor array (Section 3.3.2 and Chapter 5).

The procedure of the experiment is designed to provide repeated bi-directional constant-current test pulses at various states of charge, to allow any effects of state of charge on current distribution to be observed. Furthermore, both of the current distribution measurement methods employed in this experiment capture data almost simultaneously, as they utilise sensor arrays rather than scanning sensors. As a result, repeated measurements may be taken during a current pulse so that any change in current distribution during that time may be observed.

Measurements from the flow-through sensor show that most of the time the current distribution of the test cell is highly uniform, with the exception of a set of measurements taken at a low state of charge, after several days of cell cycling. Corresponding terminal voltage data suggests that the cell is operating abnormally during this time. This non-uniform current distribution is used as a test case for the magnetic tomography system alongside a typical uniform distribution taken at a higher state of charge on the same day.

Results from the magnetic tomography system for these two test cases are presented, and the effect of varying a small selection of forward model parameters on solution quality is investigated. It is found that approximate agreement with the flow-through sensor measurements is possible, and solutions are somewhat robust to reasonable magnitudes of error in the forward model definition. On the other hand, making significant improvements to the solution quality through altering model parameters is impractical. This highlights the importance of careful hardware design and accurate forward model definition. Some ‘time-lapses’ of images from both measurement methods over the course of a single pulse are presented, demonstrating that current distribution may be resolved in both space and time using magnetic tomography of a flow-through sensor.

## 6.1 Hypothesis and Motivation

The primary purpose of this experiment is to test whether the magnetic imaging system and solver previously described may be used for magnetic tomography, to produce non-invasive spatially resolved measurements of current distribution in a real lead acid cell. Results from applying the solver to simulated and measured data (Chapter 4) indicate that under certain conditions the current distribution may be reconstructed accurately, although errors in measurement of magnetic field and problem geometry are shown to have a detrimental effect on solution quality. By applying the method to real measurements, the effect of experimental errors may be seen in the results. It is also important to try out the magnetic imaging method in practice in order to gain a better understanding of the limitations of the hardware and experimental procedure in order to work towards better studies in future.

To verify the results from the solver, an invasive measurement method (the flow-through sensor array) is also employed. The flow-through sensor has also been shown to work in simulation and with real measurements taken on a resistive model (Chapter 5). It is therefore used as a control or baseline measurement system against which to compare the magnetic tomography system. It is hypothesised that the error between the results from the two measurement systems will be reasonably small.

While an example exists in the literature of using such a sensor array on a fuel cell [67], it has not been applied to any lead acid cell before. The literature review presented in Section 2.2 shows that there are few other techniques which can produce an instantaneous spatially resolved measurement of current distribution in an electrochemical cell. As such, the flow-through sensor array results form not only a control against which to verify the non-invasive measurement results, but also demonstrate a potentially useful technique which is novel in this application.

## 6.2 Method

### 6.2.1 Experimental system

Figure 6.1 shows the cell and sensing system, including data and power flows. The magnetic sensor system, current source, and test cell design shown in Figure 6.1 are as described in Chapter 3. The flow-through sensor (FTS) system described in Chapter 5 (see also Appendix II – FTS Arduino Firmware and Appendix III – FTS Octave Code) is also employed and shown in the system diagram. Data from the magnetic imaging system is interpreted by a solver (Chapter 4

and Appendix IV – Solver Octave Code) and compared against compensated data from the flow-through sensor. Table 6.1 gives some of the parameters used in the experiment.

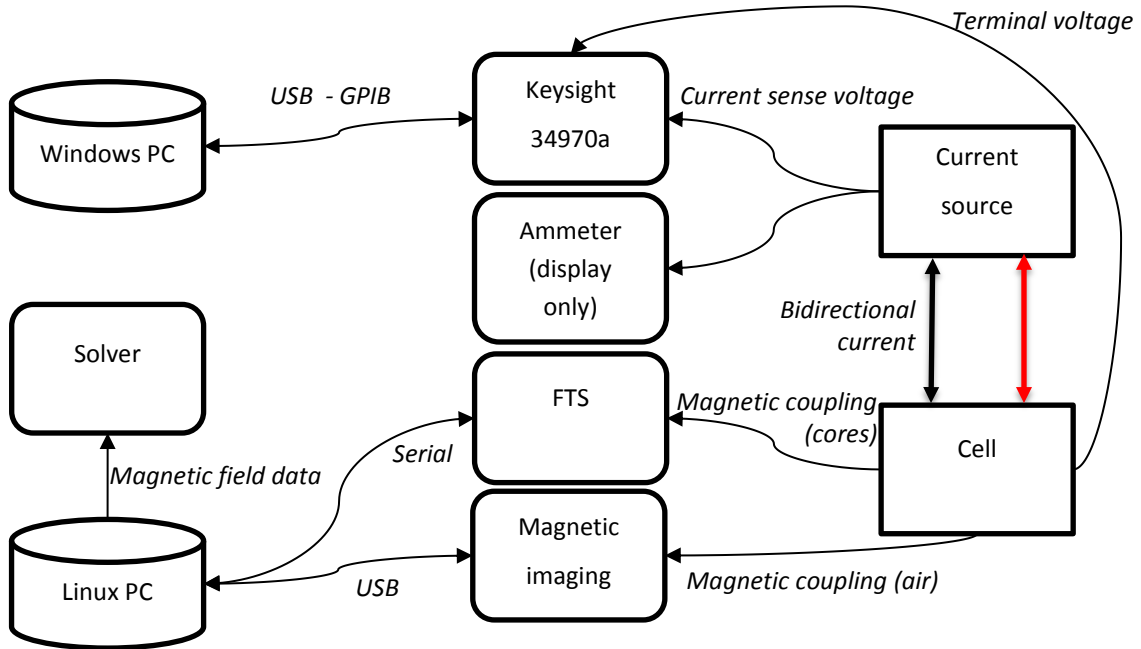


Figure 6.1 - System diagram.

Parameter	Value
Labview measurement rate	1 s <sup>-1</sup> during test pulses, 0.2 s <sup>-1</sup> during discharge pulses
Magnetic sensor gain	1090 lsb/Gauss
FTS sensor gain	1090 lsb/Gauss
Current distribution image resolution	5 × 4
Magnetic sensor frame rate	Approx. 0.8 s <sup>-1</sup>
FTS frame rate	Approx. 3 s <sup>-1</sup>
Test current pulse	5 A, 30 s
Discharge current pulse	3.2 A, 1800 s
Charge voltage	2.35-2.4 V
Electrolyte specific gravity at 100 % SoC	1.285 kg L <sup>-1</sup>
Nominal cell capacity @ 0.2 C	5 A h
Measured cell capacity @ 0.2 C	7.9 A h

Table 6.1– Experimental parameters.

The grid model is intended to match the real plate grid in terms of resistance distribution. This is achieved by removing the paste from a sample grid (Figure 6.2) taken from the same battery, and measuring the position and thicknesses of the grid members using Vernier callipers and a micrometer screwgauge. The grid member resistances are found by dissecting the grid and measuring the resistance of each grid member using a Keithley 2612 Sourcemeter [107] to take 4-wire resistance measurements. The resistances of the different grid members

are realised in the model by adjusting the thickness of the member in the  $xz$  plane (the plane of the plate) in order to control the cross-section area of each member, while keeping the  $y$  thickness constant. The resulting model is shown in Figure 6.3.

The experiment is carried out in a fume cupboard due to the open, unsealed cell design presenting a risk of acidic vapour and production of flammable hydrogen and oxygen due to the gassing reaction (2.4). The fume cupboard itself contains ferrous material, probably steel, as part of the splashback. This material can be detected using a magnet. This material has an effect on the surrounding magnetic field including that which is measured by the sensor array. Therefore it must also be included in the forward model (Figure 6.4). It is not possible at the time of conducting the experiment to measure the magnetic permeability of the material. A value of  $\mu_r = 500$  is chosen for the forward model. The distance from cell to wall is also subject to some uncertainty as the ferrous material is housed behind a plastic coating of unknown thickness.

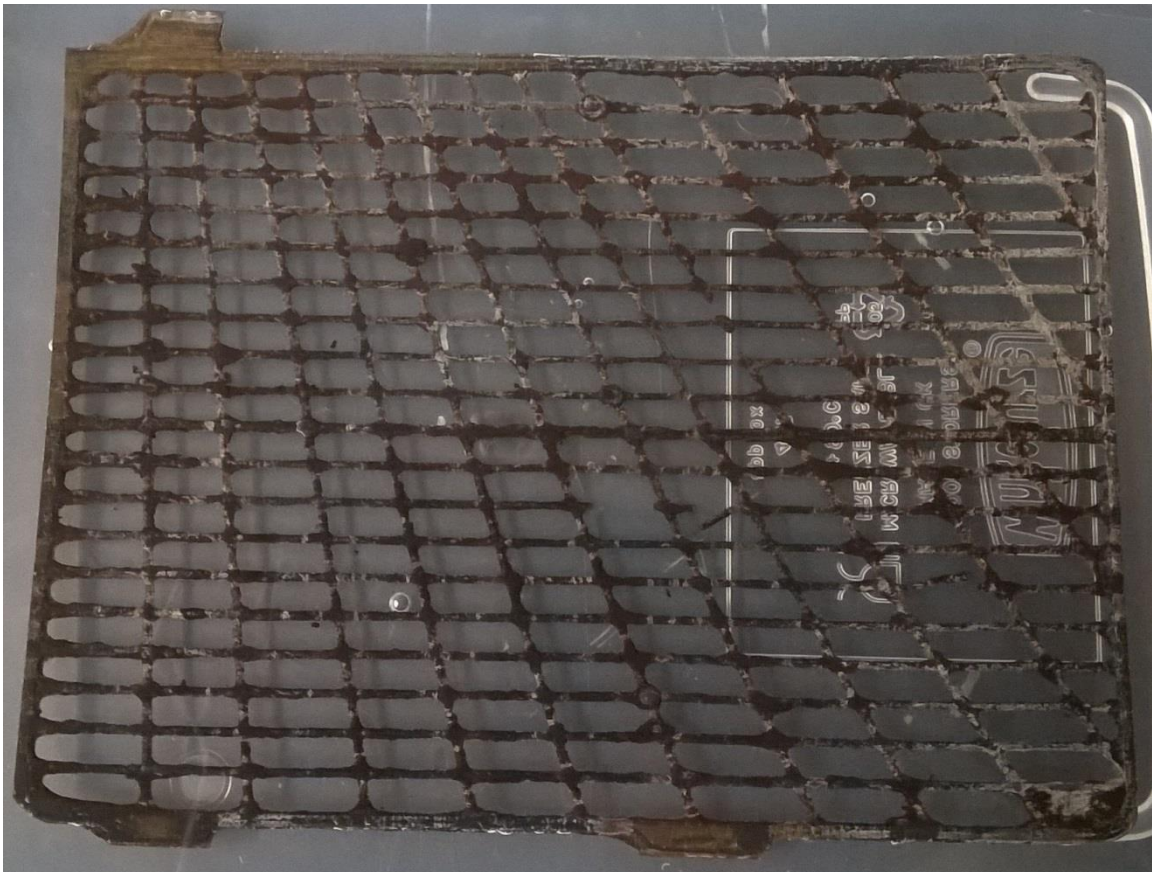


Figure 6.2 – Unpasted plate grid.

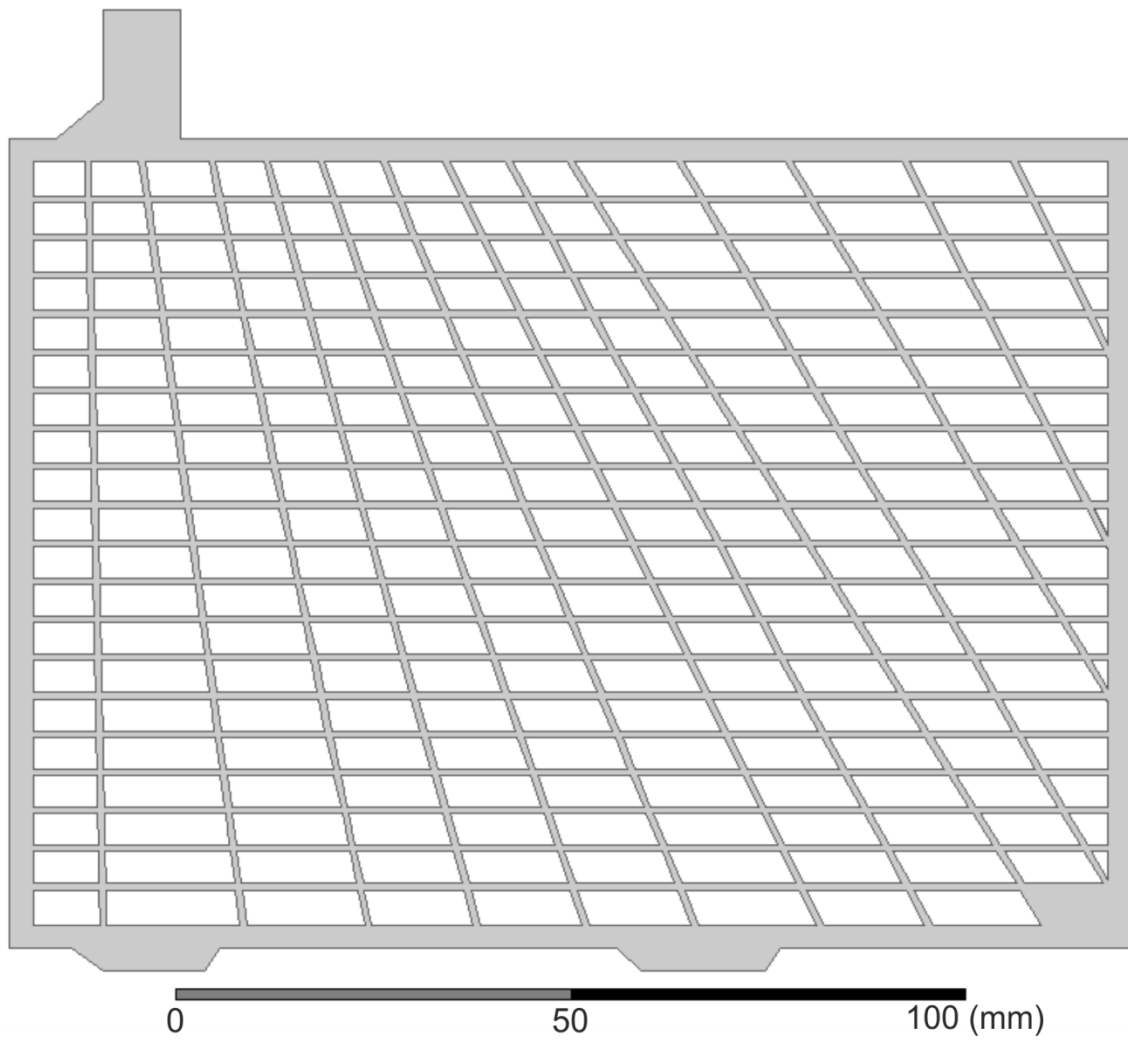


Figure 6.3 - Modelled plate grid.

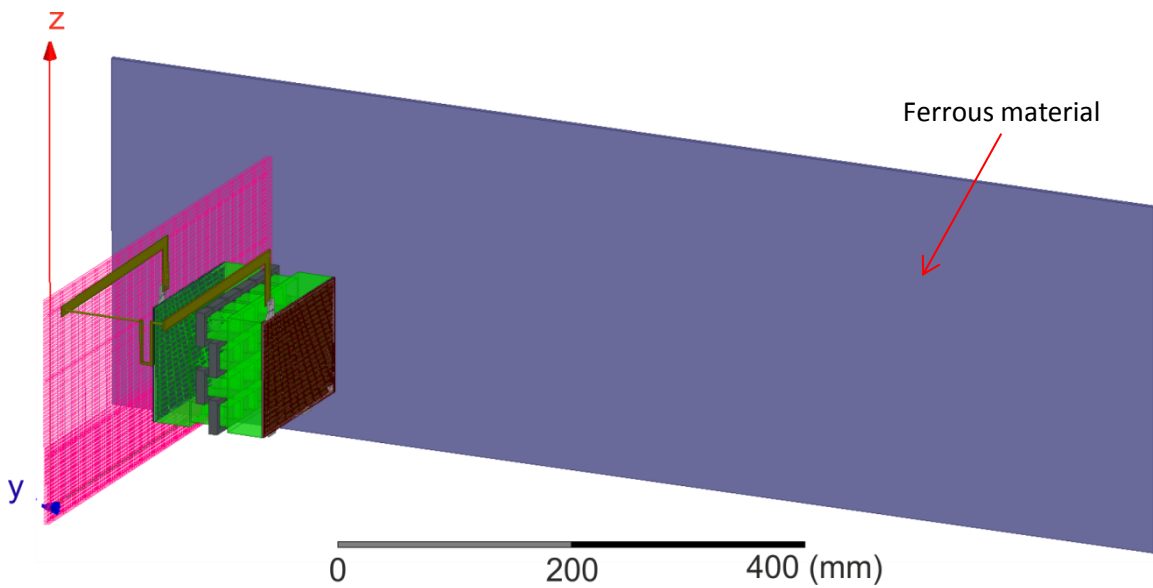


Figure 6.4 – Revised forward model, with ferrous back wall included.

## 6.2.2 Procedure

The current profile used is shown in Figure 6.5. The timing of the current pulses can be seen from the cell terminal voltage measurements (30 s discharging, 30 s rest, 30 s charging). In between current pulses the cell is bypassed, but current still flows in the current source and terminal wires. During this time, 'dark' frames are obtained by both the magnetic imaging system and the flow-through sensor. The bypassing is automated by the microcontroller that controls the flow-through sensor, but the polarity of the current is controlled by the user via a manual switch. The magnetic tomography system uses a moving time-averaging (median) filter to remove transient magnetic noise from both the dark frame and the image frame. The images presented use 5 frames for the moving average, except for the time-lapse image (

Figure 6.26) where 3 image frames are used to allow more reconstructions to be made during the current pulse.

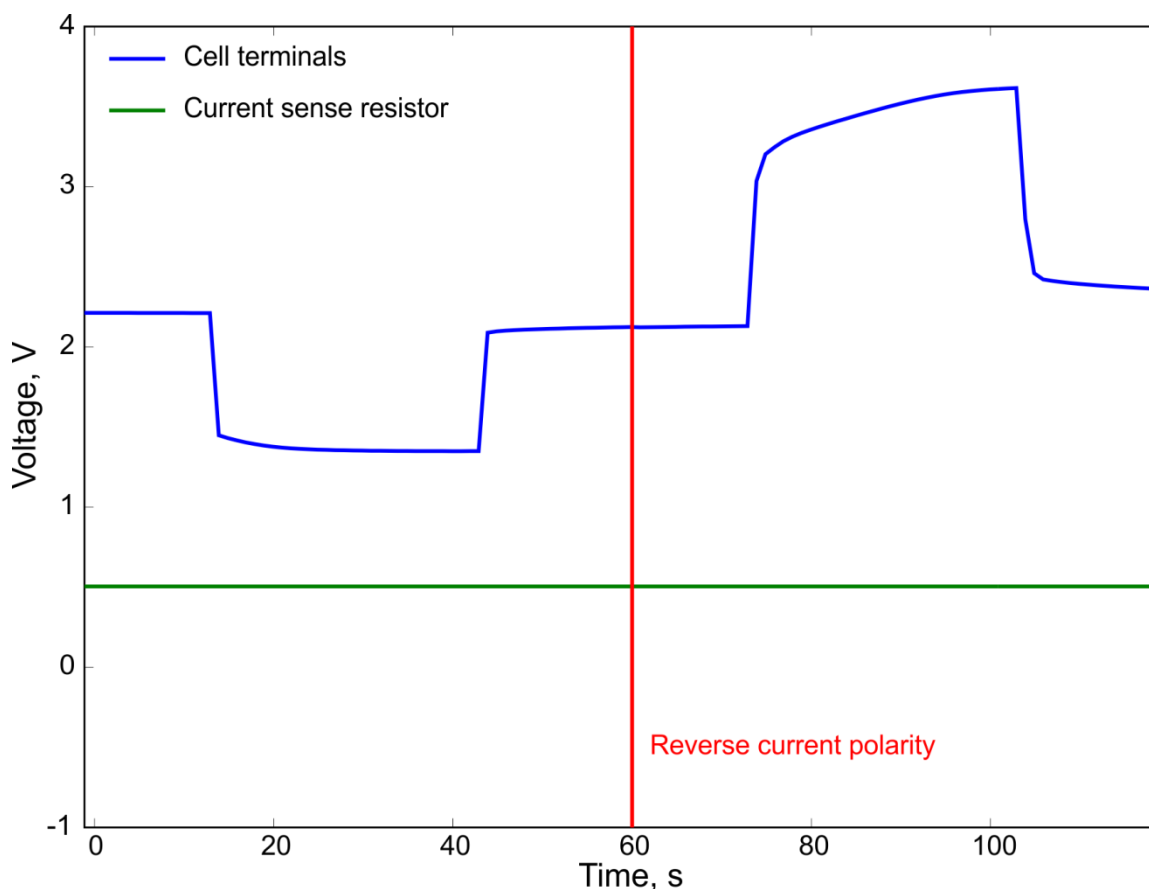


Figure 6.5 – Example current profile for one discharge-charge cycle at 5 A.

A complete set of discharge-charge cycles at one state of charge is shown in Figure 6.6. Current polarity switch intervals of 60 s are indicated – notice the position of the  $t = 555$  s marker is not half-way through the 30 s rest period, indicating that there is some slippage in the timings of the current pulses. This is due to the way the timing is generated in the FTS microcontroller code rather than using a dedicated signal generator. The condition to switch the bypass switch is only evaluated at the end of a complete FTS measurement cycle, so up to + 0.4 s (approx) is added to each discharge or charge pulse. In the pulse train shown in Figure 6.6 the cumulative

error in  $t$  over 10 pulses (570 s) is approximately + 3 s. The set of five discharge-charge cycles is repeated twice at each state of charge of interest.

The magnitude of the current can be approximately calculated from the voltage across the  $0.1 \Omega$  current sense resistor – cell current is also directly measured using a Fluke handheld multimeter but not plotted. The current demand to the current source is set before measurements are taken and a value of current is noted at the start and at the end of the 10 pulse test profile. Variation in terminal current over the course of the pulse cycle is found to be < 8 mA for all tests conducted, and is further decreased if the current source is allowed to reach a steady operating temperature before use. The zero-current glitches in the current sense voltage plot shown in Figure 6.6 (at  $t = [225 \text{ s}, 375 \text{ s}, 435 \text{ s}]$ ) are due to switching the direction of current. Not every current direction switching event is captured by the current sensor voltage measurement because the sampling is asynchronous with the direction switching.

**The procedure to apply bidirectional current pulses and obtain measurements is given in**

Table 6.2. Five discharge-charge cycles are applied at each state of charge. The cell is tested at SoC = [100 %, 80 %, 60 %, 40 %, 20 %]. The 0.2 C capacity of the cell was previously measured at 7.9 A h (Section 3.4.2). To discharge the cell by 20 %, a 3.2 A current is applied for 0.5 h. The cell is allowed to rest for > 0.5 h before beginning the next set of test cycles. Figure 6.7 shows the terminal and current sense voltages for a nearly complete set of tests on day 7 of testing, *i.e.*, after the cell has been cycled for a number of days. The terminal voltage collapses at SoC = 40 % and so further discharging is not performed. The results from this set of tests are presented in Section 6.3, as the fatigued cell produces an interesting test case in terms of its current distribution. Note the current sense voltage is maintained at either 0.5 V (for testing) 0.32 V (for discharging) for the full duration of the tests, even when the cell is being rested (except briefly during current direction switching).

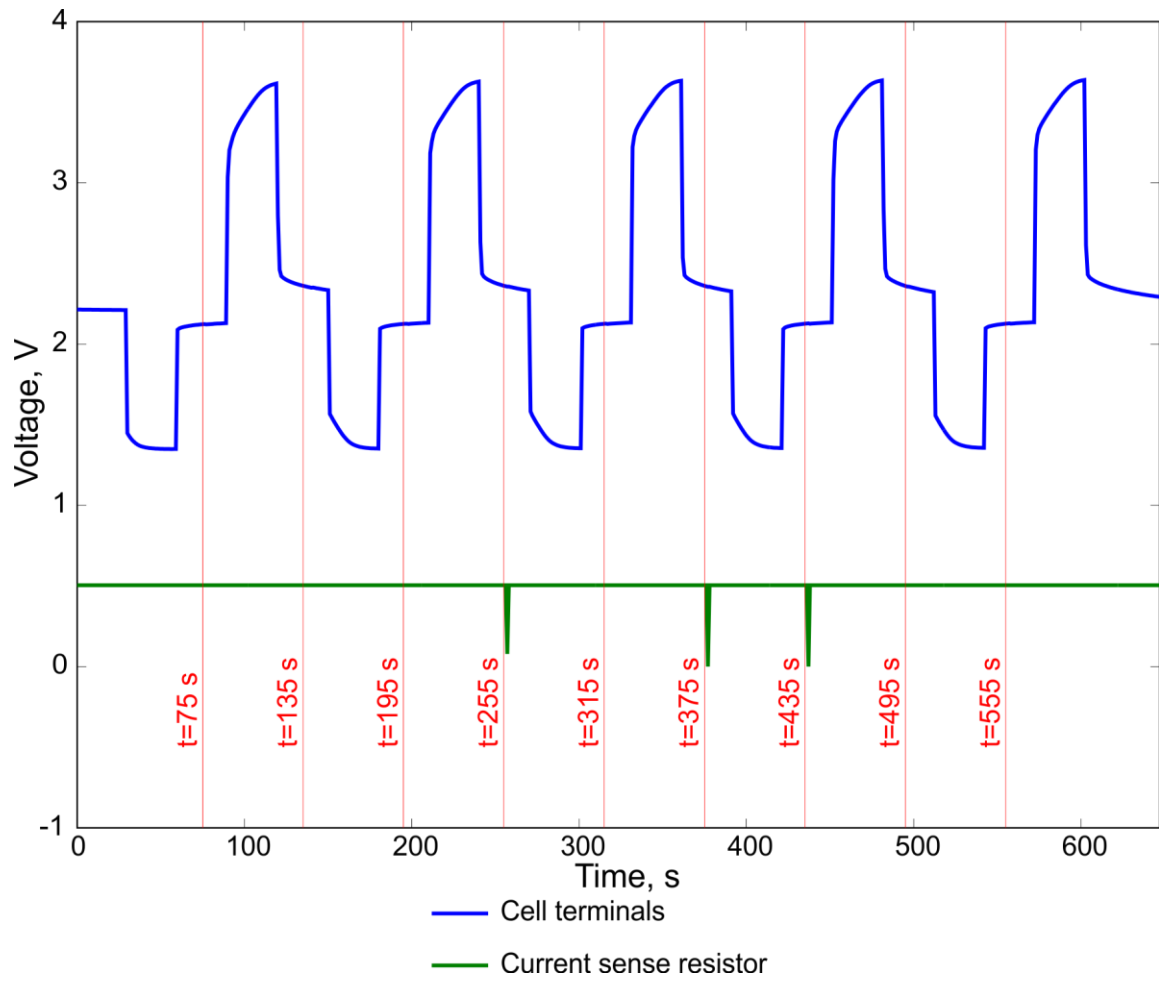


Figure 6.6 – Set of 5 discharge-charge cycles.

Step	Description	Purpose
1	Set manual switch to 'disconnected' position. This ends float charging.	
2	Start magnetic imaging software + hardware.	Setup
3	Start FTS software + hardware.	
4	Start Labview datalogging.	Measurement
5	Set cell bypass switch to 'bypass'.	
6	Set current source to 5 A and connect manual switch in 'discharge' position.	Setup
7	Begin recording magnetic images.	
8	Begin pulse and measure routine in FTS software and set stopwatch.	
9	At $t = [75, 135, \dots, 555]$ s, reverse direction of manual DPDT switch.	Measurement
10	After pulse and measure routine ends, halt magnetic imaging software.	
11	Repeat steps 7 – 10, giving two sets of 5 cycles.	
12	Set current source to 3.2 A and connect manual switch in 'discharge' position.	Control cell
13	Set cell bypass switch to 'through' for 30 minutes to discharge by 20 %.	SoC
14	Rest 30 minutes.	
15	Repeat steps 5-12 until SoC = 20 % or until cell no longer has positive cell voltage.	Measurement
16	Float charge overnight.	Control cell SoC

**Table 6.2– Experimental procedure.**

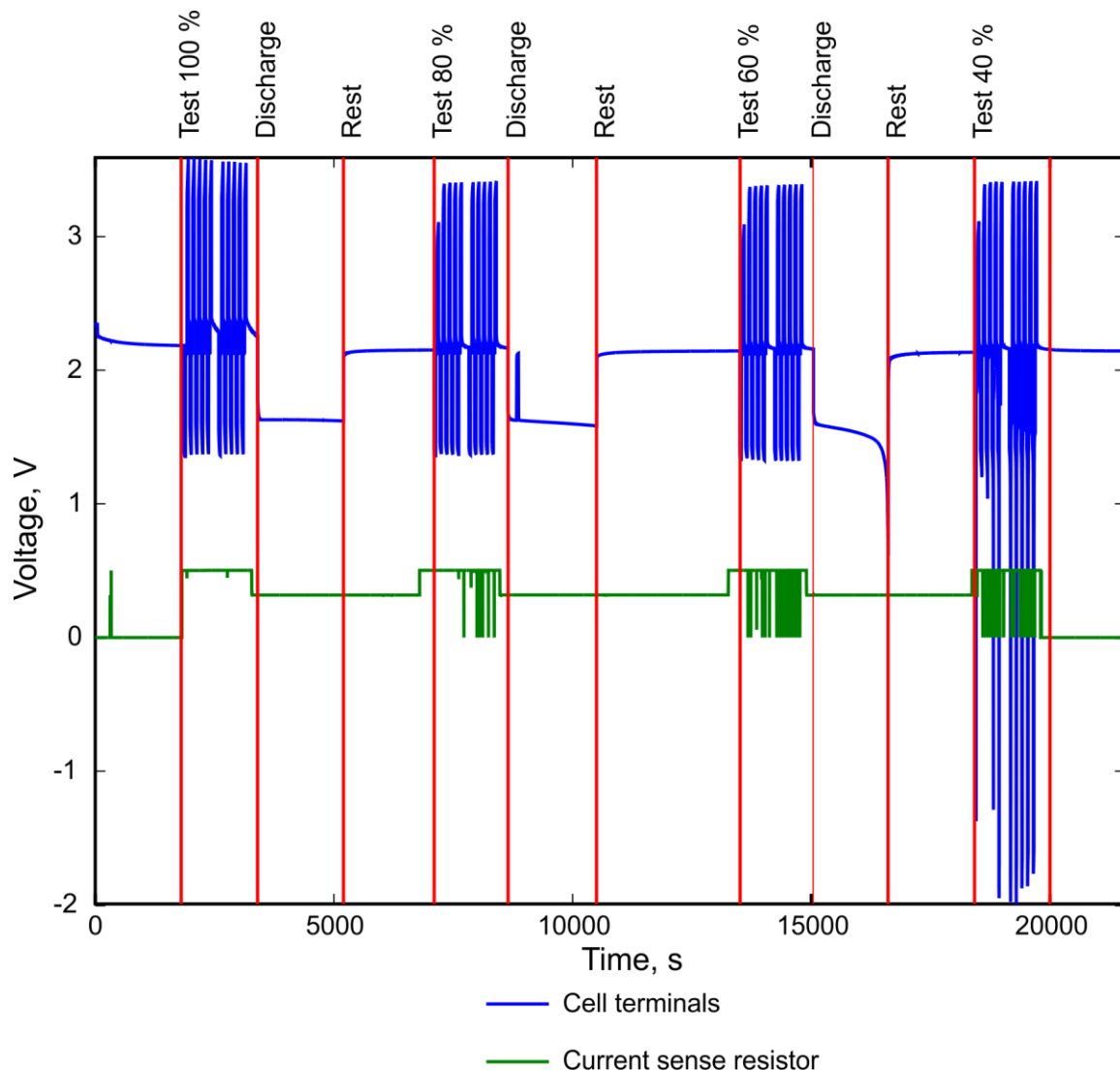


Figure 6.7 – Terminal voltage for a set of tests at [100 %, 80 %, 60 %, 40 %] SoC.

## 6.3 Results and Discussion

### 6.3.1 Cell terminal voltage

Since data is taken at a rate of 0.8 frames per second, for 8-10 sets of 10 charge-discharge cycles, there is a significant amount of magnetic data obtained from the experimental procedure described in Section 6.2.2. In order to observe the performance of the imaging and solver system, two example cases are identified, providing differing current distributions. The first example case is the 1<sup>st</sup> discharging pulse at 100 % SoC, on day 7 of testing (of which the complete terminal voltage and current sense voltage data is shown in Figure 6.7). The terminal voltage for this discharging pulse is shown in Figure 6.8. It is preceded and followed by rest periods – the open circuit voltage before the pulse commences (at the end of a long rest period) is 2.19 V and reaches 2.13 V, 30 s after the discharge pulse ends. During the 5 A

discharging pulse, the terminal voltage measures 1.43 V at the start of the pulse and reaches 1.35 V at the end of the pulse.

For comparison, data is also taken from the 1<sup>st</sup> discharge pulse in the set of data taken at 40 % SoC (Figure 6.9). The open circuit voltage immediately before the pulse is 2.14 V and settles to 1.94 V 30 s after the pulse ends. During the 5 A pulse, the terminal voltage measures 1.34 V initially and falls to -1.38 V at the end of the pulse. This negative terminal voltage indicates that the cell is not operating normally. It is possible that the cell has lost capacity during testing and is actually deeply discharged, rather than at 40 % of its actual current capacity. Figure 6.7 shows that the terminal voltage reaches below 0 V at various points in this set of tests, as well as reaching below 1 V while discharging the cell from 60 % to 40 % (around  $t = 16500$  s).

While operating the cell in this region is not applicable to normal use and may cause damage to the cell, it appears to cause a highly non-uniform current distribution which makes a good test case for the imaging system. The current distributions observed in the two test cases are presented in Section 6.3.2.

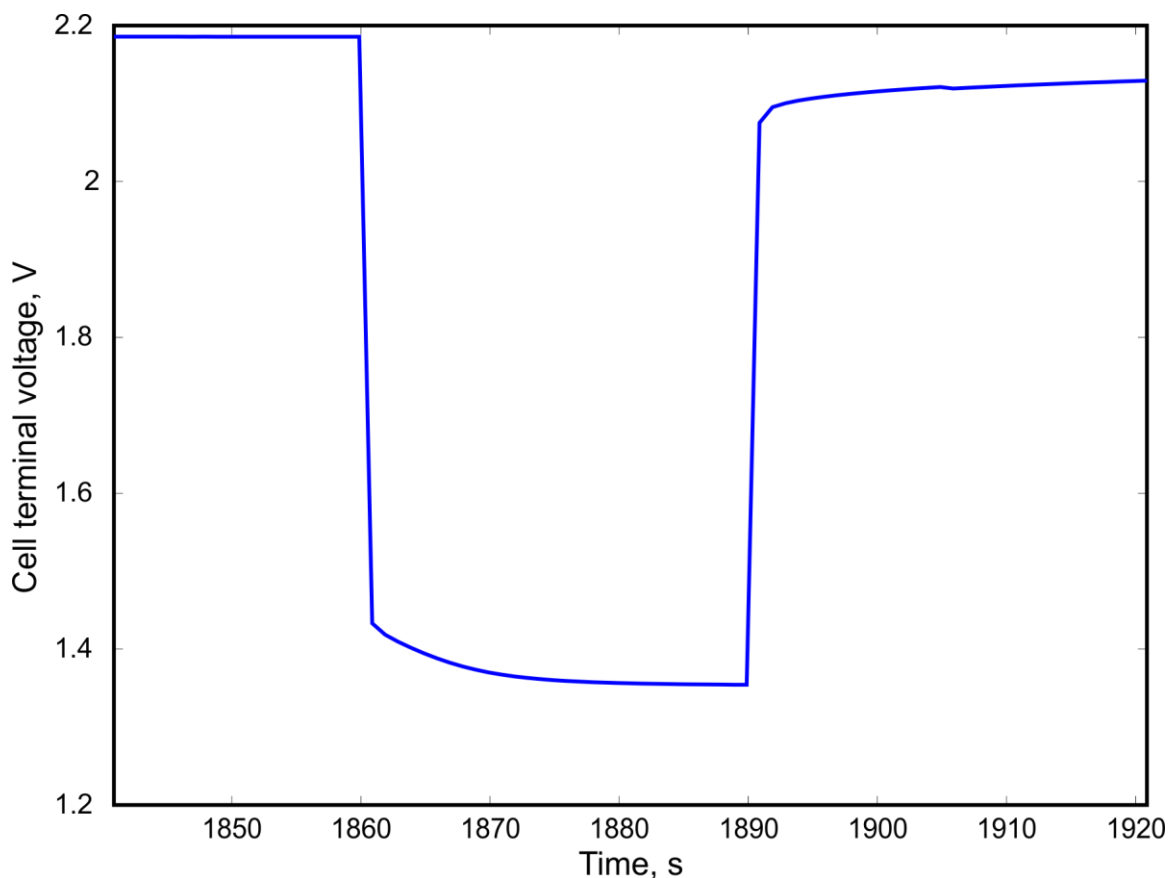


Figure 6.8 – Terminal voltage during 1<sup>st</sup> pulse, 100 % SoC, day 7.

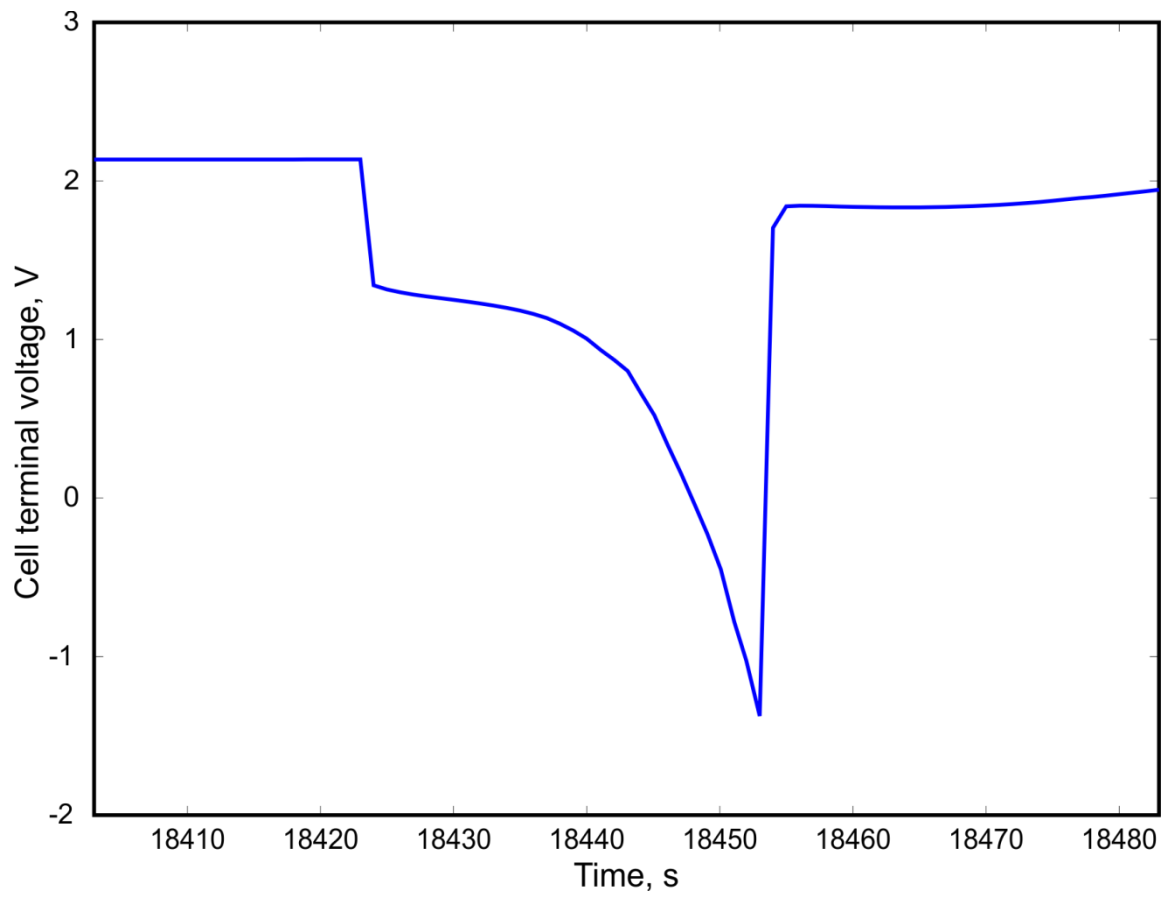


Figure 6.9 – Terminal voltage during 1<sup>st</sup> pulse, 40 % SoC, day 7.

### 6.3.2 Flow-through sensor measurements

The purpose of these measurements is to provide current distribution data against which to compare the solution from the magnetic imaging system. To test the performance of the magnetic imaging system at reconstructing different current distributions it is necessary to identify some test cases which exhibit different degrees of non-uniformity,  $i_{max}/i_{min}$ .

Figure 6.10 shows an example of the data from the flow-through sensor from day 7, 100 % SoC. The measured current distribution is almost uniform, with an  $i_{max}/i_{min} = 1.12$ . The uniformity of the current distribution could be due to the separation between the plates causing increased electrolyte resistance. In a commercial battery such as the Shield 027 the plates are separated by a porous material approximately 1 mm thick, whereas in this cell the plate separation is 102 mm. Therefore the electrolyte resistance dominates the resistance of the cell, and voltage drop across the plate resistance becomes negligible by comparison with the voltage drop across the electrolyte resistance.

**An example of a larger degree of non-uniformity is found during the SoC = 40 % tests. The cell exhibits a current distribution which becomes more non-uniform over the course of the first pulse after the rest period.**

**$i_{max}/i_{min} = 1.93$  in the example shown in Figure 6.11. This image corresponds to the end of the discharge pulse shown in Figure 6.9. The terminal voltage measures approximately – 1.38 V at the time at which the current distribution measurement is taken.**

Figure 6.12 shows how the current distribution changes over the course of this pulse.

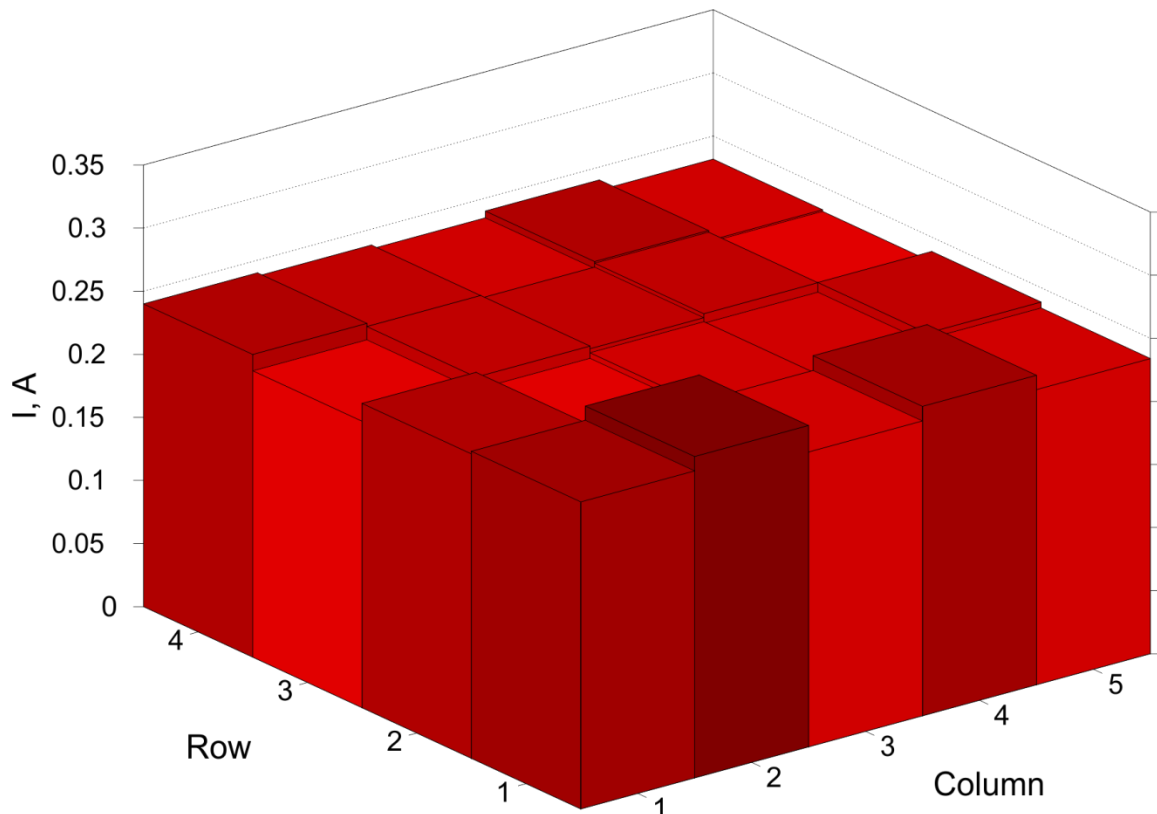


Figure 6.10 – 78<sup>th</sup> frame, 1<sup>st</sup> pulse at 100 % SoC, day 7.

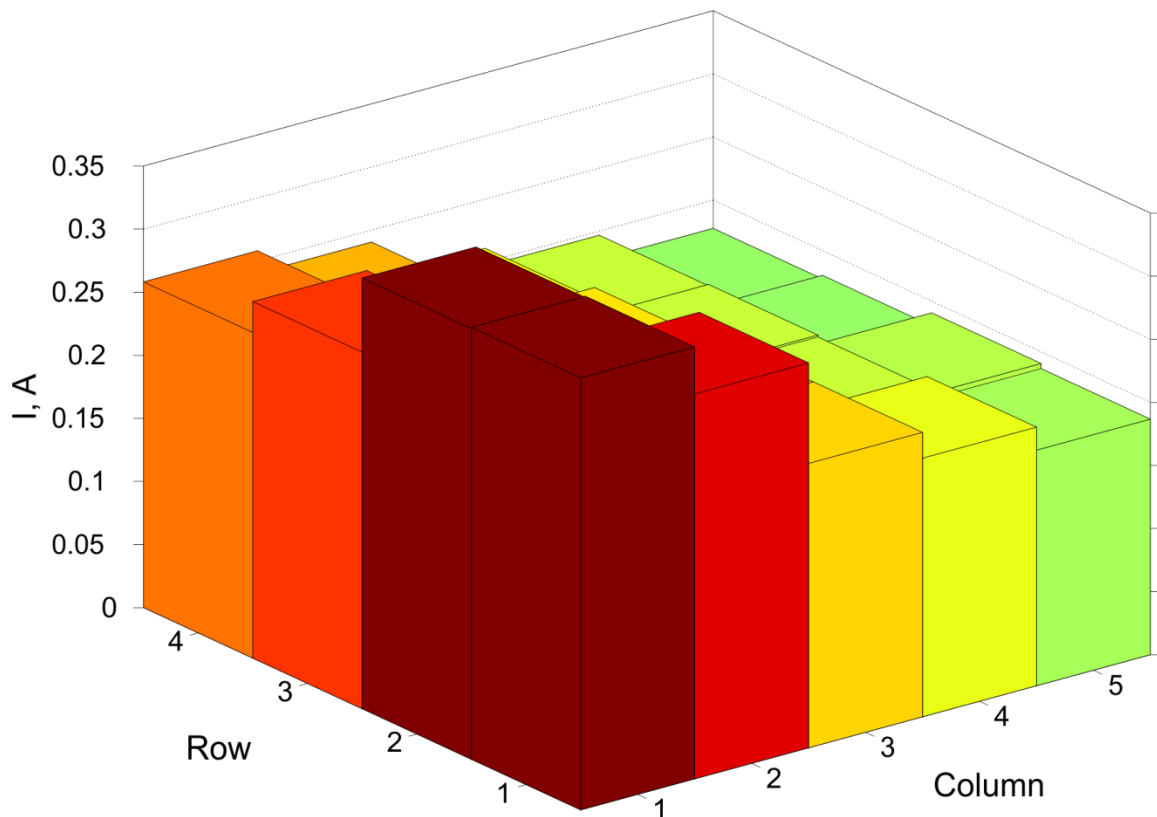


Figure 6.11 – 78<sup>th</sup> frame, 1<sup>st</sup> pulse at 40 % SoC, day 7.

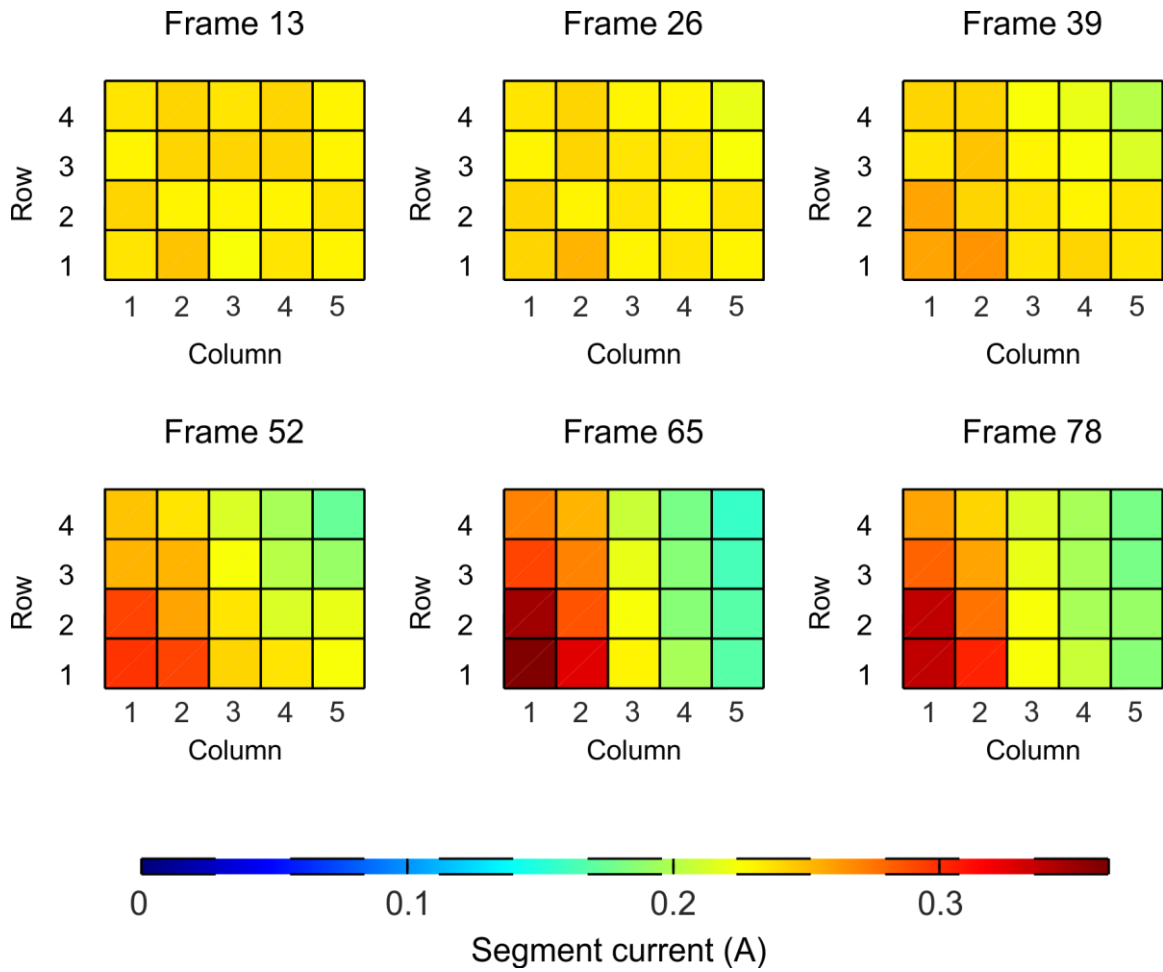


Figure 6.12 – Time lapse of six equally-spaced images taken using the flow-through sensor array. 1<sup>st</sup> pulse at 40 % SoC, day 7.

### 6.3.3 Magnetic imaging results

It is necessary to include the ferrous cores in the forward model. The manufacturers data for the electrical steel used (see [101] for the published datasheet or Appendix I for more recent data) reports the relative permeability  $\mu_r = 1432$  at the lowest magnetisation given ( $b = 18$  mT,  $f = 50$  Hz). The magnetic cores in the flow-through sensor are operated at an even lower value of magnetisation than that – an Ansys Maxwell simulation yields a maximum value of approximately 5 mT within the cores at 5 A cell current. Extrapolating the gradient of the smallest two data points towards zero yields  $\mu_r = [1132, 1215]$  for  $b = [0$  mT, 5 mT] (Figure 6.13). It is assumed that the data given for operation at 50 Hz is accurate at 0 Hz.

The uncertainty in the value of  $\mu_r$  does not completely remove the useful information from the reconstructions. Figure 6.14 shows reconstructions of the uniform and non-uniform current distributions, where the core permeability has been varied over the range  $\mu_r = [960 : 1432]$ . Although some distortion of the current distribution is visible in all the

reconstructions (compared to the flow-through sensor data), it is still possible to tell the uniform and the non-uniform cases apart. Furthermore, some of the artefacts of the distorted solutions are preserved over the range of values of  $\mu_r$  tried. This suggests that either another source of error is present or that the true value of  $\mu_r$  lies outside the range tried. Figure 6.15 shows solutions where  $\mu_r$  is varied over a larger range. This time, some of the distortion artefacts are less apparent in the  $\mu_r = 500$  solutions.

Figure 6.16 shows the mean absolute error plotted against regularisation parameter for  $\mu_r = [500, 1200, 2000]$ . The black dots indicating  $\lambda_0$  show that the  $\mu_r = 500$  solution does in fact have a lower MAE than the others when regularised at  $\lambda = \lambda_0$ . However, this is not true if a higher regularisation parameter is chosen on the uniform problem. On the non-uniform problem, the  $\mu_r = 500$  model has the best MAE even when over-regularised. The black dots on Figure 6.16 show that the value of  $\lambda_0$  itself does not vary significantly with  $\mu_r$  in the core.

How well the solution matches the flow-through sensor data in terms of degree of non-uniformity is another way of quantifying solution quality. This is also highly dependent on regularisation parameter (Figure 6.17). A small regularisation parameter gives a solution that is more non-uniform than the corresponding flow-through sensor measurement. The optimum value of  $\lambda$  for the uniform solution appears to be approximately 0.2, after which the degree of non-uniformity increases away from the ideal value. For the non-uniform problem, too high a regularisation parameter causes the solutions to overshoot the desired degree of non-uniformity. The degree of non-uniformity becomes equal to that of the flow-through sensor measurement at approximately  $\lambda = 0.27$ . The uniform and the non-uniform solutions display similar degree of non-uniformity at very high values of  $\lambda$ . Varying the core permeability does not appear to have a strong effect on this characteristic. The smallest mean absolute error for  $\mu_r = 1200$  is found when  $\lambda_r = 1.6$  for the uniform problem and  $\lambda_r = 1.8$  for the non-uniform problem. An example of the reconstructions when  $\lambda_r = 1.7$  is shown in Figure 6.18. The most uniform solution to the uniform problem, in terms of  $i_{max}/i_{min}$ , is found when  $\mu_r = 1200$  and  $\lambda_r = 1.4$ , which is shown in Figure 6.19. Mean absolute errors and degrees of non-uniformity are summarised in Table 6.3.

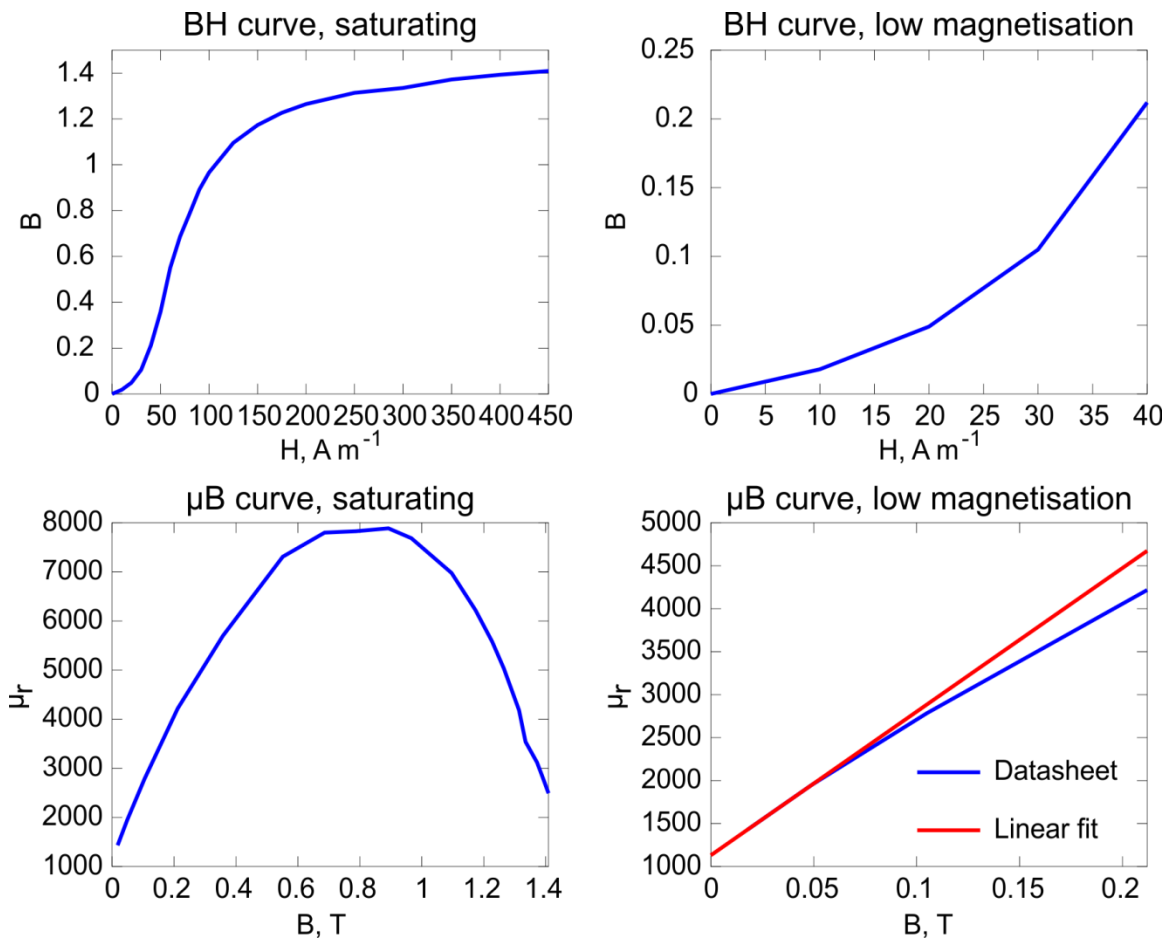


Figure 6.13 -  $BH$  and  $\mu B$  curves of M330-35A electrical steel, showing saturation and detail at low magnetisation. A linear fit to the smallest two data points provides an approximate extrapolation of  $\mu$  at very low magnetisation. See Appendix I for data.

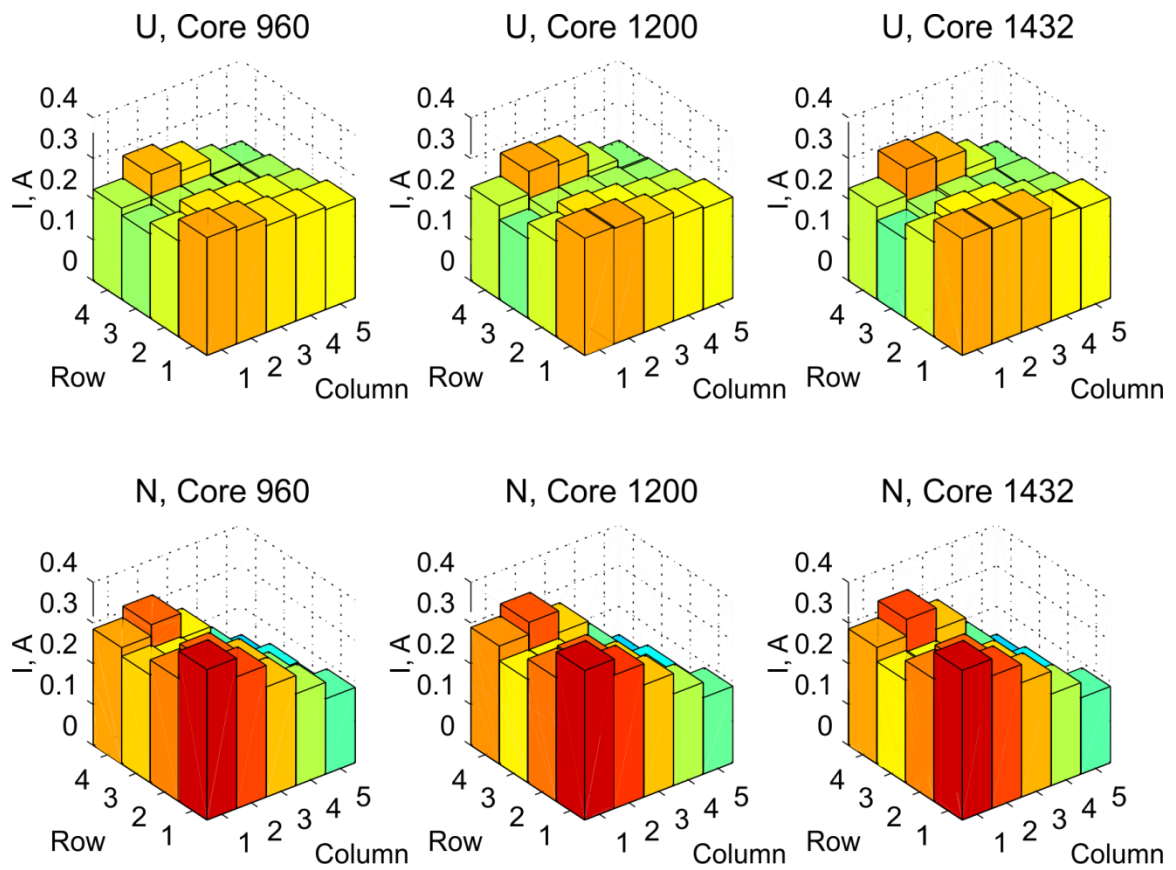


Figure 6.14 – Reconstructions of the uniform (top row) and non-uniform (bottom row) current distributions, for three different values of core  $\mu_r$ .  $\lambda$  is set to the value given by the L-curve (i.e.,  $\lambda_r = 1$ ).

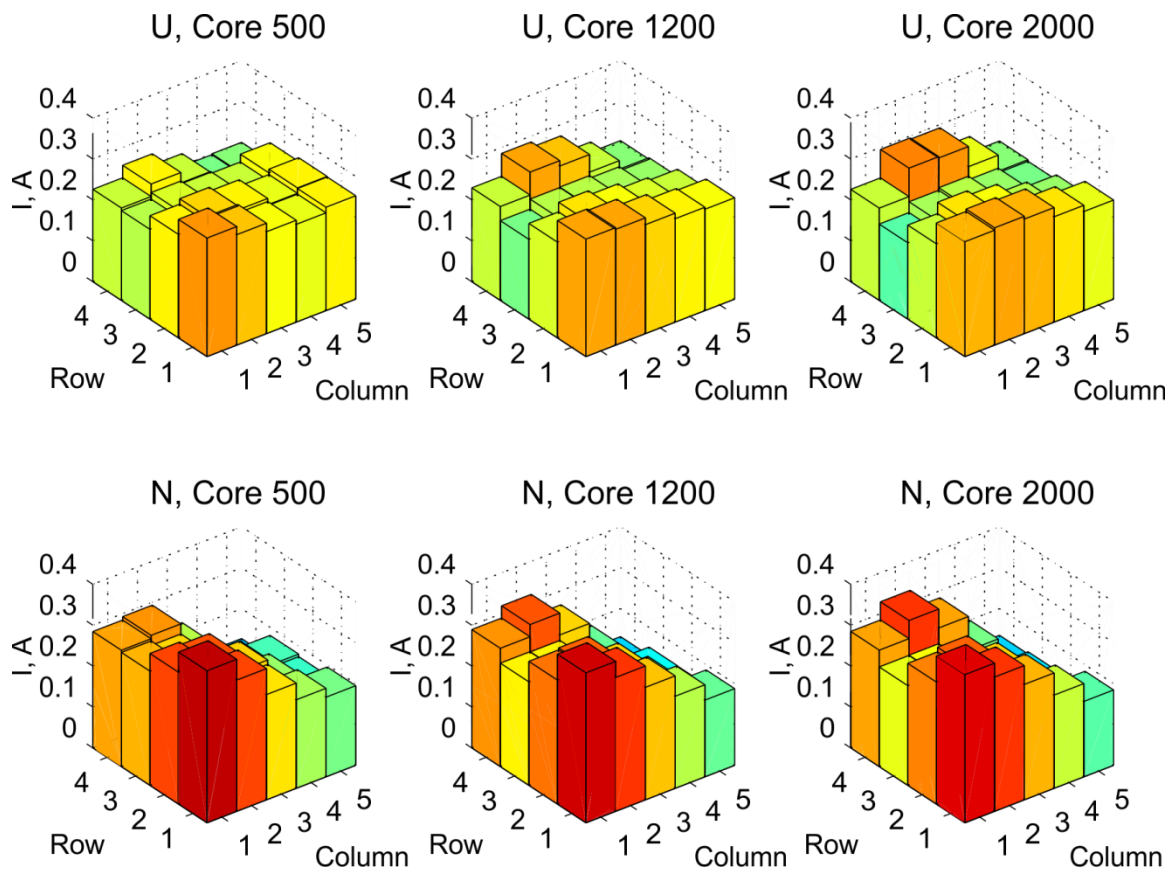


Figure 6.15 – Reconstructions of the uniform (top row) and non-uniform (bottom row) current distributions, for three different values of core  $\mu_r$ .  $\lambda$  is set to the value given by the L-curve (i.e.,  $\lambda_r = 1$ ).

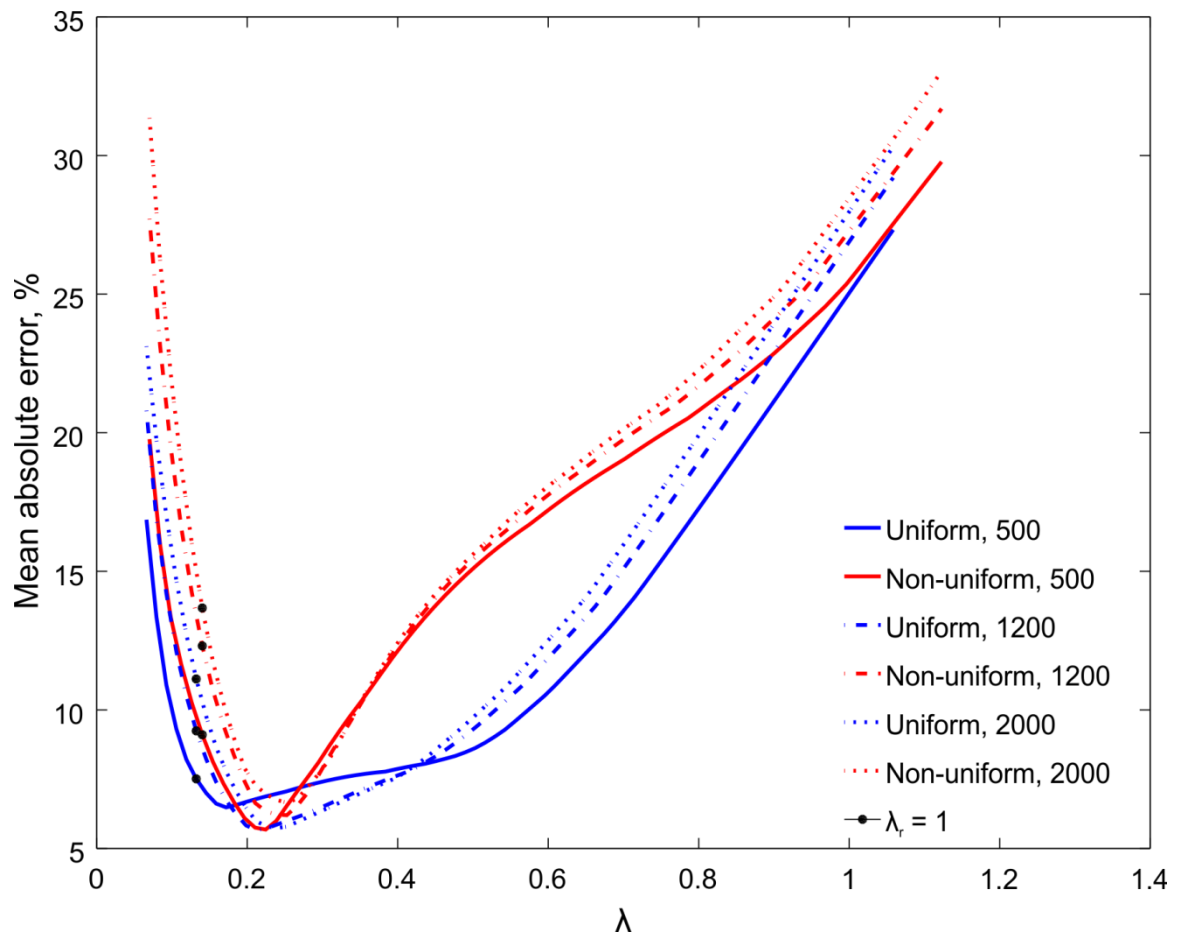


Figure 6.16 - Mean absolute error (MAE) against  $\lambda$ , for  $\mu_r = [500, 1200, 2000]$  in the cores.

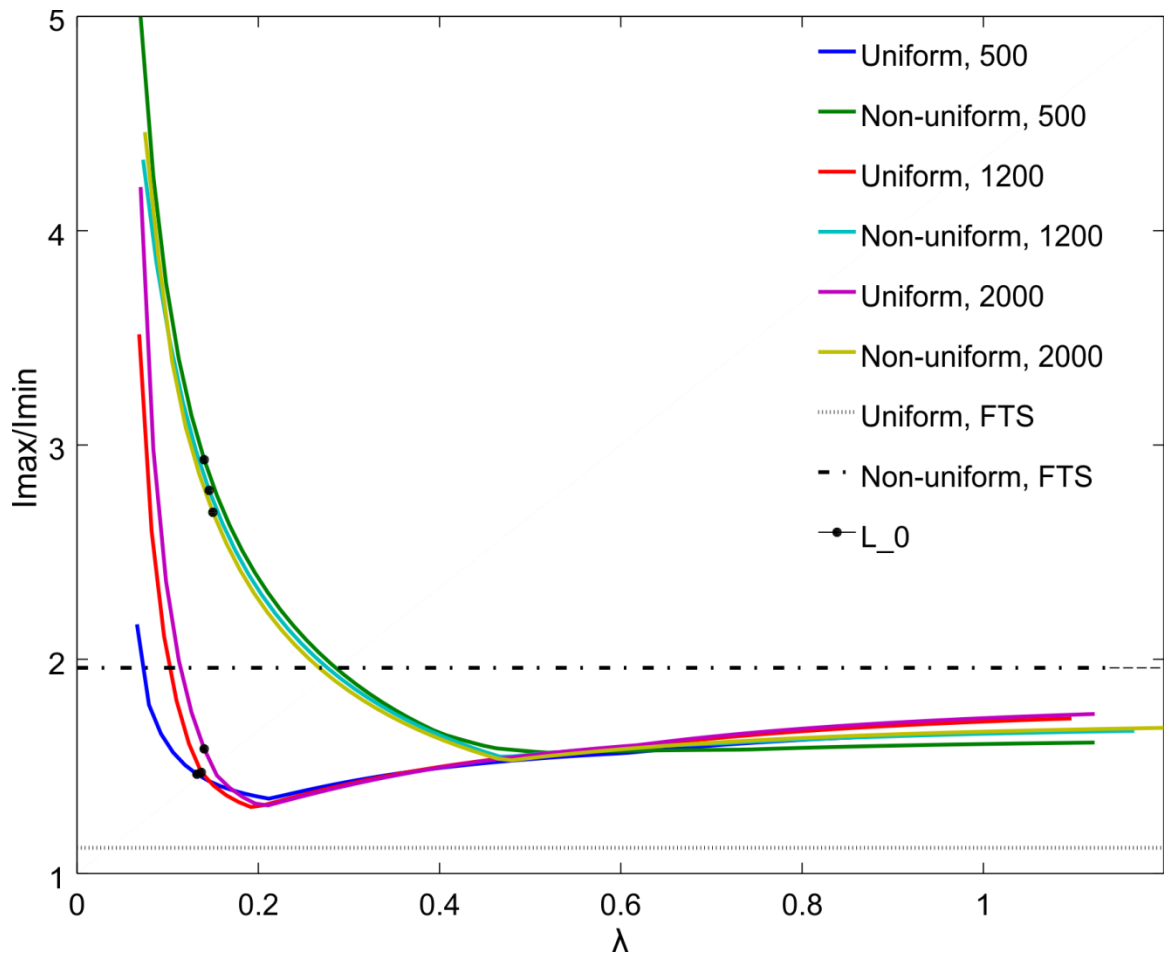


Figure 6.17 – Effect of regularisation parameter on degree of non-uniformity. The degree of non-uniformity in the corresponding flow-through sensor data is shown as dotted lines. A uniform/non-uniform solution close to its respective dotted line is considered a good solution.

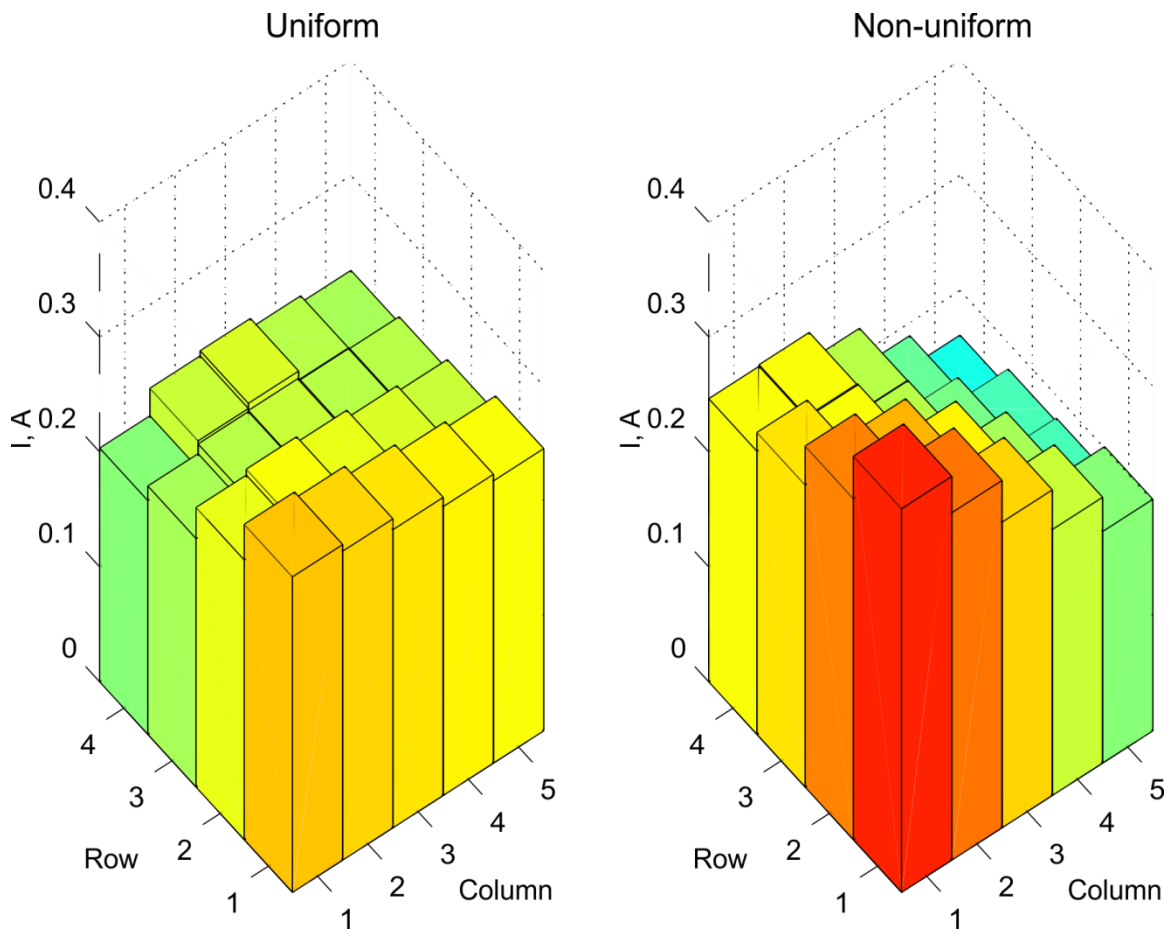


Figure 6.18 - Over-regularised solutions, using  $\mu_r = 1200$ ,  $\lambda_r = 1.7$ .

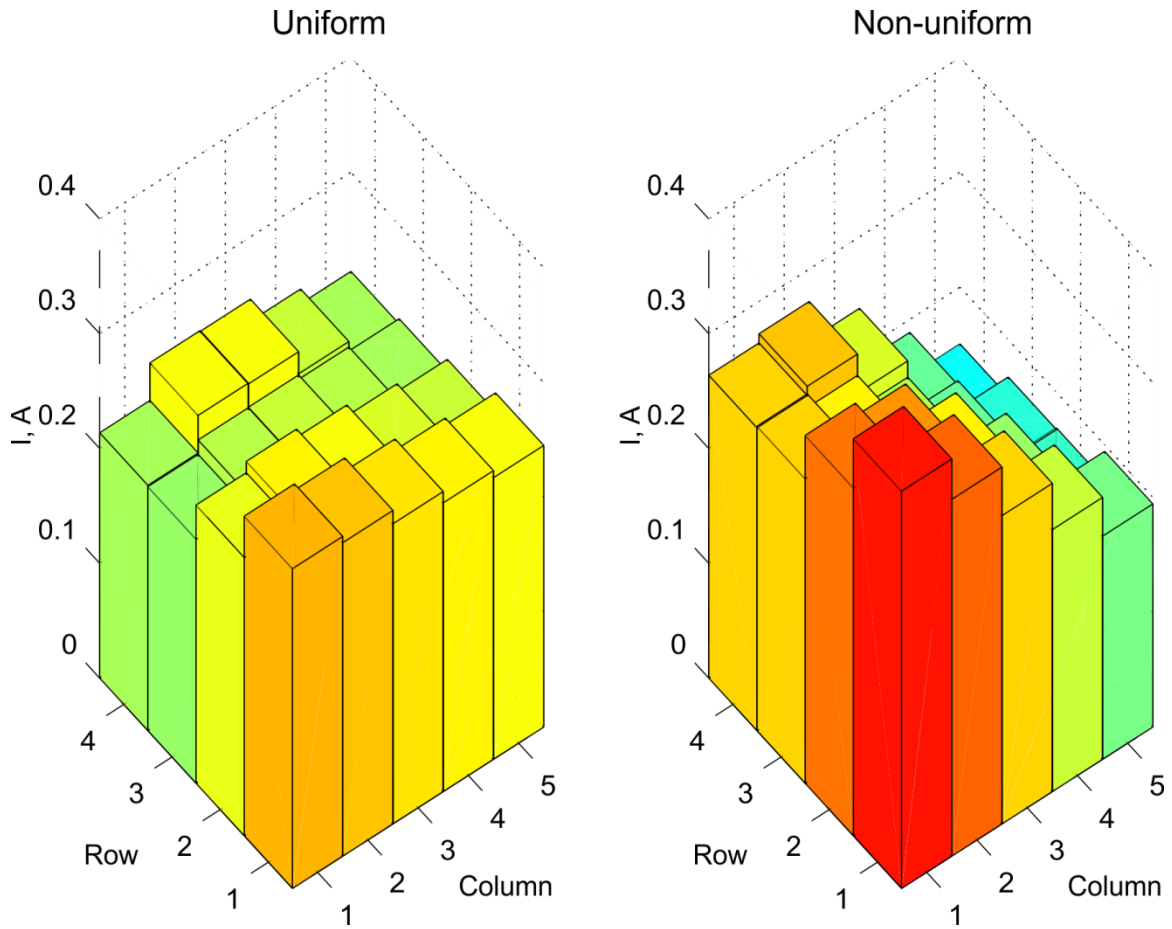


Figure 6.19 – Over-regularised solutions, using  $\mu_r = 1200$ ,  $\lambda_r = 1.4$ .

	Uniform problem	Non-uniform problem
MAE in current, % ( $\lambda_r=[1,1.4,1.7]$ )	9.24 %, 6.24 %, <b>5.72 %</b>	12.31 %, 7.42 %, <b>6.23 %</b>
$i_{max}/i_{min}$ ( $\lambda_r=[1,1.4,1.7]$ )	1.47, <b>1.31</b> , 1.35	2.79, 2.30, <b>2.07</b>

Table 6.3 – Mean absolute error solution and degree of non-uniformity in current distribution, for uniform and non-uniform problems, and three different values of  $\lambda_r$ . Correct degree of non-uniformity is 1.12 for the uniform problem and 1.93 for the non-uniform problem according to the flow-through sensor.  $\mu_r = 1200$ . Best values are highlighted in bold.

Another source of error which may be investigated is positional measurements. Dimensional errors may be caused by tolerance in the assembly of the experimental setup, errors in measurement of the actual dimensions of the test cell and sensors, and placement of the magnetic transducers within the sensor ICs. The residual norm,  $\rho$ , of the solution is one measure of solution quality. In this case,  $\rho = \|\mathbf{B}_s \xi - \mathbf{B}_0\|$  for the inverse problem  $\xi = \mathbf{B}_s^{-1} \mathbf{B}_0$ . It may be described as the difference between the measured data and the result of applying the forward model to the solution. A variable offset in the  $x$  and  $z$  directions is applied to the position of the sensors relative to the cell, and residual norm corresponding to the corner of the L-curve is plotted for each position. Figure 6.20 shows the effect of varying

the  $xz$  offset on the residual norm for both uniform and non-uniform problems. The profiles are very similar. In fact the minimum  $\rho$  is found at an  $xz$  offset equal to (2 mm, 1.5875 mm) for all values of  $\mu_r$  shown except  $\mu_r = 500$ . The solutions produced at this value of  $xz$  offset are shown in Figure 6.23. The solutions are different to the zero offset ones shown in Figure 6.14, but are still distorted. Again, the solutions do not appear strongly affected by varying  $\mu_r$  over the range [960 : 1432].

The distribution of mean absolute error in the solution over  $xz$  offset, original current distribution, and core  $\mu_r$  is not as stable as the distribution of  $\rho$ . Figure 6.21 shows the distribution of mean absolute error over  $xz$  offset for  $\mu_r = 1200$  and  $\lambda = 2$ . This time there is a difference between the uniform and non-uniform solutions. The locations of the mean absolute error minima for the three  $\mu_r$  values and two current distribution types are summarised in Figure 6.22. There is some variation between the locations, suggesting that the offset values which produce the smallest errors may not necessarily be any more correct than a zero offset value. However, there is some tendency for the minima to lie in the positive  $z$  direction, so there may be a measurement error present in  $z$ . Solutions where an offset of (0 mm, 1.5875 mm) is applied (Figure 6.24) appear very similar to the zero offset solutions (Figure 6.14).

**Figure 6.25 shows the relationship between  $\lambda$  and mean absolute error for the  $xz$  offset values (0 mm, 0 mm), (0 mm, 1.5875 mm) and (2 mm, 1.5875 mm), corresponding to the zero-offset case and the apparent optimum values of offset given by looking at the mean absolute error distribution and the  $\rho$  distribution respectively. Only the  $\mu_r = 1200$  solutions are used, and both uniform and non-uniform problems are included. The ‘best MAE’ offset value of (0 mm, 1.5875 mm) does in fact outperform the zero offset solution on almost all values of  $\lambda$ , not just the  $\lambda = 0.2$  used to plot Figure 6.21. The smaller value of  $\lambda_0$  for the ‘best  $\rho$ ’ offset value of (2 mm, 1.5875 mm) is expected, since  $\lambda_0$  is derived from the L-curve, a plot of  $\rho$  against solution norm  $\|\xi^2\|$ . The ‘best  $\rho$ ’ offset produces better solutions at low values of  $\lambda$ , but is outperformed by the other two for values of  $\lambda$  approximately greater than  $\lambda_0$ . The plots show that all the solutions would benefit to some degree from over-regularisation. The most pronounced minima are those for the zero offset and ‘best MAE’ offset. These minima all occur at a value of  $\lambda_r$  between 1.5 and 1.8.**

**Table 6.4 gives the mean absolute error and degree of non-uniformity for the zero-offset and ‘best MAE’ offset solutions. Over regularising to  $\lambda_r = 1.7$  improves mean absolute error of all solutions shown, as shown in Figure 6.25. Over-regularising also brings the degree of non-uniformity closer to that found in the flow-through sensor measurements. The ‘best MAE’ offset solutions also exhibit a better degree of non-uniformity than the zero offset ones. The mean absolute error values are of a similar magnitude to those of a comparable set of simulated results (see Figure 4.45 and**

Table 5.1).

Nonetheless, the reconstructions with zero positional offset added are sufficiently accurate that the time-lapse image taken on day 7, 40 % SoC (Figure 6.26) is similar to that obtained by the flow-through sensor (Figure 6.12).

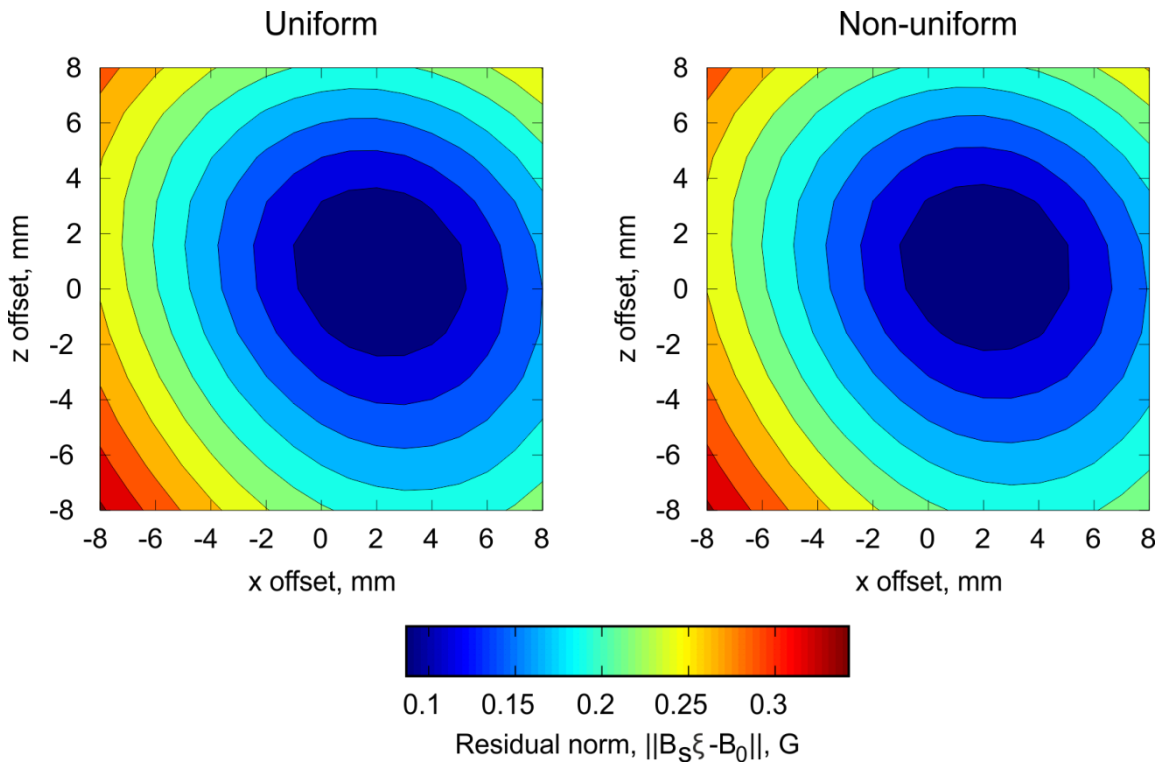


Figure 6.20 - The effect of varying  $xz$  offset on the optimum value of residual norm,  $\rho$ , given by the L-curve.  $\mu_r$  in the cores is 1200.

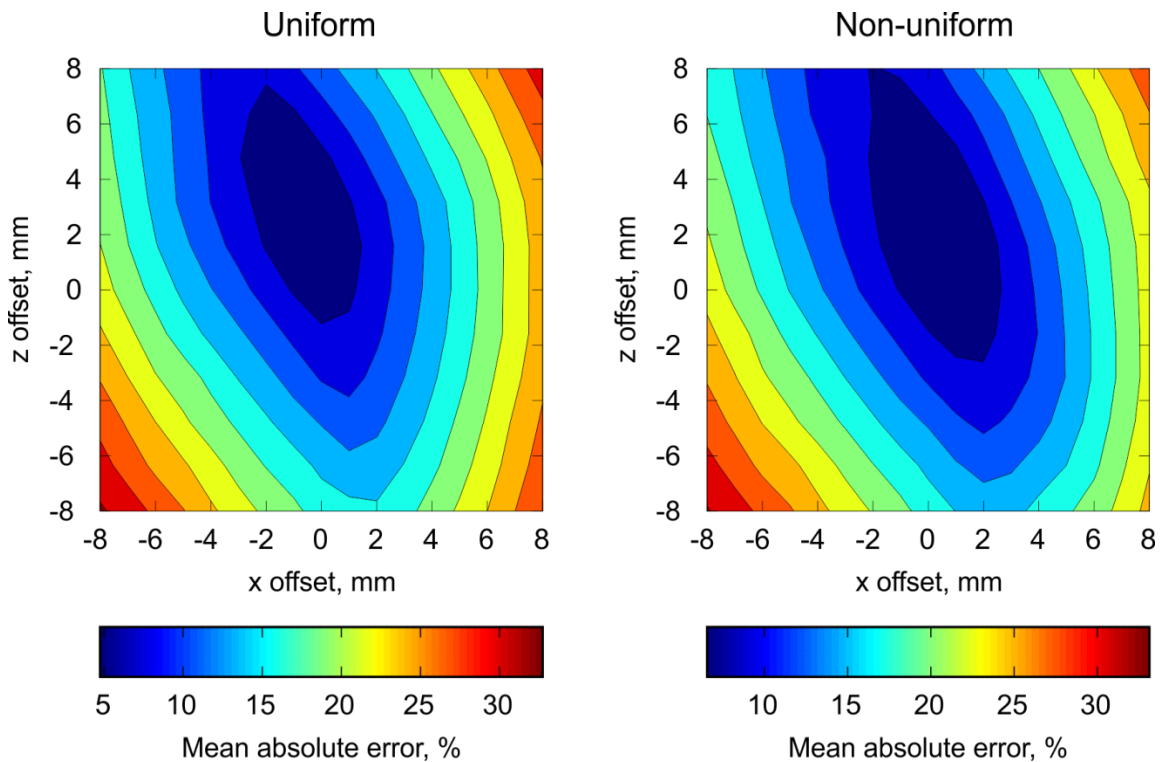


Figure 6.21 - The effect of varying  $xz$  offset on mean absolute error.  $\lambda$  is held constant at 0.2 for each solution rather than using the L-curve method.  $\mu_r$  in the cores is 1200.

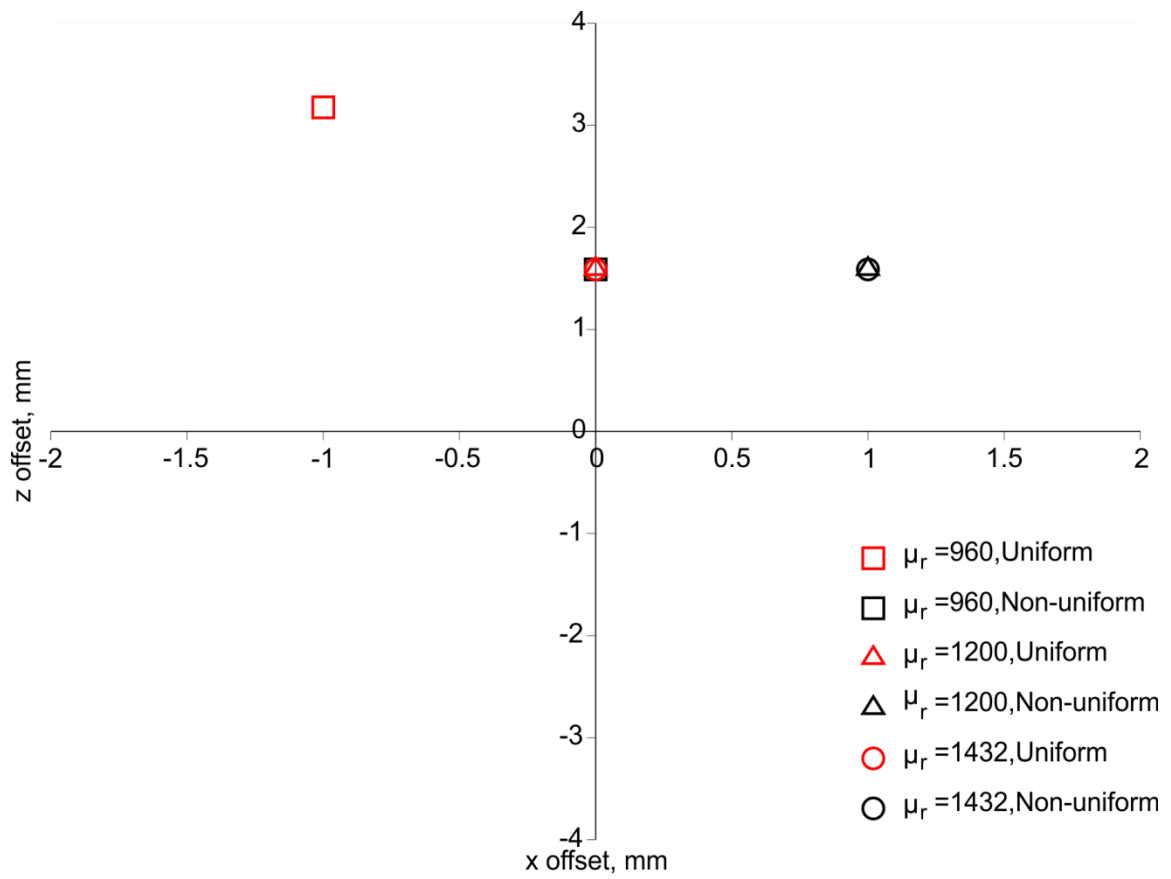


Figure 6.22- Locations of the minima in mean absolute error for each value of  $\mu_r$ , and both the uniform and the non-uniform distributions.

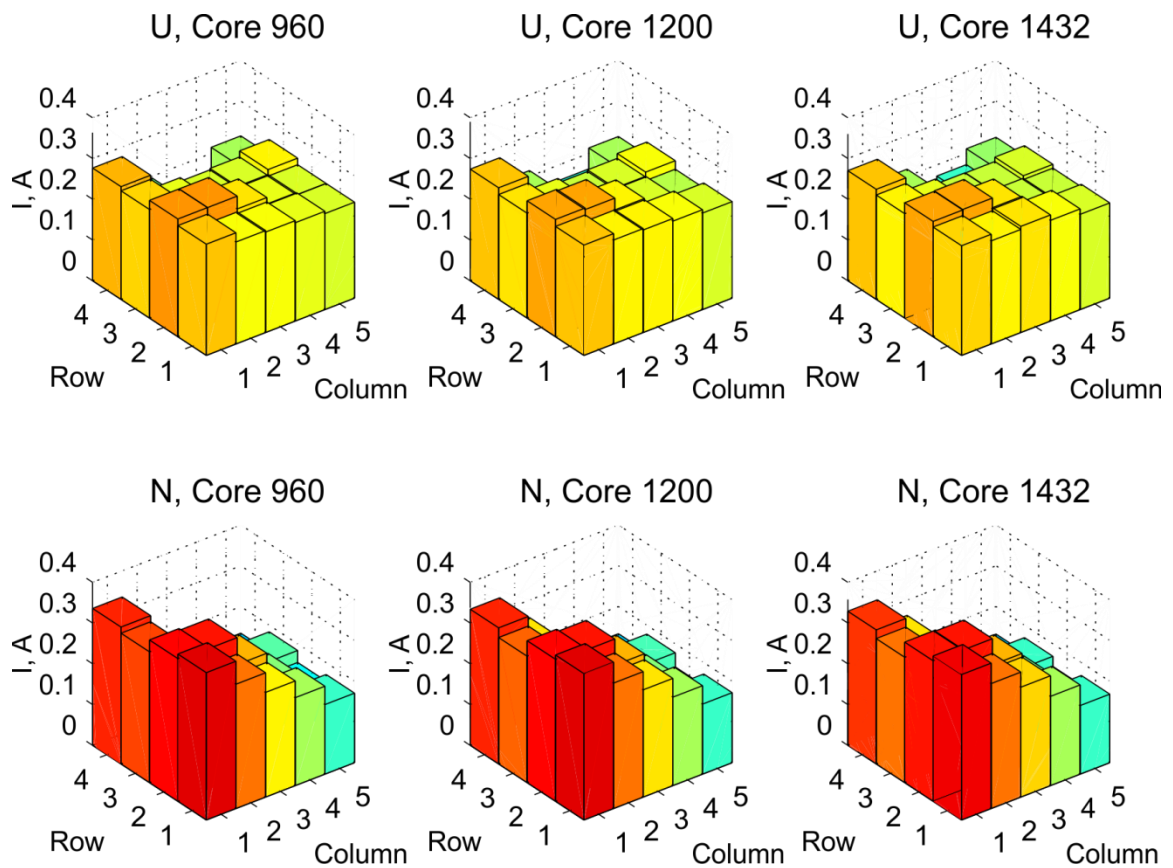


Figure 6.23 – Reconstructions of the uniform (top row) and non-uniform (bottom row) current distributions, for three different values of core  $\mu_r$ .  $xz$  offset is set to (2 mm, 1.5875 mm).  $\lambda$  is set to the value given by the L-curve (i.e.,  $\lambda_r = 1$ ).

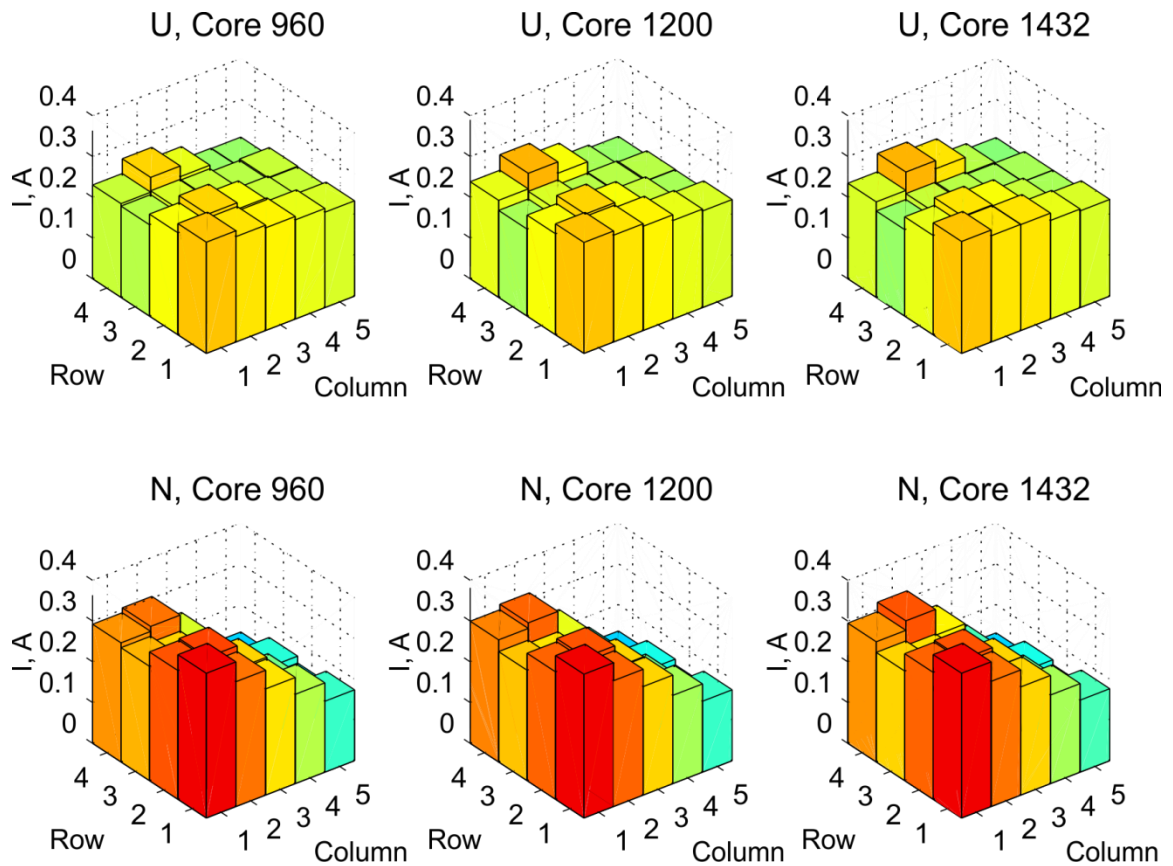


Figure 6.24 - Reconstructions of the uniform (top row) and non-uniform (bottom row) current distributions, for three different values of core  $\mu_r$ .  $xz$  offset is set to (0 mm, 1.5875 mm).  $\lambda$  is set to the value given by the L-curve (i.e.,  $\lambda_r = 1$ ).

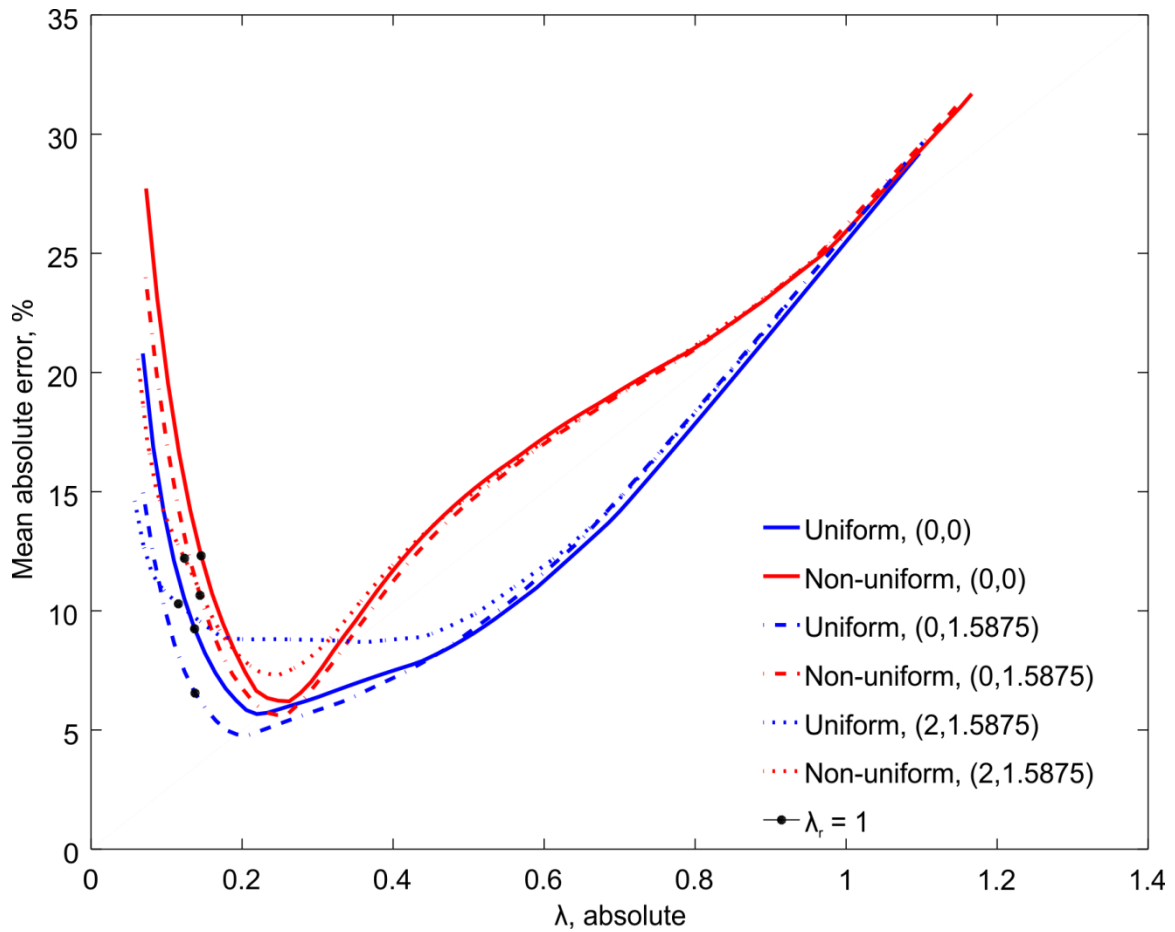


Figure 6.25 – Mean absolute error (MAE) against  $\lambda$ , for  $xz$  offset = (0 mm, 0 mm),  $xz$  offset at ‘best  $\rho$ ’ position, (2 mm, 1.5875 mm), and for a common ‘best MAE’ position (0 mm, 1.5875 mm).  $\mu_r$  in the cores is 1200.

	Uniform problem	Non-uniform problem	$xz$ offset, mm
MAE in current, % ( $\lambda_r=[1,1.7]$ )	9.24 %, 5.72 %	12.31 %, 6.23 %	(0, 0)
$i_{max}/i_{min}$ ( $\lambda_r=[1,1.7]$ )	1.47, 1.34	2.78, 2.07	(0, 0)
MAE in current, % ( $\lambda_r=[1,1.7]$ )	6.55 %, 5.08 %	10.65 %, 5.63 %	(0, 1.5875)
$i_{max}/i_{min}$ ( $\lambda_r=[1,1.7]$ )	1.32, 1.27	2.61, 2.05	(0, 1.5875)

Table 6.4 – Mean absolute error solution and degree of non-uniformity in current distribution, for uniform and non-uniform problems, two different values of  $xz$  offset and two different values of  $\lambda_r$ . Correct degree of non-uniformity is 1.12 for the uniform problem and 1.93 for the non-uniform problem according to the flow-through sensor.

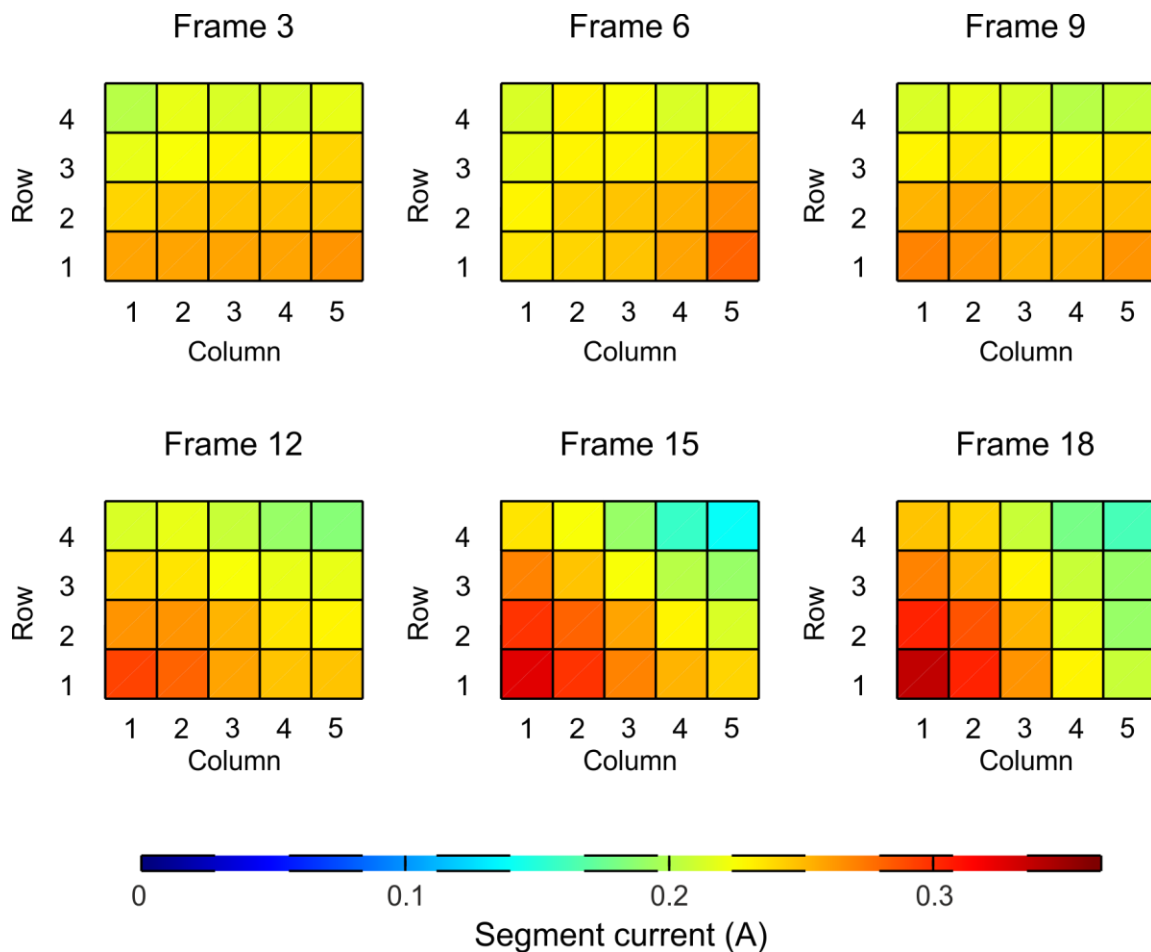


Figure 6.26 - Time lapse of six equally-spaced images taken using the magnetic tomography system. 1<sup>st</sup> pulse at 40 % SoC, day 7.  $\mu_r = 1200$ , zero offset,  $\lambda_r = 1.6$ .

## 6.4 Evaluation

### 6.4.1 Error sources

The magnetic inverse problem requires an accurate forward model in order to provide accurate solutions. One source of uncertainty in the model is the magnetic properties of the materials used, namely the flow-through sensor cores, and the ferrous splashback built into the fume hood. In the case of the cores, data is available from the manufacturer (albeit at 50 Hz rather than DC and at a higher magnetisation). This allows an estimate of the magnetic properties in the forward model to be made. Increasing and decreasing the permeability about this estimation shows that while the solutions produced using different simulated core materials can be differentiated visually, the difference is not so great as to mask the distinction between the uniform and non-uniform examples given. The magnetic properties of the ferrous sheet mounted in the fume hood splashback are even less certain. The material may be detected using a permanent magnet but is unknown and not visible. Its permeability must be

guessed and its position is subject to uncertainty due to the unknown thickness of plastic it is mounted behind.

The dimensions and material properties of the forward model should match as closely as possible to those in the real cell it is simulating. In this case, large dimensions ( $l > 100$  mm) are measured using a 1 mm grade ruler, medium dimensions ( $2$  mm  $> l > 120$  mm) are measured using a Vernier calliper and small dimensions such as material thicknesses ( $0.5$  mm  $> l > 25$  mm) are measured using a micrometer screw gauge. The ruler is the source of the largest measurement errors out of these three methods. Offsetting the simulated sensor positions allows the robustness of the solutions to errors in the large dimensions of the model to be investigated. Comparing Figure 6.23 with Figure 6.24 shows how the solution is distorted differently, depending on whether the simulated sensors are offset by (2 mm, 1.5875 mm) or (0 mm, 1.5875 mm), respectively. However, the overall shape is similar, with a minimum at the bottom left of the non-uniform solutions, and a greater degree of non-uniformity for the non-uniform than the uniform solutions.

The plot of mean absolute error against  $xz$  offset ( Figure 6.21) also demonstrates the robustness of the approximate solution to small errors in position – the dark blue area representing the minimum mean absolute error (approximately 5 %) for uniform solutions is approximately 4 mm wide and 8 mm tall. That is a reasonable level of precision for measurements taken with a 1 mm graduated ruler. Furthermore, the mean absolute error increases smoothly as the offset moves away from the optimum position, meaning that small dimensional errors should not have a disproportionately large effect on solution errors.

An attempt is made to use the values of offsets which optimise either the mean absolute error or the residual norm, in order to correct the measured dimensions. However, the values of offset which optimise these two quantities do not agree and are in some cases dependent on the modelled magnetic properties of the cores. In the case of optimising mean absolute error, the  $xz$  offset depends on problem type and core permeability. This variation in the  $xz$  offset needed to optimise different measures of solution quality makes it difficult to justify using an  $xz$  position other than the measured one (*i.e.*,  $xz$  offset = (0 mm, 0 mm)). It is difficult to search for any optimum model parameter in this way when there multiple parameters which are also subject to uncertainty, since a multi-dimensional optimisation becomes impractical considering the computing time taken to simulate the model, and the interaction between different model properties influencing measures of solution quality. While the system relating

currents at a known position to magnetic measurements at a known position is linear, the relationship between unknown positions of currents and magnetic measurements is not. A simple example to illustrate this is the inverse relationship between  $d$  and  $b$  in (2.44). Another general problem with using mean absolute error or residual norm to cancel out model errors is that only two current distributions have been considered in Section 6.3.3. Optimising more than two experimental parameters based on these two special cases constitutes over-fitting.

#### 6.4.2 Validity of results

The experimental setup used clearly differs from the normal operating conditions of a commercial lead acid battery in a number of ways. Firstly, the plate separation chosen in order to comfortably fit the flow-through sensor is 102 mm, which is much greater than that found in the battery from which the cell electrodes were taken. This is one possible cause of the highly uniform current distributions observed in the vast majority of measurements. Although the intended application of the magnetic imaging system is to observe current distribution so that uniformity may be improved, it appears that the test cell used results in measurements which are almost all highly uniform. In addition, the large volume of electrolyte used to fill the gap between the plates means that the bulk electrolyte concentration does not vary with state of charge to the extent that it does in a commercial battery.

Another difference between the test cell design and the normal operation of the electrodes used is the lack of a separator material. In a commercial cell, the plates are separated by a porous material through which electrolyte may pass. The stack of plates and separators is under some pressure so that the active material does not expand. This helps preserve the integrity of the active material over the lifetime of the battery. The lack of separator material and plate pressure probably contributed to the very short lifetime observed in this test cell. Inspection of the negative (Pb) plate after removing the electrolyte once all measurements were taken shows that the active mass has undergone some expansion and shedding during its use. This can be seen when comparing Figure 6.27 (before) with Figure 6.28 (after) – after use the negative active mass is protruding from the grid whereas before use it forms more of a smooth surface. Also, there is a significant amount of material deposited at the bottom of the plate after use. There are also deposits present above the top of the plate, which have been deposited when the electrolyte has bubbled due to the gassing reaction (2.4). The terminal voltage of the cell (Figure 6.9) at low state of charge at the end of the experimental run also indicates damage to the cell. Since most lead acid cells in commercial batteries are pressurised

and separated, this failure mode is not particularly applicable (although shedding of plates in normal use has been reported in the literature [36]).

A third difference between the test cell design and a commercial battery is that the plates are not interleaved. Each plate in the test cell only interacts with one other plate, whereas in a parallel stack of plates in a lead acid cell each plate interacts with two others (except for the plates at each end of the stack) (see Figure 4.11). This means that the active material in each plate of the test cell is not being shared with a plate either side as it would be in a normal application. This is a possible explanation for the measured capacity of the cell (7.9 A h) being larger than was predicted (5 A h) from the nominal capacity of the battery. A consequence of this is that the current control circuit was designed for 5 A, so the cell was tested at 0.625 C. More interesting current distribution behaviour may occur at higher rates.



Figure 6.27 – Negative plate before use.

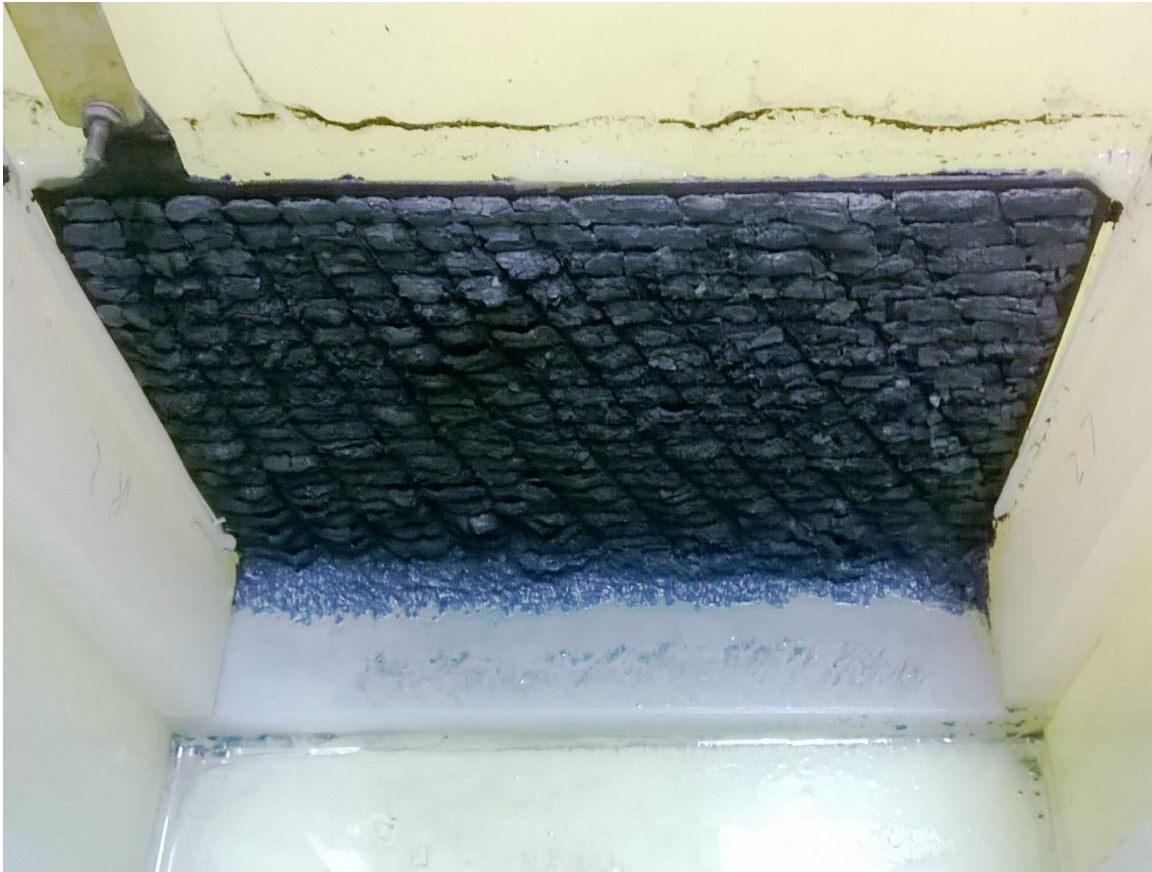


Figure 6.28 – Negative plate after use showing shedding of active mass.

## 6.5 Summary of Chapter 6

Magnetic tomography, a non-invasive method of estimating current distribution using magnetic field measurements, was performed on a lead acid test cell. To verify the results, a flow-through sensor (an invasive current distribution measurement device) was used concurrently. The results from the two methods are approximately in agreement. Although some error between the two sets of results remains, it is of a similar magnitude to that of a comparable simulated problem. The magnetic tomography system includes a ‘forward model’, built in Ansys Maxwell, which must be reasonably accurate with respect to the real test cell if the results are to be accurate. Some investigation into the effect of some plausible model parameter errors (positional error and magnetic properties of materials) is conducted, and the solutions are found to be somewhat robust to errors of a plausible magnitude in the model parameters investigated.

The approximate solutions are shown to be robust to positional errors of the order of 1 - 2 mm, and modelled permeability of the modelled magnetic cores over the range  $\mu_r = [500 - 2000]$ . A typical best value of mean absolute error achieved is between 5 – 7 %, and the

solutions are visibly different from the baseline images created using the invasive method. Further improvement of solution quality may require a better level of precision in the forward model definition, or some reduction in the number of parameters in the model. An example of this is the inclusion of the ferrous material in the fume cupboard. A better solution may be possible if its position and magnetic properties were known, but also it would be easier if it weren't present. This illustrates how the cell geometry and materials must be kept as simple as possible to avoid having to accurately model many parameters which may be too numerous to easily optimise. While the majority of the measurements taken were highly uniform and did not change greatly over time, it was possible to obtain a time-resolved series of images showing the cell transitioning from a 'healthy' terminal voltage and a fairly uniform current distribution to an abnormal terminal voltage and a more non-uniform current distribution.

The results from the flow-through sensor are also promising in themselves. Capturing a full 2D array of current measurements almost simultaneously is not possible with many of the current distribution methods currently used for the study of lead acid cells. The measurement device used is based on a design used in the field of fuel cell measurement, but miniaturised to use with a test cell based on plates taken from a commercial starting-lighting-ignition car battery. The flow-through sensor is also suitable for creating time-resolved series' of images. Furthermore it proved easy to deploy once constructed and does not rely on a simulated forward model, since it was calibrated against a real current, rather than modelled data.

While it was necessary to obtain data against which to verify the magnetic tomography system, the forward model would be simpler without the magnetic cores in the flow-through sensor. This would likely lead to better solutions due to fewer unknown model parameters. The flow-through sensor also places a limit on the minimum plate separation, which is detrimental to the validity of the results.

## 7 Conclusion and Future Work

### 7.1 Conclusion

A practical system for obtaining current distribution estimations of a lead acid cell by magnetic tomography has been developed and tested. Doing so has required several novel contributions to the field of study to be made. In particular, efforts have been made to bridge the gap between theoretical and simulated inverse problem methods and real-world conditions.

A  $32 \times 8$  array of magnetic sensors was employed to take simultaneous readings of the magnetic field adjacent to a single lead acid cell. The measurements were used in conjunction with a special basis projection inverse problem solver. It was found in simulated problems that the special basis projection method is sensitive to errors in grid resistance distribution in the forward model. The method was developed further to improve its compatibility with commercial grid-paste lead acid cell electrodes, which may have a complicated resistance distribution due to their inhomogeneous structure. Firstly, it was shown that a special basis projection solver could be used alongside commercial 3D finite element software, allowing complex grid designs to be modelled. Secondly, it was shown that by generating an excess of partial current data to extend the basis for the solution, some uncertainty in the active mass resistance distribution could be accommodated.

The accuracy of the solutions was tested by comparison against readings from a  $5 \times 4$  array of magnetic core current sensors. A similar design has been used for studying a fuel cell with a larger cross section area than an automotive lead acid cell [67]. The design was altered to improve the available electrolyte flow area for a given cell cross section area. This was achieved by creating a bespoke rectangular core design. Rows of cores were combined, allowing inner vertical core members to be shared between adjacent segments. The 4 rows were stacked in an overlapping pattern to minimise the cross section area occupied by the horizontal core members. The interaction between cores was also studied, and a comparison was made between combined-core and individual-core designs.

The test cell was operated in a constant-current mode at 0.625 C for 30 s at a time, alternating between charging and discharging. Measurements were taken using the magnetic sensor array and the flow-through sensor during the current pulses to capture magnetic field due to the cell current, and also before and after the current pulses in order to capture the ambient magnetic field. Ambient magnetic field was obtained while the current was bypassing the cell rather

than turned off entirely, so that magnetic field due to the current control circuit was also removed. The control circuit is a linear power amplifier with feedback taken from a current sense resistor. Measurements were taken of the cell charging and discharging, and at a range of states of charge. The test cell was built around a pair of commercial automotive (starting-lighting-ignition) battery electrodes, but the cell case and terminals were built especially for testing the magnetic tomography system.

The readings from the two measurement methods were found to be in approximate agreement on two distinct current distributions. Mean absolute errors of approximately 5 – 7 % remained between the magnetic tomography solutions and the flow-through sensor measurements. This is a similar magnitude of error to a comparable simulated problem. While only an approximate match was achieved, the error in the magnetic tomography solutions was shown to be somewhat robust to errors in positional measurements and magnetic material definitions. Both methods were shown to be capable of producing time-resolved current distribution images, since they both employ an array of sensors rather than a single scanning sensor.

One of the intended applications of the current distribution measurement system is to optimise cell electrode design for improved uniformity. However, the cell current distribution was found to be much more uniform than is reported in the literature for most of the duration of testing. It is possible that this is due to the design of the experimental hardware and procedure. Therefore the system used may be unsuitable for observing typical non-uniform conduction as intended. However, some non-uniformity was observed after several days of testing, which was likely due to cell fatigue. The system could be used as a method of observing the current distribution of fatigued or damaged cell electrodes, for example where active material has been shed.

## **7.2 Future Work**

Magnetic tomography of electrochemical cells is not a mature research area. An important design objective was to provide a simple case for the solver, in the absence of comprehensive prior knowledge and available literature on the practical application of a magnetic tomography system to a lead acid cell. The end goal of a current distribution system (such as the two systems presented in this thesis) is greater knowledge of cell behaviour, but the most useful direct application of the work presented in this thesis is likely to be further development of current distribution measurement methods. Some of the design choices made reduce the

applicability of the results to real-world cell behaviour. However, the modest solution error and tolerance of experimental errors provides a proof of concept for practical magnetic tomography in this application, and some of the specific problems with the method can be targeted for improvement in future research. Some specific incremental improvements to the experiment are suggested in Section 7.2.1, followed by some more ambitious improvements and research goals in Section 7.2.2.

### **7.2.1 Short term improvements**

The highly uniform current distribution observed does not provide a very good source of training data for optimising the solver. Therefore some modifications to the experiment which result in a more diverse range of current distributions would be useful. A more demanding current profile could be tried – other studies have found current distribution to be dependent on cell state of charge and current rate. Therefore it is possible that a greater variety of non-uniform current distributions may be observed if the cell is charged/discharged at a higher rate. Similarly, longer current pulses could be used during testing in order to observe the cell as its state of charge alters. Changing the current profile would not require altering any of the sensor systems or the test cell, although a higher rate current would require a modified current source circuit. While the implementation of different current profiles and larger currents is straightforward, it is not guaranteed to produce a usefully wide range of test cases.

A more direct (but more laborious) approach to altering the current distribution is to mask some of the current segments. For example, the two right-hand columns of current segments may be masked off with a non-conducting, non-permeable material, such as polypropylene, in order to imitate the ‘step change’ test case that was used frequently in the simulated problems in Chapter 4. The step-changing current distribution makes a useful test case as it gives some illustration of how the solver responds to high spatial frequencies. However, this method may lead to some complicated effects in terms of the path taken by conducting ions in the electrolyte. Another possible way of forcing a non-uniform current distribution is to deliberately damage the electrode, either by removing active mass from selected areas of the plate or by passivating the active mass by applying a non-conducting, chemically resistant coating.

The definition of magnetic materials present in the experimental setup was shown to affect the magnetic tomography solutions. Conducting the experiment in a fume hood which does not contain any ferrous material would remove one such source of error. To eliminate the

effect of the flow-through sensor cores, a dummy flow-through sensor array, having the same volume and dimensions as the real one, could be constructed from a material such as polypropylene. A set of measurements may be taken using the flow-through sensor, before substituting the non-ferrous dummy. The magnetic tomography system could then be used to estimate the current distribution and the solution compared against the flow-through sensor results taken previously. Assuming cell conditions (state of charge, acid stratification, etc.) do not change between the two measurements then the comparison is valid.

The use of a solid-state relay for the bypass switch proved very useful as it removed human error from the timing of switching, and allowed automatic file naming of the flow-through sensor data depending on whether the reading was of the ambient field or of a test current. Automating the current direction switch in a similar way would extend these advantages further – timing of the direction switching would be more accurate and also data could be automatically labelled according to whether it corresponded to charging or discharging. Similarly, automatic file naming of the magnetic sensor array data according to bypass and direction state would make recovering and interpreting the data more convenient.

### **7.2.2 Longer term improvements**

Positional uncertainty in the system may be reduced by integrating the cell with the magnetic sensor array. Rather than using the multiple PCB layout in the current system, all sensors could be mounted to a single large PCB, which could then be mounted directly onto the test cell using screws or similar. Revising the sensor array layout may also make it possible to increase the number and/or the density of sensors. Some careful electromagnetic modelling of the array layout could help identify the maximum density before interference between sensors becomes a problem. A tear-down of the magnetic sensors to identify the location of the magnetic transducers would also help create an accurately-dimensioned forward model. A completely different approach to removing some forward model errors is to build the basis or partial fields from real data. This method is demonstrated in Chapter 4 on a resistive circuit, and was also used to calibrate the flow-through sensor, but was not attempted on an electrochemical cell. It would likely require a more sophisticated version of the ‘masking’ discussed in Section 7.2.1, but which allows only one current segment to conduct at a time.

The above recommendations would enhance the conclusions that can be drawn from the magnetic tomography experiment. However, there may be a more fundamental problem with the validity of the experiment - the extended plate separation required to insert a current

distribution measurement device may be altering the current distribution. If the magnetic tomography method can be verified to the point where a second current distribution measurement system is not necessary, then it becomes possible to remove the invasive current distribution measurement device. If it is not justifiable to have this much confidence in the magnetic tomography system then miniaturising the invasive measurement device becomes a useful research goal. Some work is presented in Section 5.2.1 regarding fully-combined iron cores, which could contribute to a smaller device thickness ( $y$ -dimension in the coordinate system used throughout this thesis), in turn allowing reduced plate separation. Other design changes such as a smaller magnetic sensor or an alternative encapsulation material may allow further reduction in device thickness.

The ability to take time-resolved measurements makes both of the current distribution methods presented potentially useful as on-line diagnostic devices. Integrating the flow-through sensor (or another type of current distribution sensor array) into the space between plates of a commercial cell is largely a miniaturisation problem, albeit quite an ambitious one. Aiming to reduce the plate separation should be an aim of future research regardless, even if it does not reach the point where separation is the same as that in a commercial cell. Measuring multiple cells in a battery makes the electromagnetic effects more complicated than those in a single cell. In the case of the hypothetical miniaturised flow-through sensor, leakage from adjacent cells will affect readings. In the case of magnetic tomography, constructing an accurate forward model of all current paths becomes more difficult as more cells are included. The interleaved structure of a cell in a lead acid starting-lighting-ignition battery means that each electrolyte current is flowing in the opposite direction to its neighbours, so the magnetic field due to that component of current then becomes partially cancelled out. Similarly, adjacent plate currents are opposite and will also partially cancel. It is likely that the cell nearest the end of the battery would be easiest to image, but a truly useful diagnostic measurement ought to detect the operation of all the cells in the battery.

## 8 References

- [1] M. Winter and R. J. Brodd, "What are batteries, fuel cells, and supercapacitors?," *Chem. Rev.*, vol. 104, no. 10, pp. 4245–4269, 2004.
- [2] B. G. Pollet, I. Staffell, and J. L. Shang, "Current status of hybrid, battery and fuel cell electric vehicles: From electrochemistry to market prospects," *Electrochim. Acta*, vol. 84, pp. 235–249, 2012.
- [3] O. Haas and E. J. Cairns, "Electrochemical energy storage," *Annu. Reports Prog. Chem. Sect. C Phys. Chem.*, vol. 95, pp. 163–197, 1999.
- [4] M. S. Whittingham, "Materials challenges facing electrical energy storage," *MRS Bull.*, vol. 33, no. 4, pp. 411–419, 2008.
- [5] A. Lahyani, P. Venet, A. Guermazi, and A. Troudi, "Battery/Supercapacitors Combination in Uninterruptible Power Supply (UPS)," *IEEE Trans. Power Electron.*, vol. 28, no. 4, pp. 1509–1522, 2013.
- [6] J. O. G. Posada, A. J. R. Rennie, S. P. Villar, V. L. Martins, J. Marinaccio, A. Barnes, C. F. Glover, D. A. Worsley, and P. J. Hall, "Aqueous batteries as grid scale energy storage solutions," *Renew. Sustain. Energy Rev.*, vol. 68, no. 2, pp. 1174–1182, 2016.
- [7] T. Feehally, A. J. Forsyth, R. Todd, M. P. Foster, D. Gladwin, D. A. Stone, and D. Strickland, "Battery energy storage systems for the electricity grid: UK research facilities," *8th IET Int. Conf. Power Electron. Mach. Drives (PEMD 2016)*, p. ., 2016.
- [8] T. R. Ayodele and A. S. O. Ogunjuyigbe, "Mitigation of wind power intermittency: Storage technology approach," *Renew. Sustain. Energy Rev.*, vol. 44, pp. 447–456, 2015.
- [9] B. Zakeri and S. Syri, "Electrical energy storage systems: A comparative life cycle cost analysis," *Renew. Sustain. Energy Rev.*, vol. 42, pp. 569–596, 2015.
- [10] J. P. Deane, B. P. Ó Gallachóir, and E. J. McKeogh, "Techno-economic review of existing and new pumped hydro energy storage plant," *Renew. Sustain. Energy Rev.*, vol. 14, no. 4, pp. 1293–1302, 2010.
- [11] N. Hill, C. Brannigan, D. Wynn, R. Milnes, H. van Essen, E. den Boer, A. van Grinsven, T. Ligthart, and R. van Gijlswijk, "EU Transport GHG: Routes to 2010 II: The role of GHG emissions from infrastructure construction, vehicle manufacturing, and ELVs in overall transport sector emissions," 2012.
- [12] J. Neubauer and E. Wood, "The impact of range anxiety and home, workplace, and public charging infrastructure on simulated battery electric vehicle lifetime utility," *J. Power Sources*, vol. 257, pp. 12–20, 2014.
- [13] B. M. Al-Alawi and T. H. Bradley, "Review of hybrid, plug-in hybrid, and electric vehicle market modeling Studies," *Renew. Sustain. Energy Rev.*, vol. 21, pp. 190–203, 2013.
- [14] Automotive Council UK, "Driving success – a strategy for growth and sustainability in the UK automotive sector," 2013.
- [15] S. Schaeck, A. O. Stoermer, F. Kaiser, L. Koehler, J. Albers, and H. Kabza, "Lead-acid batteries in micro-hybrid applications. Part I. Selected key parameters," *J. Power*

- Sources*, vol. 196, no. 3, pp. 1541–1554, Feb. 2011.
- [16] H.A.Kiehne, "Batteries for Electric Road Vehicles," in *Battery Technology Handbook*, 2nd ed., Expert Verlag, 2003, pp. 149–168.
- [17] E. Karden, S. Ploumen, B. Fricke, T. Miller, and K. Snyder, "Energy storage devices for future hybrid electric vehicles," *J. Power Sources*, vol. 168, no. 1, pp. 2–11, May 2007.
- [18] P. T. Moseley, B. Bonnet, A. Cooper, and M. J. Kellaway, "Lead-acid battery chemistry adapted for hybrid electric vehicle duty," *J. Power Sources*, vol. 174, no. 1, pp. 49–53, 2007.
- [19] A. J. Salkind, A. G. Cannone, and F. A. Trumbure, "Lead Acid Batteries," in *Handbook of Batteries*, D. Linden and T. B. Reddy, Eds. McGraw-Hill, 2002, p. 23.1-23.88.
- [20] J. M. Turner, "Following the Pb: An Envirotechnical Approach to Lead-Acid Batteries in the United States," *Environ. Hist. Durh. N. C.*, vol. 20, pp. 29–56, 2015.
- [21] P. Haefliger, M. Mathieu-Nolf, S. Lociciro, C. Ndiaye, M. Coly, A. Diouf, A. L. Faye, A. Sow, J. Tempowski, J. Pronczuk, A. P. F. J. Filipe, R. Bertollini, and M. Neira, "Mass lead intoxication from informal used lead-acid battery recycling in Dakar, Senegal," *Environ. Health Perspect.*, vol. 117, no. 10, pp. 1535–1540, 2009.
- [22] D. Linden, "Theoretical cell voltage, capacity and energy," in *Handbook of Batteries*, 3rd ed., D. Linden and T. B. Reddy, Eds. McGraw-Hill, 2001, p. 1.9-1.14.
- [23] M. R. Palacín, "Recent advances in rechargeable battery materials: a chemist's perspective," *Chem. Soc. Rev.*, vol. 38, no. 9, p. 2565, 2009.
- [24] E. Karden, P. Shinn, P. Bostock, J. Cunningham, E. Schoultz, and D. Kok, "Requirements for future automotive batteries - A snapshot," *J. Power Sources*, vol. 144, pp. 505–512, 2005.
- [25] J. X. Weinert, A. F. Burke, and X. Wei, "Lead-acid and lithium-ion batteries for the Chinese electric bike market and implications on future technology advancement," *J. Power Sources*, vol. 172, no. 2, pp. 938–945, 2007.
- [26] M. Calábek, K. Micka, P. Bača, and P. Křivák, "Influence of grid design on current distribution over the electrode surface in a lead-acid cell," *J. Power Sources*, vol. 85, pp. 145–148, 2000.
- [27] W. G. Sunu and B. W. Burrows, "Mathematical Model for Design of Battery Electrodes I. Potential distribution," *J. Electrochem. Soc.*, vol. 129, no. 4, pp. 688–695, 1982.
- [28] W. Sunu and B. Burrows, "Mathematical Model for Design of Battery Electrodes II. Current Density Distribution," *Electrochem. Sci. Technol.*, vol. 131, no. 1, pp. 1–6, 1984.
- [29] P. Král, P. Křivák, P. Bača, M. Calábek, and K. Micka, "Current distribution over the electrode surface in a lead-acid cell during discharge," *J. Power Sources*, vol. 105, no. 1, pp. 35–44, 2002.
- [30] A. Alagheband, M. Azimi, H. Hashemi, M. Kalani, and D. Nakhaie, "Optimization of grid configuration by investigating its effect on positive plate of lead-acid batteries via numerical modeling," *J. Energy Storage*, vol. 12, pp. 202–214, 2017.

- [31] Y. Guo, Y. Li, G. Zhang, H. Zhang, and J. Garche, "Studies of current and potential distributions on lead-acid batteries: I. Discharge of automotive flooded positive plates," *J. Power Sources*, vol. 124, no. 1, pp. 271–277, 2003.
- [32] Y. Guo, W. Li, and L. Zhao, "A study of current and potential distributions on tubular positive plate," *J. Power Sources*, vol. 116, no. 1–2, pp. 193–202, Jul. 2003.
- [33] G. S. Zhang, C. E. Shaffer, C.-Y. Y. Wang, and C. D. Rahn, "In-Situ Measurement of Current Distribution in a Li-Ion Cell," *J. Electrochem. Soc.*, vol. 160, no. 4, pp. A610–A615, Feb. 2013.
- [34] J. Kowal, D. Schulte, D. U. Sauer, and E. Karden, "Simulation of the current distribution in lead-acid batteries to investigate the dynamic charge acceptance in flooded SLI batteries," *J. Power Sources*, vol. 191, no. 1, pp. 42–50, 2009.
- [35] D. U. Sauer, E. Karden, B. Fricke, H. Blanke, M. Thele, O. Bohlen, J. Schiffer, J. B. Gerschler, and R. Kaiser, "Charging performance of automotive batteries-An underestimated factor influencing lifetime and reliable battery operation," *J. Power Sources*, vol. 168, no. 1, pp. 22–30, May 2007.
- [36] P. Ruetschi, "Aging mechanisms and service life of lead-acid batteries," *J. Power Sources*, vol. 127, no. 1–2, pp. 33–44, 2004.
- [37] D. Schulte, T. Sanders, W. Waag, J. Kowal, D. U. Sauer, and E. Karden, "Automatic device for continuous measurement of potential distribution and acid stratification in flooded lead-acid batteries," *J. Power Sources*, vol. 221, pp. 114–121, Jan. 2013.
- [38] R. Kaiser, "Optimized battery-management system to improve storage lifetime in renewable energy systems," *J. Power Sources*, vol. 168, no. 1 SPEC. ISS., pp. 58–65, 2007.
- [39] R. Ponraj, S. D. McAllister, I. F. Cheng, and D. B. Edwards, "Investigation on electronically conductive additives to improve positive active material utilization in lead-acid batteries," *J. Power Sources*, vol. 189, no. 2, pp. 1199–1203, 2009.
- [40] H. Metzendorf, "The capacity limiting role of the electronic conductivity of the active material in lead-acid batteries during discharge," *J. Power Sources*, vol. 7, no. 3, pp. 281–291, 1982.
- [41] D. B. Edwards and S. Zhang, "Influence of different aspect ratio additives on the performance of lead-acid batteries," *J. Power Sources*, vol. 135, no. 1, pp. 297–303, 2004.
- [42] E. Gyenge, J. Jung, S. Splinter, and A. Snaper, "High specific surface area, reticulated current collectors for lead-acid batteries," *J. Appl. Electrochem.*, vol. 32, pp. 287–295, 2002.
- [43] D. Pavlov, "Calculation of the Active Materials for Lead-Acid Cells," in *Lead-Acid Batteries: Science and Technology*, Elsevier B.V., 2011, pp. 607–622.
- [44] T. Huang, W. Ou, B. Feng, B. Huang, M. Liu, W. Zhao, and Y. Guo, "Researches on current distribution and plate conductivity of valve-regulated lead-acid batteries," *J. Power Sources*, vol. 210, pp. 7–14, 2012.

- [45] P. T. Moseley, "Positive plate additives," *J. Power Sources*, vol. 64, no. 1, pp. 47–50, 1997.
- [46] M. L. Soria, F. Trinidad, J. M. Lacadena, J. Valenciano, and G. Arce, "Spiral wound valve-regulated lead-acid batteries for hybrid vehicles," *J. Power Sources*, vol. 174, no. 1, pp. 41–48, 2007.
- [47] L. T. Lam, N. P. Haigh, C. G. Phyland, and A. J. Urban, "Failure mode of valve-regulated lead-acid batteries under high-rate partial-state-of-charge operation," *J. Power Sources*, vol. 133, no. 1, pp. 126–134, 2004.
- [48] D. Pavlov, "Fundamentals of Lead-Acid Batteries," in *Lead-Acid Batteries: Science and Technology*, Elsevier B.V., 2011, pp. 29–114.
- [49] D. Pavlov, "Invention and development of the Lead-Acid Battery," in *Lead-Acid Batteries: Science and Technology*, Elsevier B.V., 2011, pp. 3–28.
- [50] C. Kalyvas, A. Kucernak, D. Brett, G. Hinds, S. Atkins, and N. Brandon, "Spatially resolved diagnostic methods for polymer electrolyte fuel cells: A review," *Wiley Interdiscip. Rev. Energy Environ.*, vol. 3, no. 3, pp. 254–275, 2014.
- [51] J. T. Clement, D. S. Aaron, and M. M. Mench, "In Situ Localized Current Distribution Measurements in All-Vanadium Redox Flow Batteries," *J. Electrochem. Soc.*, vol. 163, no. 1, pp. A5220–A5228, 2016.
- [52] J. Newman and W. Tiedemann, "Porous-electrode theory with battery applications," *AIChE J.*, vol. 21, no. 1, pp. 25–41, 1975.
- [53] J. Newman and W. Tiedmann, "Potential and Current Distribution in Electrochemical Cells," *J. Electrochem. Soc.*, vol. 140, no. 7, pp. 1961–1968, 1993.
- [54] P. C. Rieke and N. E. Vanderborgh, "Thin Film Electrode Arrays for Mapping the Current-Voltage Distributions in Proton-Exchange-Membrane Fuel Cells," *J. Electrochem. Soc.*, vol. 134, no. 5, pp. 1099–1104, 1987.
- [55] M. K. Carpenete, D. M. Bemardi, and J. A. Wertz, "The use of Hg/Hg<sub>2</sub>SO<sub>4</sub> reference electrodes in valve-regulated lead/acid cells," *J. Power Sources*, vol. 63, pp. 15–22, 1996.
- [56] S.-H. Ng, F. La Mantia, and P. Novák, "A multiple working electrode for electrochemical cells: a tool for current density distribution studies," *Angew. Chem. Int. Ed. Engl.*, vol. 48, no. 3, pp. 528–532, Jan. 2009.
- [57] W. W. Focke, "On the mechanism of transfer enhancement by eddy promoters," *Electrochim. Acta*, vol. 28, no. 8, pp. 1137–1146, 1983.
- [58] L. R. Czarnetzki and L. J. J. Janssen, "Electrode current distribution in a hypochlorite cell," *J. Appl. Electrochem.*, vol. 19, no. 5, pp. 630–636, 1989.
- [59] M. M. Britton, "Magnetic resonance imaging of electrochemical cells containing bulk metal," *ChemPhysChem*, vol. 15, no. 9, pp. 1731–1736, 2014.
- [60] M. M. Britton, P. M. Bayley, P. C. Howlett, A. J. Davenport, and M. Forsyth, "In Situ, Real-Time Visualization of Electrochemistry Using Magnetic Resonance Imaging," *J.*

- Phys. Chem. Lett.*, vol. 4, no. 17, pp. 3019–3023, 2013.
- [61] A. J. Pearse, E. Gillette, S. B. Lee, and G. W. Rubloff, “The reaction current distribution in battery electrode materials revealed by XPS-based state-of-charge mapping,” *Phys. Chem. Chem. Phys.*, vol. 18, no. 18, pp. 19093–19102, 2016.
- [62] J. Liu, M. Kunz, K. Chen, N. Tamura, and T. J. Richardson, “Visualization of charge distribution in a lithium battery electrode,” *J. Phys. Chem. Lett.*, vol. 1, no. 14, pp. 2120–2123, 2010.
- [63] J. M. Campillo-Robles, D. Goonetilleke, N. Sharma, D. Soler, and P. Türkyilmaz, “Seeing inside lead-acid batteries using neutron imaging,” in *10th International Conference on Lead-Acid Batteries, LABAT 2017*, 2017, no. June.
- [64] A. Santoro, P. D’Antonio, and S. M. Caulder, “A Neutron Powder Diffraction Study of  $\alpha$  and  $\beta$ -PbO<sub>2</sub> in the Positive Electrode Material of Lead-Acid Batteries,” *Electrochem. Sci. Technol.*, pp. 1451–1459, 1983.
- [65] Corporate (Honeywell), “Solid State Sensors: Linear Current Sensors.” [Online]. Available: <http://www.farnell.com/datasheets/198815.pdf>. [Accessed: 10-Oct-2017].
- [66] Corporate (LEM), “Current Transducer LA 55-P.” [Online]. Available: <http://www.farnell.com/datasheets/1449960.pdf>. [Accessed: 10-Oct-2017].
- [67] C. Wieser, A. Helmbold, and E. Gülzow, “A new technique for two-dimensional current distribution measurements in electrochemical cells,” *J. Appl. Electrochem.*, vol. 30, pp. 803–807, 2000.
- [68] P. C. Hansen and D. P. O’Leary, “The Use of the L-Curve in the Regularization of Discrete Ill-Posed Problems,” *SIAM J. Sci. Comput.*, vol. 14, no. 6, pp. 1487–1503, 1993.
- [69] P. C. Hansen, “Regularization Tools: A Matlab Package for Analysis and Solution of Discrete Ill-Posed Problems,” *Numer. Algorithms*, vol. 6, no. March, pp. 1–35, 1994.
- [70] R. Kress, L. Kühn, and R. Potthast, “Reconstruction of a current distribution from its magnetic field,” *Inverse Probl.*, vol. 18, no. 4, pp. 1127–1146, Aug. 2002.
- [71] B. J. Roth, N. G. Sepulveda, and J. P. Wikswo, “Using a magnetometer to image a two-dimensional current distribution,” *J. Appl. Phys.*, vol. 65, pp. 361–372, 1989.
- [72] D. Hofer, T. Wiesner, and B. G. Zagar, “Analyzing 2D current distributions by magnetic field measurements,” in *Instrumentation and Measurement Technology Conference (I2MTC), 2012 IEEE International*, 2012, pp. 2061–2066.
- [73] B. Fishbine, “SQUID Magnetometry: Harnessing the Power of Tiny Magnetic Fields,” *Los Alamos Research Quarterly*, pp. 4–11, 2003.
- [74] J. Lenz and A. S. Edelstein, “Magnetic Sensors and Their Applications,” *IEEE Sens. J.*, vol. 6, no. 3, pp. 631–649, 2006.
- [75] K.-H. Hauer, R. Potthast, T. Wüster, and D. Stolten, “Magnetotomography—a new method for analysing fuel cell performance and quality,” *J. Power Sources*, vol. 143, no. 1–2, pp. 67–74, 2005.

- [76] T. Kiwa, K. Tanaka, S. Kasuya, K. Sakai, and K. Tsukada, "Ion transportation of electrolytes in a flow channel mapped by an HTS SQUID scanning system," *IEEE Trans. Appl. Supercond.*, vol. 25, no. 3, pp. 3–6, 2015.
- [77] K.-H. Hauer, R. Potthast, and M. Wannert, "Algorithms for magnetic tomography—on the role of a priori knowledge and constraints," *Inverse Probl.*, vol. 24, pp. 1–18, 2008.
- [78] L. Warnes, "Linear Electric Circuits," in *Analogue and Digital Electronics*, Macmillan, 1998, p. 2.
- [79] J. E. Green, D. A. Stone, M. P. Foster, and A. Tennant, "Spatially Resolved Measurements of Magnetic Fields Applied to Current Distribution Problems in Batteries," *IEEE Trans. Instrum. Meas.*, vol. 64, no. 4, pp. 951–958, 2015.
- [80] D. Benitez, P. Gaydecki, S. Quek, and V. Torres, "Development of a solid-state multi-sensor array camera for real time imaging of magnetic fields," *J. Phys. Conf. Ser.*, vol. 76, Jul. 2007.
- [81] G. Nolte and G. Curio, "On the calculation of magnetic fields based on multipole modeling of focal biological current sources," *Biophys. J.*, vol. 73, no. 3, pp. 1253–62, Sep. 1997.
- [82] S. Quek, D. Benitez, P. Gaydecki, and V. Torres, "Modeling Studies on the Development of a System for Real-Time Magnetic-Field Imaging of Steel Reinforcing Bars Embedded Within Reinforced Concrete," *IEEE Trans. Instrum. Meas.*, vol. 57, no. 3, pp. 571–576, Mar. 2008.
- [83] H. T. Harrison, G. Cooke, D. A. Hewitt, D. A. Stone, and J. E. Green, "Magnetic tomography for lead acid batteries," *J. Energy Storage*, vol. 12, pp. 1–10, 2017.
- [84] C. (NXP), "I2C Bus Specification and User Manual," 2014. [Online]. Available: [http://www.nxp.com/documents/user\\_manual/UM10204.pdf](http://www.nxp.com/documents/user_manual/UM10204.pdf).
- [85] J. Axelson, *USB Complete: Everything You Need to Develop USB Peripherals*, 3rd ed. Lakeview Research, 2005.
- [86] Corporate (Honeywell), "3-Axis Digital Compass IC HMC5883L," 2010. [Online]. Available: [http://www51.honeywell.com/aero/common/documents/myaerospacecatalog-documents/Defense\\_Brochures-documents/HMC5883L\\_3-Axis\\_Digital\\_Compass\\_IC.pdf](http://www51.honeywell.com/aero/common/documents/myaerospacecatalog-documents/Defense_Brochures-documents/HMC5883L_3-Axis_Digital_Compass_IC.pdf). [Accessed: 25-Mar-2015].
- [87] C. (NXP), "PCA9546A 4-channel I2C-bus switch with reset," 2014. [Online]. Available: [http://www.nxp.com/documents/data\\_sheet/PCA9546A.pdf](http://www.nxp.com/documents/data_sheet/PCA9546A.pdf). [Accessed: 25-Mar-2015].
- [88] C. (NXP), "PCA9547 8-channel I2C-bus multiplexer with reset," 2014. [Online]. Available: [http://www.nxp.com/documents/data\\_sheet/PCA9547.pdf](http://www.nxp.com/documents/data_sheet/PCA9547.pdf). [Accessed: 25-Mar-2015].
- [89] C. (NXP), "PCA9548A Data sheet," 2014. [Online]. Available: <https://www.nxp.com/docs/en/data-sheet/PCA9548A.pdf>. [Accessed: 25-Mar-2015].
- [90] C. (Microchip), "PIC18F2455/2550/4455/4550 Data Sheet," 2009. [Online]. Available: <http://ww1.microchip.com/downloads/en/DeviceDoc/39632e.pdf>. [Accessed: 25-Mar-2015].

- [91] C. (Microchip), "MPLAB® ICD 3 In-Circuit Debugger User's Guide." [Online]. Available: <http://ww1.microchip.com/downloads/en/DeviceDoc/51766B.pdf>. [Accessed: 25-Mar-2015].
- [92] J. Sarvas, "Basic mathematical and electromagnetic concepts of the biomagnetic inverse problem," *Phys. Med. Biol.*, vol. 32, no. 1, pp. 11–22, Jan. 1987.
- [93] A. N. Tikhonov, A. V. Goncharsky, V. V. Stepanov, and A. G. Yagola, *Numerical Methods for the Solution of Ill-Posed Problems*. Springer, 1995.
- [94] P. Spitzer, S. Wunderli, K. Maksymiuk, A. Michalska, A. Kisiel, Z. Galus, and G. Tauber, "Reference Electrodes for Aqueous Solutions," in *Handbook of Reference Electrodes*, G. Inzelt, A. Lewenstam, and F. Scholz, Eds. Berlin, Heidelberg: Springer Berlin Heidelberg, 2013, pp. 77–143.
- [95] Corporate (Shield Batteries), "Automotive & Commercial Brochure." [Online]. Available: <http://www.shieldbatteries.co.uk/documents/automotive.pdf>. [Accessed: 13-Oct-2017].
- [96] Corporate (Mapei), "MAPEI Kerapoxy Datasheet." [Online]. Available: <http://www.tilemountain.co.uk/pdf/kerapoxy.pdf>. [Accessed: 25-Mar-2015].
- [97] C. (NXP), "PSMN3R9-60PS," 2013. [Online]. Available: [http://www.farnell.com/datasheets/1705528.pdf?\\_ga=2.165371135.1335405004.1498568445-1899270619.1467124387](http://www.farnell.com/datasheets/1705528.pdf?_ga=2.165371135.1335405004.1498568445-1899270619.1467124387). [Accessed: 10-Oct-2017].
- [98] Corporate (Vishay Semiconductors), "VOM1271 Photovoltaic MOSFET Driver with Integrated Fast Turn-Off, Solid-State Relay," 2014. [Online]. Available: <https://www.vishay.com/docs/83469/vom1271t.pdf>. [Accessed: 10-Oct-2017].
- [99] B. Borchers, "Tikhonov regularization in the non-negative least square - NNLS (python:scipy)." [Online]. Available: <https://scicomp.stackexchange.com/questions/10671/tikhonov-regularization-in-the-non-negative-least-square-nnls-pythonscipy%0A>. [Accessed: 30-Jun-2017].
- [100] C. (Cogent), "Magnetic Qualities - Non-Oriented Electrical Steel." [Online]. Available: <https://cogent-power.com/products/non-oriented-electrical-steel/magnetic-qualities>. [Accessed: 10-Oct-2017].
- [101] Corporate (Cogent), "Typical magnetic data for SURA® M330-35A," 2008. [Online]. Available: <https://cogent-power.com/cms-data/downloads/m330-35a.pdf>. [Accessed: 10-Oct-2017].
- [102] Corporate (ST Microelectronics), "LSM303DLHC," 2013. [Online]. Available: <http://www.st.com/content/ccc/resource/technical/document/datasheet/56/ec/ac/de/28/21/4d/48/DM00027543.pdf/files/DM00027543.pdf/jcr:content/translations/en.DM00027543.pdf>. [Accessed: 10-Oct-2017].
- [103] Corporate (NXP), "FXOS8700CQ," 2017. [Online]. Available: [www.nxp.com/files/sensors/doc/data\\_sheet/FXOS8700CQ.pdf](http://www.nxp.com/files/sensors/doc/data_sheet/FXOS8700CQ.pdf). [Accessed: 10-Oct-2017].
- [104] Corporate (Allegro Microsystems), "A1308 and A1309," 2017. [Online]. Available:

<http://www.allegromicro.com/~media/Files/Datasheets/A1308-9-Datasheet.ashx>.  
[Accessed: 10-Oct-2017].

- [105] JordanDee, "Triple Axis Magnetometer - HMC5883L Breakout Quickstart Guide," *Sparkfun*, 2011. [Online]. Available: <https://www.sparkfun.com/tutorials/301>. [Accessed: 10-Oct-2017].
- [106] Corporate (Electrolube), "ER2223 Epoxy Resin," 2013. [Online]. Available: <https://www.electrolube.com/core/components/products/tds/044/ER2223.pdf>. [Accessed: 10-Oct-2017].
- [107] Corporate (Keithley Instruments Inc), "2600B System SourceMeter SMU Instruments Datasheet." [Online]. Available: [https://www.tek.com/sites/default/files/media/media/resources/Series2600B\\_DataSheet.pdf](https://www.tek.com/sites/default/files/media/media/resources/Series2600B_DataSheet.pdf). [Accessed: 10-Oct-2017].

## Appendix I – $bh$ data for M330-35A Electrical Steel

Manufacturer's data, unpublished at the time of writing. From private correspondence with Cogent power technical support, permission has been given for use in this document.

Peak magnetic field strength, $h$ ( $A\ m^{-1}$ )	Peak magnetic polarisation, $b$ (T)	Relative permeability, $\mu_r$
10	0.018	1432
20	0.049	1950
30	0.105	2785
40	0.212	4218
50	0.358	5698
60	0.551	7308
70	0.686	7799
80	0.787	7828
90	0.892	7887
100	0.966	7687
125	1.096	6977
150	1.173	6223
175	1.227	5580
200	1.265	5033
250	1.314	4183
300	1.335	3540
350	1.372	3119
400	1.393	2771
450	1.409	2492
500	1.420	2260
750	1.462	1551
1000	1.489	1185
1250	1.511	962
1500	1.530	812
2000	1.562	622
2500	1.588	505
5000	1.681	268
7500	1.751	186
10000	1.807	144
25000	1.931	61 (Estimated)
50000	1.999	32 (Estimated)
75000	2.021	21 (Estimated)
100000	2.029	16 (Estimated)

## Appendix II – FTS Arduino Firmware

### Main.ino

```

char junk; //
boolean bypass = true; //variable for controlling the bypass switch
#include <Wire.h> //I2C Arduino Library
#include <stdint.h> //for converting to int8 etc.
#include <myHMC.h>

void setup() {

  Serial.begin(9600);
  Wire.begin();

  //setup the digital pins according to APins list;
  setupMuxPins();

  //Load the default values into Conf. registers
  byte *IDlist=IDreg();
  configSensors(IDlist,CONFA,0x10);
  configSensors(IDlist,CONFB,0x20);

  //Setup the SSR control pin
  pinMode(18,OUTPUT);
}

void loop() {
  //This bit is just to emulate the user interface and calls the
  actual configSensors part when requested
  byte choice;
  byte *datalist;
  static byte *IDlist;
  byte *conflist;
  byte *maglist;
  byte val;

  //IDlist=IDreg();
  //Serial.write(IDlist,28);

  delay(50);
  //Serial.println("Take reading? y/n");
  Serial.write('S');//writing one character as a prompt for Octave
  while (Serial.available()<1){
    //Do nothing//
  }
  if (Serial.available()>=1){
    choice = Serial.read();
  }
  while (Serial.available()>=1){
    Serial.read();//reading everything in the input buffer
  }

  switch (choice){

    case 'i': //Read IDlist

```

```

        IDlist=IDreg();
        Serial.write(IDlist,28);
        break;
    case 'r': //Read config registers
        conflist=getConfig(IDlist,CONFA);
        Serial.write(conflist,28);

        conflist=getConfig(IDlist,CONFB);
        Serial.write(conflist,28);

        break;
    case 'w': //Write to config registers
        while(Serial.available()<1){
            //do nothing//
        }
        if (Serial.available()>=1){
            val=Serial.read();
            configSensors(IDlist,CONFA,val);
        }
        while(Serial.available()<1){
            //do nothing//
        }
        if (Serial.available()>=1){
            val=Serial.read();
            configSensors(IDlist,CONFB,val);
        }
        break;
    case 't': //Trigger a measurement by writing to mode register
        configSensors(IDlist,MODE,SING_MEAS);
        break;
    case 'f': //Fetch magnetic data
        maglist=readSensors(IDlist);
        Serial.write(maglist,168);
        break;
    case 's': //Switch the solid state relay
        digitalWrite(18,bypass);
        bypass = !bypass;
        delay(100);
        if (bypass){
            //'[B]ypass cell'
            Serial.write('B');
        }
        else {
            //'[T]hrough cell'
            Serial.write('T');
        }
        break;
    default: Serial.write('K'); break;
}
while (Serial.available()>=1){
    Serial.read();//reading everything in the input buffer
}
delay(100);
}

```

**myHMC.cpp**

```

#include "Arduino.h"
#include <Wire.h>
#include "myHMC.h"

byte APins[7]={17,16,2,3,4,5,6};
byte pca_reset=7;

//*****//
byte * readSensors(byte IDlist[28]){
  byte count = 0;
  byte *magvals;
  static byte maglist[168];

  for(byte muxnum=0;muxnum<7;muxnum++){
    chooseMUX(muxnum);
    for(byte line = 0;line<4;line++){
      chooseLine(line); //replace these with a for loop
      if(IDlist[count]=='4'){
        magvals=read6reg(DOX_MSB); //read the 6 data registers starting
        from X axis MSB register
        for (byte subcount=0;subcount<6;subcount++){
          //write out the 6 bytes to the appropriate position in an
          overall magdata array
          //count is the sensor number 0-27, subcount is the data register
          number 0-5
          int magpos = 6*count+subcount;
          maglist[magpos]=magvals[subcount];
          //maglist[magpos]=count;

        }
        count++;
      }
    }
  }
  return maglist;
}
//*****//
void configSensors(byte IDlist[28], byte reg,byte val){
  //Changes register reg to value val and reads back
  //Requires that IDlist has been populated so we don't try and read
  unpopulated sensors
  byte count = 0;

  for(byte muxnum=0;muxnum<7;muxnum++){
    chooseMUX(muxnum);

    for(byte line = 0;line<4;line++){

      chooseLine(line);
      if(IDlist[count]=='4'){
        writeconfig(reg,val);
      }

      count++;
    }
  }
}

```

```

}
}
//*****//

byte * getConfig(byte IDlist[28], byte reg){
//Changes register reg to value val and reads back
//Requires that IDlist has been populated so we don't try and read
unpopulated sensors
byte count = 0;
static byte conflist[28];

for(byte muxnum=0;muxnum<7;muxnum++){
  chooseMUX(muxnum);

  for(byte line = 0;line<4;line++){

    chooseLine(line);
    if(IDlist[count]=='4'){
      conflist[count]=readlreg(reg);
    }

    count++;
  }
}
return conflist;
}
//*****//
byte * IDreg(){
//IDreg writes straight to serial and also returns IDlist to void
loop() using a pointer/static variable ting
//https://www.tutorialspoint.com/cprogramming/c_return_arrays_from_fun
ction.htm

byte count = 0;
static byte IDlist[28];
for(byte muxnum=0;muxnum<7;muxnum++){
  chooseMUX(muxnum);

  // Serial.print("Mux ");Serial.println(muxnum);
  for(byte line = 0;line<4;line++){

    chooseLine(line);
    IDlist[count]=readID();
    count++;
  }
}
//Write whole IDlist as a 28-byte buffer
//Serial.print("IDlist=");Serial.write(IDlist,count);
//Serial.println("");
return IDlist;
}
//*****//
byte readID(){
//Have set the return values to 0x48 ans 0x34 so that they can be
transmitted as bytes and show up as a
//recognisable character in Arduino Serial Monitor (unlike 1 and 0
which turn into spaces which is hard to read)

```

```

byte *ir;

ir=read3reg(IDA); //read the three registers starting from IDA/0x0A
if ((ir[0x00]!=0x48)|| (ir[0x01]!=0x34)|| (ir[0x02]!=0x33)) {return
0x48;}
return 0x34;

}
//*****//
void writeconfig(byte reg, byte confbyte){
//Write to first byte of conf register
Wire.beginTransaction(addr);
Wire.write(reg);
Wire.write(confbyte);
Wire.endTransmission();
}
//*****//
byte readlreg(byte reg){
byte val;
//Get first byte of conf register
Wire.beginTransaction(addr);
Wire.write(reg);
Wire.endTransmission();

Wire.requestFrom(addr,1);
if(1<=Wire.available()) {val=Wire.read();}

return val;
}
//*****//
byte * read3reg(byte startreg){
static byte val[3];
int i = 0;
Wire.beginTransaction(addr);
Wire.write(startreg);
Wire.endTransmission();

int n = Wire.requestFrom(addr,3);
val[0]=Wire.read();
val[1]=Wire.read();
val[2]=Wire.read();
return val;
// Serial.print(val[0]);Serial.print(val[1]);Serial.println(val[2]);
}
//*****//
byte * read6reg(byte startreg){
static byte val[6];

Wire.beginTransaction(addr);
Wire.write(startreg);
Wire.endTransmission();

int n = Wire.requestFrom(addr,6);
// if (n<6){Serial.println("not recieved 6bytes");}
for (byte i=0;i<n;i++)

```

```

    {
        val[i]=Wire.read();
    }
    return val;
}
//*****//
void chooseMUX(byte muxnum){
//This sets up one mux with the hardware address 0x74/MUX/ADDR
digitalWrite(APins[0],LOW);
digitalWrite(APins[1],LOW);
digitalWrite(APins[2],LOW);
digitalWrite(APins[3],LOW);
digitalWrite(APins[4],LOW);
digitalWrite(APins[5],LOW);
digitalWrite(APins[6],LOW);

digitalWrite(APins[muxnum],HIGH);

//Toggling the reset, as values can sometimes persist when changing
multiplexer
digitalWrite(pca_reset,LOW);
digitalWrite(pca_reset,HIGH);

}
//*****//

byte chooseLine(byte line){
//This talks to a MUX and selects one line
byte linebyte;

linebyte= 0x01<<line;

Wire.beginTransmission(MUX_ADDR); //Hardware address of a PCA9546A
with pin A2 pulled high = 0x74
Wire.write(linebyte);
Wire.endTransmission();

}

//*****//
void setupMuxPins(){
pinMode(APins[0], OUTPUT);
pinMode(APins[1], OUTPUT);
pinMode(APins[2], OUTPUT);
pinMode(APins[3], OUTPUT);
pinMode(APins[4], OUTPUT);
pinMode(APins[5], OUTPUT);
pinMode(APins[6], OUTPUT);
pinMode(pca_reset, OUTPUT);

digitalWrite(APins[0],LOW);
digitalWrite(APins[1],LOW);
digitalWrite(APins[2],LOW);
digitalWrite(APins[3],LOW);
digitalWrite(APins[4],LOW);
digitalWrite(APins[5],LOW);

```

```

    digitalWrite(APins[6],LOW);

    digitalWrite(pca_reset,LOW);
    delay(50);
    digitalWrite(pca_reset,HIGH);
}

```

## myHMC.h

```

#ifndef MYHMC_H
#define MYHMC_H

#include "Arduino.h"

//function prototypes
void setupMuxPins();

byte * readSensors(byte IDlist[28]);

void configSensors(byte IDlist[28], byte reg,byte val);
void writeconfig(byte reg, byte confbyte);

byte * getConfig(byte IDlist[28],byte reg);

byte * IDreg();
byte readID();

byte readlreg(byte reg);
byte * read3reg(byte startreg);
byte * read6reg(byte startreg);

void chooseMUX(byte muxnum);
byte chooseLine(byte line);
//end function prototypes

//I2C Address for the PCA9546A (..with pin A2 pulled high)
#define MUX_ADDR 0x74
//I2C Address for The HMC5883
#define addr 0x1E
//

//Register list (see HMC datsheet, page 11)
#define CONFA 0x00
#define CONFB 0x01
#define MODE 0x02
#define DOX_MSB 0x03
#define DOX_LSB 0x04
#define DOZ_MSB 0x05
#define DOZ_LSB 0x06
#define DOY_MSB 0x07
#define DOY_LSB 0x08
#define STATUS 0x09
#define IDA 0x0A
#define IDB 0x0B
#define IDC 0x0C
//

//Measurement modes (see HMC datasheet, page 14
#define CONT_MEAS 0x00

```

```

#define SING_MEAS 0x01
#define IDLE 0x02
//

#endif //MYHMC_H_

```

## Appendix III – FTS Octave Code

### Main – rwcswitch.m

```

function rwcswitch()
cd path\to\library\functions

s1=setup();
%Default values of Configuration registers. Do not need to actually
be written from here as they are done in firmware at startup
CONFA=0x10;
CONFB=0x20;
%Firmware does not populate IDreg by default, therefore need to call
getID in software by default
hnd=readhandshake(s1);
id=getID(hnd,s1);
ssr_state_char='B'; %initialise SSR value as 'bypass' (this is set
separately in firmware
again =logical(1);
while again == true

    choice=mainMenu();

    switch (choice)
    case 0
        again = logical(0);
    case 1
        [CONFA CONFB]=confMenuTree(CONFA,CONFB);
        hnd=readhandshake(s1);
        putConfig(hnd,s1,CONFA,CONFB);
    case 2
        hnd=readhandshake(s1);
        HMC_CONF_readback=getConfig(hnd,s1);
        confToUser(id,HMC_CONF_readback);
    case 3
        hnd=readhandshake(s1);
        triggerMeas(hnd,s1);
        hnd=readhandshake(s1);
        md=getData(hnd,s1);
        dataToUser(id,md)
    case 4
        [magfilename magpath]=filenamer(ssr_state_char)
        if magfilename != 0
            cd(magpath);
            [filenumber magfilename]=firstavailablefilename(magfilename)
            [time_limit file_limit]=stopcondmenu()
            tic
            start_time=time;
            current_time=start_time;
            for i = [1:file_limit]

```

```

        if (kbhit(1) == 'x') || (current_time > start_time +
time_limit)
            break
        endif
        hnd=readhandshake(s1);
        triggerMeas(hnd,s1);
        hnd=readhandshake(s1);
        md=getData(hnd,s1);
        current_time=time;
        timeinfo=gmtime(current_time);
        [config.nsamples config.datarate config.selftest
config.gain]=interpretConf(CONFA,CONFB);
        save(magfilename,"md","timeinfo","config","id");
        [filenumber magfilename]=filenameupdate(filenumber,
magfilename);
    endfor
    toc
    endif
    case 5
        hnd=readhandshake(s1);
        id=getID(hnd,s1);
    case 6
        hnd=readhandshake(s1);
        default(hnd,s1);
    case 7
        hnd=readhandshake(s1);
        ssr_state_char=toggle_SSR(hnd,s1,ssr_state_char);
    case 8
        if ssr_state_char == 'B'

            [magfilename magpath]=filenamer('T'); %make a base name
(recycling the function which takes ssr state, but ssr state checking
also takes place in auto_saver)
            for counter=1:4
                if (kbhit(1) == 'x')
                    break
                endif
                auto_saver([magfilename(1:end-4),num2str(counter),'.mat'],
magpath, ssr_state_char,30,9999,CONFA,CONFB,hnd,s1,id);%save 30s dark
frames
                hnd=readhandshake(s1);
                ssr_state_char=toggle_SSR(hnd,s1,ssr_state_char);
                auto_saver([magfilename(1:end-4),num2str(counter),'_mat'],
magpath, ssr_state_char,120,9999,CONFA,CONFB,hnd,s1,id);%save 30
seconds of image frames

                hnd=readhandshake(s1);
                ssr_state_char=toggle_SSR(hnd,s1,ssr_state_char);
                %auto_saver(magfilename, magpath,
ssr_state_char,9999,10,CONFA,CONFB,hnd,s1);%save 2 dark frames
            endfor
            auto_saver([magfilename(1:end-4),num2str(counter+1),'.mat'],
magpath, ssr_state_char,30,9999,CONFA,CONFB,hnd,s1,id);%save 30s dark
frames
        endif
    endswitch
endwhile
unsetup(s1);

```

```
endfunction
```

```
%%%%%%%%%%%%%%%%%%%%%%%%%%%%%%%%%%%%%%%%%%%%%%%%%%%%%%%%%%%%%%%%%%%%%%%%%
```

```
function choice=mainMenu()
    [choice, ok] = listdlg ("ListString", {"Write Configuration",...
        "Read Configuration", "Quick reading", "Multiple readings", "Reload ID
Register", "Refresh Menu", "Toggle Bypass Switch", "Auto Readings"},
        "SelectionMode", "Single", "Name", "FTS Main Menu",
"CancelString", "Exit", ...
        "ListSize", [300 300]);
    if ok ~= 1
        choice = 0;
        disp("Exit FTS");
    endif
endfunction
```

```
function s1=setup()
    if ispc
        s1=serial("COM4",9600);
    elseif isunix
        s1=serial("/dev/ttyACM0",9600);
    endif
    srl_flush(s1);
endfunction
```

```
function [confa confb]=getsettings()
    [confa confb]=makeConf(1,"norm",440,0.75);
endfunction
```

```
function hnd=readhandshake(s1);
    hnd=char(srl_read(s1,1));
    if hnd=='K'
        hnd=char(srl_read(s1,1));
    endif
endfunction
```

```
function default(hnd,s1)
    if (hnd=='S')
        srl_write(s1,'n');
    endif
endfunction
```

```
function ID=getID(hnd,s1)
    ID=zeros(1,28);
    if (hnd=='S')
        srl_write(s1,'i');
        %pause(1);
        ID=srl_read(s1,28)
        %pause(1);
    endif
endfunction
```

```
function putConfig(hnd,s1,confa,confb)
    if (hnd=='S')
        srl_write(s1,'w');
        bytes=srl_write(s1,char(confa))
        pause(10e-3);
    endif
endfunction
```

```

        bytes=srl_write(s1,char(confb))

    endif
endfunction

function HMC_CONF_readback = getConfig(hnd,s1)
    if (hnd=='S')
        srl_write(s1,'r')
        HMC_CONF_readback=srl_read(s1,56)
    endif
endfunction

function triggerMeas(hnd,s1)
    if (hnd=='S')
        srl_write(s1,'t')
    endif
endfunction

function magData=getData(hnd,s1)
    if (hnd=='S')
        srl_write(s1,'f');
        magData=srl_read(s1,168);
    endif
endfunction

function unsetup(s1)
    srl_close(s1);
endfunction

function confToUser(ID,HMC_CONF_readback)
    %This bit converts the hex values in CONF_readback to individual
    parameters
    for (sensornumber=1:28)
        if (ID(sensornumber)=='4')
            sensornumber
            [n d b
g]=interpretConf(HMC_CONF_readback(sensornumber),HMC_CONF_readback(sen
sornumber+28))
            endif
        endfor
    endfunction

function dataToUser(ID,data)
    %This bit converts the 2 bytes into signed integers
    for (i=0:27)
        if (ID(i+1)=='4')
            sensornumber=i+1
            x0=bitshift(int16(data(6*i+1)),8)+int16(data(6*i+2))
            z0=bitshift(int16(data(6*i+3)),8)+int16(data(6*i+4))
            y0=bitshift(int16(data(6*i+5)),8)+int16(data(6*i+6))
        endif
    endfor
endfunction

function state_char=toggle_SSR(hnd,s1,state_char_old)
    if (hnd == 'S')
        srl_write(s1,'s');
        state_char=srl_read(s1,1);
    end
endfunction

```

```

    if state_char == 'B'
        disp("Bypassing cell")
    elseif state_char == 'T'
        disp("Current through cell")
    endif
else
    state_char=state_char_old
endif
endfunction

function auto_saver(magfilename,
magpath,ssr_state_char,time_limit,file_limit,CONFA,CONFB,hnd,s1,id)
    %[magfilename magpath]=filenamer(ssr_state_char);
    if magfilename != 0
        cd(magpath);
        if ssr_state_char == 'B'
            magfilename=[magfilename(1:end-4),'_dark.mat'];
        endif
        [filenumber magfilename]=firstavailablefilename(magfilename)
        %[time_limit file_limit]=stopcondmenu()
        tic
        start_time=time;
        current_time=start_time;
        for i = [1:file_limit]
            if (kbhit(1) == 'x') || (current_time > start_time +
time_limit)
                break
            endif
            hnd=readhandshake(s1);
            triggerMeas(hnd,s1);
            hnd=readhandshake(s1);
            md=getData(hnd,s1);
            current_time=time;
            timeinfo=gmtime(current_time);
            [config.nsamples config.datarate config.selftest
config.gain]=interpretConf(CONFA,CONFB);
            save(magfilename,"md","timeinfo","config","id");
            [filenumber magfilename]=filenameupdate(filenumber,
magfilename);
        endfor
        toc
    endif
endfunction

```

## Library

```

function [nextA nextB]=confMenuTree(prevA,prevB)
    [nsampleschoice drchoice biaschoice gainchoice]
=interpretConf(prevA,prevB)
    again=logical(1);
    while again == true;
        confchoice=confMenu;
        switch confchoice
            case 0
                again = logical(0);
            case 1
                gainchoice=gainMenu(gainchoice)

```

```

    case 2
        nsampleschoice=aveMenu(nsampleschoice)
    case 3
        biaschoice=biasMenu(biaschoice)
    case 4
        drchoice=drMenu(drchoice)
    case 5
        [nsampleschoice drchoice biaschoice
gainchoice]=interpretConf(0x10,0x20)
    case 6
        [nsampleschoice drchoice biaschoice gainchoice]=loadConf()
    case 7
        saveConf(nsampleschoice, drchoice, biaschoice, gainchoice)
    endswitch
endwhile
[nextA nextB]=makeConf(nsampleschoice, biaschoice, gainchoice,
drchoice);
endfunction

%Conf menu branches into sub-menus
function choice = confMenu()
    [choice, ok] = listdlg ("ListString", {"Gain", "Number of
averages",...
    "Self Test", "Data Rate", "Set all to default", "Load a config
file",...
    "Save current config"}, "SelectionMode", "Single", "Name", "FTS Conf.
Menu", "CancelString", "Write to Sensors");
    if (ok != 1)
        choice=0;
    endif
endfunction

function choice = gainMenu(previous)
    gain_LUT=[1370 1090 820 660 440 390 330 230];
    [sel, ok] = listdlg ("ListString", {"1370", "1090 (default)",
"820", "660", "440",...
    "390", "330", "230"}, "SelectionMode", "Single", "Name", "Gain
Settings");
    if (ok != 1)
        choice=previous;
    else
        choice=gain_LUT(sel);
    endif
endfunction

function choice = aveMenu(previous)
    ave_LUT=[1 2 4 8];
    [sel, ok] = listdlg ("ListString", {"1 (default)",
"2", "4", "8"}, "SelectionMode",...
    "Single", "Name", "Number of samples to average");
    if (ok != 1)
        choice=previous;
    else
        choice=ave_LUT(sel);
    endif
endfunction

function choice = biasMenu(previous)

```

```

    bias_LUT=["normal ";"positive";"negative"];
    [sel, ok] = listdlg ("ListString", {"None (default)", "Positive",
    "Negative"},
                       "SelectionMode", "Single", "Name", "Self-test
bias");
    if (ok != 1)
        choice=previous;
    else
        choice=bias_LUT(sel,:);
    endif
endfunction

function choice = drMenu(previous)
    dr_LUT=[0.75 1.5 3 7.5 15 30 75];
    disp("Data rate setting has no effect in single-measurement mode")
    [sel, ok] = listdlg ("ListString", {"0.75", "1.5", "3", "7.5", "15
(Default)", "30", "75"},
                       "SelectionMode", "Single", "Name", "Data
rate");
    if (ok != 1)
        choice=previous;
    else
        choice=dr_LUT(sel);
    endif
endfunction

function [nc dc bc gc]=loadConf()
    load ./config.mat;
    nc=nsamples;
    dc=datarate;
    bc=bias;
    gc=gain;
endfunction

function saveConf(nc, dc, bc, gc)
    nsamples=nc;
    datarate=dc;
    bias=bc;
    gain=gc;
    save config.mat nsamples datarate bias gain;
endfunction

%Set some limits for the number of files or max run time for repeated
read to file
function [maxtime maxfiles]=stopcondmenu()
    prompt={"Run for (max)(s)" "Number of files (max)"};
    default={"9999" "9999"};
    stop_cstr=inputdlg(prompt,"Enter stop conditions",1,default);

    maxtime=str2double(stop_cstr{1});
    maxfiles=str2double(stop_cstr{2});
endfunction

function [filenumber filename_new] = filenameupdate(filenumber,
filename_old)
    ndigits=size(num2str(filenumber),2);
    if filenumber == 1
        ndigits=0;
    endif

```

```

filename_old_short = strtrunc(filename_old,size(filename_old,2)-
(4+ndigits));
filename_new=filename_old;
filenumber++;
filename_new=strcat(filename_old_short,num2str(filenumber),".mat");
endfunction

```

```

function [filenumber filename_new] =
firstavailablefilename(filename_old)

filename_old_short = strtrunc(filename_old,size(filename_old,2)-4)
filename_new=filename_old;
filenumber=1;
while exist(filename_new)==2;
    filenumber++;
    filename_new=strcat(filename_old_short,num2str(filenumber),".mat");
endwhile
endfunction

```

```

function [fullname, fpath] = filenamer(ssr_state_char)
if ssr_state_char=='B'
    [fname,fpath,fltidx]=uiputfile("./magdata_dark.mat","Save Magnetic
Measurements");
else
    [fname,fpath,fltidx]=uiputfile("./magdata.mat","Save Magnetic
Measurements");
endif
fullname=strcat(fpath,fname);
endfunction

```

## Appendix IV - Solver Octave Code

### Main - regtools\_ma.m

```

%%%%%%%%%%%%%%%%%%%%%%%%%%%%%%%%%%%%%%%%%%%%%%%%%%%%%%%%%%%%%%%%%%%%%%%%
%Load measured data
%%%%%%%%%%%%%%%%%%%%%%%%%%%%%%%%%%%%%%%%%%%%%%%%%%%%%%%%%%%%%%%%%%%%%%%%
%load log of dead sensors
mask = load('-ascii','path\to\mask.txt');
%define path to measured data
B0path='path\to\measured\b\files';
load([B0path,'\fileindex.mat']);
%Find frames at edges of current pulse
[bx by bz switch_frames]=Bswitch_read(B0path);
%Dark frames precede edge
dark_range=[switch_frames(1)-5:switch_frames(1)-1];
%Image frames come after edge
image_range=[switch_frames(1):switch_frames(1)+5];
%Average Dark frames
B03_dark=[mean(bx(:,:,dark_range),3) (mask==1)';mean(by(:,:,dark_range)
,3) (mask==1)';mean(bz(:,:,dark_range),3) (mask==1)'];
%Take a range of images
B03_image=[bx(:,:,image_range) (mask==1)';by(:,:,image_range) (mask==1) '
;bz(:,:,image_range) (mask==1)'];
%Mask image and dark for dead sensors
B03_image=[bxi(mask==1)';byi(mask==1)';bzi(mask==1)'];

```

```

B03_dark=[bxd(mask==1)';byd(mask==1)';bzd(mask==1)'];

B03=B03_image-B03_dark;
B0=B03(:);
%%%%%%%%%%%%%%%%%%%%%%%%%%%%%%%%%%%%%%%%%%%%%%%%%%%%%%%%%%%%%%%%%%%%%%%%

%%%%%%%%%%%%%%%%%%%%%%%%%%%%%%%%%%%%%%%%%%%%%%%%%%%%%%%%%%%%%%%%%%%%%%%%
%Load partial data
%%%%%%%%%%%%%%%%%%%%%%%%%%%%%%%%%%%%%%%%%%%%%%%%%%%%%%%%%%%%%%%%%%%%%%%%
%partial set 1 simulates a low conductance paste material
BpathCell(1)=cellstr('path\to\partial\b\files\sulfpaste');
%partial set 2 simulates a high conductance paste material
BpathCell(2)=cellstr('path\to\partial\b\files\leadpaste');
nsegs=20;
B=zeros(size(B0,1),nsegs*2);
Btemp=zeros(size(B0,1),nsegs);
for pset=1:2
for i=1:nsegs
[bx(:, :, i) by(:, :, i) bz(:, :, i)
Btemp(:, i)]=fetchbfiles6(char(BpathCell(pset)), i, 14, 16, 11, 9, 2);
endfor
partorder=(reshape([1:20], 5, 4)');
Btemp=Btemp(:, partorder(:));
B(:, (pset-1)*nsegs+1:pset*nsegs)=Btemp; %Put into complete set of
partials
endfor

B=B.*10^4; %Convert to Gauss
Bnq=B;
B=quantize(B, 1090);
%%%%%%%%%%%%%%%%%%%%%%%%%%%%%%%%%%%%%%%%%%%%%%%%%%%%%%%%%%%%%%%%%%%%%%%%

%%%%%%%%%%%%%%%%%%%%%%%%%%%%%%%%%%%%%%%%%%%%%%%%%%%%%%%%%%%%%%%%%%%%%%%%
%Tikhonov regularisation
%%%%%%%%%%%%%%%%%%%%%%%%%%%%%%%%%%%%%%%%%%%%%%%%%%%%%%%%%%%%%%%%%%%%%%%%
%See regtools by P.C. Hansen for function definitions
[U, s, V]=csvd(B);
figure;
[reg_corner, rho, eta, reg_param]=l_curve(U, s, B0);
[reg_corner2, rho_c, eta_c]=l_corner(rho, eta, reg_param, U, s, B0)
reglist=(0.5:0.1:8);

[xl, rho, eta]=tikhonov(U, s, V, B0, [reglist.*reg_corner 0.2]);
%%%%%%%%%%%%%%%%%%%%%%%%%%%%%%%%%%%%%%%%%%%%%%%%%%%%%%%%%%%%%%%%%%%%%%%%

%Combine extended sets of partials
xl=xl(1:20, :)+xl(21:40, :);

%%%%%%%%%%%%%%%%%%%%%%%%%%%%%%%%%%%%%%%%%%%%%%%%%%%%%%%%%%%%%%%%%%%%%%%%
%Plotting
%%%%%%%%%%%%%%%%%%%%%%%%%%%%%%%%%%%%%%%%%%%%%%%%%%%%%%%%%%%%%%%%%%%%%%%%
figure;
bar3_sk(reshape(xl(:, 6), 4, 5)); caxis([0 max(xl(:, 6))+0.01]);
%%%%%%%%%%%%%%%%%%%%%%%%%%%%%%%%%%%%%%%%%%%%%%%%%%%%%%%%%%%%%%%%%%%%%%%%

```

## Library

```

function [bx by bz switch_frames]=Bswitch_read(Bpath)
oldpath=pwd;

```

```

cd(Bpath)
[bx by bz file_index]=fetch_manyframes();
[dx swix]=find_switchon(bx);
[dy swiy]=find_switchon(by);
[dz swiz]=find_switchon(bz);

switch_frames=find(swix>4);

cd(oldpath);
endfunction

function [Vx Vy Vz]=fetch_specific_frames(fileNameRoot,fileSubIndex)
%Fetches Bxyz from a folder containg text files. Saves multiple 2D
%matrices as a 3D array if asked to fetch more than one frame
if ispc ==1
slash='\';
elseif isunix == 1
slash='/';
endif

%Set to 1 for average mode
avgset=0;
%Set to 1 for limited mode
limitset=1;
%Set a maximum allowed value for field strength in limited mode
limit = 1.24; %threshold
limres = 0+eps; %result of limit
cudir=pwd; %saves current directory as a string
fileindex=zeros(1,size(glob("*x*.txt"),1)); %Preallocate fileindex

Vxavg=0; %clear average value variables
Vyavg=0;
Vzavg=0;
avgcounter=0;
for j=1:size(fileSubIndex,2)
avgcounter=avgcounter+1;
%generates filenames to fetch x, y, z component files
filex = strcat(fileNameRoot,"x",num2str(fileSubIndex(j)),".txt");
filey = strcat(fileNameRoot,"y",num2str(fileSubIndex(j)),".txt");
filez = strcat(fileNameRoot,"z",num2str(fileSubIndex(j)),".txt");

%Reads magnetic field data as 3 arrays, 1 per dimension
tempx = load("-ascii", filex);
tempy = load("-ascii", filey);
tempz = load("-ascii", filez);

p=0;
q=0;

[sizeZ, sizeX] = size(tempx);

if sizeX > 32
tempx = tempx(:,1:32);
tempy = tempy(:,1:32);
tempz = tempz(:,1:32);
end

```

```

if sizeZ > 8
tempX = tempX(1:8,:);
tempY = tempY(1:8,:);
tempZ = tempZ(1:8,:);
end

[sizeZ, sizeX] = size(tempX);

if limitset == 1
for i = 1:(sizeX*sizeZ)
if tempX(i)>limit || tempY(i)>limit || tempZ(i)>limit
tempX(i) = tempX(i-1);
tempY(i) = tempY(i-1);
tempZ(i) = tempZ(i-1);
p = p+1; %counter for how many times limiter is used per plot
end

if tempX(i)< -limit || tempY(i) < -limit || tempZ(i) < -limit
tempX(i) = tempX(i-1);
tempY(i) = tempY(i-1);
tempZ(i) = tempZ(i-1);
q=q+1; %counter for how many times limiter is used per plot
end
end
Vx(:,:,j)=tempX;
Vz(:,:,j)=-tempY;
Vy(:,:,j)=-tempZ;
end
if size(Vx,3) > 1
Vx=median(Vx,3);
Vy=median(Vy,3);
Vz=median(Vz,3);
endif

endfunction

%Fetches simulated B files and puts them in orientation compatible
with
%measured B files. Ie x increasing left to right, z increasing top to
bottom
function [Bx By Bz Bcol] =
fetchbfiles6(Bpath,num,rowint,colint,rowstart,colstart,layer)
%increasing colstart moves measurement to the right, effectively
moving cell to the left. Max = 21. Neutral = 11
%increasing rowstart moves measurement up?, moving cell down. Max = 17.
Neutral = 9
%Fetch 'measured' data (actually simulated for now)
oldpath=pwd;
cd(Bpath);

Bxtmp=csvread(strcat('BxSm',layer,num2str(num)','.csv'),colstart,rowsta
rt);
%Bxtmp=rowfilter(Bxtmp,20);
rows=round([1:rowint:size(Bxtmp,1)]);
cols=round([1:colint:size(Bxtmp,2)]);
Bx=Bxtmp(rows,cols);

```

```

Bytmp=csvread(strcat('BySm',layer,num2str(num)','.csv'),colstart,rowsta
rt);
%Bytmp=rowfilter(Bytmp,20);
By=Bytmp(rows,cols);

Bztmp=csvread(strcat('BzSm',layer,num2str(num)','.csv'),colstart,rowsta
rt);
%Bztmp=rowfilter(Bztmp,20);
Bz=Bztmp(rows,cols);

%Change orientation to match measured B.
Bx=Bx';
By=By';
Bz=Bz';

if size(Bx,2)>32
Bx=Bx(:,1:32);
By=By(:,1:32);
Bz=Bz(:,1:32);
endif

if size(Bx,1)>8
Bx=Bx(1:8,:);
By=By(1:8,:);
Bz=Bz(1:8,:);
endif

%load mask
mask=ones(size(Bx));
mask=load('-ascii','path/to/mask.txt');

B=[Bx(mask==1)' ; By(mask==1)' ; Bz(mask==1)' ];

Bcol=B(:);

cd(oldpath)
endfunction

```

## Appendix V – Magnetic Imaging Code Acknowledgement

Magnetic imaging system hardware, embedded firmware and PC-side software is © James Green. All enquiries regarding the code should be directed to him at

Dr James Green  
 Department of Electronic & Electrical Engineering  
 The University of Sheffield  
 3 Solly Street  
 Level 1  
 Sheffield  
 S1 4DE

Email: [j.e.green@sheffield.ac.uk](mailto:j.e.green@sheffield.ac.uk)

